Samarium Oxide Based Nanomaterials for Heterogeneous Catalysis

Gregory K. Hodgson

A thesis by publication

Submitted to the Faculty of Graduate and Postdoctoral Studies

In partial fulfillment of the requirements for the degree of

Doctor of Philosophy in Chemistry

uOttawa

Université d'Ottawa – University of Ottawa

Department of Chemistry & Biomolecular Sciences

Faculty of Science

For Grayson, il mio tesoro.

May you keep smiling, forevermore.

"There was truth and there was untruth, and if you clung to the truth even against the whole world, you were not mad."

–George Orwell, from '1984'

"Intelligence is the ability to adapt to change."

–Stephen Hawking

Abstract

The emergence of unique or enhanced physical, chemical and optical material properties at the nanoscale underlies the swift rise of nanomaterials science over recent decades. Within this interdisciplinary field, catalysis performed by nanomaterials (i.e. nanocatalysis) is one area where differences between nanoscale and bulk material properties offer particularly attractive opportunities for application. The consequent pursuit of viable nanomaterials with unprecedented catalytic activity has inevitably expanded across the periodic table, whereby a number of highly efficient precious metal, metal oxide and composite nanostructured catalysts have been developed for a wide range of synthetic organic and inorganic transformations. The lanthanide series has not been excluded from this search, but is still underrepresented in catalysis despite some rich chemistry and reactivity which sets these elements apart from many other metals. More recently however, the necessary paradigm shift away from commonly utilized but expensive, potentially toxic precious metal catalysts, and toward more sustainable alternatives, has seen an upsurge in the development of novel nanomaterials for heterogeneous catalysis: the general topic of this doctoral thesis.

Heterogeneous nanocatalysis offers distinct advantages over homogeneous catalysis. Catalyst recyclability, ease of separation from reaction mixtures, and minimal product contamination all contribute to the higher overall effectiveness of heterogeneous catalysts relative to their homogeneous counterparts. The use of light as an abundant reagent, both in nanomaterial fabrication and for photocatalysis, is another attractive prospect. This dissertation addresses both points, describing the iterative development and application of photochemically-prepared samarium oxide based nanomaterials for heterogeneous catalysis and photocatalysis. Through a series of related peer-reviewed publications and associated commentary, the evolution of the application-driven design of a nanomaterial which is both efficient and effective for a diversity of heterogeneous catalytic and photocatalytic transformations

is presented. Major findings include 1) both colloidal and supported samarium oxide nanoparticles can be prepared photochemically and comprise primarily Sm_2O_3 but may contain localized mixed valences or dynamic surface oxidation states; 2) colloidal samarium oxide nanoparticles possess high activity for Brønsted acid and oxidative catalysis, but recyclability and overall effectiveness is less than optimal due to a combination of polydispersity and size-dependent catalytic activity; 3) a similarly-prepared “second generation” samarium oxide/titanium dioxide nanocomposite presented several advantages over its predecessor, performing highly efficient and effective pure heterogeneous, dual photoredox-Lewis acid catalysis in two different types of synthetically relevant photocyclizations. Effects of different nanoparticle supports, rare insights into the catalytic mechanisms and behaviour of these nanomaterials–obtained at the single molecule level by innovative application of Total Internal Reflection Fluorescence Microscopy (TIRFM) to catalysis research–as well as advances in TIRFM data analysis protocols, are also discussed.

Acknowledgements

I would like to begin by expressing profound gratitude to my supervisor, Tito Scaiano. Thank you Tito, first and foremost for the opportunity to work and learn in one of the most renowned and well-equipped laboratories for photochemistry and nanomaterials science. You recognized a source of potential energy, and invited me into your group after only a brief first meeting. Thank you for that show of confidence, and for taking a chance on me. Over the many meetings that followed, I grew to appreciate more and more the wealth of photochemical knowledge you possess, and I thank you for sharing even a fraction of it with me. For all you have contributed to my growth as a scientist, perhaps the most valuable element was your hands-off approach. Allowing me the freedom to explore different research directions as I saw fit, to write manuscripts and to speak at conferences, to experience successes, and failures, and to follow the research wherever it may lead, has been instrumental in the development of my critical thinking and science communication skills. It has helped me learn to become a capable independent researcher, but it has also taught me a lot about mentoring and effective leadership. For that, I will forever be grateful.

My sincere thanks to Tom Baker and Linda Johnston, not only for serving on my thesis advisory committee, but for your course lectures and your feedback and your intriguing questions at every milestone in my graduate studies. You set outstanding examples of professionalism and I have learned much from you both. I am also indebted to Matthew Thompson and Andrew Vreugdenhil, who were excellent mentors, supervised my undergraduate thesis, and stimulated my interest in graduate level research and in chemistry in general.

In less than five years, a lot has changed. Many amazing nouns have come into my life, and others have faded away. But my time in the Scaiano group would not have been the same without Christopher McTiernan, Spencer Pitre, Matt Decan, Geniece Hallett-Tapley, and Michel Grenier, who each made this chapter memorable in his or her own way, both inside and outside of the lab. Learning from, and working alongside each of you has made me a better science-person, and occasionally provided a dash of welcomed comic relief besides. Thank you all for that.

I further wish to thank my parents, Julie and Doug, and my sister Roxanne, who have always encouraged me to pursue anything I wanted to do, and without whom I would not be where I am today. Earning a doctorate has been my primary goal for years and I have worked very hard to attain it. However, a great many things fell into place in order for me to arrive here, in this moment. The most incredible part of this journey is that I found the love of my life along the way. Stefania, amore mio, I have you to thank most of all. In a few short years, you have helped to shape a green undergraduate into a proficient scientist. I have learned more from you than I could in a lifetime of study, and I cherish every memory and every day of the life we are building together. Your deep knowledge of chemistry, keen intellect, and ability to passionately discuss everything from our research, to politics, to art, to philosophy, has helped me to grow in so many ways. You have shown me new places, new culture, and made me a proud husband and father. The sequence of events necessary to bring us together is staggering; countless little decisions, and chance encounters, all led me to you. To begin with an ocean between us, and a cultural divide that could be even larger, words cannot express how fortunate I feel to have you, and now Grayson, at the centre of my life. Vi voglio bene, grazie mille. Grazie a tutti, thank you.

Contribution Statement

All of the research presented within this dissertation was conducted under the supervision of Professor Tito Scaiano. The body of this thesis is based upon four peer-reviewed publications for which I am the leading author. So while the majority of the experimental work and manuscript writing was completed by me personally, it would be discourteous and unfair to assert that I acted on an entirely independent basis! I have been fortunate to have had opportunities to collaborate with a number of colleagues during my time in the Scaiano group, many of whom I now consider friends. These amazing people made invaluable contributions to my general training and knowledge of chemistry, and some of our work together resulted in peer-reviewed publications. Cases where I made a direct contribution to the project, but am listed as co-author of the publication, have been noted in the appropriate portion of the List of Publications but have not been discussed in detail in this thesis. In this section I wish to point out some of my own direct contributions to the work that is covered in each body chapter of this thesis, and also to respectfully highlight the intellectual and physical contributions made by each of my collaborators.

The photochemical synthesis and characterization of samarium oxide nanoparticles, my first project as a graduate student, was largely overseen by Dr. Stefania Impellizzeri and Dr. Geniece Hallett-Tapley, both of whom are former postdoctoral researchers in the Scaiano group, and now professors themselves. Along with Dr. Scaiano himself, Dr. Hallett-Tapley and Dr. Impellizzeri provided daily supervision of my experiments, hands-on training, intellectual support, suggested experiments, and were plagued with my endless questions. The halochromic molecular assembly used to probe the Brønsted acidity of Sm_2O_3NP was synthesized by Dr. Impellizzeri. The remainder of the experiments were performed by me personally, either independently or in the presence of Dr. Impellizzeri or Dr. Hallett-Tapley. This work would not have been possible without either of them and I credit them both with teaching me many of the laboratory and research skills that started me on the right path toward a successful doctoral research program.

The application of the Brønsted acidity of Sm_2O_3NP in the Pechmann reaction to produce coumarin 153, as a means of fluorescence activation to facilitate monitoring the catalysis at the single molecule level, was conceived by Dr. Impellizzeri. Although I performed all of the experimental work myself, Dr. Impellizzeri was heavily involved in training me on everything from column and preparative thin layer chromatography to Total Internal Reflection Fluorescence Microscopy (TIRFM) and Fluorescence Lifetime Imaging (FLIM). Fellow graduate students Matt Decan (now Dr. Decan) and Spencer Pitre (now Dr. Pitre) also contributed by my knowledge of TIRFM and FLIM techniques. Dr. Scaiano and Dr. Impellizzeri suggested several of the experiments, and we regularly engaged in productive discussions, especially regarding the interpretation of single molecule data. I personally programmed the MatLab protocol used to increase the efficiency and reliability of the analysis of TIRFM image data, and I was the main contributor to writing the manuscript.

In the investigation of oxidative catalysis by Sm_2O_3NP, Dr. Impellizzeri designed the supramolecular system that shifted the wavelength of fluorescence upon product formation and thereby facilitated monitoring the catalysis by single molecule fluorescence microscopy. We performed many of the bench scale and TIRFM experiments together, and both made significant contributions to writing the manuscript. Dr. Impellizzeri performed catalyst recyclability experiments and much of the optimization of bench scale reaction conditions. I performed the majority of control experiments, as well as those related to the catalytic behaviour and mechanism, both on the bench scale and at the single molecule level.

I conceived of the idea to support samarium oxide nanoparticles on various matrices for heterogeneous (photo)catalysis. I explored chemical and photochemical routes toward this goal, and optimized the photochemical synthesis of the final nanocomposite material. I tested several candidate systems for catalysis before my colleague, Spencer Pitre, suggested I read an inspiring review by Yoon on photoredox catalysis. I selected the Lewis acid mediated systems that were eventually heterogenized, conducted background research, performed all of the experimental work, and wrote the manuscript. Spencer and I engaged in helpful discussions about photoredox catalysis and Dr. Scaiano provided guidance and supervised the project.

Table of Contents

List of Publications

Publications Presented in this Thesis

Hodgson, G. K.; Impellizzeri, S.; Hallett-Tapley, G. L.; Scaiano, J. C. Photochemical Synthesis and Characterization of Novel Samarium Oxide Nanoparticles: Toward a Heterogeneous Brønsted Acid Catalyst. *RSC Adv*. **2015**, *5*, 3728-3732.

Hodgson, G. K.; Impellizzeri, S.; Scaiano, J. C. Dye Synthesis in the Pechmann Reaction: Catalytic Behaviour of Samarium Oxide Nanoparticles Studied Using Single Molecule Fluorescence Microscopy. *Chem. Sci*. **2016**, *7*, 1314-1321.

Hodgson, G. K.; Impellizzeri, S.; Scaiano, J. C. Single Molecule Study of Samarium Oxide Nanoparticles as a Purely Heterogeneous Catalyst for One-Pot Aldehyde Chemistry. *Catal. Sci. Technol*. **2016**, *6*, 7113-7121.

Hodgson, G. K.; Scaiano, J. C. Heterogeneous Dual Photoredox-Lewis Acid Catalysis Using a Single Bifunctional Nanomaterial. *ACS Catal*. **2018**, *8*, 2914-2922.

Co-Authored Publications Not Discussed in this Thesis

Impellizzeri, S.; Simocelli, S.; Fasciani, C.; Marin, M. L.; Hallett-Tapley, G. L.; Hodgson, G. K.; Scaiano, J. C. Mechanistic Insights into the Nb_2O_5 and Niobium Phosphate Catalyzed *In Situ* Condensation of a Fluorescent Halochromic Assembly. *Catal. Sci. Technol*. **2015**, *5*, 169-175.

Impellizzeri, S.; Simoncelli, S.; Hodgson, G. K.; Lanterna, A. E.; McTiernan, C. D.; Raymo, F. M.; Aramendia, P. F.; Scaiano, J. C. Two-Photon Excitation of a Plasmonic Nanoswitch Monitored by Single Molecule Fluorescent Microscopy. *Eur. J. Chem*. **2016**, *22*, 7281-7287.

List of Figures

List of Schemes

List of Supplementary Videos

Supplementary Video 1 Pertains to Chapter 3, and provides a representative example of one of many TIRFM image sequences showing bright bursting events against a dark background, corresponding to Sm_2O_3NP-mediated fluorescence activation by catalytic formation of single molecules of emissive coumarin 153 from non-emissive reagents. This raw data, obtained by TIRFM, was used to analyze and interpret catalyst behaviour at the single molecule level.

Accessible via the internet, free of charge, at:
http://pubs.rsc.org/en/content/articlelanding/2016/sc/c5sc03214h#!divAbstract

Supplementary Video S1 Pertains to Chapter 4, providing a representative example of one of many TIRFM image sequences showing bright bursting events against a dark background. Single molecule bursting events correspond to Sm_2O_3NP-mediated fluorescence shifting by catalytic oxidation of a fluorescent hydroxyl-functionalized coumarin substrate coupled to a non-catalytic condensation with indolium to generate a fluorescent product with substantially red-shifted absorbance and emission. This raw data, obtained by TIRFM, was used to analyze catalyst behaviour and mechanistic dynamics.

Accessible via the internet, free of charge, at:
http://pubs.rsc.org/en/content/articlelanding/2016/cy/c6cy00894a#!divAbstract

List of Tables

List of Abbreviations

[ ]	concentration
4-HEBA	4-(2-hydroxyethoxy)-benzoic acid
ATR	attenuated total reflectance
BA	Brønsted acid
BE	binding energy
CB	conduction band
CW	continuous wave
DABCO	1,4-diazabicyclo[2.2.2]octane
DCA	dicinnamalacetone
DCM	dichloromethane
DMF	dimethylformamide
DMSO	dimethylsulfoxide
DLS	dynamic light scattering
DR	diffuse reflectance
E_{bg}	band gap energy
EI	electron impact
EDG	electron-donating group
EDS	energy dispersive X-ray spectroscopy
Em	emission
EM-CCD	electron multiplier charge coupled device
E_{red}	reduction potential
ESI	electrospray ionization
EtOAc	ethyl acetate
EtOH	ethanol
equiv	equivalent
EWG	electron-withdrawing group
Ex	excitation
FACS	fluorescence activated cell sorting
FCS	fluorescence correlation spectroscopy

FLIM	fluorescence lifetime imaging
FTIR	Fourier transform infrared
GLRT	generalized likelihood ratio test
H^+	proton
h^+	hole(s)
H_0	Hammett acidity function
HPLC	high performance liquid chromatography
hν	light
I-2959	Irgacure 2959
ICP	inductively coupled plasma
i-Pr_2NEt	*N,N*-diisopropylethylamine
LA	Lewis acid
LED	light emitting diode
MeCN	acetonitrile
MeO	methoxy
MeOH	methanol
MS	mass spectrometry
NA	numerical aperture
NIR	near infrared
NMR	nuclear magnetic resonance
NP	nanoparticle
ox	oxidation
PFA	probability of false alarm
Ph	phenyl
pK_a	acid dissociation constant
ppm	parts per million
PSF	point spread function
px	pixel
Q-TOF	quadrupole time of flight
rbf	round-bottom flask
red	reduction

ROI	region of interest
ROMP	ring-opening metathesis polymerization
rpm	revolutions per minute
$Ru(bpy)_3^{2+}$	tris(2,2'-bipyridyl)ruthenium(II)
SCE	saturated calomel electrode
SEM	scanning electron microscopy
SET	single electron transfer
Sm_2O_3NP	samarium oxide nanoparticles
S/N	signal to noise
TEM	transmission electron microscopy
TFA	trifluoroacetic acid
THF	tetrahydrofuran
TIR	total internal reflection
TIRFM	total internal reflection fluorescence microscopy
TLC	thin layer chromatography
TOF	turnover frequency
TON	turnover number
UV	ultraviolet
VB	valence band
Vis	visible
XPS	X-ray photoelectron spectroscopy
XRD	X-ray diffraction
δ	chemical shift
η	refractive index
θ_c	critical angle
θ_i	angle of incidence
λ	wavelength

1. Introduction

1.1 Opening Remarks

This doctoral thesis comprises a series of four peer-reviewed publications and the associated supporting information, presented in chronological order alongside additional commentary intended to provide further insights and to emphasize the already strong ties between chapters. Taken together, these works embody the general topic of this dissertation: the iterative design of a versatile, multifunctional samarium-functionalized nanomaterial for application in heterogeneous catalysis. Throughout this thesis, a distinction will repeatedly be drawn between efficiency and overall effectiveness of nanomaterials for catalytic applications. The objective here is as much to provide an additional means by which to evaluate and compare the relative utilities of different catalysts as it is to incite thought-provoking dialogue regarding the responsible and sustainable development of new nanomaterials for catalysis. It may therefore be useful to begin by defining the terms '*efficiency*' and '*effectiveness*' in the context of this thesis. Efficiency refers to the physical, chemical and optical characteristics of a nanomaterial, such as acidity, light absorption and catalytic activity in specific reactions (i.e. substrate conversion, product yield and selectivity). Effectiveness on the other hand, will instead reflect a larger perspective in terms of real-world applications; it will focus on catalyst recyclability, ease of separation, lack of product contamination, and general sustainability. Effectiveness will also be used to highlight the importance of subtle differences between variations of heterogeneous and homogeneous catalysis, which can carry significant weight in scaled up applications.

Another recurring theme within this thesis will therefore be the importance of expanding the toolkit available to the modern chemist, for characterizing the catalytic

behaviour of nanomaterials. Single molecule fluorescence microscopy has emerged as one of those contemporary tools, and a portion of this thesis is devoted not only to demonstrating its utility in providing invaluable insights into catalytic mechanisms and for distinguishing pure from hybridized heterogeneous or homogeneous catalysis, but also to improving the efficiency, reliability and general ease of incorporating single molecule techniques into catalysis research. In particular, the research presented in this thesis made significant use of Total Internal Reflection Fluorescence Microscopy (TIRFM), a technique originally developed and conventionally used to image biological samples.

Relative to widefield epifluorescence microscopy, TIRFM benefits from a higher signal to noise (S/N) ratio owing to the spatial restriction of fluorophore excitation, and hence observable fluorescence, to within a region close to the sample surface (Figure 1.1). Laser light impinging upon a cover glass supporting a sample medium of lower refractive index (η), when its angle of incidence (θ_i) exceeds the critical angle (θ_c), will not be refracted into the sample medium; rather, it experiences total internal reflection, generating an evanescent wave propagating parallel to the sample surface and decaying exponentially in the axial dimension. It is this exponential decay that enhances the S/N ratio by ensuring that only individual fluorophores located within the evanescent field are excited.[1-3]

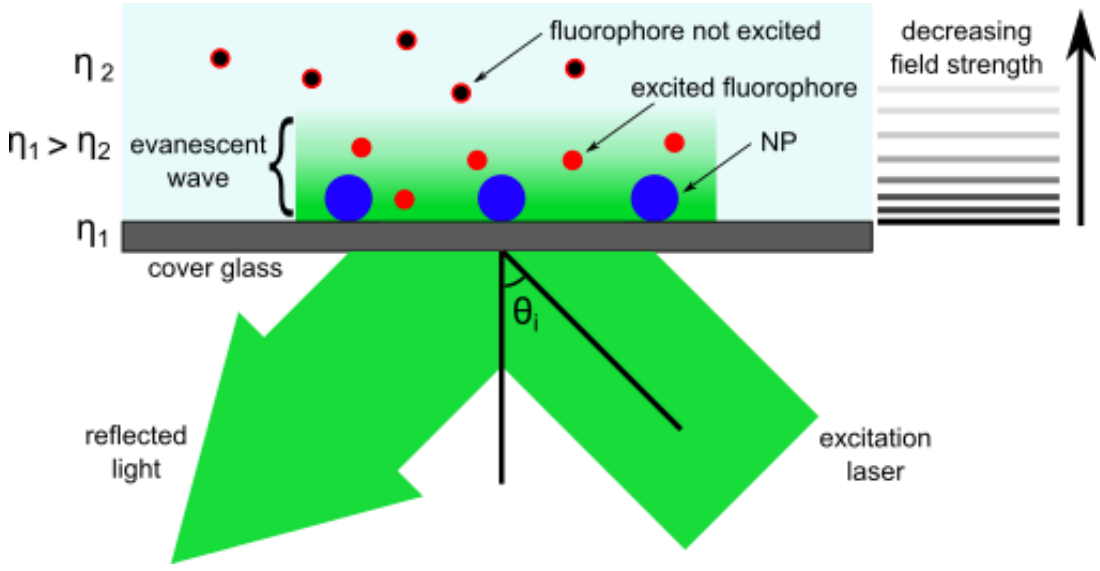

Figure 1.1 Diagram showing fundamental aspects of TIRFM configured to study nanocatalysis and the origin of the increased S/N ratio relative to widefield epifluorescence microscopy.

The critical angle is given by Equation 1:[2]

$$\theta_c = \mathbf{sin^{-1}}\left(\frac{\eta_2}{\eta_1}\right) \quad (1)$$

In addition to θ_i, the distance (d) that the region of increased S/N ratio extends outward from the sample surface also depends upon the excitation wavelength (λ_i), and is given by Equation 2:[2]

$$d = \frac{\lambda_i}{4\pi[\eta_1^2 \sin^2(\theta_i) - \eta_2^2]^{1/2}} \quad (2)$$

By coating or functionalizing a microscope coverslip with catalytically active nanoparticles (NPs) and subsequently recording an image sequence while exposing the sample to an aqueous or organic medium containing a mixture of suitable reagents, spatiotemporal catalytic conversion can be followed in real time, at the single molecule level, via catalytic fluorescence activation, fluorescence wavelength shifting, or Förster Resonance Energy Transfer (FRET) mechanisms.[3,4] These strategies for adapting TIRFM, as well as other techniques such as Fluorescence Correlation Spectroscopy (FCS), Fluorescence Lifetime Imaging (FLIM), and confocal fluorescence microscopy, to study catalysis, have led to outstanding contributions to the chemistry body of knowledge.[5] Such techniques are progressively making their way into mainstream organic and materials chemistry research, where co-localization of NPs, active sites and catalytic product formation has become an impressive tool for better understanding catalytic reaction mechanisms and kinetics.[6]

The catalytic systems described in this thesis are not only interesting from the perspective of single molecule catalysis research, these specific examples of nanocatalysis each present efforts toward enhancing the efficiency of a range of synthetically relevant organic transformations through the development of heterogeneous nanocatalysis. In this context, nanomaterials based upon lanthanides such as samarium, which is actually more abundant than many transition metals, may present an opportunity to develop highly active, easily separable, reusable heterogeneous nanocatalysts that could become sustainable alternatives to common organometallic homogeneous catalysts and bulk oxide heterogeneous catalysts alike.

1.2 Synopsis

The body of this thesis will begin with the first reported preparation of samarium oxide nanoparticles (Chapter 2). This photochemical synthesis was adapted from seminal work by Tito Scaiano and co-authors at the University of Ottawa, on photochemical routes to noble metal nanostructures such as gold and silver nanoparticles.[7] Characterization of these samarium oxide nanoparticles revealed that they are roughly spherical, highly polydisperse (ca. 70-700 nm), and are composed primarily of Sm_2O_3. Moreover, this new nanomaterial, labeled as Sm_2O_3NP, was found to possess significant Brønsted acidity. This property suggested that Sm_2O_3NP might function as a potent heterogeneous Brønsted acid (BA) catalyst, and efforts to realize the material's potential for such an application commenced without delay. Incidentally, the outcome of this work hinted at more than one potential application of samarium-based NPs in different types of heterogeneous catalysis, which ultimately formed the backbone of my doctoral research. In point of fact, the customized halochromic supramolecular assembly (Figure 2.3) used to demonstrate the Brønsted acidity of Sm_2O_3NP, and the final product of the chemistry illustrated in Figure 4.1, which allowed the reaction to be monitored at the single molecule level, both share the same chromophore. The same is true of the product of the catalytic system used in my first peer-reviewed publication as co-author, to study heterogeneous BA catalysis by solid niobium oxide materials (Section 7.1). Upon the basis of a preliminary investigation into the acidic properties of Sm_2O_3NP, specifically the identification of the presence of Brønsted acid sites on the surfaces of Sm_2O_3NP, an obvious target for their first practical application in catalysis was to evaluate the performance of the new nanomaterial in a well-known BA catalyzed reaction (Chapter 3).

Quantification of the acidic properties of Sm_2O_3NP, described in Chapter 2, initiated a full-scale investigation of the utility of colloidal Sm_2O_3NP for Brønsted acid catalysis. Chapter 3 covers this research in detail, showing that Sm_2O_3NP are indeed an efficient catalyst for the preparation of a useful organic dye under mild conditions. Incorporating single molecule fluorescence microscopy into the investigation of catalyst behaviour compounded the impact and originality of this work, by establishing a benchmark for distinguishing between pure and hybridized heterogeneous and

homogeneous catalysis. The innovative computer programming protocol developed in order to assist with handling the analysis of large quantities of image data obtained by TIRFM not only reduced the time required for TIRFM data analysis by many orders of magnitude, it also removed a large element of experimental bias and greatly improved the accuracy and precision of results. This achievement was critical to facilitating a large scale single molecule investigation of the catalytic behaviour of a new nanomaterial, complete with all of the required control experiments and optimization of conditions, in a timely fashion, and has already paved the way for colleagues to move forward with similar single molecule investigations. In this case, the interpretation of TIRFM experimental results revealed that BA catalysis by Sm_2O_3NP was not a purely heterogeneous process. Although catalysis did occur on the surfaces of NPs, only the smallest NPs in the polydisperse material represented the catalytically active species. The subpopulation of active NPs were subsequently discovered to form a stable colloid and thus to act in a 'semi'-heterogeneous fashion. These insights, obtained upon the basis of single molecule experiments where none were apparent at the bench scale, further led to the realization that the active colloidal catalytic NPs could easily be separated from the product by increasing the ionic strength. In this way, single molecule fluorescence microscopy directly contributed to enhancing the overall effectiveness of the semi-heterogeneous BA catalyst.

The research presented in Chapter 4 carries forward the concept of effectiveness, by incorporating a supramolecular strategy that 1) increased phase separation *a priori* by building high ionic strength directly into the catalytic system; 2) allowed the product yield to be determined by ensemble-averaged absorption spectroscopy; and 3) facilitated a study of both the catalytic behaviour and mechanism at the single molecule level. Given that bulk Sm(III) and Sm(II) oxides are known to interconvert,[8] it was logical to next pursue applications of Sm_2O_3NP in redox catalysis. Chapter 4 describes the successful use of Sm_2O_3NP for heterogeneous catalytic oxidation of an OH–functionalized substrate for one-pot aldehyde-like chemistry. The advantage of this design is that hydroxylated substrates are easier to procure synthetically, and less expensive to obtain commercially, relative to the corresponding aldehyde. As an added benefit, the interesting nature of the heterogeneous catalytic

mechanism exhibited by Sm_2O_3NP is likely to factor into the lack of any observed over-oxidation to the carboxylic acid. We again relied upon single molecule fluorescence microscopy to identify the true catalytically active species (again the small NPs in polydisperse Sm_2O_3NP) and additionally were able to employ sequential two-colour TIRFM to establish an experimental basis for the proposed catalytic mechanism. This mechanistic behaviour resembles that of ruthenium NPs while catalyzing alcohol oxidation coupled to Wittig olefination chemistry, and the experimentally observed ability of Sm_2O_3NP to also catalyze that reaction points to possible similarities between the efficiencies of samarium- and more expensive ruthenium-based nanomaterials for applications in catalysis.

Efforts toward heterogeneous redox catalysis by Sm_2O_3NP partially inspired later work using supported samarium oxide NPs for the first examples of fully heterogeneous dual photoredox-Lewis acid catalysis (Chapter 5). Inspiration for the latter was also drawn from the known potency of samarium-based Lewis acids (LAs) such as samarium triflate, the reducing power of SmI_2 and insights discussed in Chapters 3 and 4 related to the apparent size- and surface-dependent nature of the catalytic activity exhibited by Sm_2O_3NP. The decision to combine samarium oxide nanoparticles with titanium- and cerium-based supporting oxides came after efforts to reduce the average size and polydispersity of Sm_2O_3NP were unsuccessful. Laser drop ablation and calcination of the as-prepared Sm_2O_3NP were each attempted but caused either particle decomposition or catalytic deactivation. However, the research described in Chapters 3 and 4 indicated that smaller, more catalytically active NPs were already present in the original polydisperse Sm_2O_3NP material. Unfortunately, efforts to isolate these NPs by innovatively applying Fluorescence Activated Cell Sorting (FACS), a flow cytometry technique, to nanomaterials science were fruitless due to NP instability in the separation medium (unpublished results). Serendipitously, augmenting the photochemical NP synthesis by carrying it out in the presence of titanium dioxide led to the formation of a samarium oxide/titanium dioxide nanocomposite containing very small (ca. 1.2 nm) and much more monodisperse NPs. Not only did this development improve the efficiency of the nanocatalyst preparation, the nanomaterial prepared with this new methodology, labeled $Sm_xO_y@TiO_2$, was

found to possess considerable Lewis acidity and photocatalytic activity. Chapter 5 provides a detailed account of the application of $Sm_xO_y@TiO_2$ for efficient and effective heterogeneous dual photoredox-LA catalysis. Heterogeneous analogues of popular homogeneous photoredox systems were explored, as well as preliminary substrate scopes; in all instances, $Sm_xO_y@TiO_2$ exhibited significant utility for both intermolecular net reductive, and intramolecular net neutral, Lewis acid mediated photocyclizations. Through these two model examples of synthetically relevant heterogeneous dual photoredox-LA catalysis, the first of their kind in this emerging field, $Sm_xO_y@TiO_2$ was shown to be a potentially viable substitute for less sustainable, precious metal based catalysts. This investigation laid the groundwork for further studies centred about the development of new bifunctional nanomaterials for sustainable heterogeneous, an area where rapid expansion is expected to be imminent.

1.3 References

(1) Esfandiari, N. M.; Blum, S. A. *J. Am. Chem. Soc*. **2011**, *133*, 18145-18147; Sambur, J. B.; Chen, P. *Annu. Rev. Phys. Chem*. **2014**, *65*, 395-422.

(2) Martin-Fernandez, M. L.; Tynan, C. J.; Webb, S. E. D. *J. Microsc*. **2013**, *252*, 16-22.

(3) Decan, M. R.; Impellizzeri, S.; Marin, M. L.; Scaiano, J. C. *Nature Commun*. **2014**, *5*, 4612.

(4) De Cremer, G.; Sels, B. F.; De Vos, D. E.; Hofkens, J.; Roeffaers, M. B. J. *Chem. Soc. Rev*. **2010**, *39*, 4703-4717; Carillo, A. I.; Stamplecoskie, K. G.; Marin, M. L.; Scaiano, J. C. *Catal. Sci. Technol*. **2014**, *4*, 1989-1996; Marin, M. L.; Hallett-Tapley, G. L.; Impellizzeri, S.; Fasciani, C.; Simoncelli, S.; Netto-Ferreira, J, C.; Scaiano, J. C. *Catal. Sci. Technol.* **2014**, *4*, 3044-3052; Impellizzeri, S.; Simoncelli, S.; Fasciani, C.; Marin, M. L.; Hallett-Tapley, G. L.; Hodgson, G. K.; Scaiano, J. C. *Catal. Sci. Technol.* **2015**, *5*, 169-175. Hodgson, G. K. Impellizzeri, S.; Scaiano, J. C. Chem. Sci. **2016**, *7*, 1314-1321.

(5) Roeffaers, M. B. J.; De Cremer, G.; Libeert, J.; Ameloot, R.; Dedecker, P.; Bons, A.-J.; Buckins, M.; Martens, J. A.; Sels, B. F.; De Vos, D. E.; Hofkens, J. *Angew. Chem. Int. Ed*. **2009**, *48*, 9285-9289; Buurmans, I. L. C.; Weckhuysen, B. M. *Nature Chem*. **2012**, *4*, 873-886; Hensle, E. M.; Blum, S. A. *J. Am. Chem. Soc.* **2013**, *135*, 12324-12328; Ristanovic, Z.; Kerssens, M. M.; Kubarev, A. V.;

Hendriks, F. C.; Dedecker, P.; Hofkens, J.; Roeffaers, M. B. J.; Weckhuysen, B. M. *Angew. Chem. Int. Ed*. **2015**, *54*, 1836-1840.

(6) Janssen, K. P. F.; De Cremer, G.; Neely, R. K.; Kubarev, A. V.; Van Loon, J.; Martens, J. A.; De Vos, D. E.; Roeffaers, M. B. J.; Hofkens, J. *Chem. Soc. Rev.* **2014**, *43*, 990-1006; Hodgson, G. K.; Impellizzeri, S.; Scaiano, J. C. *Catal. Sci. Technol*. **2016**, *6*, 7113-7121.

(7) McGilvray, K. L.; Decan, M. R.; Wang, D.; Scaiano, J. C. *J. Am. Chem. Soc.* **2006**, *128*, 15980-15981; Scaiano, J. C.; Netto-Ferreira, J. C.; Alarcon, E.; Billone, P.; Bueno-Alejo, C. J.; Crites, C. L.; Decan, M. R.; Fasciani, C.; Gonzalez-Bejar, M. Hallett-Tapley, G. L.; Grenier, M.; McGilvray, K. L.; Pacioni, N. L.; Pardoe, A.; Rene-Boisneuf, L.; Schwartz-Narbonne, R.; Silvero, M. J.; Stamplecoskie, K.; Wee, T. *Pure Appl. Chem.* **2011**, *83*, 913-930; Scaiano, J. C.; Stamplecoskie, K. G.; Hallett-Tapley, G. L. *Chem. Commun.* **2012**, *48*, 4798-4808; Malyshev, D.; Bosca, F.; Crites, C.-O. L.; Hallett-Tapley, G. L.; Netto-Ferreira, J. C.; Alarcon, E. I.; Scaiano, J. C. *Dalton Trans.* **2013**, *42*, 14049-14052; Scaiano, J. C.; Stamplecoskie, K. G.; McGilvray, K. L.; Pacioni, N. L. *E. Rad. Chem. Biol. Mat.* **2012**, DOI: 10.1002/9780470971253.rad068; Alarcon, E.; Bueno-Alejo, C. J.; Noel, C. W.; Stamplecoskie, K. G.; Pacioni, N. L.; Poblete, H.; Scaiano, J. C. *J. Nanopart. Res.* **2013**, *15*, 1374, 1-14.

(8) Sarma, D. D.; Hegde, M. S.; Rao, C. N. R. *J. Chem. Soc. Faraday Trans. 2*, **1981**, *77*, 1509-1520; Ekstrom, A.; Lapszewicz, J. A. *J. Am. Chem. Soc.* **1988**, *110*, 5226-5228; Jiang, Z.; Zhou, W.; Tan, D.; Zhai, R.; Bao, X. *Surf. Sci.* **2004**, *565*, 269-278; Juel, M.; Samuelsen, B. T.; Kildemo, M.; Raaen, S. *Surf. Sci.* **2006**, *600*, 1155-1159; Kuchowicz, M.; Kocaczkiewicz, J. *Surf. Sci.* **2008**, *602*, 3721-3727; Nguyen, T.-D.; Mrabet, D.; Do, T.-O. *J. Phys. Chem. C* **2008**, *112*, 15226-15235; Nguyen, T.-D.; Dinh, C.-T.; Do, T.-O. *Langmuir*, **2009**, *25*, 11142-11148; Nguyen, T.-D.; Dinh, C.-T.; Nguyen, D.-T.; Do, T.-O. *J. Phys. Chem. C* **2009**, *113*, 18584-18595; Xu, Q.; Hu, S.; Cheng, D.; Feng, S.; Han, Y.; Zhu, J. *J. Chem. Phys.* **2012**, *136*, 154705; Cheng, D.; Xu, Q.; Han, Y.; Ye, Y.; Pan, H.; Zhu, J. *J. Chem. Phys.* **2014**, *140*, 094706.

2. Photochemical Synthesis and Characterization of Novel Samarium Oxide Nanoparticles: Toward a Brønsted Acid Catalyst

2.1 Preamble to Chapter 2

The first step toward developing a new material for applications in heterogeneous catalysis is often fundamental experimentation. Hindsight may be 20/20, but real research is usually dynamic and exploratory, expanding and evolving over time, typically involving some degree of trial-and-error. Rarely does one possess the foresight and ability to conceive of a complex and optimally functioning chemical system *a priori*, purposefully set out to realize it in a laboratory setting, and be fortuitous enough that the outcome is precisely as anticipated. Unexpected results, low yields, side-reactions and outright failures take research in new directions and can sometimes provide insights which ultimately produce serendipitous scientific discoveries. This is particularly true in nanomaterial science, where often the only way to truly comprehend the full breadth of potential applications for a newly conceived material is to first make it.

The following chapter describes an initial foray into the realm of nanomaterials science, outlining the development of a published synthetic protocol and material characterization for a new nanostructured catalyst: samarium oxide nanoparticles. The original motivation for this line of research was to expand the scope of a tried and tested photochemical method for the preparation of various metal and metal oxide nanoparticles, with the underlying suspicion that the unique, rich chemistry of the lanthanide series, if combined with the known emergence of unconventional properties on the nanoscale, might translate to previously unrecognized applications in catalysis.

2.2 Postprint Version of Manuscript

First published in: *RSC Adv.* **2015**, *5*, 3728-3732.

Abstract

Samarium oxide nanoparticles (Sm_2O_3NP) were prepared photochemically for the first time. Characterization shows spherical, polydisperse Sm_2O_3NP stabilized by 4-HEBA, a substituted benzoic acid. The Sm_2O_3NP also possess Brønsted acidity. This new material may prove to be a potent heterogeneous acid catalyst.

Introduction

In the ongoing pursuit of new and useful catalytic materials, nanochemistry has become a popular strategy for discovery and innovation. Widespread research has led to a library of nanoparticle (NP) synthesis techniques, and cutting-edge photochemical methods have recently provided environmentally benign, cost-effective synthetic routes.[1,2] Many nanomaterials consist of well-characterized components possessing catalytic properties that can only be accessed at the nanoscale. In this context, gold and silver NPs and nanoclusters are prime examples.[3] Other nanocatalysts are modelled after well-performing bulk metal catalysts in an effort to increase efficiency further.[4] The lanthanide series remains relatively unexplored, and represents a potentially untapped resource for the development of new nanostructures with as-yet undocumented catalytic properties. Samarium-based compounds may present such an opportunity. As an element, samarium is actually quite abundant[5] and already has some niche applications (e.g. samarium–cobalt magnets).[6] Samarium triflate is a potent Lewis acid catalyst,[7] and SmI_2 has been utilized extensively as a versatile reducing agent for single electron transfer reactions.[8] Other samarium-based homogeneous catalysts have been employed in the degradation of polychlorinated biphenyls[9] and in the dehydration of alcohols.[10] Bulk samarium oxide catalyzes the oxidation of methane, ethane and ethylene.[11,12,13] Little is known however, about how samarium and its oxides (Sm_2O_3 and SmO) behave at the nanoscale. Of the few examples of samarium oxide NP synthesis in the literature,[13,14] lengthy procedures, safety concerns and supercritical conditions are obvious disadvantages. Faster, safer,

environmentally friendly synthetic strategies are required if the potential to use these and other lanthanide-based materials for catalysis is to be investigated further. Here we report a simple photochemical route to novel samarium oxide nanoparticles (Sm_2O_3NP) possessing physicochemical properties that have the potential to make this new nanomaterial a potent heterogeneous Brønsted acid catalyst.

Results and Discussion

Novel Sm_2O_3NP were prepared photochemically, by UVA irradiation of the benzoin Irgacure-2959™ (I-2959) photoinitiator in the presence of samarium nitrate hexahydrate (Scheme 2.).

Scheme 2.1 Photochemical preparation of Sm_2O_3NP in CH_3CN. The small arrow in equation 2 denotes the eventual reduction of the intermediate to 4-HEBA. In equation 3, *n* equals 1 or 2 but not 3, as metallic samarium has not been observed.

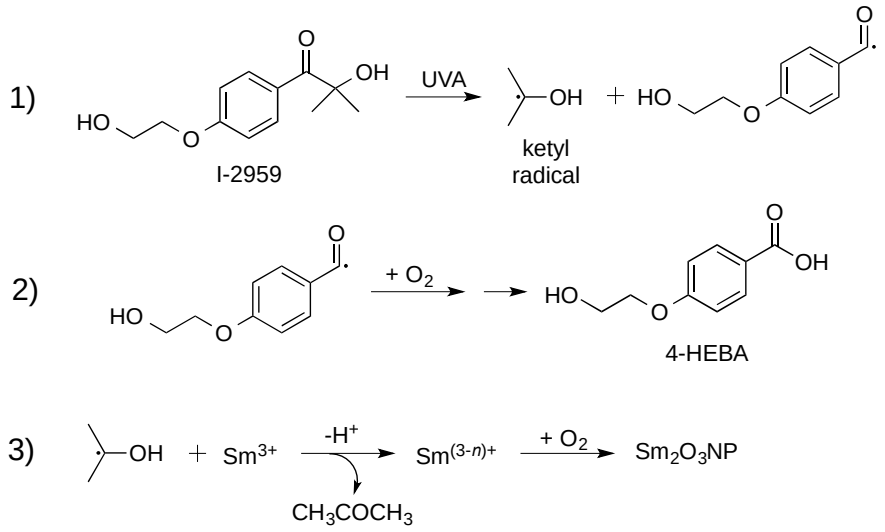

Similar mechanisms have been used to describe the photochemical synthesis of a variety of metallic and metal-oxide nanostructures.[1] For example, cobalt oxide NPs have been prepared by initial photoreduction of $CoCl_2$ using Irgacure-907,[15] followed by air oxidation of the cobalt nanoparticles. Samarium however, oxidizes much more readily than cobalt and thus we believe that it is never fully reduced to Sm^0. Although a millimolar concentration of photoinitiator would result in cessation of ketyl radical generation after only minutes of irradiation, a precipitate did not form until much later, at which point the partially reduced samarium precursor had been oxidized

to Sm_2O_3NP. Dynamic Light Scattering (DLS) was used to monitor the NP growth over time, and indicated an initial stage of rapid growth followed by slower growth over the course of several hours (Figure S2.1, Supporting Information). This experiment demonstrated that oxygen is required for the reaction, and also that reduction and oxidation occur concurrently during the initial phase of Sm_2O_3NP formation.

This procedure yielded a flaky brown-orange solid that rapidly settles out of many common solvents, and that is easily suspended in strong, polar aprotic solvents such as DMF and DMSO. For example, zeta potential measurements gave an average value of +23.1 mV in DMSO, indicating moderate colloidal stability. Energy Dispersive X-ray Spectroscopy (EDS) identified the primary constituents of the material to be samarium and oxygen (Figure S2.2, Supporting Information).

X-ray Photoelectron Spectroscopy (XPS) detected samarium exclusively in the +3 oxidation state, confirming that the material is comprised of Sm_2O_3. This was evident from the presence of a doublet that dominated the 1050.0–1150.0 eV region of the XPS survey of the material (Figure S2.3, Supporting Information). Peak splitting is well known to be the result of *j-j* coupling, which in this case gave rise to two intense peaks centred at 1084.0 and 1110.3 eV. These binding energies (BEs) correspond to the $3d_{5/2}$ and $3d_{3/2}$ states of Sm^{3+} present in Sm_2O_3, respectively,[13,16-19,20] consistent with the facile oxidation of samarium to Sm_2O_3–the more stable of the two oxides.[18,19,20] Further, no direct evidence of Sm^{2+} was obtained (a detailed interpretation of all XPS results is given in the Supporting Information). Traces of SmO could nonetheless be present, but it would exist as a transient surface species and represent only a minute fraction of the material's composition at any given time.[11,13,17,21] Samarium is redox active, so it is possible that the material may respond to its chemical environment by alternating between Sm_2O_3 and SmO to some extent. In any event, quantification of the core level Sm 3d peak data revealed that the material contains roughly 40% samarium by mass.

X-ray Diffraction (XRD) showed broad peaks roughly consistent with bulk phase Sm_2O_3 (Figure S2.4, Supporting Information).[10,13,22] Peak broadening is a direct result of NP formation and is commonly associated with amorphous solids.[13,17,22,23] SEM revealed remarkably spherical, polydisperse particles with a mean diameter of

417 ± 114 nm (Figure 2.1). This value was obtained by manually sizing 450 individual NPs from a single SEM image using ImageJ software (Figure S2.5 Supporting Information). Dynamic Light Scattering performed on the same batch of Sm_2O_3NP (in DMSO) gave a larger mean diameter of 510 ± 122 nm (Table S2.1, Supporting Information). Although the magnitudes of the standard deviation in the SEM and DLS results put the two values within range of one another, the mean hydrodynamic diameter being greater than the mean diameter obtained by SEM analysis allows for the possibility that ligands may be coordinated to the NP surface. The most likely candidate for such a stabilizer is 4-(2-hydroxyethoxy)-benzoic acid (4-HEBA) formed during Sm_2O_3NP synthesis (Scheme 2.). This compound has previously been identified as a photoproduct of I-2959 and is known to contribute to NP stability. The formation of 4-HEBA under ambient conditions is generally considered to involve trapping of the acyl radical by oxygen, formation of an intermediate peracid, and eventual reduction to 4-HEBA under ambient conditions.[1] ^{1}H NMR spectroscopy performed upon Sm_2O_3NP dissolved in DMSO-d_6 detected 4-HEBA even after extensive washing (Figure S2.6-S2.7 Supporting Information). Loss of the weak proton shift at 12.7 ppm might suggest deprotonation of 4-HEBA and coordination of the resulting carboxylate to Lewis acidic Sm(II) sites on the surfaces of Sm_2O_3NP. However, intact 4-HEBA could also interact with the NP surface via hydrogen bonding, and the absence of the 12.7 ppm signal could be due to rapid proton exchange or to the general peak broadening observed in Figure S2.7 as a result of the presence of a subpopulation of unstable particles in the colloid. No other organic species were detected in the ^{1}H NMR spectrum but elemental analysis concluded that the material is comprised of 38% carbon and 4.5% hydrogen (Table S2.2, Supporting Information). The presence of 4-HEBA accounts for the 38% carbon, which was also qualitatively detected by XPS. However, the molar quantity of 4-HEBA could not be reliably determined from core level C 1s XPS data due to probable sample contamination from adsorbed atmospheric carbon that could enhance the measured intensity of the C 1s peak.

In order to ensure that the individual Sm_2O_3NP shown in Figure 2.1 are not comprised of smaller NP subunits, TEM imaging was performed and showed no

evidence of any internal structure or defects in the NP surface (Figure S2.8, Supporting Information). Efforts to decrease the average size and polydispersity of the Sm_2O_3NP by altering the synthetic conditions were unsuccessful. Similarly, any NPs too small to be obtained via centrifugation of the post-irradiation solution could not be harvested using a non-solvent approach; adding an excess of toluene to a concentrated volume of supernatant after centrifuging out the larger Sm_2O_3NP did not result in precipitation, even after several days at 4°C. Laser drop ablation of a suspension of Sm_2O_3NP in MilliQ H_2O did produce a small number of NPs of diameter less than 50 nm but did not reduce the level of polydispersity (Figure S2.9, Supporting Information). The optimal conditions for laser drop ablation, subsequent washing of the sample and the overall efficiency of the process require further investigation, and will be reported along with any observed effects of size and polydispersity upon the catalytic activity of Sm_2O_3NP.

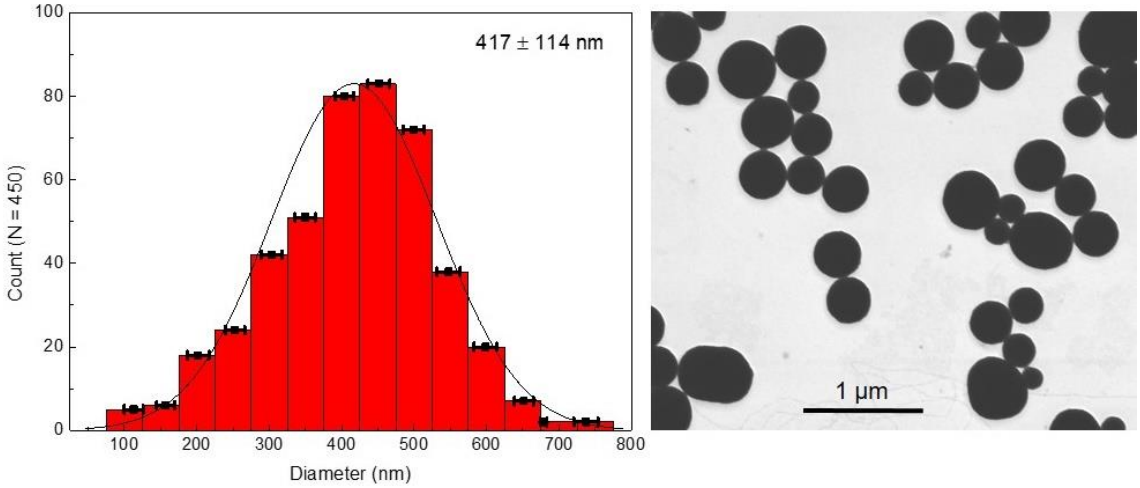

Figure 2.1 *Upper panel*: SEM image of Sm_2O_3NP. *Lower panel*: histogram showing the size distribution of Sm_2O_3NP based on manual analysis of SEM results. Black squares represent mean diameter and error bars are the associated standard deviation for each bin. Black curve simulates a Gaussian distribution for comparison with experimental data.

Since 4-HEBA is only mildly acidic ($pK_a \approx 4$), its presence alone does not explain the level of acidity possessed by Sm_2O_3NP. Hammett indicator studies conducted using a 0.1% w/v solution of dicinnamalacetone (DCA) in toluene suggested that the Sm_2O_3NP have a Hammett acidity function (H_0) value ≤ –3.

Unfortunately, other common indicators with pK_a values less than –3, such as benzalacetophenone (pK_a –5.6) and anthraquinone (pK_a –8.2), are colourless in the base form and yellow in the acid form.[25] The colour change is thus undetectable when these indicators are exposed to the brown-orange Sm_2O_3NP. Therefore, the amount by which the H_0 value of Sm_2O_3NP falls below –3 cannot be experimentally determined using the Hammett indicator method. However, since DCA changes from yellow to red upon exposure to an acid, the total number of acid sites per gram of material can be estimated by titration of the solid acid with *n*-butylamine following exposure to the indicator. Indeed, this experiment required 40 µL 0.1 M *n*-butylamine (in toluene) to titrate 5 mg of Sm_2O_3NP previously exposed to 1 mL 0.1% w/v DCA in toluene. This corresponds to a total acid strength of 0.8 mmol/g.

Since the titration method does not differentiate between Brønsted and Lewis acid sites, the acidity of the Sm_2O_3NP was also investigated using Fourier Transform Infrared (FTIR) Spectroscopy (Figure 2.2).

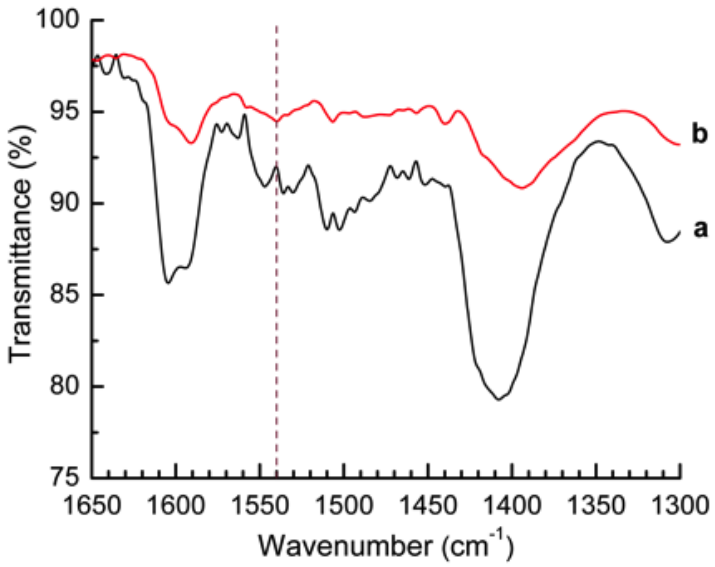

Figure 2.2 FTIR spectrum of Sm_2O_3NP before (a) and after (b) saturation with pyridine vapours. The vertical dashed line at 1540 cm^{-1} denotes the position of the characteristic pyridinium ion peak attributable to pyridine adsorbed onto Brønsted acid sites.

By comparing the FTIR spectrum of a solid acid before and after the adsorption of pyridine, the presence of Brønsted and Lewis acid sites can be detected. With the

correct experimental setup, the number of acid sites of each type can be quantified by this method. Peaks in the FTIR spectrum at 1540 cm^{-1} and 1440 cm^{-1} can often be attributed to the formation of the pyridinium ion and adsorption of pyridine upon interaction with Brønsted and Lewis acid sites, respectively.[25] As shown in Figure 2.2, saturation of Sm_2O_3NP with pyridine vapours resulted in the appearance of a weak band at 1540 cm^{-1}, possibly indicating the presence of surface Brønsted acid sites. The full-scale FTIR spectra of Sm_2O_3NP before and after exposure to pyridine are available in the Supporting Information (Figure S2.10 and Figure S2.11).

In this case the small signal at 1440 cm^{-1} is too weak to provide direct evidence of Lewis acid sites; but the FTIR spectrum of pyridine did show a strong signal in that same position (Figure S2.12, Supporting Information). However, the latter does not contain any signal in 1490–1570 cm^{-1} region, supporting evidence for the presence of pyridinium and thus Brønsted acid sites on the surfaces of Sm_2O_3NP. Overall, the Hammett acid indicator test, titration with *n*-butylamine, and pyridine adsorption experiments collectively demonstrated that the Sm_2O_3NP have $H_0 \leq -3$, a total acid strength in the vicinity of 0.8 mmol/g and possess some degree of Brønsted acidity.

As a proof-of-concept, we show that Sm_2O_3NP can efficiently protonate the halochromic coumarin-oxazine molecular assembly **1**. The absorption spectrum of **1** in CH_3CN shows a band centred at 410 nm. The addition of an acid opens the oxazine ring and generates a stable fluorescent compound **2** (Figure S2.13, Supporting Information). Within this transformation, the coumarin functionality is brought into conjugation with the cationic unit, bathochromically shifting the absorption band of the generated species by 180 nm.[23,24] A fluorescence band centred at 645 nm can then be observed by selectively exciting **2** at λ_{Ex} 570 nm. Therefore, the transformation of **1** into **2**, promoted by the addition of a Brønsted acid, can be exploited in order to activate fluorescence and thus permits the investigation of materials with distinctive acidic properties using a simple experimental setup. In this case catalytic conversion to the ring-open form **2** began shortly after exposure to Sm_2O_3NP and was complete within 30 min (Figure 2.3 and Figure S2.14, Supporting Information). This confirmed that Sm_2O_3NP possess Brønsted acidity, a property that could make Sm_2O_3NP a useful heterogeneous acid catalyst.

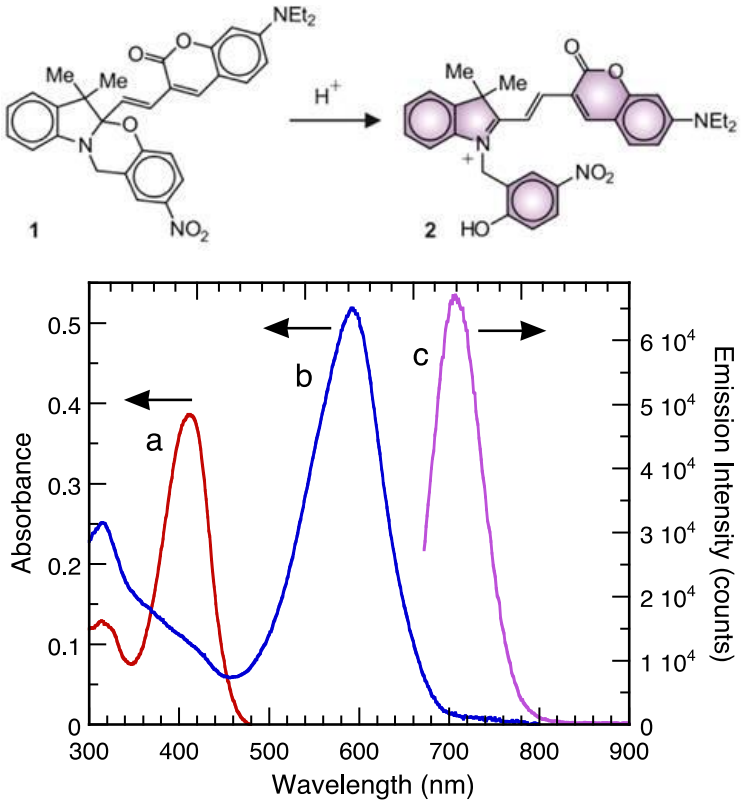

Figure 2.3 *Upper panel*: ring-opening of the halochromic switch. *Lower panel*: Absorption spectra of **1** (10 μM, CH_3CN, 25°C) before (a) and after (b) 30 min exposure to Sm_2O_3NP and subsequent centrifugation. Emission spectrum (c, λ_{Ex} = 570 nm, CH_3CN, 25°C) of **1** after 30 min exposure to Sm_2O_3NP and subsequent centrifugation.

In order to confirm that the observed Brønsted acidity of the Sm_2O_3NP is a surface effect, the impact of exposing Sm_2O_3NP to a strong base was evaluated. Sm_2O_3NP previously used to convert **1** to **2** were washed with CH_3CN, treated with 2 mM NaOH three times, washed again with CH_3CN and finally exposed to a new 10 μM solution of the closed-ring species **1**. No conversion from **1** to **2** was observed, even after 24 h (Figure S2.15, Supporting Information). However, the structural integrity of the Sm_2O_3NP was retained (Figure 2.4). Interestingly though, the surfaces of base-treated Sm_2O_3NP shown in Figure 2.4 appear roughened or non-uniformly pitted. This may indicate the disruption of several surface oxide layers in close proximity to heterogeneously distributed Brønsted acid sites. In any case, these results confirm the surface acidity of the Sm_2O_3NP.

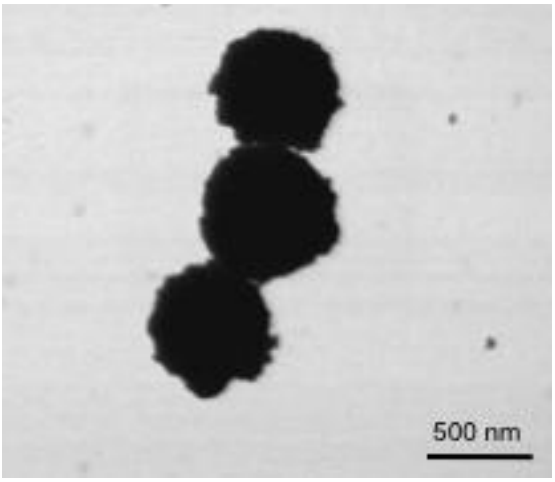

Figure 2.4 SEM image of Sm_2O_3NP after repeated exposure to 2 mM NaOH and subsequent washing with CH_3CN.

Conclusion

We describe a photochemical approach to the synthesis of a novel lanthanide-based nanomaterial – Sm_2O_3NP – under very mild conditions. To the best of our knowledge, this is the first report of photochemically prepared Sm_2O_3NP in the literature. Not only are such methods beneficial from an environmental standpoint, improvements upon traditional synthetic strategies provided by photochemical techniques are necessary to achieve time- and cost-effectiveness that facilitates streamlined production of prototype materials. This in turn permits economic exploration of less than well-travelled regions in terms of the iterative design of new catalytic materials. A thorough characterization of the physicochemical properties of the Sm_2O_3NP reported here revealed spherical particles with a 4-HEBA ligand. More importantly, the Sm_2O_3NP possess surface Brønsted acidity, with a total acid strength of approximately 0.8 mmol/g. This property endows the new material with potential as a Brønsted acid catalyst, as illustrated by the **1** → **2** conversion. We envision the eventual replacement of harsh homogeneous acid catalysts with Sm_2O_3NP and similarly designed heterogeneous nanocatalysts offering ease of separation and/or recyclability while maintaining high catalytic efficiency.

References

(1) McGilvray, K. L.; Decan, M. R.; Wang, D.; Scaiano, J. C. *J. Am. Chem. Soc.* **2006**, *128*, 15980-15981; Scaiano, J. C.; Netto-Ferreira, J. C.; Alarcon, E.; Billone, P.; Bueno-Alejo, C. J.; Crites, C. L.; Decan, M. R.; Fasciani, C.; Gonzalez-Bejar, M. Hallett-Tapley, G. L.; Grenier, M.; McGilvray, K. L.; Pacioni, N. L.; Pardoe, A.; Rene-Boisneuf, L.; Schwartz-Narbonne, R.; Silvero, M. J.; Stamplecoskie, K.; Wee, T. *Pure Appl. Chem.* **2011**, *83*, 913-930; Scaiano, J. C.; Stamplecoskie, K. G.; Hallett-Tapley, G. L. *Chem. Commun.* **2012**, *48*, 4798-4808; Malyshev, D.; Bosca, F.; Crites, C.-O. L.; Hallett-Tapley, G. L.; Netto-Ferreira, J. C.; Alarcon, E. I.; Scaiano, J. C. *Dalton Trans.* **2013**, *42*, 14049-14052; Scaiano, J. C.; Stamplecoskie, K. G.; McGilvray, K. L.; Pacioni, N. L. *E. Rad. Chem. Biol. Mat.* **2012**, DOI: 10.1002/9780470971253.rad068; Alarcon, E.; Bueno-Alejo, C. J.; Noel, C. W.; Stamplecoskie, K. G.; Pacioni, N. L.; Poblete, H.; Scaiano, J. C. *J. Nanopart. Res.* **2013**, *15*, 1374, 1-14.

(2) Bueno-Alejo, C. J.; D'Alfonso, C.; Pacioni, N. L.; González-Béjar, M.; Grenier, M.; Lanzalunga, O.; Alarcon, E. I.; Scaiano, J. C. *Langmuir*, **2012**, *28*, 8183-8189.

(3) Chen, Y.-S.; Kamat, P. V. *J. Am. Chem. Soc.* **2014**, *136*, 6075-6082; Stamplecoskie, K. G.; Kamat, P. V. *J. Am. Chem. Soc.* **2014**, *136*, 11093-11099.

(4) Rance, G. A.; Solomonsz, W. A.; Khlobystov, a. N. *Chem. Commun.* **2013**, *49*, 1067-1069; Alonso, F.; Moglie, Y.; Radivoy, G.; Yus, M. *Eur. J. Org. Chem.* **2010**, 1875-1884; Anil Kumar, B. S. P.; Harsha Vardhan Reddy, K.; Madhav, B.; Ramesh, K.; Nageswar, Y. V. D. *Tetrahedron Lett.* **2012**, *53*, 4595-4599; Hudson, R.; Li, C.-J.; Moores, A. *Green Chem.* **2012**, *14*, 622-624; Sarkar, A.; Mukherjee, T.; Kapoor, S. *J. Phys. Chem. C* **2008**, *112*, 3334-3340; Decan, M. R.; Impellizzeri, S.; Marin, M. L.; Scaiano, J. C. *Nature Commun.* **2014**, *5*, 4612.

(5) Gambogi, J.; Jackson, M. L.; Miller, L. D. *U.S. Geological Survey Minerals Yearbook: Rare Earths* USGS, 2011 edn., 2011.

(6) Cooper, C. M.; Wallace, J.; Brookhart, M.; Clark, M.; Collins, C.; Ding, W. X.; Flanagan, K.; Khalzov, I.; Li, Y.; Milhone, J.; Nornberg, M.; Nonn, P.; Weisberg, D.; Whyte, D. G.; Zweibel, E.; Forest, C. B. *Phys. Plasm.* **2014**, *21*, -; Haider, A.; Akhtar, S.; Ahmad, Z.; Farooque, M. *Key Eng. Mat.* **2010**, *442*, 250-254.

(7) Gorepatil, P. B.; Mane, Y. D.; Ingle, V. S. *Synlett*, **2013**, *24*, 2241-2244; Narsaiah, A. V.; Reddy, A. R.; Reddy, B. V. S.; Yadav, J. S. *Synth. Comm.*

2010, *40*, 1750-1757; Narsaiah, A. V.; Reddy, A. R.; Yadav, J. S. *Synth. Comm.* **2011**, *41*, 262-267.

(8) Szostak, M.; Fazakerley, N. J.; Parmar, D.; Procter, D. J. *Chem Rev.* **2014**, *114*, 5959-6039.

(9) Jackman, S. A.; Knowles, C. J.; Robinson,G. K. *Chemosphere*, **1999**, *38*, 1889-1900.

(10) Hussein, G. A. M.; Buttrey, D. J.; DeSanto, P. Jr.; Abd-Elgaber, A. A.; Roshdy, H.; Myhoub, A. Y. Z. *Thermochim. Acta*, **2003**, *402*, 27-36.

(11) Ekstrom, A.; Lapszewicz, J. A. *J. Am. Chem. Soc.* **1988**, *110*, 5226-5228.

(12) Siriwardane, R. V. *Langmuir*, **1991**, *7*, 497-502; Amorebieta, V. T.; Colussi, A. J. *J. Am. Chem. Soc.* **1996**, *118*, 10236-10241.

(13) Nguyen, T.-D.; Mrabet, D.; Do, T.-O. *J. Phys. Chem. C* **2008**, *112*, 15226-15235.

(14) Gao, J.; Zhao, Y.; Yang, W.; Tian, J.; Guan, F.; Ma, Y.; Hou, J.; Kang, J.; Wang, Y. *Mat. Chem. Phys.* **2003**, *77*, 65-69; Reverchon, E.; Porta, G. D.; Sannino, D.; Lisi, L.; Ciambelli, P.; Delmon, B.; Jacobs, P. A.; Maggi, R.; Martens, J. A.; Grange, P.; Poncelet, F. *Surf. Sci. Elsevier*, **1998**, *118*, 349-358; Zhu, W.; Xu, L.; Ma, J.; Yang, R.; Chen, Y. *J. Coll. Int. Sci.* **2009**, *340*, 119-125.

(15) Wee, T.; Sherman, B. D.; Gust, D.; Moore, A. L.; Moore, T. A.; Liu, Y.; Scaiano, J. C. *J. Am. Chem. Soc.* **2011**, *133*, 16742-16745.

(16) Mason, M. G.; Lee, S. T.; Apai, G.; Davis, R. F.; Shirley, D. A.; Franciosi, A.; Weaver, J. H. *Phys. Rev. Lett.* **1981**, *47*, 730-733.

(17) Nguyen, T.-D.; Dinh, C.-T.; Do, T.-O. *Langmuir*, **2009**, *25*, 11142-11148.

(18) Cheng, D.; Xu, Q.; Han, Y.; Ye, Y.; Pan, H.; Zhu, J. *J. Chem. Phys.* **2014**, *140*, 094706.

(19) Juel, M.; Samuelsen, B. T.; Kildemo, M.; Raaen, S. *Surf. Sci.* **2006**, *600*, 1155-1159; Kuchowicz, M.; Kocaczkiewicz, J. *Surf. Sci.* **2008**, *602*, 3721-3727.

(20) Xu, Q.; Hu, S.; Cheng, D.; Feng, S.; Han, Y.; Zhu, J. *J. Chem. Phys.* **2012**, *136*, 154705.

(21) Sarma, D. D.; Hegde, M. S.; Rao, C. N. R. *J. Chem. Soc. Faraday Trans. 2*, **1981**, *77*, 1509-1520.

(22) Shi, L.; Dong, G.; He, D. *Catal. Comm.* **2007**, *8*, 359-365.

(23) Marin, M. L.; Hallett-Tapley, G. L.; Impellizzeri, S.; Fasciani, C.; Simoncelli, S.; Netto-Ferreira, J. C.; Scaiano, J. C. *Catal. Sci. Technol.* **2014**, *4*, 3044-3052.

(24) Deniz, E.; Sortino, S.; Raymo, F. M. *J. Phys. Chem. Lett.* **2010**, *1*, 3506-3509; Swaminathan, S.; Petriella, M.; Deniz, E.; Cusido, J.; Baker, J. D.; Bossi, M. L.; Raymo, F. M. *J. Phys. Chem. A* **2012**, *116*, 9928-9933.

(25) Yurdakoc, M.; Ackay, M.; Tonbul, Y.; Yurdakoc, K.; *Turk. J. Chem*. **1999**, *23*, 319-327; Benesi, H. A. *J. Phys. Chem.* **1957**, *61*, 970-973; Yazici, D. T.; Bilgic, C. *Surf. Interface Anal*. **2010**, *42*, 959-962.

2.3 Postprint Version of Supporting Information

Experimental Protocols

Photochemical synthesis of Sm_2O_3NP. Sm_2O_3NP were prepared by photochemical partial reduction of samarium nitrate hexahydrate in CH_3CN, via UVA irradiation of the benzoin Irgacure-2959™ (I-2959) photoinitiator (Scheme 2.1) followed by spontaneous air oxidation. Samples of I-2959 were a generous gift from Ciba Specialty Chemicals Inc. Unless otherwise noted, all other reagents and solvents were obtained from Sigma Aldrich or Fisher Scientific. Irradiation time was varied according to reaction volume, path length and reagent concentrations, with 48 h of UVA irradiation proving optimal for a 3:1 mM ratio of I-2959: $Sm(NO_3)_3 \bullet 6H_2O$ in 250 mL CH_3CN. Pertinent amounts of $Sm(NO_3)_3 \bullet 6H_2O$ and I-2959 were weighed out on an analytical balance (Sartorius model 1702) and immediately added to semi-dry CH_3CN provided by a bench top solvent purification system (LC Technology Solutions Inc. model SPBT-1), into a freshly clean, oven-dried Pyrex test tube (solvent was not distilled and likely contained < 8 mM H_2O). A magnetic stir bar was added before the reaction vessel was fitted with a black rubber stopper and sealed with parafilm. The reaction was secured to a retort stand and purged with Argon for 1.5 h while stirring; this step was skipped for studies under air. It was then surrounded by three Luzchem exposure panels (model LZC-EXPO) powering a total of fifteen 8 W UVA bulbs (Hitachi model FL8-BL) and equipped with a Luzchem electronic timer (model LZC-TIM). The reaction proceeded at room temperature for the allotted time interval after which the cloudy but translucent dark orange solution was sonicated and separated

into sterile 15 mL polypropylene centrifuge tubes (Fisherbrand model 05-539-12). Samples were then centrifuged at 10,000 rpm for 30 min (Sorvall Legend T Centrifuge, Thermo Electron Corporation). The transparent yellow supernatant was decanted and stored in the dark for observation. The remaining brown-orange solid was resuspended in a minimum of dichloromethane (DCM) via sonication and combined into four pre-weighed, clean, oven-dried glass test tubes. These four samples were centrifuged for 30 min at 3000 rpm (Drucker Co., Horizon model). The clear, colourless supernatant was discarded, the solid washed twice more with CH_3CN and the final product allowed to dry overnight in a fumehood before its mass was recorded.

Sm_2O_3NP Characterization. SEM was conducted using a JEOL JSM-7500F field emission scanning electron microscope where a drop of Sm_2O_3NP suspended in CH_3CN was placed onto a carbon film coated Cu mesh grid (Electron Microscopy Sciences model CF-400-Cu) and evaporated under ambient conditions. Sample preparation was the same for TEM imaging, which was conducted on a JEOL JEM-2100F field emission TEM operating at 200 kV. XPS was performed at the John L. Holmes Mass Spectrometry facility (University of Ottawa, Canada), using an Axis Ultra DLD X-ray photoelectron spectrometer (Kratos Analytical) with a monochromatic Al Kα X-ray source, operated at 140 W and 10^{-9} Torr. The XPS survey was obtained using a pass energy of 80 eV and an acquisition time of 342 s. High resolution Sm 3d, O 1s and C 1s XPS spectra were obtained using a pass energy of 20 eV and an acquisition time of 401 s. Analysis of XPS spectra was conducted using standard CasaXPS software (version 2.3.15). The positions of peaks were corrected using 284.5 eV as a reference value for the core level C 1s peak. XRD analysis was carried out using a Rigaku model Ultima IV X-ray diffractometer with a CuK α source, and was performed at the uOttawa X-ray core facility. Zeta potential and DLS measurements were performed on Sm_2O_3NP dissolved in DMSO (2 mg/mL) using a Zetasizer Nano-ZS (Malvern Instruments, 633 nm laser) at 20°C. Samples were housed in a 1.0 cm path length Zetasizer Nano Series Dip Cell. FTIR Spectroscopy of Sm_2O_3NP before and after pyridine adsorption was carried out using a Nicolet 6700 FTIR spectrophotometer (Thermo Scientific) equipped with an Attenuated Total Reflectance

(ATR) adapter to facilitate solid sample examination. Spectra were obtained from 500-4000 cm^{-1} at 64 scans with a resolution of 4 cm^{-1}. Samples were pre-treated at 120°C for 4 h under vacuum in a Lindeberg Blue M oven. The FTIR spectrum of pyridine was obtained using an ABB Bomem MB100 FTIR spectrophotometer at 120 scans, with a resolution of 4 cm^{-1}. Sample preparation involved suspending a mixture of liquid pyridine with Nujol mineral oil between two KBr disks. Other equipment used for the characterization of Sm_2O_3NP included: an energy-dispersive X-ray spectrometer (Oxford Instruments); a Bruker Avance 300 for ^{1}H NMR spectroscopy; a Varian Cary 50 Bio UV-visible spectrophotometer and a Photon Technology International fluorimeter. Elemental analysis was carried out using a Micro Cube Elemental Analyser (Elementar, Germany) and was conducted by G. G. Hatch Isotope Laboratories, Earth Sciences Department, Faculty of Science, University of Ottawa, Canada.

Synthesis. Compound **1** was synthesized according to literature procedures (ref 19 of the main text). All reactions were monitored by thin-layer chromatography, using aluminum sheets coated with silica (60, F_{254}). NMR spectra were recorded at room temperature with a Bruker Avance 300 NMR spectrometer. Mass spectral analysis was performed with a 6890N Network GC System equipped with a 5973 Mass Selective Detector from Agilent Technologies. ESI mass spectra in positive mode were acquired with a Micromass Q-TOF I. High-resolution EI mass spectra were acquired with a HRes, Concept S1, Magnetic Sector mass spectrometer and were conducted in the John L. Holmes Mass Spectrometry Facility at the Department of Chemistry, University of Ottawa, Canada.

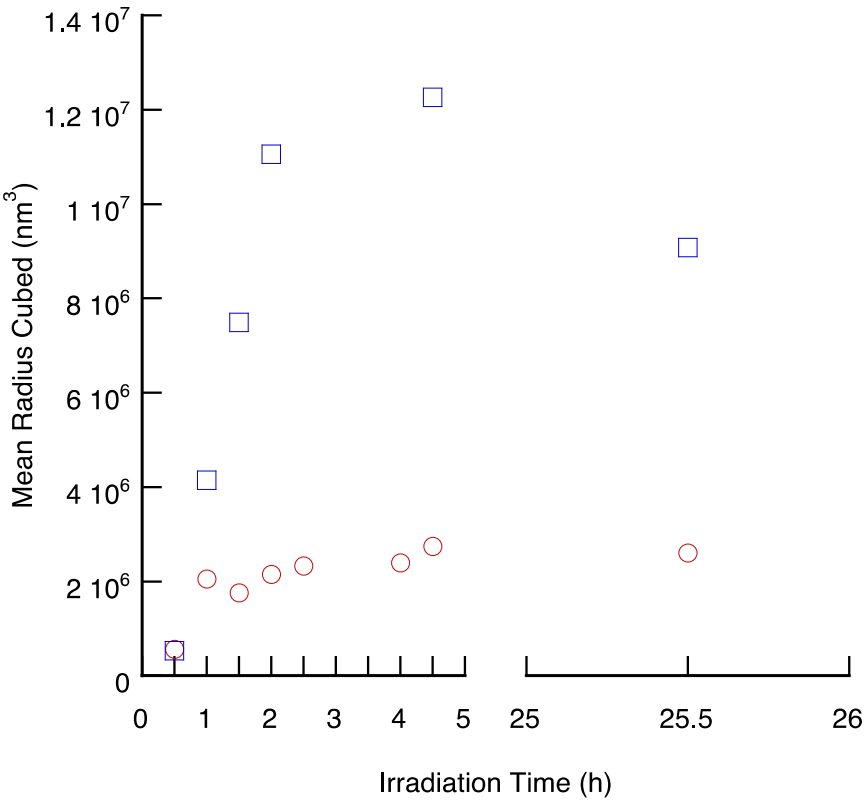

Figure S2.1 DLS performed at regular intervals during the photochemical synthesis of Sm_2O_3NP. Irradiation was consistently interrupted in order to obtain each measurement. Red circles represent the formation of Sm_2O_3NP in CH_3CN under Ar (g) and blue squares represent the data obtained when the synthesis was performed under air.

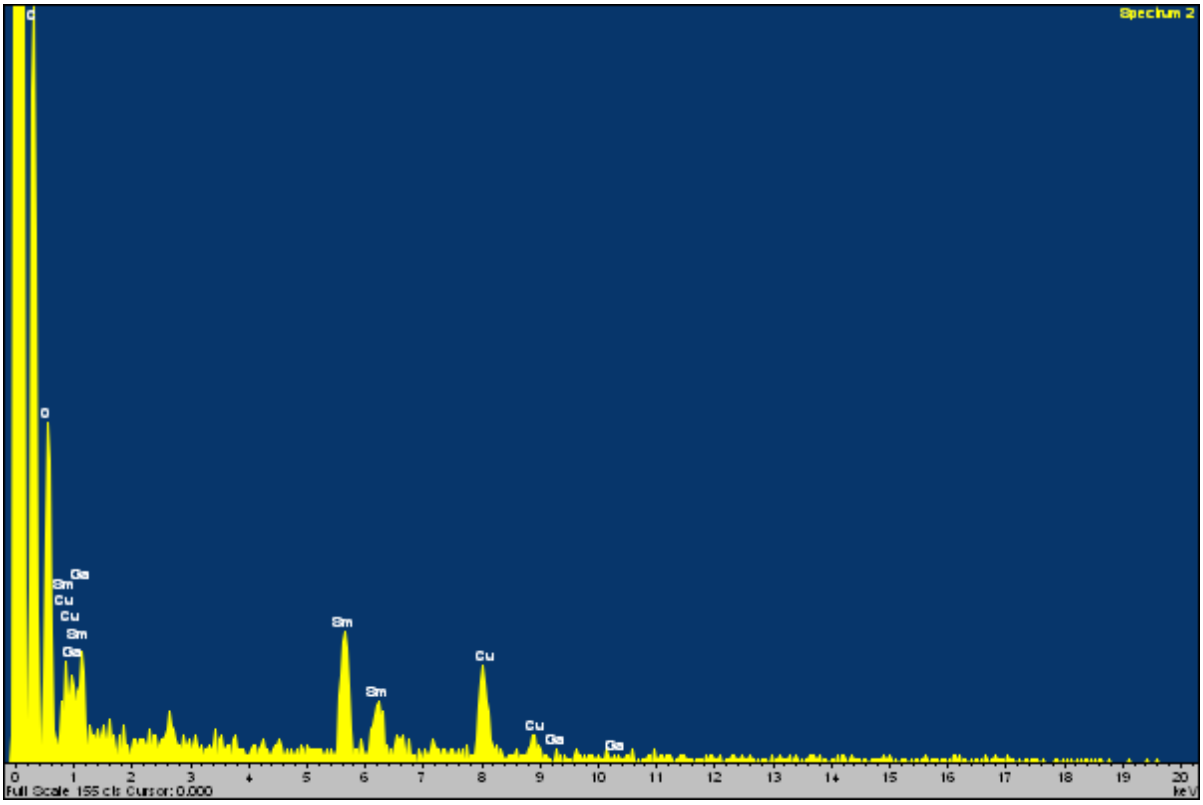

Figure S2.2 EDS spectrum of Sm_2O_3NP.

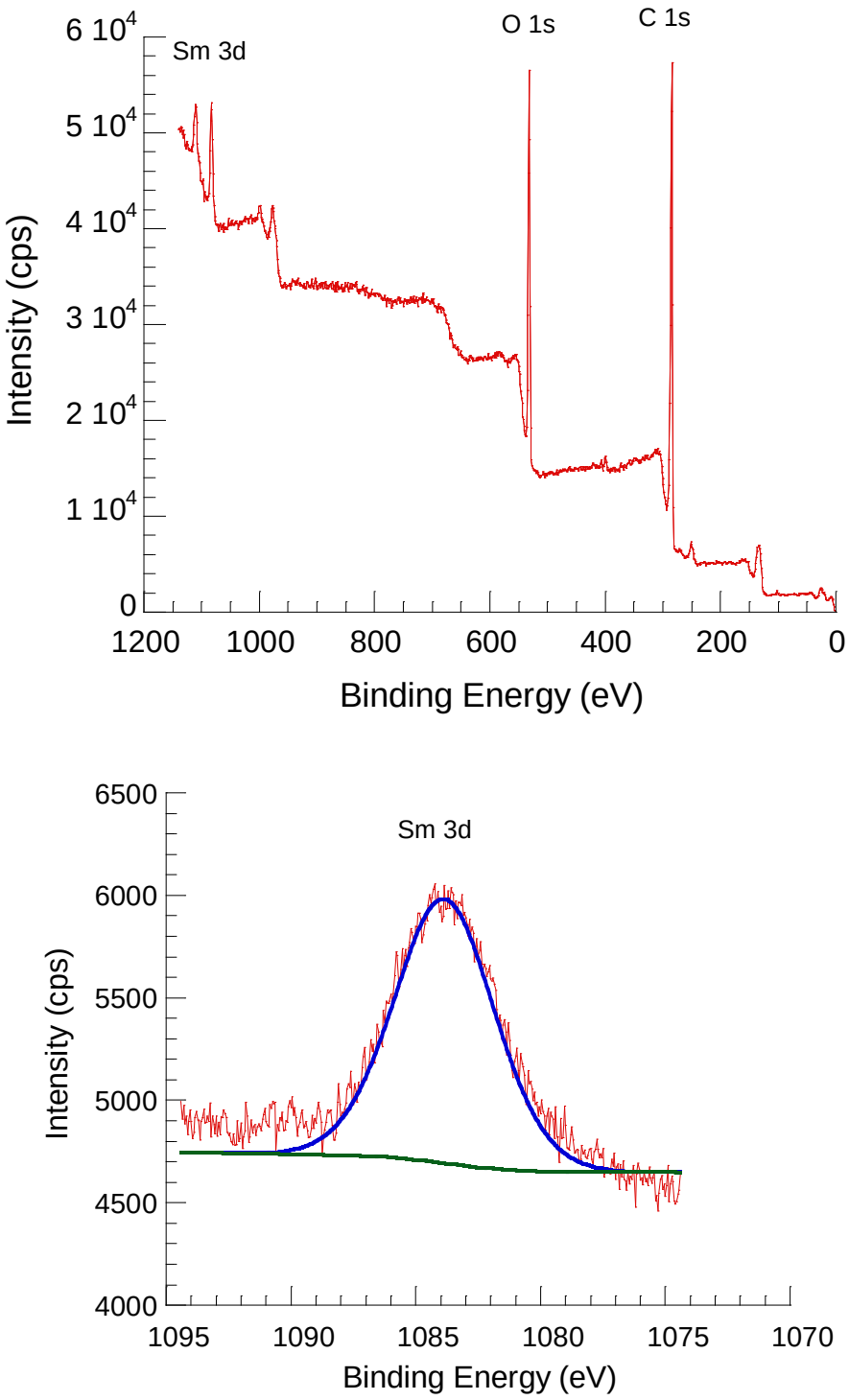

Figure S2.3 *Upper panel*: XPS spectrum over a broad range of binding energies. *Lower panel*: core level Sm 3d XPS spectrum of Sm_2O_3NP showing one of the characteristic Sm^{3+} peaks centred at 1084.0 eV.

Details of XPS Interpretation. Hyperfine splitting of each Sm_2O_3 peak or the presence of shoulders can sometimes be observed and is often attributed to the presence of ionic Sm^{2+} (i.e. SmO) or metallic samarium.[1,2] The relative proportions of Sm^0, SmO and Sm_2O_3, which can change as samarium undergoes oxidation, are then discussed according to the relative intensity of their apparent peaks. However, this form of interpretation can be misleading as it often requires extensive peak deconvolution incorporating arbitrary constraints on fitting parameters. Thus, beyond assuming a Gaussian shape, the XPS spectrum of bulk samarium metal will invariably display similar peak splitting and shoulder components.[3-5] Although the BE of the Sm^{2+} signal is generally considered to fall between those of Sm^{3+} and Sm^0, conflicting reports concerning whether the peaks ascribed to SmO appear at higher or lower BE relative to the Sm_2O_3 doublet depending upon the attributes of the material (e.g. support, dopant, preparation method) further draw the reliability of such analyses into question. Even if fitting methods did not suffer from these drawbacks, samarium is redox-active and the surfaces of samarium oxide materials have been reported to rapidly change oxidation states (a potential asset in catalysis) while the interior remains as Sm_2O_3.[4,7] Further, surface SmO could easily be generated *in situ* via reduction of Sm^{3+} initiated by bombardment with high-energy X-rays during XPS spectral acquisition. Unfortunately in this case the core level O 1s XPS spectrum could not provide any additional insight regarding the presence or absence of Sm^{2+}. Although spin-orbit splitting observed in this region can, in principle, be related to the ratio of O–Sm^{2+}/O–Sm^{3+}/surface OH groups,[1,2,6] the degree of splitting was insufficient for a reliable deconvolution procedure to be attempted. It is important to note that interpretation of the O 1s and C 1s peaks should be made with caution, as sample contamination from adsorbed atmospheric oxygen and carbon can enhance measured intensity. Suffice to say that the lack of an excess of samarium with respect to oxygen qualitatively corroborates the identification of the material as Sm_2O_3.

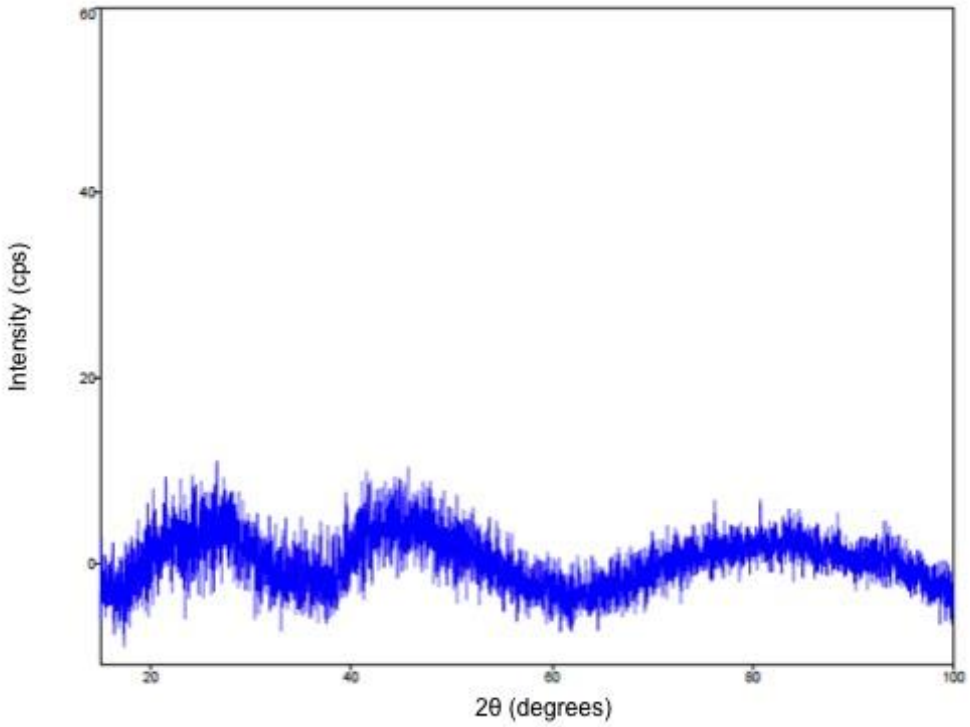

Figure S2.4 XRD spectrum of Sm_2O_3NP showing typical peak broadening associated with amorphous solid nanostructures.

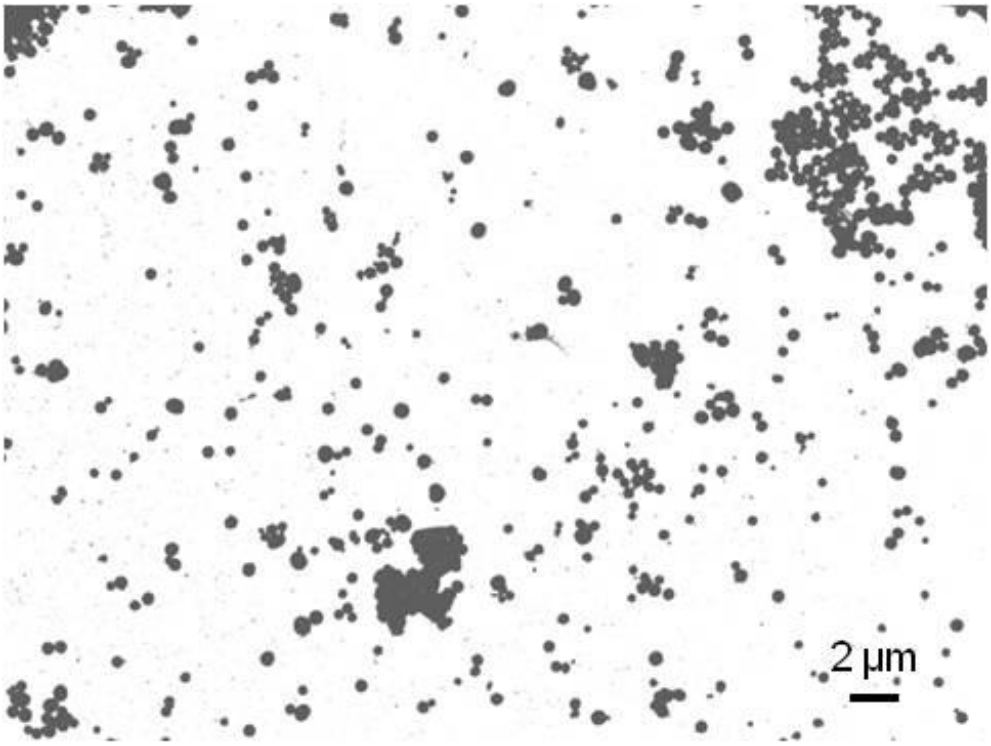

Figure S2.5 SEM image of Sm_2O_3NP used for particle sizing represented in Figure 2.1.

Table S2.1 Raw DLS data pertaining to three samples of 2 mg/mL Sm_2O_3NP dissolved in DMSO (absorbance = 0.085 at 650 nm).

Sample	Run	Hydrodynamic Diameter (nm)
1	1	734.0
1	2	466.4
1	3	605.1
2	1	385.2
2	2	571.3
2	3	374.2
3	1	498.6
3	2	574.5
3	3	381.9
Mean (nm)		510.1
Standard Deviation		122.3

Table S2.2 Elemental analysis of Sm_2O_3NP performed in duplicate.

Mass (mg)	Carbon	Hydrogen	Nitrogen	Sulfur
4.391	37.80	4.05	2.62	0.32
4.823	37.74	4.75	2.65	0.32

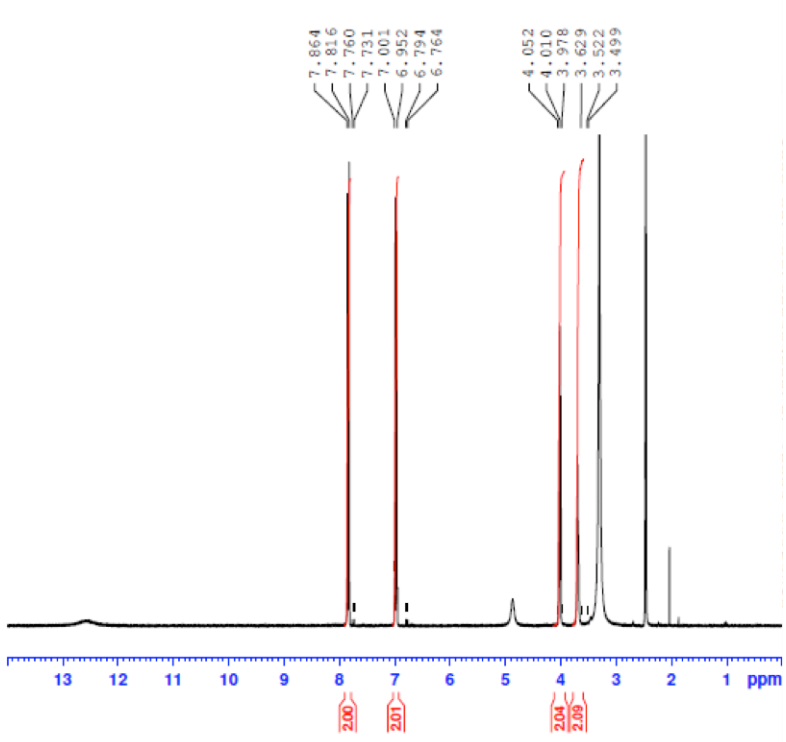

Figure S2.6 ^{1}H NMR spectrum of 4-HEBA in DMSO-d_6.

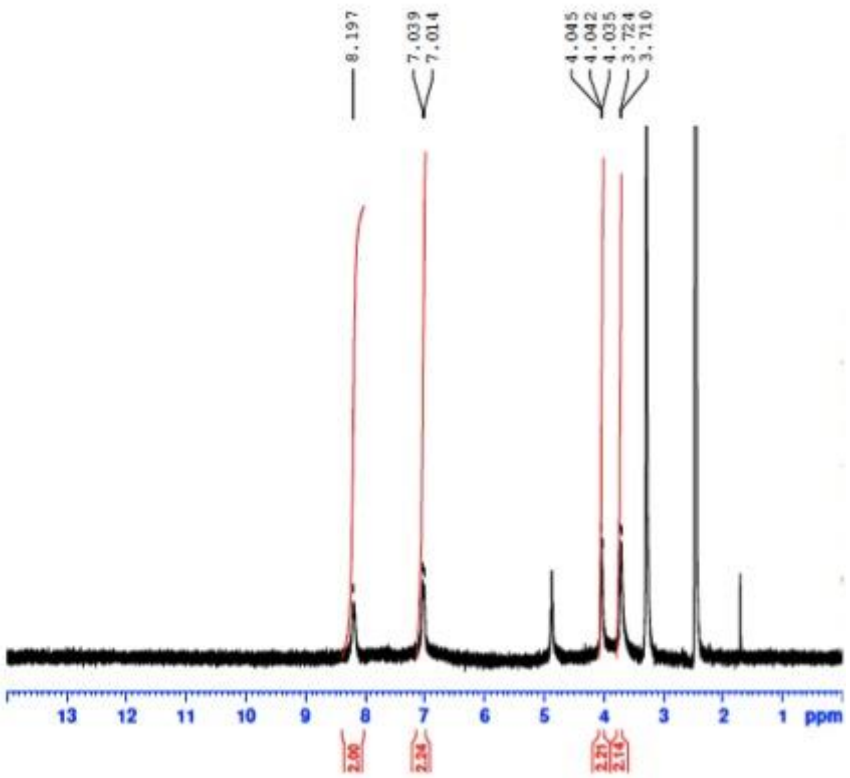

Figure S2.7 ^{1}H NMR spectrum of Sm_2O_3NP in DMSO-d_6.

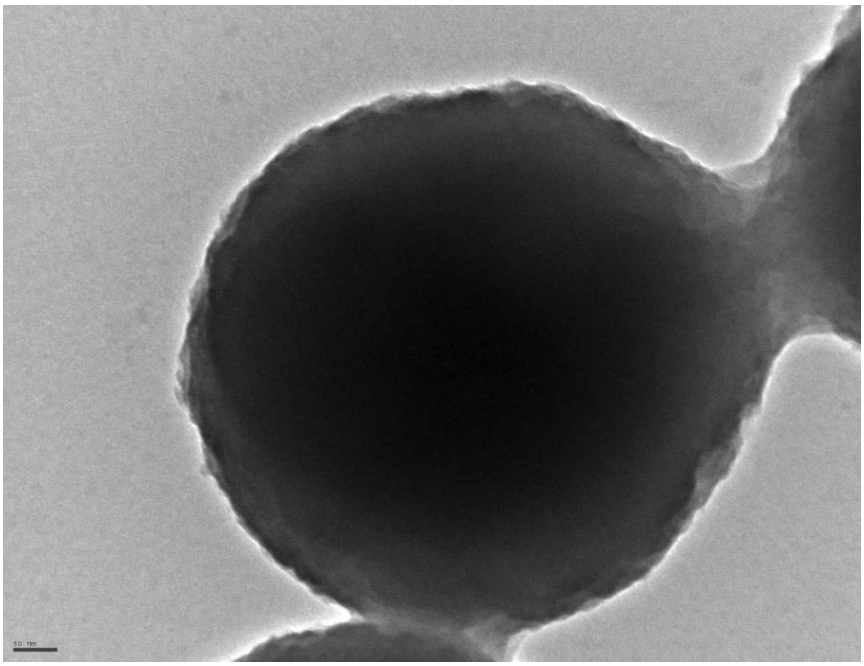

Figure S2.8 TEM image of Sm_2O_3NP, showing that each particle is not made up of smaller NPs but exists as an individual spherical unit. Scale bar = 50 nm. Image obtained on a JEOL JEM-2100F Field Emission TEM operating at 200 kV.

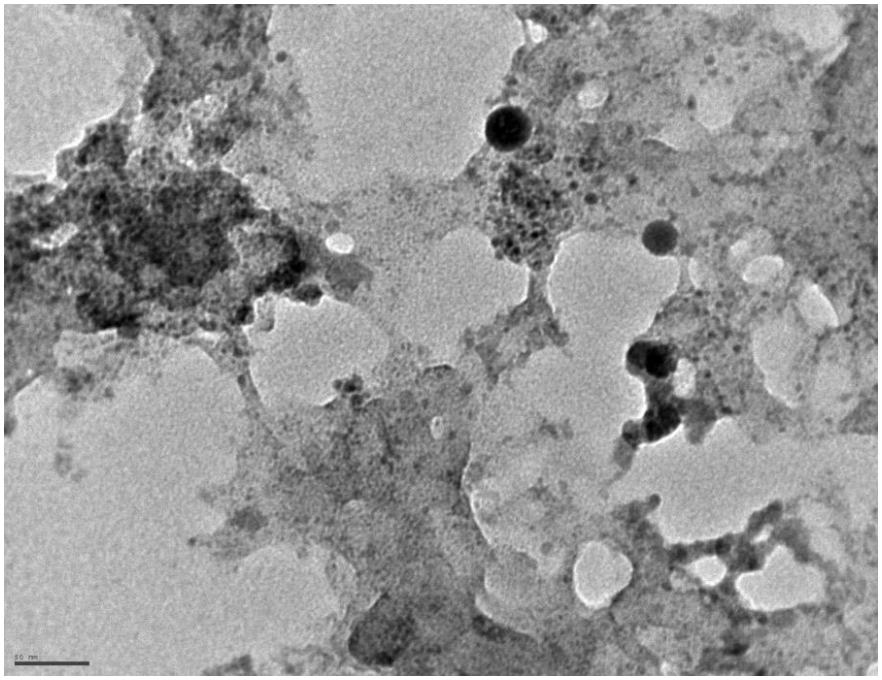

Figure S2.9 TEM image showing the raw results of laser drop ablation performed on a 0.88 mg/mL suspension of Sm_2O_3NP in MilliQ H_2O prior to purification.[8] Laser drop ablation conditions: 355 nm, 5 Hz, 5 pulses/drop. Image obtained on a JEOL JEM-2100F Field Emission TEM operating at 200 kV. Scale bar = 50 nm.

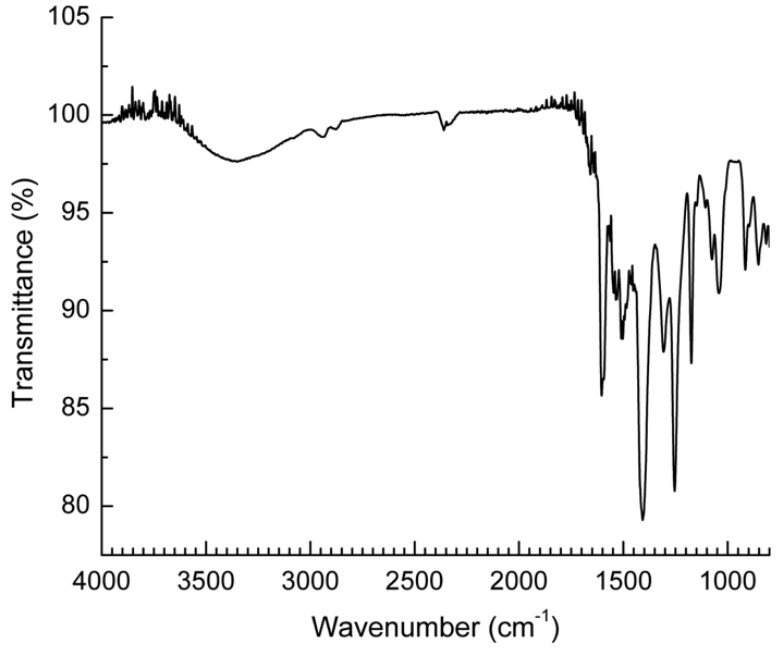

Figure S2.10 Full-scale FTIR spectrum of solid Sm_2O_3NP before exposure to pyridine vapour.

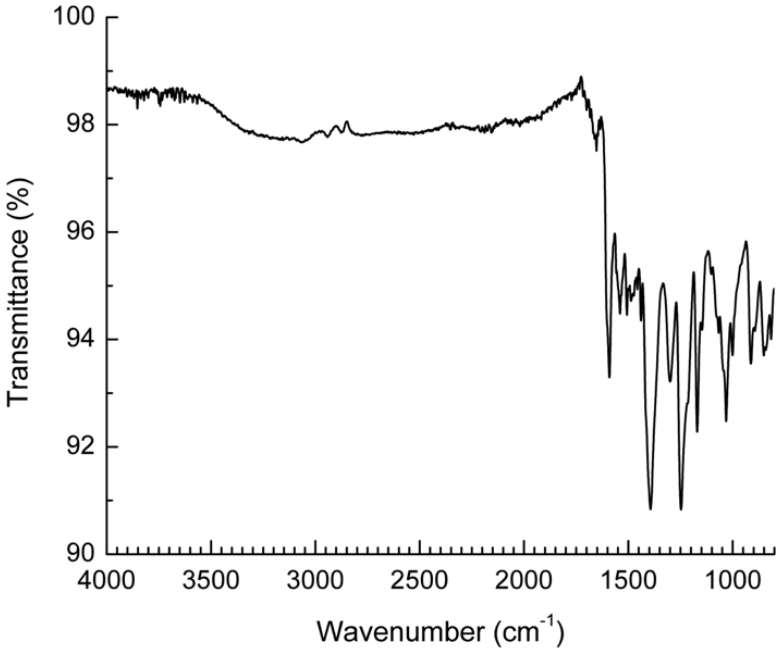

Figure S2.11 Full-scale FTIR spectrum of solid Sm_2O_3NP saturated with adsorbed pyridine vapour.

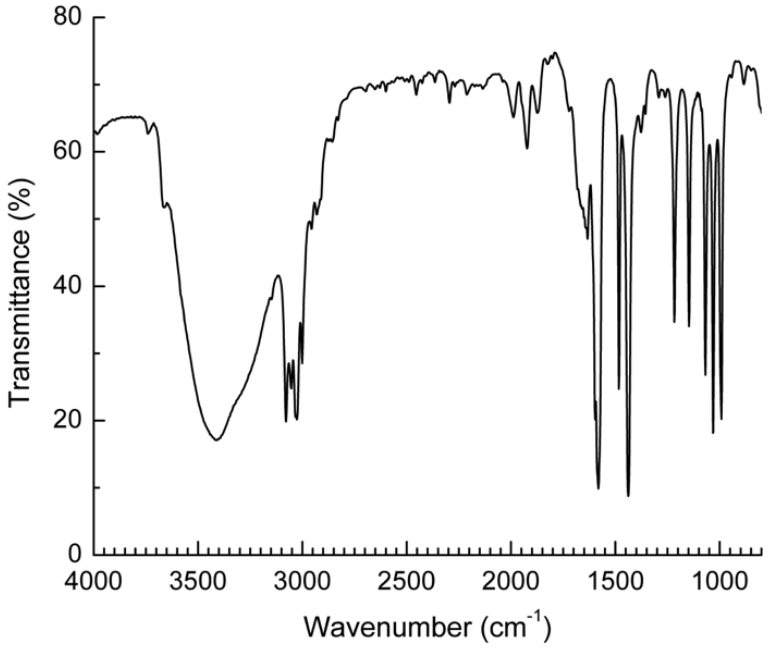

Figure S2.12 Full-scale FTIR spectrum of pyridine. A liquid sample was prepared in Nujol mineral oil and the spectrum obtained from 500-4000 cm^{-1} at 120 scans, with a resolution of 4 cm^{-1}.

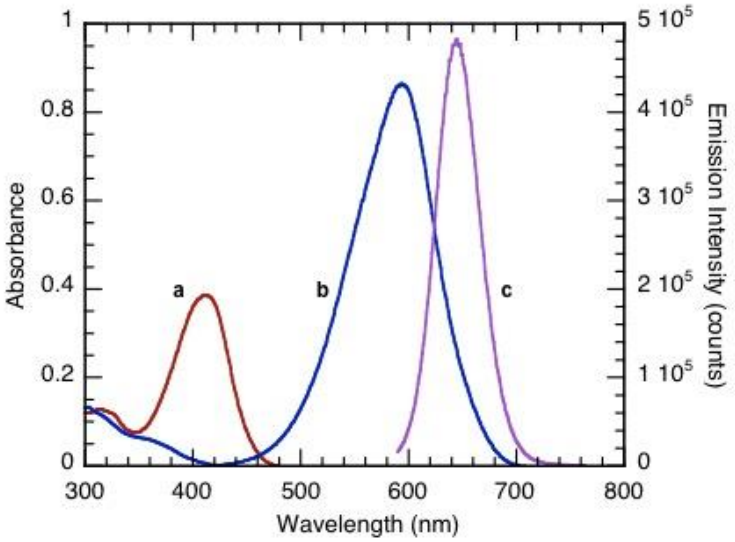

Figure S2.13 Absorption spectra of **1** (10 μM, CH_3CN, 25°C) before (**a**) and after (**b**) the addition of 10 equivalents of TFA. Emission spectrum (**c**, λ_{Ex} = 570 nm, CH_3CN, 25°C) of **1** after the addition of 10 equivalents of TFA.

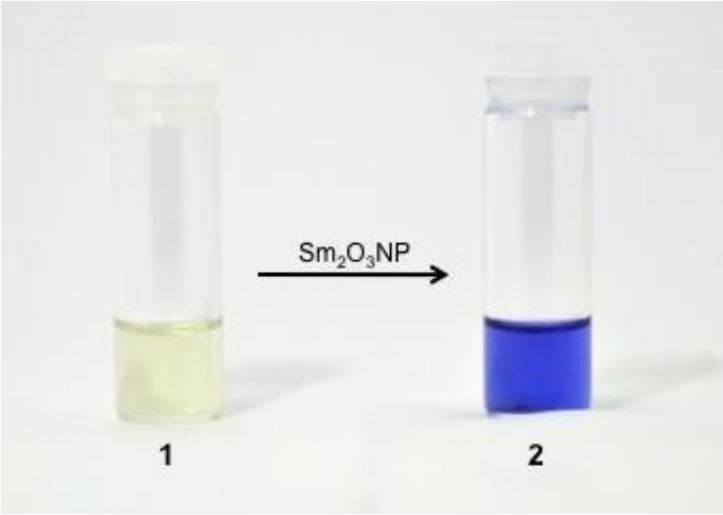

Figure S2.14 Image showing the conversion from **1** (left) to **2** (right) caused by acid-induced ring opening owing to the Brønsted acidity of Sm_2O_3NP.

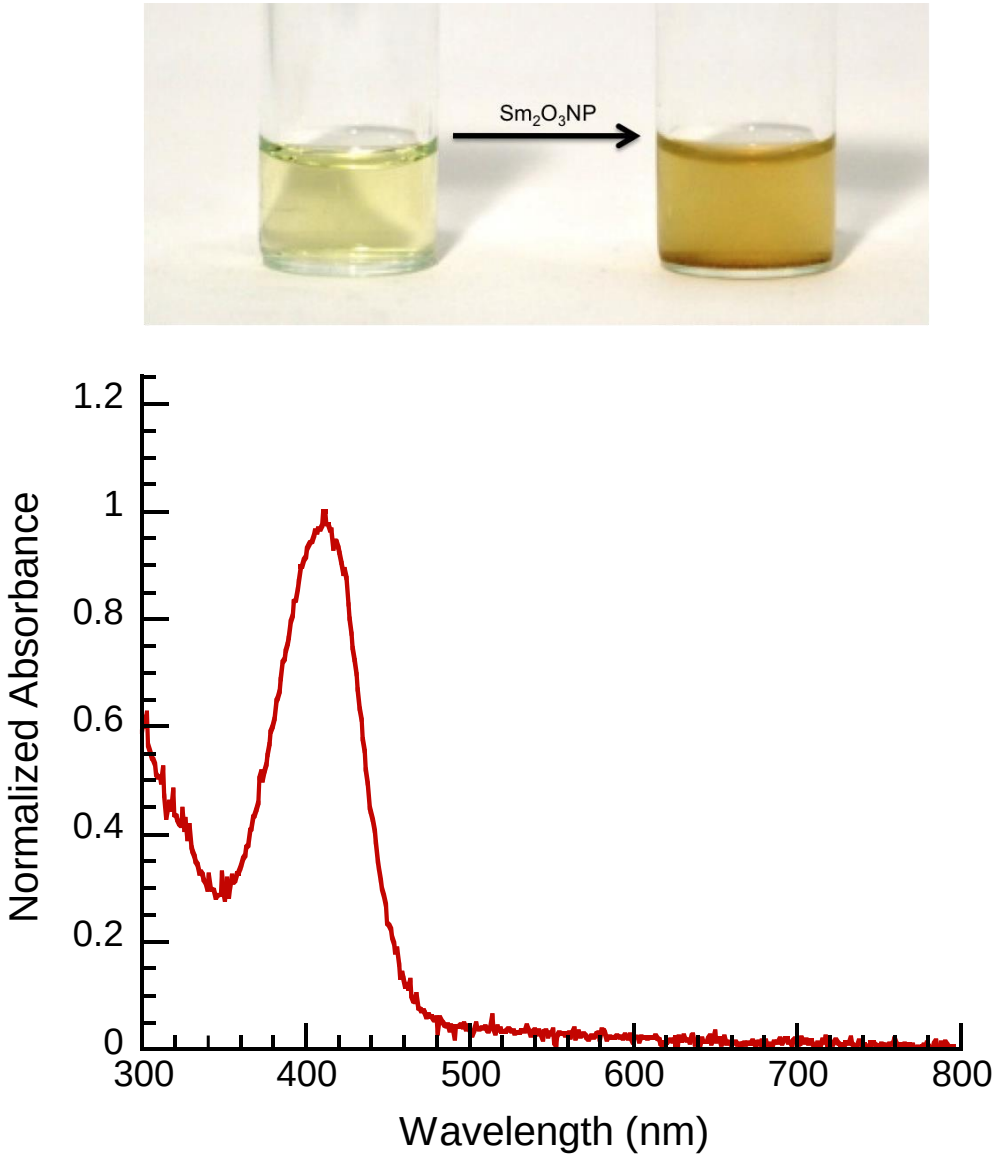

Figure S2.15 *Upper panel*: image of a 10 μM solution of **1** before (left) and 24 h after (right) addition of base treated Sm_2O_3NP. *Lower Panel:* normalized absorbance of a 10 μM solution of **1** after 24 h exposure to base treated Sm_2O_3NP and subsequent centrifugation. Note the lack of absorbance at 590 nm that would be indicative of the presence of **2**.

References:

(1) Nguyen, T.-D.; Mrabet, D.; Do, T.-O. *J. Phys. Chem. C* **2008**, *112*, 15226-15235.

(2) Nguyen, T.-D.; Dinh, C.-T.; Do, T.-O. *Langmuir*, **2009**, *25*, 11142-11148.

(3) Mason, M. G.; Lee, S. T.; Apai, G.; Davis, R. F.; Shirley, D. A.; Franciosi, A.; Weaver, J. H. *Phys. Rev. Lett.* **1981**, *47*, 730-733.

(4) Xu, Q.; Hu, S.; Cheng, D.; Feng, X.; Han, Y.; Zhu, J. *J. Chem. Phys.* **2012**, *136*, 154705.

(5) Sarma, D. D.; Hegde, M. S.; Rao, C. N. R. *J. Chem. Soc. Faraday Trans. 2*, **1981**, *77*, 1509-1520.

(6) Zhang, F.; Wang, P.; Koberstein, J.; Khalid, S.; Chan, S.-W. *Surf. Sci.* **2004**, *563*, 74-82; He, T.; Chen, D.; Jiao, X.; Wang, Y.; Duan, Y. *Chem. Mat.* **2005**, *17*, 4023-4030.

(7) Cheng, D.; Xu, Q.; Han, Y.; Ye, Y.; Pan, H.; Zhu, J. *J. Chem. Phys.* **2014**, *140*, 094706.

(8) Bueno-Alejo, C. J.; D'Alfonso, C.; Pacioni, N. L.; Gonzalez-Bejar, M.; Grenier, M.; Lanzalunga, O.; Alarcon, E. I.; Scaiano, J. C. *Langmuir*, **2012**, *28*, 8183-8189.

This manuscript has been adapted from *RSC Adv.* **2015**, *5*, 3728-3732, with permission, from the Royal Society of Chemistry. Small changes to the original manuscript provide consistent formatting and clarity with respect to the overall thesis.

2.4 Accompaniment to Chapter 2

This article, further to being my first peer-reviewed publication as primary contributing author, describes my first independently-led research project as a graduate student. In addition to achieving our goal of exploring the preparation of an interesting and potentially useful new nanocatalyst based on the lanthanide series, another valuable outcome of this project was that it necessitated training on various laboratory instruments, photochemical techniques and in material characterization. In retrospect, investing a significant amount of additional time might allow the synthetic protocol outlined in Chapter 2 to be optimized further, particularly in terms of the formation (or

the isolation) of smaller (< ca. 100 nm), more desirable Sm_2O_3NP (see Chapters 3 and 4). For instance, experimental results published in later articles (discussed in Chapters 3 and 4) suggest that increasing the ionic strength *in situ* or during the workup phase might allow a greater proportion of these smaller, active Sm_2O_3NP to be harvested. The possibility that the smaller Sm_2O_3NP form first, later to grow or coalesce into larger nanoparticles over the reported 48 h reaction cannot be excluded. In this scenario, smaller Sm_2O_3NP would therefore be present as a stable colloid at shorter irradiation times and could potentially be isolated before being allowed sufficient time to ripen, without resorting to the longer irradiation times necessary to observe a large quantity of precipitate with the naked eye. This conjecture is consistent with the general knowledge that at the millimolar concentrations used, formation of the highly reducing ketyl radical shown in Scheme 2.1 would cease after several minutes, and not hours, of UVA irradiation.

On the other hand, if one were only able to optimize the isolation of the small Sm_2O_3NP rather than increasing their effective formation (e.g. by limiting ripening), then the yield of small Sm_2O_3NP would be too low (perhaps even on the order of a few milligrams) for this protocol to be considered efficient in terms of producing usable quantities of nanocatalyst. Considering also the substantial volume of organic solvent used (250 mL MeCN), neither would it be desirable nor responsible from an environmentally conscious standpoint. In alignment with the reported objectives noted in Chapter 2 (i.e. development of a fast, green method for the preparation of Sm_2O_3NP), another parameter warranting consideration is the source of UVA irradiation. Revising the procedure to take advantage of high-power, less diffuse LEDs in place of fifteen 8 W UVA fluorescent lamps could potentially lead to reduction of the irradiation time, increased nanocatalyst yield and decreased polydispersity.

3. Dye Synthesis in the Pechmann Reaction: Catalytic Behaviour of Samarium Oxide Nanoparticles Studied Using Single Molecule Fluorescence Microscopy

3.1 Preamble to Chapter 3

This chapter describes the first catalytic application of samarium oxide nanoparticles to be investigated as part of this doctoral research program. In light of the Brønsted acid properties uncovered during routine characterization of Sm_2O_3NP, discussed in the preceding chapter, the Brønsted acid catalyzed Pechmann *trans*-esterification and condensation provided a viable tool for assessing the efficacy of the new nanomaterial for actual applications in catalysis. Indeed, the choice of the molecular components of this system (reagents and product) allowed for a thorough evaluation of the catalytic performance of Sm_2O_3NP in the synthetically relevant preparation of a common organic dye. In addition, the catalytic formation of a fluorescent moiety from non-emissive reagents (fluorescence activation) afforded the opportunity to directly monitor the process at the single molecule level using fluorescence microscopy. This feature compounded the impact of this work by unequivocally identifying the mode of catalysis exhibited by the new material. It provided a platform for bringing the use of single molecule fluorescence microscopy as a tool in catalysis research to the attention of a broader audience–hence its publication in the flagship journal of the Royal Society of Chemistry.

3.2 Postprint Version of Manuscript

First published in: *Chem. Sci*. **2016**, *7*, 1314-1321.

Abstract

Photochemically prepared samarium oxide nanoparticles (Sm_2O_3NP) efficiently catalyze the formation of coumarin 153 via the Pechmann *trans*-esterification and condensation process. The formation of the fluorescent coumarin allowed the catalytic process to be monitored in real time at the single molecule level using Total Internal Reflection Fluorescence Microscopy (TIRFM). Benchtop experiments conducted in parallel demonstrated that the observed catalysis occurred in solution rather than by pure heterogeneous catalysis and is due to a mobile population of small Sm_2O_3NP released from a polydisperse original sample containing larger particles. TIRFM provided unique insights by demonstrating that catalysis by these smaller colloidal particles is in fact a surface process, while the larger particles are merely suppliers of the small catalytic nanostructures. We refer to this behaviour as a semi-heterogeneous catalytic system. This work showcases the opportunity that single molecule fluorescence techniques can offer in terms of understanding and ultimately improving benchtop and scale-up synthesis.

Introduction

Owing to unique physicochemical properties not observed at the macroscale, nanoparticles (NPs) have found applications ranging from pharmaceuticals to optoelectronics to alternative energy sources.[1-4] Catalysis often plays an integral role in these applications and evaluating the properties and the performance of a new catalytic material is essential; in particular, the true nature of the catalytic process requires attention to establish if the process is purely homogeneous or intrinsically heterogeneous, or both.[5,6,8-10] In addition to performing heterogeneous catalysis, nanomaterials may act as precursors to homogeneous catalysis by leaching metal ions which then form catalytically active organometallic complexes in solution.[3,5,6,8,11] Nanomaterials may also exhibit ‘semi’-heterogeneous behaviour, where catalysis occurs in solution but as a consequence of the release of mobile colloidal NPs acting

as heterogeneous catalysts (this work), or by *in situ* generation of small clusters that are the truly catalytically active species. The reverse scenario, semi-homogeneous catalysis, is also a possibility; organometallic complexes intended for homogeneous catalysis have the potential to precipitate catalytically active NPs in solution.[5,6,9,10] Mechanistically different, an example has recently been reported in which catalytically active copper clusters are generated *in situ*, by the sequential reduction of copper salts to copper NPs to clusters.[12] Separation and proper disposal of homogeneous catalysts can be a costly and time-consuming process, making pure heterogeneous catalysis attractive from both an industrial and an environmental perspective. Indeed, while many colloidal metal nanostructures and NPs immobilized onto active or inactive matrices possess high degrees of catalytic activity and sometimes reusability, catalysts that operate on a purely heterogeneous basis present valuable advantages, such as easier extraction of the product; minimal product contamination; facile catalyst recovery and in many cases reusability.[8,13] Reliably identifying the mode of catalysis is therefore a priority during the development of new nanostructured catalytic materials. Unfortunately, current methods of distinguishing between homogeneous and heterogeneous catalysis leave room for improvement. For example, control experiments can be conducted using supernatant obtained by washing the catalyst with solvent.[11] Although such tests may be effective on a per-case basis, they do not provide any additional insight regarding the underlying catalytic mechanism. A bottom-up approach to catalyst design may benefit from a more generally applicable means of not only detecting the mode of catalysis, but understanding the behaviour of new catalytic materials at the single molecule level.

Powerful imaging techniques traditionally employed in the biological sector are becoming increasingly available to chemists,[2,3,5,6,14-20] providing continuity between the bench scale and single molecule level. Such techniques include Total Internal Reflection Fluorescence Microscopy (TIRFM); Fluorescence Correlation Spectroscopy and Fluorescence Lifetime Imaging Microscopy. Incorporating these tools into catalysis research can shed light on the spatiotemporal heterogeneities often displayed by solid catalysts, thereby adding a new dimension to catalyst design.[2,3,17,19] In addition to identifying the nature of the catalysis directly, catalyst dynamics at the

single molecule level can provide a valuable link between their physicochemical properties, catalytic mechanisms and their applicability on an industrial scale. This strategy of correlating macroscopic catalytic performance with single molecule studies (to which we have referred to as 'from the mole to the molecule')[6,15] allows for an iterative design process enabling rational design of materials with targeted reactivity and customized combinations of desirable properties. Using single molecule techniques to improve benchtop and scale-up strategies (or 'from the molecule to the mole') we foresee a future where improved synthetic procedures are the direct result of mechanistic details obtained in single molecule studies.

Relative to the high temperatures and pressures often employed in traditional heterogeneous catalysis, milder reaction conditions and potential catalyst reusability are attractive aspects of heterogeneous or semi-heterogeneous nanocatalysis. Nanocatalysts can also offer alternatives to the harsh experimental conditions often encountered in homogeneous catalysis, by operating closer to room temperature and eliminating the need for stoichiometric quantities of strong acids or bases.[9,13] Coumarin derivatives are routinely synthesized via the Pechmann *trans*-esterification and condensation reaction. The experimental protocol generally requires elevated temperatures and stoichiometric quantities of strongly acidic homogeneous catalysts.[21-23] We recently reported on the photochemical synthesis and characterization of novel samarium oxide nanoparticles (Sm_2O_3NP) possessing Brønsted acidity.[24] We show here that Sm_2O_3NP can efficiently catalyze the formation of coumarin 153 via the Pechmann reaction and focus on the use of TIRFM to establish the mode of catalysis at work.

Experimental

Methods

Except where otherwise noted, all reagents and solvents were obtained from either Sigma Aldrich or Fisher Scientific. Sm_2O_3NP were photochemically prepared and characterized according to reported protocols.[29] The Pechmann *trans*-esterification and condensation reaction was carried out using a 1:2 molar ratio of 8-hydroxyjulolidine (**1**) to ethyl 4,4,4-trifluoroacetoacetate (**2**). This amounted to 0.211

mmol of the latter and 0.106 mmol of limiting reagent. These reagents were added to a 10 mL round bottom flask along with a magnetic stir bar, 1.5 mL of 99% EtOH and an appropriate mass of Sm_2O_3NP. Reagents **1** and **2** as well as the coumarin 153 product (**3**) used for control experiments were obtained from Sigma-Aldrich and used without further purification. The flask was fitted with a condenser to prevent solvent evaporation. The reaction proceeded for 24 h at 65˚C (or room temperature, for certain control reactions) while stirring at approximately 500 rpm. For the control reaction carried out under LED irradiation (465 nm, 130 mW, LED ENGIN), the experiment was performed in a 3 mL quartz cuvette at room temperature while stirring. The LED is equipped with a SynJet ZFlow 65 cooler (Nuventix) coupled to a heat sink (24 W PAR20, Nuventix) to prevent heating the solution during the reaction. In some cases, the results of which are summarized in Figure 3.2, 3 mg of Sm_2O_3NP were first added to 1.5 mL 99% EtOH in a 10 mL flask equipped with a condenser and were stirred at 65°C for 24 h. The resulting solution was centrifuged for 30 min at 3000 rpm (Drucker Co., Horizon model). The orange supernatant was extracted and used to perform the Pechmann reaction by adding 1 equiv of **1** and 2 equiv of **2** according to the protocol described above. In all cases, isolated yields of **3** were obtained by preparative TLC (SiO_2, CH_2Cl_2:EtOAc 9:1 v/v). The purified product was thoroughly washed with EtOAc and the solvent was distilled under reduced pressure (Buchi Rotovapor model R-200). After the product mass was recorded, the formation of **3** was confirmed by ^{1}H NMR (Bruker AVANCE 300, $CDCl_3$) and high-resolution EI mass spectrometry (HRes, Concept S1, Magnetic Sector mass spectrometer). Mass spectra were acquired at the John L. Holmes Mass Spectrometry Facility at the University of Ottawa. Absorbance spectra were obtained using a Cary-50 UV-Visible spectrophotometer. Dynamic Light Scattering (DLS) measurements were performed on Sm_2O_3NP dissolved in DMSO (2 mg/mL) using a Zetasizer Nano-ZS (Malvern Instruments, 633 nm laser) at 20°C. SEM was conducted using a JEOL JSM-7500F field emission scanning electron microscope where a drop of Sm_2O_3NP suspended in CH_3CN was placed onto a carbon film coated Cu mesh grid (Electron Microscopy Sciences model CF-400-Cu) and evaporated under ambient conditions.

Single molecule fluorescence microscopy

TIRFM was performed with an Olympus FV1000 TIRF microscope (Olympus, Japan). Light from a CW 488 nm Ar laser was collimated and focused through a fibre-optic coupling unit before passing through a beam splitter cube (500dcxr, Chroma) and a 482/18 nm band pass filter (Semrock) which reflected the appropriate excitation light into an oil-immersion Total Internal Reflection (TIR) objective (×100, NA 1.45, Olympus, PLAPO). Fluorescence emission passed back through the TIR objective, was filtered by a 525/45 nm band pass filter (Semrock) and was then focused into an EM-CCD (Rolera EM-C^2, Q-Capture, Surrey, Canada). Single molecule TIRFM experiments were conducted by flowing a 1:2 equimolar solution of 1 nM **1** and **2** though a flow cell reactor (Chamlide model CF-S25-B) placed over a clean, round glass coverslip spin-coated with 50 µL of 0.05 mg/mL Sm_2O_3NP. The apparatus was positioned atop the objective of the TIRFM system and the sample was irradiated at λ_{Ex} 488 nm. Product emission was recorded by the EM-CCD at 10 frames/s. Each frame consisted of a 501×502 pixel (px), 80×80 µm image with a pixel size of 159 nm. The nature of the reaction under investigation (i.e. non-emissive reagents forming an emissive product) enabled the selective excitation of a small number of product molecules, the formation of which could be visualized as a 100 s, 1000 frame image sequence consisting of bright bursting events on a dark background (Supplementary Video 1).

Image analysis protocol

Analysis of TIRFM image sequences was carried out using a combination of ImageJ (NIH), MATLAB (MathWorks) and OriginLab software. In brief, 3×3 px regions of interest (ROIs) were selected based on the automated identification of stochastic emission (bursting) representing the formation of coumarin 153 product molecules. After background subtraction was performed with ImageJ (rolling ball algorithm, 10 px radius), bursting events were examined graphically. This was done by first using ImageJ to measure the mean fluorescence intensity inside each ROI for every frame in a 100 s image sequence. These data were tabulated and imported into OriginLab, where frame numbers were converted to units of time. Mean intensity was then plotted

as a function of time to generate a unique intensity-time trajectory for every ROI (e.g. Figure 3.4). Three-dimensional surface projections were constructed in ImageJ, by measuring the mean intensity of every px in an 80×80 μm focal area (complete field of view) for every frame in a 100 s image sequence of 1000 frames. The accumulated fluorescence intensity at each location was then plotted as a 3D projection.

Results and Discussion

Bench scale evaluation of Sm_2O_3NP as a Brønsted acid catalyst

The potential to utilize the Brønsted acidity of photochemically prepared Sm_2O_3NP for catalysis was evaluated using the reaction between 8-hydroxyjulolidine (**1**) and ethyl 4,4,4-trifluoroacetoacetate (**2**) to form coumarin 153 (**3**) as a model system (Scheme 3.). The Pechmann *trans*-esterification and condensation reaction is a multi-step process in which a strong acid plays multiple (proton-transfer) roles.[22] Performing the reaction for 24 h at 65˚C under air produced **3** in high yields (Table 3.1). The product was purified by preparative TLC and identified by ^{1}H NMR and EI-MS.

Scheme 3.1 Overall reaction for the preparation of coumarin 153 via the Sm_2O_3NP-catalyzed Pechmann *trans*-esterification and condensation process.

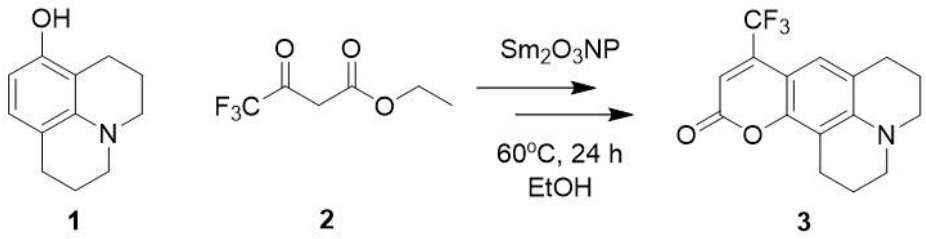

Table 3.1 Results of Sm_2O_3NP-catalyzed formation of coumarin 153 and relevant control reactions.

Catalyst	Amount of Catalyst	Time (h)	Temperature (°C)	Yield of **3** (%)
Sm_2O_3NP[a]	3 mg	24	65	93
No catalyst	–	24	65	15
4-HEBA	8.3 mg	68	65	34
Sm_2O_3NP supernatant	1.5 mL	24	65	100

[a]*Reaction performed in the dark*

The yield of **3** increased from 15% in the absence of a catalyst, to 93% using a catalytic mass of Sm_2O_3NP (8.6×10^{-3} equiv). This dramatic increase in efficiency demonstrates that Sm_2O_3NP catalyze the reaction. Since the NPs are stabilized by 4-hydroxyethoxybenzoic acid (4-HEBA), it was necessary to establish the possible

catalytic role of the stabilizer in the formation of coumarin 153. As shown in Table 3.1, a large excess of 4-HEBA in the absence of Sm_2O_3NP resulted in a significantly lower yield, even after 68 h. An isolated yield of 93% encouraged further investigation of Sm_2O_3NP as a heterogeneous alternative to commonly-used homogeneous strong acid catalysts.[21-23] However, it became apparent that the mode of catalysis was not purely heterogeneous, as evidenced by benchtop experiments designed to probe the nature of the catalytically active species. First, Sm_2O_3NP were placed under conditions identical to those used for the Pechmann reaction (i.e. catalyst mass, solvent volume, temperature and duration) but in the absence of **1** and **2**. Centrifuging the resulting mixture at 3000 rpm produced a Sm_2O_3NP pellet and an orange supernatant resembling the colour of Sm_2O_3NP dissolved in DMSO. The absorbance spectra of these two orange solutions overlapped well, and SEM imaging confirmed the suspected presence of NPs in the supernatant (Figure S3.1-S3.2, Supporting Information). It has previously been reported that the solid Sm_2O_3NP are polydisperse, ranging in size from approximately 70-700 nm.[24] As would be expected, those observed in the supernatant were at the low end of this range. Dynamic Light Scattering (DLS) suggested a mean hydrodynamic diameter less than 150 nm (Table S3.1, Supporting Information). Using this supernatant as both the solvent and the catalyst in the Pechmann reaction produced a quantitative yield of **3** in 24 h (Table 3.1). Further, it was found that just 0.2 mg of colloidal Sm_2O_3NP were responsible for this yield, indicating that the catalytically active species released from the polydisperse sample of Sm_2O_3NP constituted just 6.7% of the total mass of solid. A related example was recently reported in which copper nanoparticles release smaller particles or clusters that are ultimately responsible for the catalysis.[12]

Surprisingly, the smaller Sm_2O_3NP remained stable in EtOH even after centrifuging at 10,000 rpm for 30 min at room temperature, followed by a second centrifugation at 10,000 rpm for 30 min at 4°C. Their high colloidal stability relative to the larger Sm_2O_3NP is reflected in the zeta potential of the particles remaining in solution which, at +35 mV, is significantly higher than that of polydisperse Sm_2O_3NP in DMSO (+23 mV).[24] Interestingly, increasing the ionic strength of the solution provided a convenient means of catalyst separation. The zeta potential of colloidal

particles is inversely proportional to ionic strength, and the zeta potential at the isoelectric point is zero.[25] Increasing the ionic strength of the solution provides counterions that repress the electric double layer surrounding colloidal particles and leads to decreased particle–particle repulsion, thus destabilizing the system and favouring particle aggregation. Here, the addition of $(CH_3)_4NCl$ resulted in decreased zeta potential and a greater propensity for both spontaneous and centrifuge-assisted NP precipitation (Figure 3.1). The Sm_2O_3NP began to precipitate, upon centrifugation at 10,000 rpm for 15 min, when the zeta potential reached +9.5 mV (50 mM $(CH_3)_4NCl$). As shown in Figure 3.1, the absorbance of the solution followed a similar trend, decreasing with zeta potential and increased ionic strength.

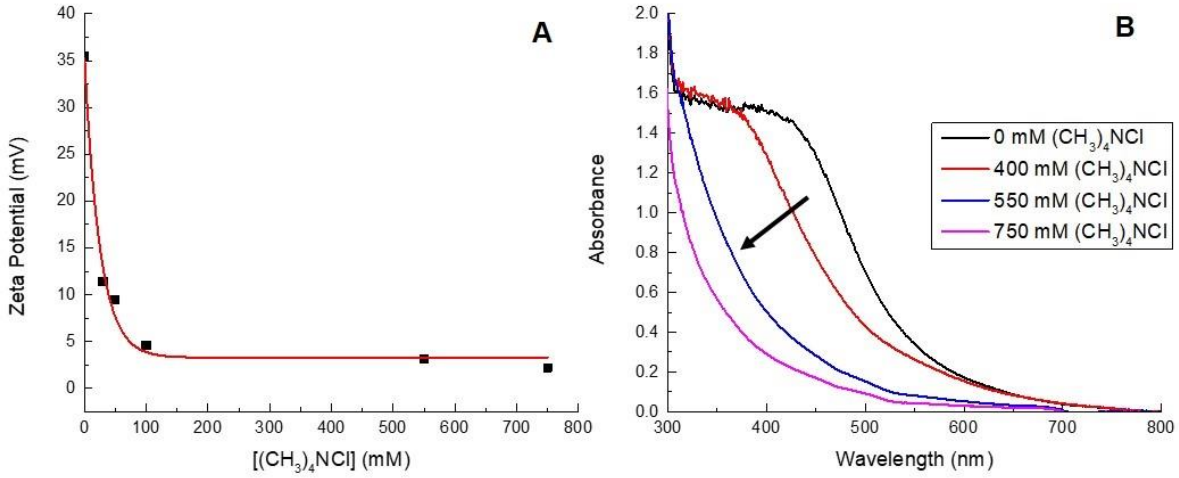

Figure 3.1 Decreasing zeta potential (A) and absorbance (B) of a solution of ≈0.2 mg Sm_2O_3NP dissolved in 1 mL 99% EtOH as a function of increasing ionic strength attained by adding various quantities of $(CH_3)_4NCl$.

In addition to offering ease of separation, non-homogeneous catalysts can often be reused several times. In this case the solid polydisperse Sm_2O_3NP can function as a pre-catalyst, providing a continuous source of catalytically active colloidal Sm_2O_3NP over several rounds of catalysis. As shown in Figure 3.2, repeatedly exposing and recovering a single 3 mg sample of the pre-catalyst provided a fresh supply of catalytically active colloidal Sm_2O_3NP, with the isolated yield of **3** steadily decreasing as the smaller Sm_2O_3NP were diminished from the polydisperse sample

of particles. Electron microscopy confirmed the presence of such particles in the original polydisperse sample (Figure 3.3).

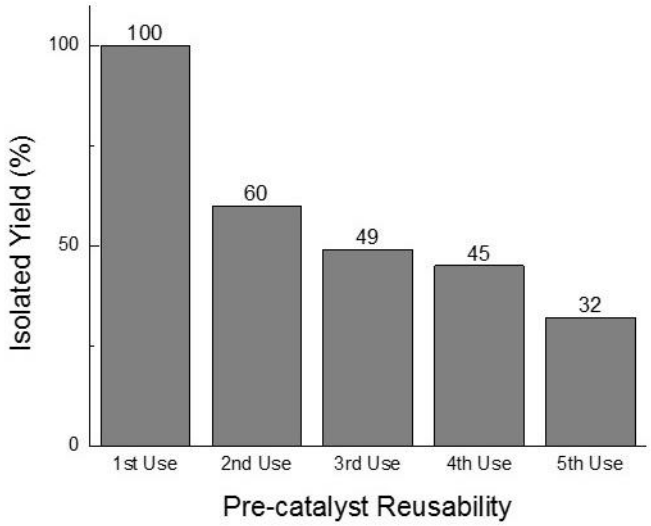

Figure 3.2 Reusability of the solid Sm_2O_3NP pre-catalyst. Each usage represents the isolated yield of coumarin 153 obtained by preparative TLC after performing the reaction between **1** (1 equiv) and **2** (2 equiv) at 65°C for 24 h in the supernatant obtained by centrifuging a sample of 3 mg Sm_2O_3NP previously stirred for 24 h at 65°C in 1.5 mL 99% EtOH.

Although the Sm_2O_3NP represent a separable, reusable catalyst for the formation of **3**, the question of the exact mode of catalysis remained unclear. Whereas metal ion leaching into solution colloidal Sm_2O_3NP could result in homogeneous catalysis, heterogeneous catalysis performed by separable, colloidal Sm_2O_3NP released from solid polydisperse Sm_2O_3NP would be better described as a semi-heterogeneous process. Benchtop experimentation demonstrated that a subpopulation of the polydisperse Sm_2O_3NP do form a stable colloidal suspension during the reaction, but was unable to unequivocally establish whether or not the catalysis occurs on the surfaces of the smaller, mobile Sm_2O_3NP. We therefore turned to single molecule fluorescence microscopy in an effort to gain a more in-depth understanding of the catalytic mechanism involved in this system.

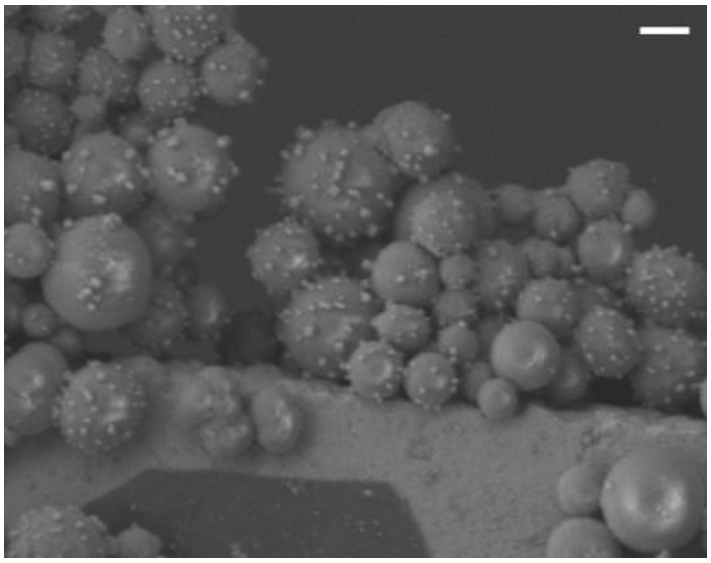

Figure 3.3 Representative SEM image demonstrating that some of the small catalytic Sm_2O_3NP, which become colloidal particles during the reaction, are already present in the original polydisperse pre-catalytic powder. Note that the sizes of the particles shown above are in good agreement with DLS performed upon supernatant containing catalytically active colloidal particles. Scale bar is 1 μm.

Investigating the catalytic behaviour at the single molecule level

In order to identify the mode of catalysis observed at the bench scale, the Sm_2O_3NP-catalyzed preparation of coumarin 153 was monitored at the single molecule level using TIRFM. This technique benefits from enhanced axial and lateral resolution provided by an evanescent field propagating parallel to the sample surface. The field is strongest at the interface between the glass coverslip and the reaction medium and decreases exponentially with distance. This effectively generates an excitation source in the form of a thin film allowing a small number of molecules to be selectively excited. Together with low sample concentration, this increases the signal-to-noise ratio by eliminating secondary fluorescence from molecules situated outside the primary focal plane.[2,6] In an appropriately designed system, TIRFM enables real-time monitoring of catalysis at the single molecule level and with single molecule sensitivity.[2,3,5-7,14-20]

The catalytic preparation of coumarin 153 induces fluorescence emission centred at 532 nm (Figure S3.3, Supporting Information). Although the Pechmann reaction is most efficient at temperatures exceeding 65˚C (in EtOH), it was necessary to work within the limits of the instrumentation used for fluorescence microscopy.

Nonetheless, even at room temperature, enough product formation could be observed to monitor the catalysis using TIRFM (Table S3.2, Supporting Information). Further, the number of catalytic events that can be observed in a short time is enhanced by continuously supplying a fresh source of reagents by flowing **1** and **2** atop the catalyst at a rate of 1 mL/h during TIRFM experiments. An additional control reaction performed at room temperature under irradiation with a 130 mW 465 nm LED provided assurance the catalysis is not affected by the CW laser irradiation (488 nm, 5 mW) used to excite **3** for TIRFM (Table S3.2, Supporting Information).

Product formation was visualized in the form of 100 s image sequences each showing stochastic fluorescence bursting on a dark background (Supplementary Video 1). Identifying the locations of bursting events and subsequently plotting fluorescence intensity as a function of time can allow for accurate discrimination between heterogeneous and homogeneous catalysis.

While homogeneous or non-catalytic product formation would lead to randomly distributed single bursting events as molecules of **3** form in solution and randomly diffuse in and out of the focal plane, heterogeneous catalysis is characterized by repetitive bursting in discrete locations, as a result of molecules of **3** repeatedly being formed on the surfaces of static catalytic particles before diffusing out of the field of view.[6,7] As shown in Figure 3.4, repetitive bursting was indeed observed when supernatant containing only the small, catalytically active Sm_2O_3NP was spin-coated onto a microscope coverslip and the reaction monitored using TIRFM. These bursting events are clearly distinguishable from background scattering when compared to intensity-time trajectories extracted from TIRFM image sequences recorded while flowing only solvent atop the catalyst (Figure S3.4, Supporting Information). Moreover, no such repetitive bursting could be observed in the absence of Sm_2O_3NP; TIRFM image sequences recorded while flowing **1** and **2** atop a clean coverslip contained only short-lived, singular bursting events corresponding to non-catalytic product formation (Figure S3.5, Supporting Information). It follows that the catalytic formation of **3** mediated by the small, colloidal Sm_2O_3NP is a surface process.

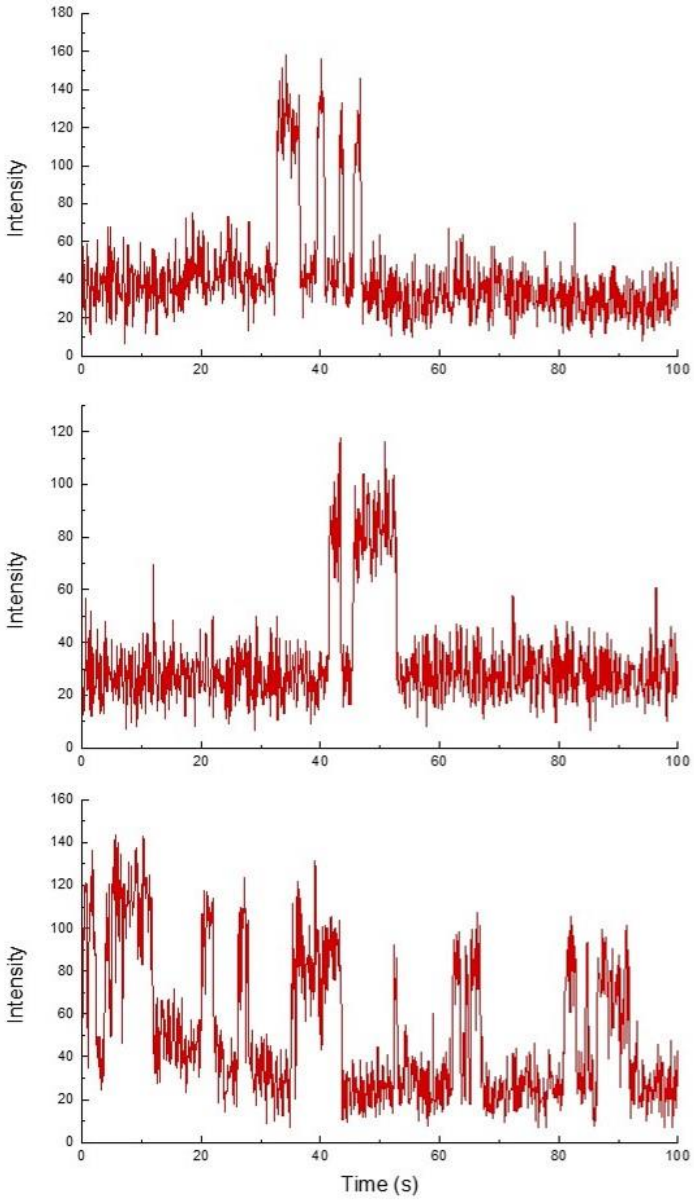

Figure 3.4 Representative intensity-time trajectories showing the intensity profile and duration of repetitive fluorescence bursts occurring at three different 3×3 px ROIs over 100 s, 1000 frame TIRFM image sequences obtained at room temperature. Note that the individual bursting events have roughly the same intensity, each representing emission from a single molecule.

Three-dimensional surface projections of TIRFM image sequences provided efficient and immediate visual confirmation of heterogeneous catalysis by colloidal Sm_2O_3NP at the single molecule level, by illustrating that fluorescence intensity from **3** accumulates in specific locations (Figure 3.5 upper panel). In contrast, the three-dimensional surface projection of the TIRFM experiment in which **1** and **2** were flowed

atop a blank coverslip shows diffuse fluorescence all over the field of view, the result of molecules of **3** forming in solution and randomly drifting in and out of the focal plane (Figure 3.5 lower panel).

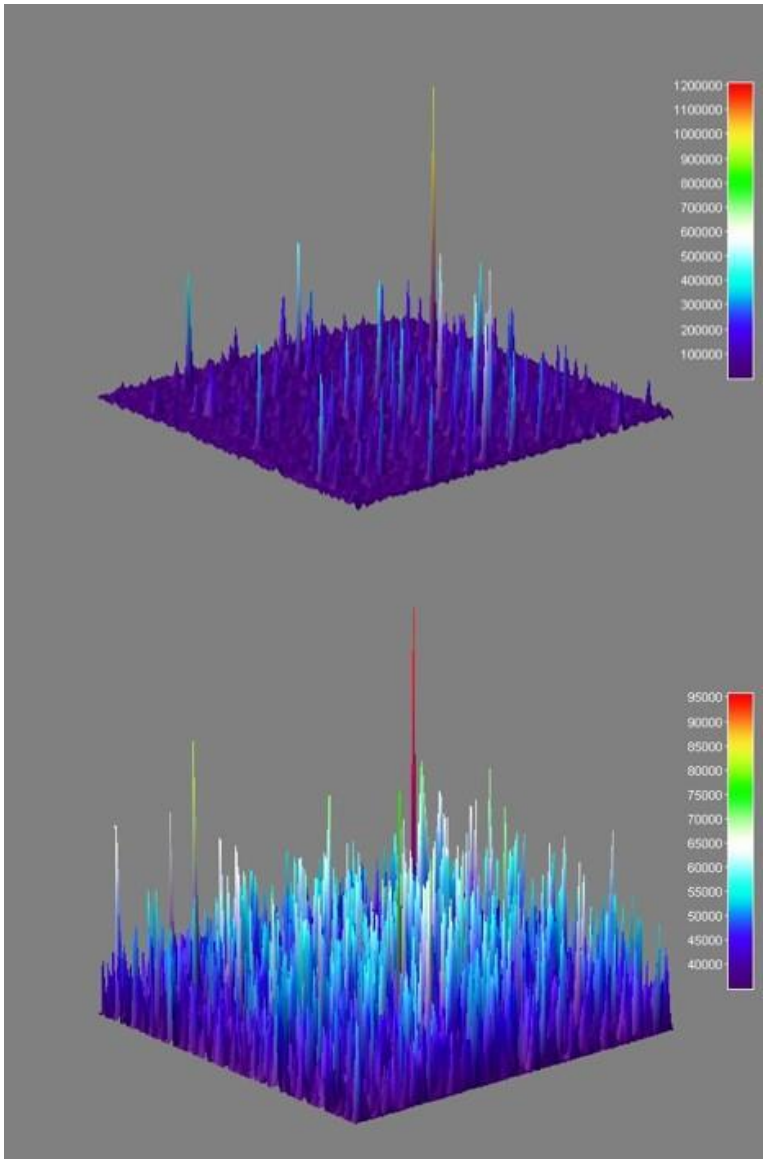

Figure 3.5 Three-dimensional surface projections showing accumulated fluorescence intensity at discrete locations, extracted from TIRFM image sequences recorded while flowing a 1:2 equimolar solution of **1** and **2** atop a microscope coverslip spin-coated with supernatant obtained after centrifuging a sample of 3 mg Sm_2O_3NP previously stirred for 24 h at 65°C (upper panel) and atop a clean coverslip in the absence of Sm_2O_3NP (lower panel). Note the difference between the maximum of the intensity scale in the upper vs lower panels, which is 1.2×10^6 and 9.5×10^4, respectively.

TIRFM also demonstrated that the polydisperse Sm_2O_3NP pre-catalyst is capable of providing a continuous supply of colloidal heterogeneous catalyst. Intensity-time trajectories corresponding to image sequences recorded while flowing **1** and **2** atop a microscope coverslip spin-coated with solid Sm_2O_3NP recovered after harvesting supernatant containing catalytically active colloidal particles four times, still showed repetitive bursting (Figure 3.6). As shown in Figure 3.6, this occurred specifically in areas where large Sm_2O_3NP were not located (high levels of scattering by large Sm_2O_3NP render them visible in TIRFM image sequences). This indicates that even after four cycles, the pre-catalyst is still able to release catalytically active colloidal particles, which is in good agreement with bench scale experiments summarized in Figure 3.2.

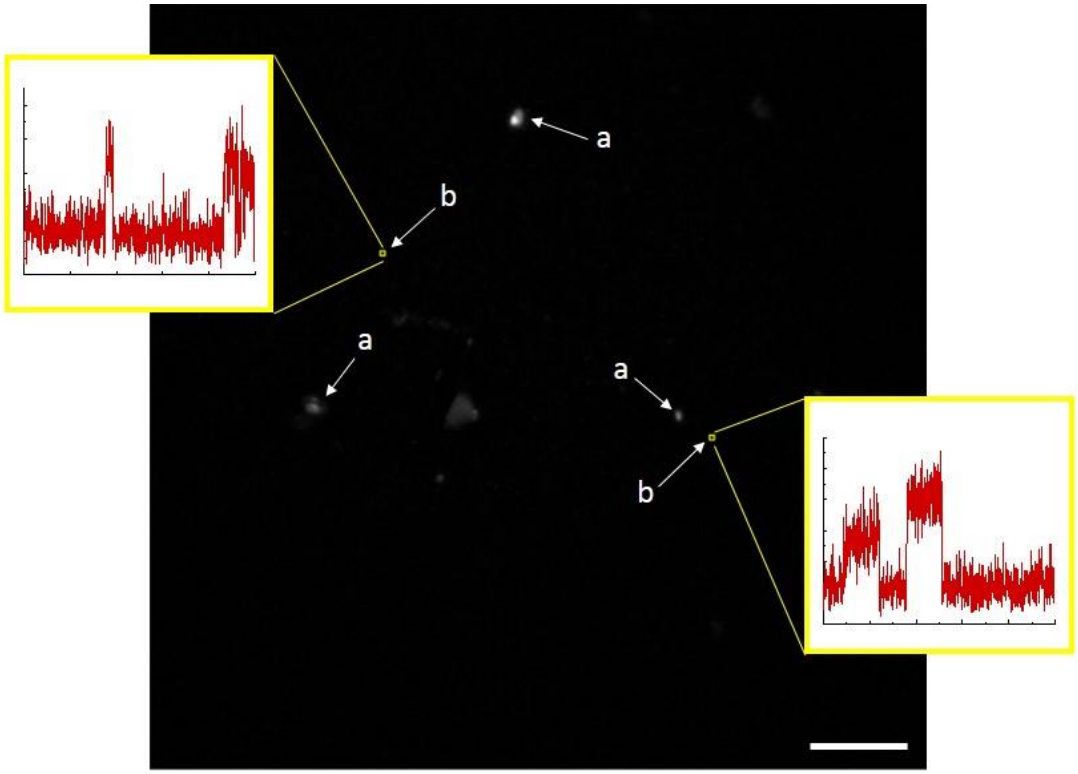

Figure 3.6 Single frame from a TIRFM image sequence recorded while flowing **1** and **2** atop a coverslip spin-coated with Sm_2O_3NP recovered after harvesting catalytically active colloidal Sm_2O_3NP four times. Large Sm_2O_3NP are visible due to scattering (a), and multiple bursting is only observed in 3×3 pixel regions where no large Sm_2O_3NP are located (b). Scale bar is 10 μm.

Using TIRFM, it was also possible to establish that the small colloidal Sm_2O_3NP responsible for the catalysis are present in the original polydisperse sample, and are not generated *in situ* via decomposition or reduction of the larger particles (see also inset in Figure 3.2). TIRFM image sequences recorded while flowing **1** and **2** atop a coverslip spin-coated with freshly prepared pre-catalytic Sm_2O_3NP also contain repetitive bursting events in discrete locations where no large particles can be identified directly in the TIRFM image sequence nor in a transmission image of the same field of view (Figure S3.6, Supporting Information). This result confirms the presence of the catalytically active species in the initial sample, which was suspected but could not be known for certain based solely upon the wide particle size distribution inherent to the original material.[24]

Conclusion

Coumarin 153 can be synthesized under mild conditions with isolated yields greater than 90% using Sm_2O_3NP as a reusable semi-heterogeneous catalyst. The power of TIRFM and the nature of the system under investigation (i.e. non-emissive reagents forming an emissive product with an appropriate excitation and emission profile) made it possible to visualize the formation of a coumarin dye at the single molecule level. Importantly, single molecule fluorescence microscopy provided insight into the mode of catalysis exhibited by Sm_2O_3NP which was not easily gleaned from initial benchtop experimentation. We suggest that linking single molecule experiments back to catalytic performance at the bench scale can be a powerful tool in the design of novel nanostructured materials, by unmasking details that are often hidden by ensemble-averaged measurements. That is, '*from the molecule to the mole"* can be a powerful strategy in the optimization of new catalysts. In this case, monitoring the catalysis at the single molecule level augmented bench scale experimentation by identifying the mode of catalysis exhibited by the truly catalytically active species, providing conclusive evidence that the Sm_2O_3NP-catalyzed synthesis of coumarin 153 occurs through a semi-heterogeneous catalytic mechanism in which small colloidal NPs released from a polydisperse sample of solid Sm_2O_3NP perform heterogeneous catalysis. At low ionic strength these colloidal NPs are remarkably stable, but can be

readily separated by simply increasing the ionic strength via addition of a suitable salt. A similar approach is currently being explored in an investigation of other catalytic systems.

References

(1) Chen, Y.-S.; Kamat, P. V. *J. Am. Chem. Soc*. **2014**, *136*, 6075.

(2) Sambur, J. B.; Chen, P. *Ann. Rev. Phys. Chem*. **2014**, *65*, 395.

(3) Buurmans, I. L. C.; Weckhuysen, B. M. *Nature Chem*. **2012**, *4*, 873.

(4) Gomes Silva, C.; Juarez, R.; Marino, T.; Molinari, R.; Garcia, H. *J. Am. Chem. Soc*. **2011**, *133*, 595.

(5) Esfandiari, N. M.; Blum, S. A. *J. Am. Chem. Soc*. **2011**, *133*, 18145.

(6) Decan, M. R.; Impellizzeri, S.; Marin, M. L.; Scaiano, J. C. *Nature Commun.* **2014**, *5*, 4612.

(7) Xu, W.; Kong, J. S.; Yeh, Y.-T. E.; Chen, P. *Nature Mater*. **2008**, *7*, 992.

(8) Davies, W.; Matty, L.; Hughes, D. L.; Reider, P. J. *J. Am. Chem. Soc.* **2001**, *123*, 10139.

(9) Atero, V.; Fontecave, M. *Chem. Soc. Rev*. **2013**, *42*, 2338.

(10) Chen, L.; Chen, G.; Leung, C.-F.; Yiu, S.-M.; Ko, C.-C. *ACS Catal.* **2015**, *5*, 356; Cherdo, S.; Ghachtouli, S. E.; Sircoglou, M.; Brisset, F.; Orio, M.; Aukauloo, A. *Chem. Commun.* **2014**, *50*, 13514; Fang, M.; Engelhard, M. H.; Zhu, Z.; Helm, M. L.; Roberts, J. A. S. *ACS Catal*. **2014**, *4*, 90.

(11) McTiernan, C. D.; Pitre, S. P.; Scaiano, J. C. *ACS Catal*. **2014**, *4*, 4034.

(12) Oliver-Messuguer, J.; Liu, L.; García-García, S.; Canós-Giménez, C.; Domínguez, I.; Gavara, R.; Doménech-Carbó, A.; Concepción, P.; Leyva-Pérez, A.; Corma, A. *J. Am. Chem. Soc.* **2015**, *137*, 3894.

(13) Hudson, R.; Li, C.-J.; Moores, A. *Green Chem*. **2012**, *14*, 622.

(14) Roeffaers, M. B. J.; De Cremer, G.; Libeert, J.; Ameloot, R.; Dedecker, P.; Bons, A.-J.; Bückins, M.; Martens, J.; Sels, B. F.; De Vos, D. E.; Hofkens, J. *Angew. Chem. Int. Ed.* **2009**, *48*, 9285.

(15) Carrillo, A. I.; Stamplecoskie, K. G.; Marin, M. L.; Scaiano, J. C. *Catal. Sci. Technol.* **2014**, *4*, 1989.

(16) De Cremer, G.; Sels, B. F.; De Vos, D. E.; Hofkens, J.; Roeffaers, B. *J. Chem. Soc. Rev*. **2010**, *39*, 4703.

(17) Hensle, E. M.; Blum, S. A. *J. Am. Chem. Soc.* **2013**, *135*, 12324; Ristanović, Z.; Kerssens, M. M.; Kubarev, A. V.; Hendriks, F. C.; Dedecker, P.; Hofkens, J.; Roeffaers, M. B. J.; Weckhuysen, B. M. *Angw. Chem. Int. Ed.* **2015**, *54*, 1836.

(18) Impellizzeri. S.; Simoncelli, S.; Fasciani, C.; Marin, M. L.; Hallett-Tapley, G. L.; Hodgson, G. K.; Scaiano, J. C. *Catal. Sci. Technol.* **2015**, *5*, 169; Marin, M. L.; Hallett-Tapley, G. L.; Impellizzeri, S.; Fasciani, C.; Simoncelli, S.; Netto-Ferreira, J. C.; Scaiano, J. C. *Catal. Sci. Technol.* **2014**, *4*, 3044.

(19) Easter, Q. T.; Trauschke, V.; Blum, S. A. *ACS Catal*. **2015**, *5*, 2290.

(20) Janssen, K. P. F.; De Cremer, G.; Neely, R. K.; Kubarev, A. V.; Van Loon, J.; Martens, J. A.; De Vos, D. E.; Roeffaers, M. B. J.; Hofkens, J. *Chem. Soc. Rev*. **2014**, *43*, 990.

(21) Selvakumar, S.; Chidambaram, M.; Singh, A. P. *Catal. Commun*. **2007**, *8*, 777.

(22) Daru, J.; Stirling, A. *J. Org. Chem.* **2011**, *76*, 8749.

(23) Gunnewegh, E. A.; Hoefnagel, A. J.; van Bekkum, H. *J. Mol. Catal. A: Chemical*, **1995**, *100*, 87; Dong, F.; Jian, C.; Kai, G.; Qunrong, S.; Zuliang, L. *Catal. Lett.* **2008**, *121*, 255; Upadhyay, K. K.; Mishra, R.; Kumar, A. *Catal. Lett*. **2008,** *121*, 118.

(24) Hodgson, G. K.; Impellizzeri, S.; Hallett-Tapley, G. L.; Scaiano, J. C. *RSC Adv*. **2015**, *5*, 3728.

(25) Attard, P. *Curr. Opin. Colloid Interface Sci.* **2001**, *6*, 366; Carlson, J. J.; Kawatra, S. K. *Miner. Process Extr. Metall. Rev.* **2013**, *34*, 269; Greenwood, R. *Adv. Colloid Interface Sci.* **2003**, *106*, 55.

3.3 Postprint Version of Supporting Information

Detailed image analysis protocol for the identification of ROIs. An in-house written MATLAB script “Spectacle.m” was used to identify ROIs potentially representing real bursting events. Spectacle.m was built around a freely available MATLAB sub-routine “Localize.m” which allows one to utilize the function “LocalizerMatlab.mex64”, originally written and made available by Peter Dedecker from the University of Luven (Belgium). This function was designed for the precise localization of single fluorescence emitters in super-resolution microscopy image analysis. This can be done using MATLAB or through the IgorPro graphical user interface. The Localizer function has been thoroughly tested against and has performed at least as well as similar super-resolution imaging software such as QuickPALM and RapidSTORM.[1] The advantage of Localizer is that it can be incorporated into larger MATLAB scripts such as Spectacle.m, where it can be tailored to meet the needs of other applications such as TIRFM that also require efficient and unbiased automated localization of fluorescence emitters.

Specifically, Localizer analyzes an image, or series of frames of an image stack, by using one of six localization algorithms (2DGauss, 2DGaussFixedWidth, Ellipsoidal2DGauss, IterativeMulitplication, Centroid, MLEwG) in combination with a segmentation algorithm, the Generalized Likelihood Ratio Test (GLRT), to identify the locations of possible fluorescence emission. The GLRT includes a Probability of False Alarm (PFA) parameter that was left at its default value of 25%. Similar to other super-resolution software, Localizer uses these algorithms to approximate the spatial distribution of the fluorescence emission detected from individual molecules, known as the Point Spread Function (PSF), by fitting it to a mathematical function. For our purposes the two-dimensional Gaussian function was selected because it provides the most detailed data and highest level of accuracy, despite requiring the longest computation time. The localization algorithm requires an initial estimation of the standard deviation of the PSF. This parameter was set to 1.5 px based on an estimation made using the ImageJ 3D super-resolution plugin. In addition, this value constitutes a logical maximum standard of deviation since all ROIs consisted of 3×3 pixel areas. Localizer finds the centre of the Gaussian distribution and identifies it as

the location of the signal. The portion of the output of the Localizer function utilized by Spectacle.m is a tabulated list of (x,y) coordinates in px units, corresponding to precise emitter locations. For image sequences Localizer analyzes image data on a frame by frame basis. The purpose of Spectacle.m, in addition to selecting only the (x,y) coordinates of emitters from the data output by Localizer, is primarily to remove artifacts by filtering the data such that only those locations where emission is detected in at least 3 consecutive frames (i.e. 0.3 s) are retained. Since these coordinates must then be converted to 3×3 px ROIs to facilitate efficient measurement of mean intensity vs time using ImageJ, Spectacle.m also conducts a nearest neighbor type analysis of the remaining coordinates. It examines every single remaining coordinate and checks that no other emitter coordinates fall within a ±3 px range in both the *x*- and *y*-directions. When any such scenarios occur, Spectacle.m randomly selects only one copy and discards the others. The purpose of this secondary function is to eliminate the possibility of overlapping ROIs once the data is imported into ImageJ and converted to 3×3 px ROIs, avoiding the painstaking process of manually cross-checking the coordinates of every single ROI to ensure that overlapping ROIs are not mistakenly counted multiple times. Finally, Spectacle.m returns a list of the remaining (x,y) coordinates which are then imported into the ImageJ ROI Manager as 3×3 px ROIs with the aid of a simple ImageJ macro written using the ImageJ macro scripting language.

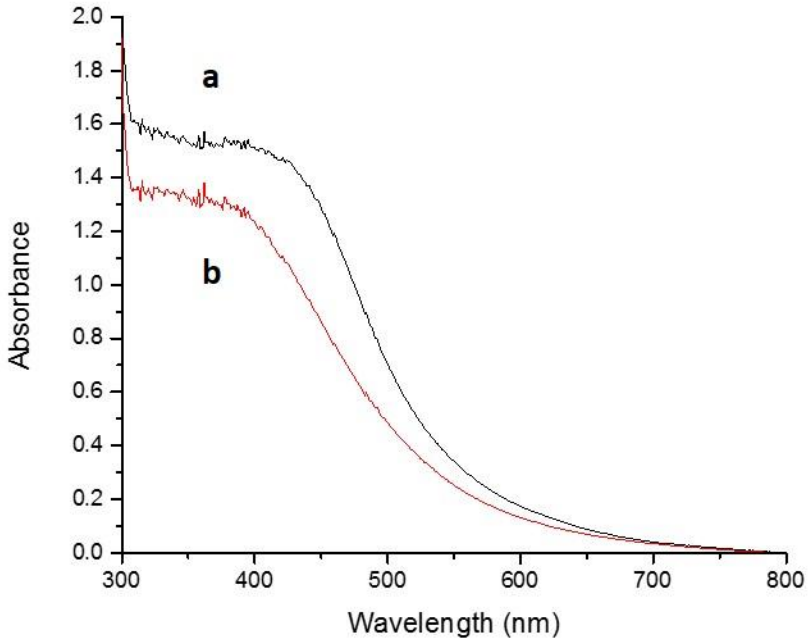

Figure S3.1 Absorbance spectra of the supernatant obtained after centrifuging a sample of 3 mg Sm_2O_3NP previously stirred for 24 h at 65°C (a); Sm_2O_3NP dissolved in DMSO (b).

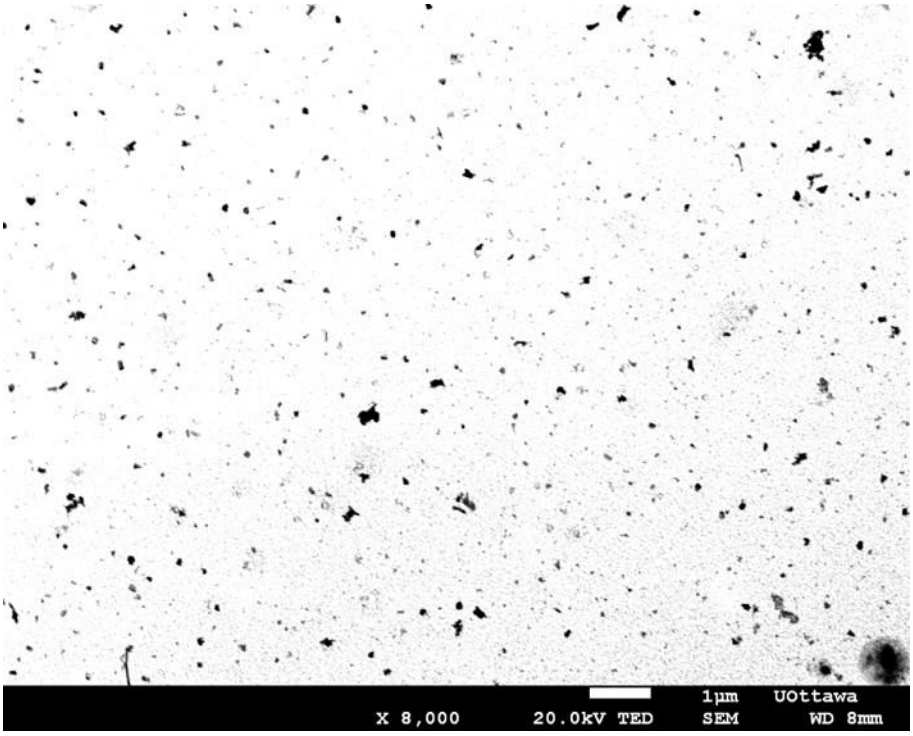

Figure S3.2 SEM image of the orange supernatant obtained after centrifuging a sample of 3 mg Sm_2O_3NP previously stirred for 24 h at 65°C.

Table S3.1 DLS data pertaining to Sm_2O_3NP present in the supernatant after centrifuging a sample of Sm_2O_3NP previously stirred in EtOH for 24 h at 65°C. All measurements were acquired at 25°C.

Measurement	Hydrodynamic Diameter Z-Average Method (nm)	Hydrodynamic Diameter Number Mean Method (nm)
1	144.0	96.28
2	143.6	81.03
3	144.2	101
4	144.6	90.23
5	142.2	87.41
6	142.5	89.29
Mean	143.5 ± 0.96	90.9 ± 6.9

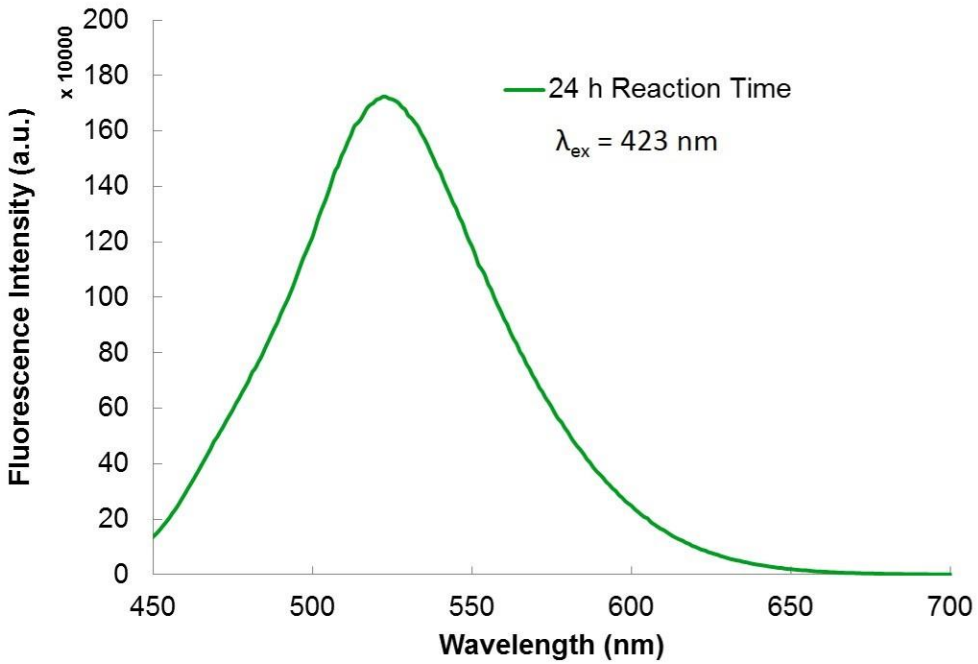

Figure S3.3 Fluorescence emission spectrum of coumarin 153 product obtained after 24 h reaction at 65°C in the presence of Sm_2O_3NP.

Table S3.2 Pechmann control reactions performed at room temperature.

Catalyst	Amount of Catalyst	Time (h)	Yield of **3** (%)
Sm_2O_3NP	3 mg	24	10
Sm_2O_3NP[a]	3 mg	24	18
Sm_2O_3NP supernatant	1.5 mL	24	40
No Catalyst	–	24	5

[a]*Reaction irradiated by a 465 nm, 130 mW blue LED*

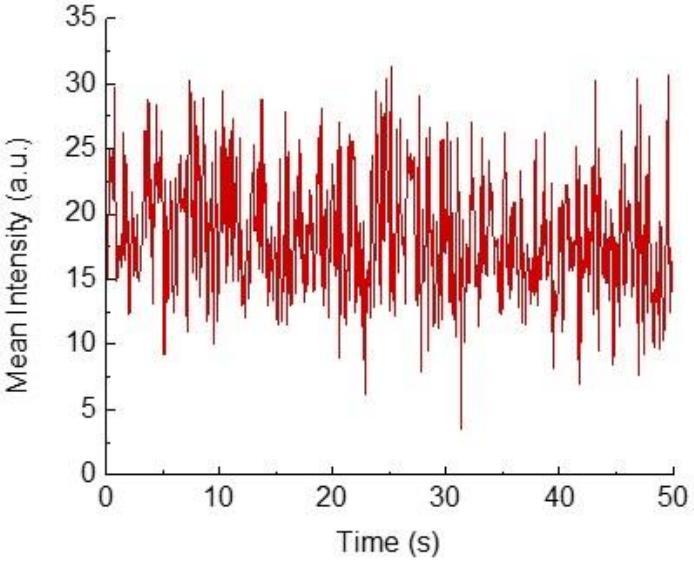

Figure S3.4 Representative background intensity vs time trajectory for a 3×3 px ROI obtained from a TIRFM image sequence where solvent only was flowed over Sm_2O_3NP.

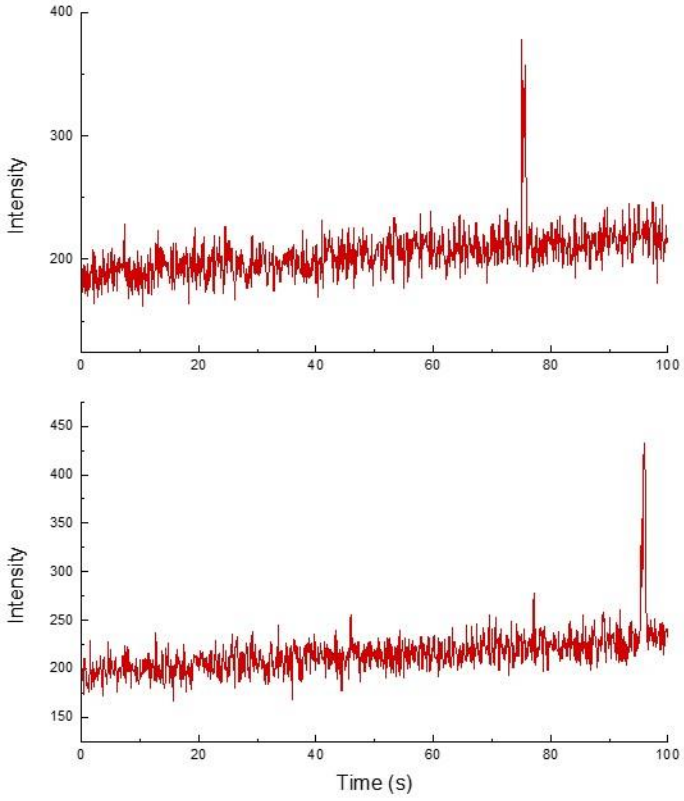

Figure S3.5 Representative intensity-time trajectories containing only singular bursting events, extracted from TIRFM image sequences recorded while flowing **1** and **2** in the absence of Sm_2O_3NP (i.e. atop a clean glass coverslip).

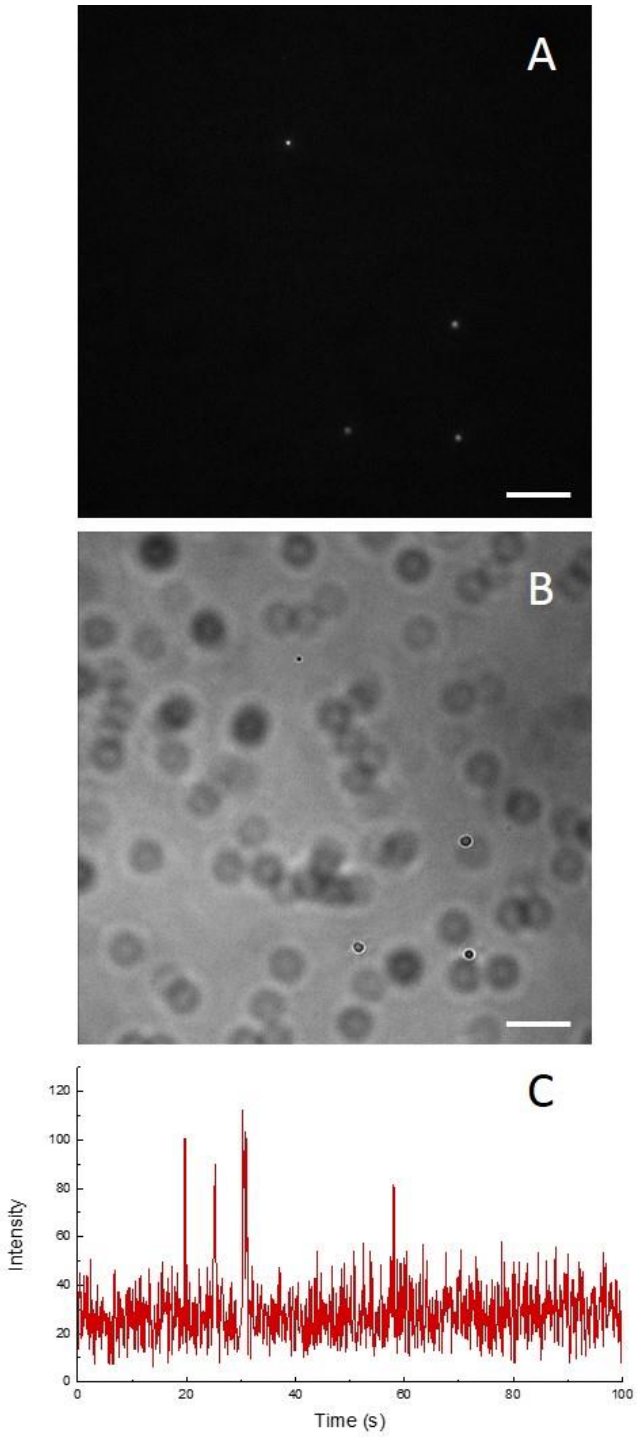

Figure S3.6 Single frame from a TIRFM image sequence recorded while flowing **1** and **2** atop a glass coverslip spin-coated with the original polydisperse, pre-catalytic Sm_2O_3NP (A); corresponding transmission image of the same field of view shown in A, demonstrating that the locations large Sm_2O_3NP are identifiable in TIRFM image sequences due to scattering (B); representative intensity-time trajectory extracted from a TIRFM image sequence described in A, showing repetitive fluorescence bursting in discrete locations as evidence of heterogeneous catalysis (C). Scale bars are 10 µm.

References

(1) Dedecker, P.; Duwe, S.; Neely, R. K.; Zhang, J. *J. Biomed. Opt*. **2012**, *17*, 126008.

This manuscript has been adapted from *Chem. Sci*. **2016**, *7*, 1314-1321, with permission, from the Royal Society of Chemistry. Small changes provide consistent formatting and clarity with respect to the overall thesis. Supplementary Video 1 may be very useful, and can be accessed online, free of charge, via the link above.

3.4 Accompaniment to Chapter 3

This publication describes the first application of Sm_2O_3NP, photochemically prepared as discussed in Chapter 2, in catalysis. Not only was the Brønsted acidity of these Sm_2O_3NP harnessed for the efficient synthesis of a common organic dye, it was incorporated into a system suitable for TIRFM, where catalytic fluorescence activation allowed the heterogeneous vs homogeneous behaviour of the nanocatalyst to be evaluated in real time with spatial and temporal precision. Although Sm_2O_3NP did allow the product to be isolated in excellent yield, the single molecule approach toward distinguishing between heterogeneous and homogeneous catalysis carried out by new nanomaterials was arguably the greater advance presented in this work, and became the major focus of this research project.

While it may be tempting to assume that catalysis performed by a solid nanostructured catalyst in solution is heterogeneous, that is not always the case. This work is an archetypal example of the situation being more complex than a discrete, clear-cut distinction between homogeneous and heterogeneous catalysis. Surely, there is a lesser defined, ‘grey’ area between the two extremes, where many possibilities for hybrid modes of catalysis can exist. The subtle differences between pure and semi-heterogeneous catalysis for example, can be difficult if not impossible to distinguish experimentally at the bench scale. The consequences of those differences however, can be far-reaching in terms of the effectiveness of the catalyst for real-world applications. Product contamination by catalytic particles might necessitate additional purification steps or impart undesirable metal toxicity. As was observed here, losses during catalyst recovery could also lead to poor performance in terms of recyclability, one of the principle assets of heterogeneous catalysis.

4. Single Molecule Study of Samarium Oxide Nanoparticles as a Purely Heterogeneous Catalyst for One-Pot Aldehyde Chemistry

4.1 Preamble to Chapter 4

In the previous study, it was found that a subpopulation of polydisperse Sm_2O_3NP acted as a semi-heterogeneous nanocatalyst which could be readily separated by increasing the ionic strength of the crude product solution during workup. However, a better scenario could be realized if the catalytic system intrinsically precluded the formation of a stable Sm_2O_3NP colloid, simply due to the magnitude of its own inherent ionic strength. This essentially describes one aspect of the approach taken toward the research described in this chapter, on the oxidative catalytic properties of Sm_2O_3NP. This investigation built directly upon the insights discussed in Chapter 3; the catalytic system was engineered such that one of the reagents as well as the final product are cationic, enabling the catalysis to be carried out in a purely heterogeneous fashion.

At the same time, and no less importantly, we were able to expand the utility of Sm_2O_3NP to a different type of catalysis. Furthermore, a second element of the system designed for this purpose allowed the catalysis to once again be monitored using single molecule fluorescence microscopy. Rather than catalytic fluorescence activation though, the supramolecular strategy employed in this investigation made use of a bathochromic shift in fluorescence upon catalysis by Sm_2O_3NP. In addition to confirming the heterogeneous nature of the catalysis and enhanced activity exhibited by the smallest Sm_2O_3NP, this approach again shed light upon unanticipated facets of the catalysis where bench scale experimentation fell short. This time, fascinating insights into the catalytic mechanism were obtained and are discussed in detail below.

4.2 Postprint Version of Manuscript

First published in: *Catal. Sci. Technol*. **2016**, *6*, 7113-7121.

Abstract

Heterogeneous catalysis holds distinct advantages over homogeneous catalysis; however, it is only truly advantageous if unaffected by metal ion leaching or *in situ* formation of a soluble catalytically active species. Herein, samarium oxide nanoparticles (Sm_2O_3NP) were employed as a redox catalyst for the first time, providing a generally applicable route to performing one-pot aldehyde chemistry beginning with an inexpensive and more readily-prepared starting material–an alcohol. The reaction is efficient under mild conditions and does not suffer from over-oxidation of the starting material to its corresponding carboxylic acid. This key asset of the Sm_2O_3NP catalyst hinges upon a lack of release of free aldehyde into the system. Single molecule fluorescence microscopy revealed that catalysis is restricted to the surfaces of small nanoparticles in a polydisperse nanomaterial, where the product of the oxidative process can be selectively revealed via a subsequent coupling reaction, which occurs without the intermediacy of a free aldehyde. Instead the catalytically active particles act as docking stations, holding the pre-aldehyde until intercepted by a second reagent to complete the oxidation and subsequent reaction in a single step. Coupling this supramolecular strategy to our single molecule approach revealed the interesting nature of the catalytic mechanism and demonstrated that the catalysis is a purely heterogeneous process. Samarium is quite abundant relative to many transition metals (e.g. Ru, Ir, Pt) and thus Sm_2O_3NP-based nanomaterials may present an opportunity to develop more sustainable catalysts for common organic transformations.

Introduction

In recent years, single molecule fluorescence microscopy has become a valuable tool in the study of chemical reactions, providing fundamental mechanistic insights for their development and improvement.[1-19] In the context of transition metal and metal nanoparticle (NP) catalysis, single molecule techniques offer a means to determine

the true nature of the catalysis, whether it be homogeneous, heterogeneous or some combination that defies traditional classification.[20-24] For example, Blum and co-workers used single molecule fluorescence microscopy to demonstrate the homogeneous nature of a ruthenium catalyst by imaging a ring-opening metathesis polymerization (ROMP).[25,26] In a recent report, we employed Total Internal Reflection Fluorescence Microscopy (TIRFM) to establish that copper nanoparticles (CuNP) can effectively promote the 1,3-dipolar cycloaddition between an azide and a terminal alkyne (click chemistry) through a purely heterogeneous pathway.[27] Discerning the active regions of catalysts is also of great interest, and has been the focus of a number of recent single molecule catalysis reports.[1,2,18] Hofkens and co-workers successfully used single molecule techniques to map the catalytic activity of zeolites and mesoporous materials.[10,13-15] The field has progressed to a stage in which single molecule–single particle studies yield enough information to improve the performance of a catalytic system at the bench scale, through heterogenization of the catalytic process or by describing how key aspects of catalyst preparation or modification impact its activity, or the mode by which the catalysis proceeds.[2-4,10,13,14,25,26]

Single molecule techniques also offer the opportunity to evaluate the performance and the behaviour of a catalyst when conventional bench scale techniques are inadequate or not applicable. For instance, they can provide a useful alternative to large scale catalyst production in situations where catalyst preparation requires lengthy procedures, harsh experimental conditions or gives low yields. Provided that the synthesis of the material does not present safety concerns or other drawbacks, catalysts are routinely synthesized in relatively large quantities and catalytic activity is assessed at the bench scale through screening of multiple reagents and reaction conditions, often accompanied by high throughput combinatorial analysis. However, this trial and error approach becomes vastly inefficient when catalyst or reagent preparation is particularly challenging, costly or scarcely efficient. Single molecule fluorescence microscopy circumvents these obstacles by providing a viable alternative; it is a bottom-up approach permitting the examination of catalytic activity when traditional approaches are limited, and thereby extends the realm of possibilities in catalysis research.

We recently developed a simple and safe synthetic strategy for the photochemical preparation of samarium oxide nanoparticles (Sm_2O_3NP) under mild conditions.[28] Within this contribution, we reported for the first time that Sm_2O_3NP possess Brønsted-type acidity. Although our synthetic protocol offers several advantages with respect to previously reported methods, the low percent yield obtained did not allow for a systematic screening of substrates to investigate the catalytic performance of Sm_2O_3NP. Nevertheless, using single molecule microscopy, we were able to investigate the activity of these Sm_2O_3NP utilizing very low quantities of catalyst. We have already examined one potential application of this new material in the Brønsted acid catalyzed synthesis of coumarin dyes via the Pechmann *trans*-esterification and condensation pathway.[22] Although the process produced high yields for several catalytic cycles under mild conditions, monitoring the catalysis at the single molecule level revealed startling information about the catalyst performance and potential for scaled up synthesis. TIRFM demonstrated that the active species is in fact comprised of smaller NPs present in the polydisperse solid nanomaterial, and that the reaction occurs heterogeneously on the surfaces of these colloidal NPs. Despite the ability to separate the catalyst by increasing the ionic strength of the solution after the reaction, we elected to act on the insight provided by single molecule fluorescence microscopy, and investigate other catalytic systems where the behaviour of the Sm_2O_3NP might be improved upon in order to take full advantage of pure heterogeneous catalysis. The supramolecular system described here achieved this objective by increasing the ionic strength of the reaction mixture enough to maintain phase-separation between the product and the catalytically active nanoparticles. We refer to this strategy of building upon information gained at the single molecule level to improve bench scale catalytic performance as *'from the molecule to the mole'*.

Herein, we sought to determine whether Sm_2O_3NP can be employed as a redox catalyst for the purpose of conducting one-pot aldehyde chemistry beginning with a more readily prepared and inexpensive starting material–the corresponding alcohol. The electronic configuration of samarium is highly responsive to small changes in the local chemical environment, and this sensitivity may be responsible for the interesting diversity of surface and subsurface oxidation states observed in different samarium-

based nanomaterials.[29] Efforts to understand the nature of these valence changes as they relate to temperature, particle size, morphology and composition have suggested that while in most cases the Sm^{3+} oxidation state dominates over Sm^{2+}, mixed valences are likely to exist on the surfaces of samarium-based nanomaterials.[30-35] Whether these mixed valences are of a homogeneous (Sm_2O_{3-x}) or heterogeneous (site specific integer valence) nature is still unknown for the general case, and may well be a material-specific property.[30] Regardless of their source, such oxygen deficiencies can allow for the capture and release of oxygen under redox conditions, a quality that has garnered some interest for the development and characterization of samarium-based redox catalysts.[32-34,36] To the best of our knowledge, this report is the first example in which Sm_2O_3NP have been investigated for redox-type catalysis. Partial oxidation of the starting alcohol occurs on the surfaces of Sm_2O_3NP, and thus the catalytic nanoparticles also act as protective docking stations for the activated alcohol until it can be intercepted by another reagent to complete the oxidation and subsequent reaction in one pot. This strategy allows the synthesis of aldehyde-derived compounds to proceed without the intermediacy of a free aldehyde and prevents over-oxidation to the carboxylic acid, a common problem in aldehyde oxidation chemistry. The supramolecular strategy employed herein not only improved upon our previous work by ensuring that the catalytic process is fully heterogeneous, it also offered a facile means to monitor product yields at the bench scale and at the single molecule level (*vide infra*).

Results

Benchtop Experimentation. In order to investigate the Sm_2O_3NP-catalyzed oxidation of alcohols both at the bench scale and at the single molecule level, we synthesized the –OH functionalized fluorescent compound **1** (Figure 4.1). Compound **1** absorbs at 380 nm and is strongly emissive at 450 nm; by replacing the hydroxyl functionality with an aldehyde as in compound **2**, both the absorption and emission wavelengths shift to 450 and 490 nm, respectively (Figure S4.1-S4.2, Supporting Information). Interestingly, the emission spectrum of the supernatant obtained by centrifuging (3000 rpm, 30 min) a solution of Sm_2O_3NP and **1** previously stirred for 24

hours at 65°C contains an emission band centered at 465 nm (Figure S4.3, Supporting Information). This band is slightly red-shifted with respect to **1** (at 450 nm) and blue-shifted with respect to **2** (at 490 nm) but is still consistent with a coumarin-type structure, which we refer to as the partially oxidized activated alcohol compound on the Sm_2O_3NP surface (abbreviated '**[2]$_s$**'). However, this red shift is insufficient to permit estimation of the yield of **[2]$_s$** obtained in the reaction by spectroscopic methods. Only upon addition of an equimolar amount of **3** (relative to **1**) were we able to estimate the yield of both **[2]$_s$** and **4**, using absorbance spectroscopy. Compound **3** is unreactive toward the –OH functional group but reacts with aldehydes in EtOH to generate the supramolecular assembly **4** (Figure 4.1) in a single step, with quantitative yields and without the addition of a catalyst.[37] In a previous report, we elucidated the mechanism for this condensation.[38]

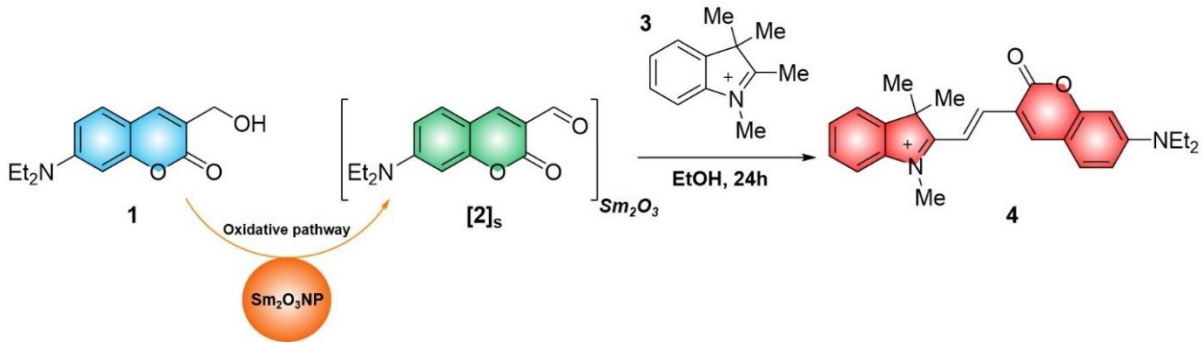

Figure 4.1 Proposed scheme for the Sm_2O_3NP-catalyzed oxidation of **1** to the activated alcohol compound **[2]$_s$** and its subsequent reaction with the indolium cation **3** to yield the supramolecular assembly **4**.

The extended conjugation within **4** causes a substantial red-shift to the absorption and emission bands of this compound, with the absorption band centered at 575 nm and the emission band at 635 nm. The full spectroscopic characterization of compounds **1**, **2** and **4** is illustrated in Figure S4.1 and Figure S4.2 of the Supporting Information. Since the condensation between **[2]$_s$** and **3** occurs quantitatively, the percent yield of **4** indirectly corresponds to the oxidation of **1** and yield of **[2]$_s$** obtained during the Sm_2O_3NP-catalyzed oxidation of **1**. Knowing that the molar extinction coefficient of **4** is 14218 M^{-1} cm^{-1} at 575 nm, the yield of **[2]$_s$** can easily be estimated by monitoring the appearance of the absorption band of **4**, as illustrated in Figure S4.1.

For a typical reaction, 12 mg of **1**, 9 mg of **3** and variable amounts of Sm_2O_3NP were dissolved in 2 mL of EtOH and stirred for 24 h at 65°C. High temperature is not explicitly necessary but encourages the condensation between **[2]$_s$** and **3** (Table 4.1). The known Brønsted acidity of the Sm_2O_3NP[28] does not affect the reagents' stability nor their activity. In order to maximize the recovery of **4**, the catalyst was centrifuged and washed three times with EtOH and the supernatants combined and dried under reduced pressure. The residue was then dissolved in 2 mL of EtOH, diluted 100 fold and analyzed by UV-Vis spectroscopy. The results are summarized in Table 4.1.

Table 4.1 Catalytic performance of Sm_2O_3NP under various reaction conditions. Percent yields of the Sm_2O_3NP-catalyzed oxidation of **1** to **[2]$_s$** were obtained by monitoring the condensation reaction (24 h) between **[2]$_s$** and **3** to generate the supramolecular assembly **4**. For entries **a-h**, mol% reflects the amount of polydisperse Sm_2O_3NP. For entries **i-j**, the amount is given as mol% catalytically active small Sm_2O_3NP isolated from the polydisperse nanomaterial. For entry **g**, the reaction vessel was purged but Ar (g) was not bubbled through the solution and the ethanol solvent was not distilled.

Reaction	Amount of Catalyst	Temperature (°C)	Atmosphere	Yield of **4** (%)
a	1.5 mg (8.9 mol %)	65	air	13
b	1.5 mg (8.9 mol %)	65	O_2	19
c	2 mg (12 mol %)	65	air	27
d	5 mg (30 mol %)	65	air	51
e	No catalyst	65	air	5
f	No catalyst	65	O_2	5
g	5 mg (30 mol %)	65	Ar	48
h	5 mg (30 mol %)	25	air	38
i	2 mL supernatant (3.4 mol %)	25	air	33
j	2 mL supernatant (3.4 mol %)	65	air	51

The results reported in Table 4.1 indicate that Sm_2O_3NP promote the catalytic oxidation of the hydroxyl-functionalized **1**. Indeed, the generation of **4** should indicate the presence of **[2]$_s$**, because the active methylene in **3** is not reactive toward hydroxyl functionalities. The presence of **4** is thus an indirect confirmation of the successful oxidation of **1**. Oxygen may enhance the performance of the catalyst slightly, as control experiments conducted in the absence of Sm_2O_3NP are not affected by the reaction atmosphere. However, O_2 (g) is not explicitly necessary (compare reactions **d** and **g**, Table 4.1). An SEM image of Sm_2O_3NP recovered after reaction **d** (Figure

S4.4, Supporting Information) shows that some intact spherical structures are still observable. This observation seems to suggest that the catalyst could potentially be reused but that some degradation occurs, leading to a lesser performance after the first cycle. Recyclability tests for reaction **d** yielded 14.4% of **4** for a second cycle and 9.8% for a third cycle. Most likely the low degree of reusability is due to catalyst degradation (as possibly suggested by SEM images) and the loss of the small nanoparticles responsible for most of the catalysis (*vide infra*).

Our results show that Sm_2O_3NP are unable to fully oxidize alcohols and release free aldehyde product. However, Sm_2O_3NP are capable of forming the partially oxidized activated alcohol compound **[2]$_s$**; this in fact may be Sm_2O_3NP' greatest asset, as it effectively prevents over-oxidation to the carboxylic acid, while **[2]$_s$** shows enough aldehyde-like reactivity to be scavenged by **3**. It is intriguing how Sm_2O_3 is capable of oxidizing **1** to **[2]$_s$** in the absence of oxygen (see Table 4.1). We suggest that in this case Sm_2O_3 acts as a sacrificial oxidant to form **[2]$_s$** followed by its facile recovery (or re-oxidation) by air or oxygen *in situ* or during post-reaction handling. In fact, this is fully consistent with previous reports of samarium oxide materials reversibly alternating between stable Sm_2O_3 and SmO surface states[28-34] and also with our own observations during the synthesis of Sm_2O_3NP,[28] where ketyl radicals partially reduce Sm^{3+} (most likely never fully reduced to Sm^0), that spontaneously undergoes air oxidation to Sm_2O_3 and over a period of time forms Sm_2O_3NP. Thus, it is not surprising that if the Sm_2O_3 surface undergoes some reduction to SmO through the process shown in Figure 4.1, it can readily revert to Sm(III) (see also Figure S4.5 of the Supporting Information).

We have recently reported on another catalytic system, in which the Brønsted acidity of Sm_2O_3NP was exploited in the synthesis of a coumarin dye.[22] Although the catalysis occurred heterogeneously on the surfaces of small Sm_2O_3NP present in the polydisperse nanomaterial, we demonstrated that the catalytically active particles formed a stable colloidal suspension which required the addition of a suitable salt in order to facilitate separation of the catalyst after the reaction. Based on the results of that investigation, and the similar reaction conditions employed here (solvent and temperature) for one-pot aldehyde redox chemistry, we tested for the presence of

colloidal Sm_2O_3NP in the reaction mixture to establish the potentially different catalytic roles played by small versus large Sm_2O_3NP. In this case, the previously-reported colloidal stability of Sm_2O_3NP in EtOH did not set any limitation upon the potential to utilize pure heterogeneous catalysis; the supramolecular catalytic system benefitted from the ionic strength provided by cationic compounds **3** and **4**, which kept the zeta potential of the Sm_2O_3NP low enough that they remained in the solid phase during the reaction and did not form a stable colloidal suspension. This was confirmed by the formation of a pellet comprised of Sm_2O_3NP upon centrifugation (30 min at 3000 rpm), after a reaction was performed in which the solid polydisperse nanomaterial and solvent were replaced with supernatant containing only the small Sm_2O_3NP in an initially stable colloidal suspension in EtOH (as in reaction **i**, Table 4.1). The latter was obtained by stirring the polydisperse Sm_2O_3NP in EtOH for 24 h at 65°C, centrifuging at 3000 rpm for 30 min, and collecting the supernatant.

Similar to our previous report, a combination of bench scale and single molecule experiments revealed that the small Sm_2O_3NP are the sole catalytically active species. This was initially suggested by the fact that identical yields of **4** (51%) were obtained when the reaction was performed using either the polydisperse solid nanomaterial or the solution of supernatant containing only the subpopulation of small Sm_2O_3NP able to form a stable colloidal suspension when an identical mass of polydisperse Sm_2O_3NP powder was pre-exposed to an identical volume of EtOH under reaction conditions (Table 4.1 reaction **i** vs **d**). More direct evidence was provided by single molecule experiments carried out using TIRFM (*vide infra*), which conclusively demonstrated that the catalytic oxidation of compound **1** performed by the small (and not the large) Sm_2O_3NP is a heterogeneous process. Poor recovery of this minute fraction of active component could also have contributed to the low degree of catalyst recyclability that was observed. Indeed, a high loading (30 mol%) of the polydisperse nanomaterial was required in order to provide a sufficient number (3.4 mol%) of the catalytically active small NPs required to obtain an acceptable yield.

Distinguishing pure heterogeneous catalysis from homogeneous catalysis, or a mixture of the two processes, is a critical step in the evaluation of new catalytic materials.[11,17,20-25,27,39] A typical absorption spectrum for a reaction is illustrated in

Figure S4.1 of the Supporting Information. The spectrum shows that both the starting material **1** and the product **4** are present in the reaction mixture, and also suggests traces of the absorption band of **[2]$_S$**, consistent with the emission of **[2]$_S$** detected in the supernatant (containing no large inactive Sm_2O_3NP) obtained by centrifugation (3000 rpm, 30 min) of a solution of **1** and Sm_2O_3NP previously stirred for 24 h at 65°C (Figure S4.3, Supporting Information). Unfortunately, standard chromatographic techniques did not allow for effective isolation or quantitation of compound **[2]$_S$** from this solution. However, adding compound **3** afterward and stirring the mixture for an additional 24 h at 65°C resulted in the formation of the fully condensed species **4** (14%), indicating that the partially oxidized activated alcohol saturated the surfaces of the small, active Sm_2O_3NP where it was protected from over-oxidation and simply waiting to react with **3**. The lower yield obtained was likely due to a partial loss of unreacted **1** during centrifugation and removal of the large Sm_2O_3NP prior to the addition of **3**.

Although the inability to detect **[2]$_S$** by HPLC suggested that it exists strictly on the surfaces of colloidal Sm_2O_3NP stable in EtOH in the absence of **3**, the details of its role in the overall reaction mechanism remained unclear. While bench scale experimentation did show that only a small subpopulation of the polydisperse nanomaterial was catalytically active, it provided no concrete insight into the overall reaction mechanism. We therefore turned to single molecule fluorescence microscopy, which unequivocally demonstrated that the mechanism proceeds via the heterogeneously-catalyzed oxidation of compound **1** to **[2]$_S$** exclusively on the surfaces of small Sm_2O_3NP, where the partially oxidized activated alcohol is then intercepted by compound **3** to generate **4** without the intermediacy of a free aldehyde.

Single Molecule Fluorescence Microscopy. In order to establish the mode of catalysis at work and to elucidate the mechanistic details of the Sm_2O_3NP-catalyzed oxidation of **1**, we investigated the reaction at the single molecule level using TIRFM. The supramolecular strategy employed to monitor the oxidation of **1** at the bench scale provided an additional benefit, by red-shifting the emission band of the product of interest such that it could be selectively excited and its emission easily distinguished from that of **1** at the single molecule level. The emission band of **[2]$_S$** (at 465 nm,

Figure S4.3, Supporting Information) is too close to that of **1** (Figure S4.2, Supporting Information) to allow for reliable differentiation via TIRFM and, at the single molecule level, excitation of **[2]$_s$** using a 488 nm light source does not rule out simultaneous excitation of small populations of **1**. However, species **4** possesses strong emission at 635 nm. Selective excitation of **4** at 633 nm allowed its fluorescence to be monitored using a 676/29 nm band pass emission filter, thus providing a reliable and efficient means of obtaining significant insights into the catalyst's behaviour which, although inaccessible using bench scale techniques, could be gained by monitoring the reaction using TIRFM. Experiments were conducted by recording TIRFM image sequences of various lengths while flowing an equimolar mixture (1–5 nM) of **1** and **3** in EtOH atop a glass microscope coverslip spin-coated with Sm_2O_3NP. A representative image sequence is illustrated in Supplementary Video S1.

Analysis of TIRFM image sequences revealed repetitive fluorescence bursting events (sharp jumps in intensity) at discrete locations in the 80×80 μm^2 TIRFM field of view, which can easily be distinguished above a baseline consisting of background scattering and dark counts (Figure 4.2 and Figure S4.6, Supporting Information). Individual bursting events are caused by the activation of fluorescence as single molecules of species **4** are formed at specific locations. The recorded intensity spikes when emission from a single molecule is detected in a 3×3 pixel region of interest and subsequently returns to the baseline as the molecule diffuses away, assisted by the continuous flow of reagents and solvent. It follows that the detection of multiple distinct bursts at a given location signifies the precise coordinates of a catalytic site provided by a stationary Sm_2O_3NP, and corresponds to a heterogeneous catalytic process in which no free aldehyde species is released.[18,22,27] In contrast, non-catalytic or homogeneously catalyzed formation of molecules of **4** in solution is manifested as singular bursting events within defined regions of interest, as single molecules diffuse in and out of the focal plane. This is likely to occur more frequently as the concentration of reagents increases, and so when attempting to distinguish between homogeneous and heterogeneous catalysis it is necessary to establish a concentration range in which a satisfactory number of repetitive, co-located bursting events can be observed without causing an overwhelming number of singular bursts to be detected.[13]

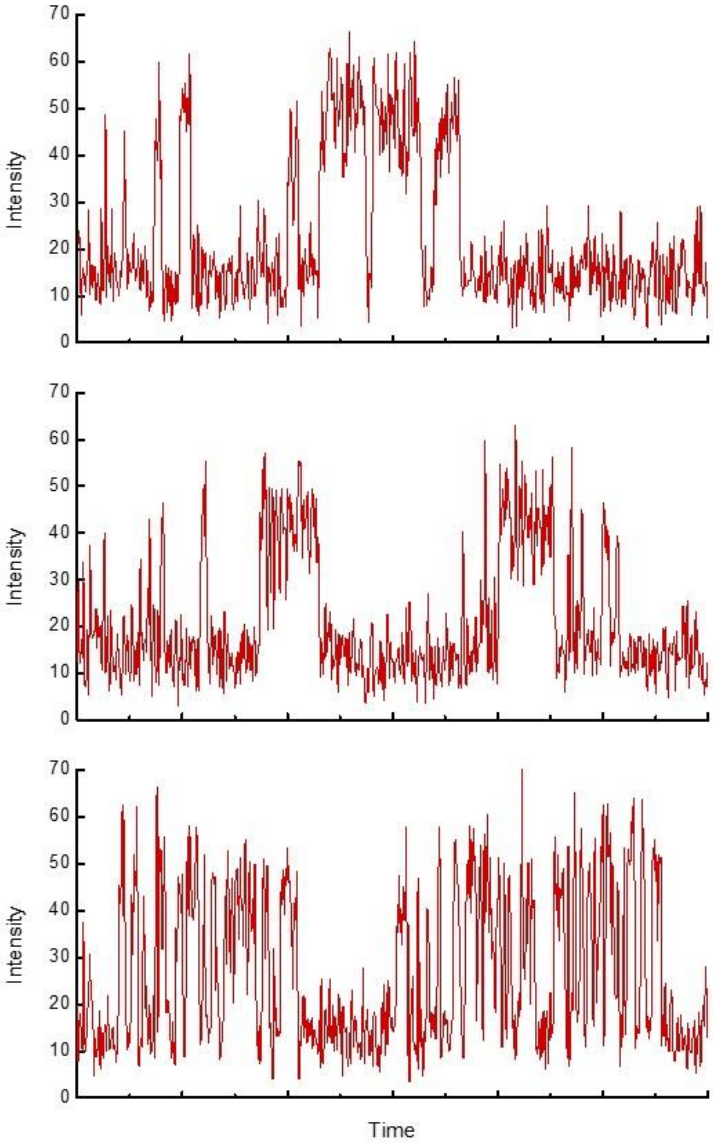

Figure 4.2 Emission bursting events from single molecules of species **4**. Representative 60 s excerpts from intensity-time trajectories corresponding to 3×3 pixel regions of interest in 100-200 second TIRFM image sequences recorded at room temperature while flowing an equimolar solution of 5 nM **1** and **3** atop a microscope coverslip spin-coated with Sm_2O_3NP. Exposure time was 100 ms/frame. Repetitive bursting at each location is indicative of heterogeneous catalysis. Note the consistent intensity of individual bursts, which each represent fluorescence emission from a single molecule of species **4**.

In this system, many cases of repeated bursting were indeed observed over catalytic Sm_2O_3NP for reagent concentrations ranging from 1 to 5 nM (Figure 4.2). In order to confirm that the selected bursts belong to the emissive species **4**, we recorded

their emission spectrum with an Andor spectrograph coupled to our single molecule microscope system (Figure S4.7, Supporting Information). The signal was recorded by passing the epifluorescent signal through the spectrograph (λ_{Ex} = 637 nm) and using a 690/70 nm band pass emission filter installed into the FLIM system.

Using TIRFM, it was also possible to observe and compare the catalytic activity exhibited by small and large Sm_2O_3NP, both known to be present in the polydisperse nanomaterial (Figure S4.8, Supporting Information).[22] High levels of scattering by large Sm_2O_3NP cause excitation light to impinge upon the emission filter at various angles, rendering such particles visible in TIRFM image sequences. The locations of these large particles can be confirmed via correlation with a widefield transmission image of the same sample area (Figure S4.9, Supporting Information). Repetitive bursting was observed in various locations in the TIRFM field of view but importantly, it was never observed on nor in the immediate vicinity of visually identifiable larger Sm_2O_3NP. This remained the case even when burst localization was preceded by further reduction of scattering through frame by frame subtraction of a background image sequence recorded while flowing only solvent atop the same sample of catalyst before seamlessly switching to an equimolar flow of reagents. This procedure was facilitated by the fact that the degree of scattering due to large Sm_2O_3NP remains relatively constant over the time scale of TIRFM experiments (Figure S4.10, Supporting Information). Even if catalytic bursting on the large Sm_2O_3NP were still completely masked by scattering, one would expect to detect bursting around the edges of the large particles. However, no such bursting was observed through either automated burst localization or manual selection of ROIs on or around the large Sm_2O_3NP. This image analysis protocol has been successfully utilized to both detect bursting on highly scattering niobium oxide based catalysts[38] (λ_{Ex} = 633 nm) and to rule out acid-catalysis by large Sm_2O_3NP[22] (λ_{Ex} = 488 nm) in another system. Therefore, bursting (and thus formation of **4**) does not occur at the large, visible Sm_2O_3NP but is highly localized, consistent with the explanation that heterogeneous catalysis occurs solely at the locations of the nanometric particles. This conclusion is supported by bench scale experiments in which the same yield of **4** was obtained when starting from either the polydisperse nanomaterial or by first isolating and

utilizing the small Sm_2O_3NP for catalysis (see Table 4.1 entries **d** vs **j**, **h** vs **i** and associated discussion).

Mechanistic Investigation. In addition to providing additional evidence that heterogeneous catalytic oxidation of compound **1** is restricted to the surfaces of the small Sm_2O_3NP, a final TIRFM experiment was designed in order to gain further insight into the overall catalytic mechanism. Based on the results of bench scale experiments (i.e. inability to isolate $\mathbf{[2]_s}$ and spectroscopic evidence of a coumarin-type structure possessing an emission band between those of **1** and a synthetically prepared free aldehyde **2**), as well as on single molecule studies indicating that the Sm_2O_3NP-catalyzed oxidation of **1** is indeed a surface process, we considered the possibility that an activated alcohol species is formed exclusively on the nanometric particle surface as a direct product of the catalysis and that this species $\mathbf{[2]_s}$ is then intercepted by **3**, generating **4** without free aldehyde mediation. A unique advantage of the flow reactor cell used to perform TIRFM is the ability to seamlessly change the reagent solution without disturbing the microscope optics or displacing the sample, allowing the same sample area to be imaged under various experimental conditions. We were thus able to achieve a realistic depiction of the catalytic process by performing a sequential dual-colour TIRFM experiment.

In brief, we flowed a 5 nM solution of **1** over a glass coverslip spin-coated with Sm_2O_3NP and imaged the sample using 488 nm laser excitation and a 550 nm long pass emission filter (Figure 4.3A1). Without disturbing the sample or altering the microscope optics, we then switched the excitation wavelength to 633 nm and, using a 676/29 nm band pass emission filter, recorded a second image sequence while flowing a 5 nM solution of **3** over the activated sample (Figure 4.3B1). By comparing the coordinates in which catalytic activity was detected under the two sets of experimental conditions, we observed distinct regions of activity common to both image sequences. Figure 4.3A1 and B1 are still frame images from the two image sequences, with yellow boxes highlighting two regions of interest that are common to each image. As shown by the corresponding fluorescence intensity-time trajectories, bursting events in these distinct regions are examples of **1** being activated to $\mathbf{[2]_s}$ on small Sm_2O_3NP (Figure 4.3A2-3), and subsequent condensation of the surface bound

activated species with **3** to generate **4** (Figure 4.3B2-3) in identical locations. The correlation experiment confirms that full formation of **4** is observed wherever the hydroxyl-substituted reagent **1** is partially oxidized to **[2]$_S$**, demonstrating that the catalysis is a heterogeneous coupled process in which both reactions leading to **4** occur at the surfaces of the small, catalytically active Sm_2O_3NP.

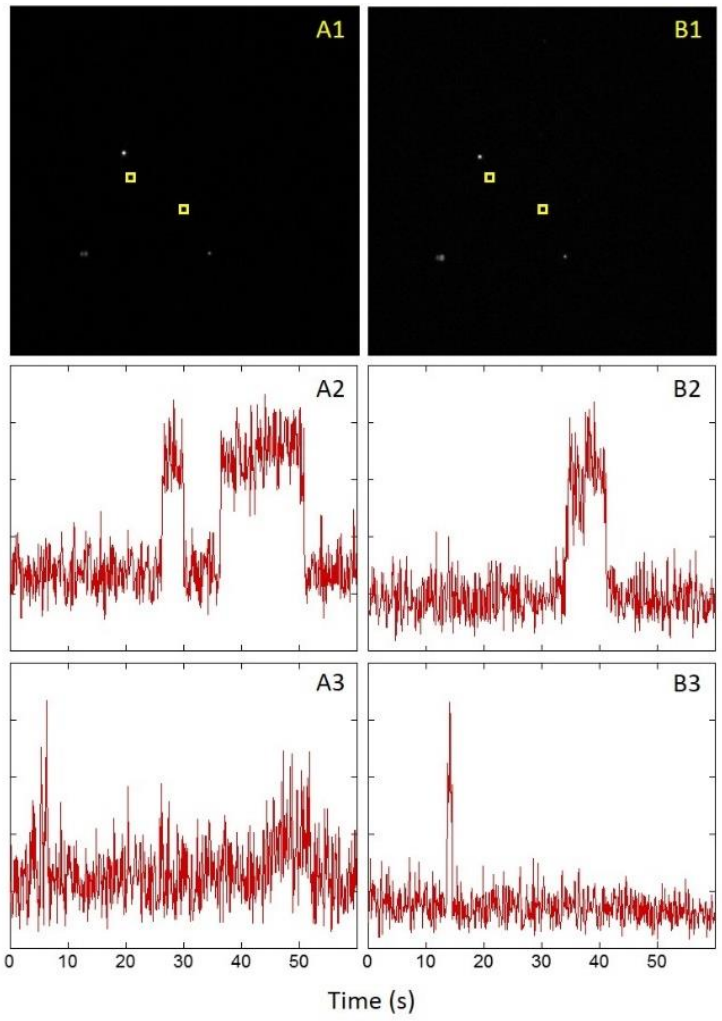

Figure 4.3 Spatial colocalization of the activation of **1** and the generation of **4**. Single frames of TIRFM image sequences of (**A1**) emission from activated alcohol imaged with excitation at 488 nm and a 550 nm long pass filter and (**B1**) emission from **4** resulting from condensation between **[2]$_S$** and the indolium cation **3** imaged with excitation at 633 nm and a 676/29 nm band pass filter. Yellow boxes highlight the coordinates of identical 3×3 pixel regions of interest in the two images, from which the corresponding fluorescence intensity trajectories (**A2**-**3** and **B2**-**3**) of single catalytic spots showing stochastic on/off-events were derived. The trajectories show that activity resulting from the Sm_2O_3NP-catalyzed surface activation of **1** (**A2** and A**3**) occurs in the same location as bursting originating from **4** (**B2** and **B3**).

Discussion

Investigating the catalytic mechanism at the single molecule level points to a strictly surface-localized catalytic process in which a direct product of the catalysis (species **[2]$_s$**) is formed exclusively on the nanometric particle surface and is then intercepted by **3**, generating **4** without free aldehyde mediation. A tentative mechanism is illustrated in Figure 4.4, showing the oxidation of **1** and condensation of **[2]$_s$** with **3** as coupled processes involving an partially oxidized activated alcohol on the Sm_2O_3NP surface.

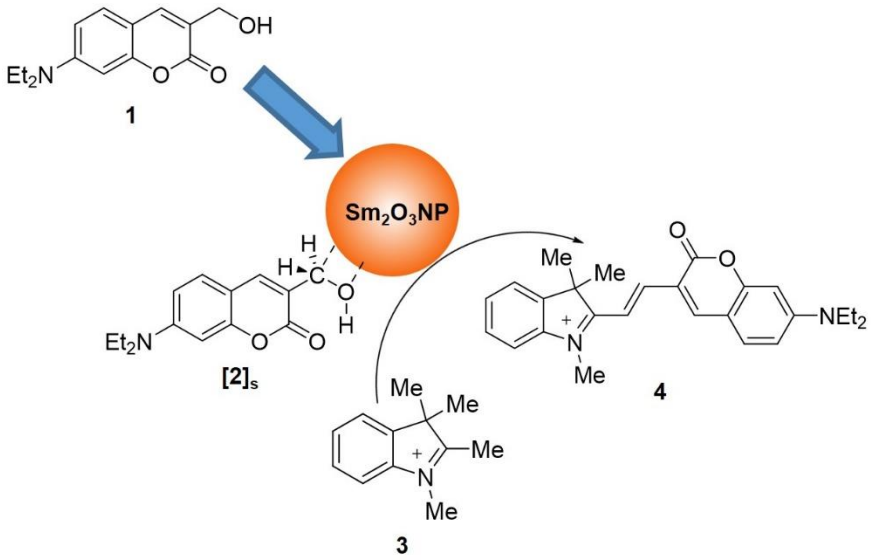

Figure 4.4 Proposed mechanism for the overall catalytic process. The heterogeneously-catalyzed oxidation of **1** occurs exclusively at the surfaces of small Sm_2O_3NP and is followed by condensation of the surface bound partially oxidized activated alcohol **[2]$_s$** with **3** to generate the emissive product **4**.

This behaviour resembles that of ruthenium nanoparticles (RuNP) supported on mesoporous silica that we proposed as a heterogeneous catalyst for oxidative Wittig coupling reactions.[17] In our report, we observed that the Wittig olefination product using benzyl alcohol as starting material occurs without the intermediacy of the aldehyde (the common Wittig substrate). Thus, we proposed the alcohol oxidation and the olefination as codependent processes coupled on the surfaces of RuNP. Inspired by these considerations, we tested our Sm_2O_3NP as a heterogeneous catalyst for the Wittig olefination of benzyl alcohol with, and without the Wittig reagent methyl(triphenylphosphoranylidene)acetate. In stunning resemblance to the

behaviour of supported RuNP, gas-chromatography results (Figure S4.11, Supporting Information) show the olefination product (methyl cinnamate) only in the presence of the Wittig reagent, while the aldehyde supposedly generated by the single oxidation of benzyl alcohol was not observed. Not only does this demonstrate that the scope of Sm_2O_3NP-catalyzed redox chemistry extends beyond the synthesis of **4**, samarium is more readily abundant than ruthenium and thus a more desirable material in the move toward sustainable catalysis. Indeed, Sm_2O_3NP-based nanomaterials may represent a starting point in the development of a generally applicable heterogeneous catalyst for sustainable one-pot aldehyde chemistry.

Conclusion

We have reported on the first utilization of Sm_2O_3NP for purely heterogeneous redox catalysis in one-pot aldehyde chemistry. The catalyst shows promise in multiple reactions involving aldehydes (e.g. Wittig chemistry), allows one to begin with a less expensive and more readily-prepared alcohol precursor and is unaffected by undesirable over-oxidation to the corresponding carboxylic acid. We have shown that Sm_2O_3NP efficiently activate the hydroxyl-functionalized starting material for a subsequent *in situ* enamine-type condensation but that the reaction proceeds without the intermediacy of a freely diffusing aldehyde. Examining the system at the single molecule level was critical to uncovering this interesting aspect of the catalytic mechanism, and highlighted the enhanced understanding that can be achieved using single molecule techniques for catalysis research. Such methods are no longer solely the realm of biology; their applicability in mainstream inorganic chemistry and nanomaterials science has spread dramatically and is being realized at a new higher level. In this case, a supramolecular strategy was implemented based on information provided by a previous single molecule study in order to achieve the full benefit of pure heterogeneous catalysis and also facilitated the elucidation of the interesting catalytic mechanism using single molecule fluorescence microscopy. TIRFM unequivocally established that small Sm_2O_3NP catalyze the activation of the alcohol on their surfaces and demonstrated that the coupled processes proceed through a heterogeneous catalytic mechanism. Such insight into the mode of catalysis at work

and the reactive species involved is essential to the evaluation of new nanomaterials and could only be obtained by studying the catalysis at the molecular level, where traditional ensemble-averaged experiments proved inadequate. This work showcases the opportunity provided by single molecule techniques when applied to catalysis research, including the benefit of progression *'from the molecule to mole'*–a bottom-up approach in which knowledge obtained through single molecule studies is used to improve scaled up catalyst performance as part of an iterative design process.

Methods

Materials. Sm_2O_3NP were prepared and characterized according to our previously published protocol.[28] The synthesis of compounds **1**, **2**, **3** and **4** is described in the Supporting Information.

Experimental. Acetonitrile (MeCN) was purified with a LC Technology Solutions Inc. SPBT-1 Bench Top Solvent Purification System. Chemicals were purchased from Sigma-Aldrich or Fisher Scientific. All the reactions were monitored by thin-layer chromatography, using aluminum sheets coated with silica (60, F_{254}). NMR spectra were recorded at room temperature with a Bruker Avance 300 spectrometer. Mass spectral analysis was performed with a 6890N Network GC System equipped with a 5973 Mass Selective Detector from Agilent Technologies. ESI mass spectra in positive mode were acquired with a Micromass Q-TOF I. High-resolution EI mass spectra were acquired with a HRes, Concept S1, Magnetic Sector mass spectrometer and were conducted in the John L. Holmes Mass Spectrometry Facility at the Department of Chemistry and Biomolecular Sciences, University of Ottawa. Emission spectra were recorded with a PTI spectrofluorometer. Absorbance spectra were recorded using a Cary 50 UV−Visible spectrophotometer. For the UV-Vis analysis of reactions **a-j**, the catalyst (when present) was separated by centrifugation and washed three times with EtOH. The combined supernatants were dried under reduced pressure, redissolved in 2 mL of EtOH and further diluted 100 fold. For each sample, the concentration of **4** was calculated by absorption values at λ = 575 nm. The molar extinction coefficient of **4** in EtOH at λ = 575 nm was calculated by performing a calibration curve with known concentrations of **4** and was estimated at 14218 M^{-1} cm^{-1}.

Single Molecule Fluorescence Microscopy. Glass coverslips (25 mm, Fisher) were cleaned by soaking in piranha solution for 30 min followed by thorough washing with MilliQ H_2O (18.2 MΩ cm^{-1} at 25°C; 0.22 μm filter), then dried with argon. Sm_2O_3NP were dispersed in EtOH (0.05 mg/mL) and deposited on a clean coverslip through spin coating (50 μL, 1000 rpm, 90 s). The Sm_2O_3NP-catalyzed formation of **4** was analyzed by flowing equimolar solutions of **1** and **3** in EtOH at 1 mL h^{-1} through a flow cell reactor (Chamlide model CF-S25-B) over the catalyst-loaded microscope coverslip. Fluorescence imaging was performed with an Olympus FV1000 TIRF (Olympus, Japan). The instrument is equipped with a 488 nm Ar laser (CW), a 633 nm He-Ne laser (CW) and an EM-CCD (Rolera EM-C2, Q-Capture). The laser beam was collimated and focused through a fibre-coupling unit. The microscope is equipped with an oil-immersion TIR (total internal reflection) objective (×100, NA 1.45, Olympus, PLAPO). A 550 nm long pass (Semrock) or a Chroma ET655 emission filters (676/29 nm band pass) were used to monitor bursting events at the single molecule level. The fluorescence spectrum of **4** was recorded with a Fluorescent Lifetime Imaging system (MicroTime 200, PicoQuant, Berlin, Germany). The instrument is equipped with a frequency doubled, picosecond pulse diode laser (637 nm, 93 ps, 40 MHz, LDH-P-FA-640L; PicoQuant). A beam splitter (Z638rdc, Chroma) was used to separate excitation and emission light. The emission signal was collected by a Shemrock SR-163 spectrograph (Andor Technology, South Windsor, USA) using a 690/70 nm band pass emission filter. Fluorescence microscope images and TIRFM image sequences were analyzed using ImageJ (NIH) and MatLab. Stochastic bursting events in TIRFM image sequences were identified and labeled as 3×3 pixel regions of interest. ImageJ was then used to perform scattering subtraction (rolling ball algorithm, 10 pixel radius) before measuring the mean fluorescence intensity in each region of interest for every frame in a TIRFM image sequence. These data were then used to generate intensity vs time trajectories using OriginLab software.

References

(1) Chen, P.; Zhou, X.; Shen, H.; Andoy, N. M.; Choudhary, E.; Han, K.-S.; Liu, G.; Meng, W. *Chem. Soc. Rev.* **2010**, *39*, 4560-4570.

(2) Chen, P.; Zhou, X.; Andoy, N. M.; Han, K.-S.; Choudhary, E.; Zou, N.; Chen, G.; Shen, H. *Chem. Soc. Rev.* **2014**, *43*, 1107-1117.

(3) Buurmans, I. L. C.; Weckhuysen, B. M. *Nature Chem.* **2012**, *4*, 873-886.

(4) Cordes, T.; Blum, S. A. *Nature Chem.* **2013**, *5*, 993-999.

(5) Janssen, K. P. F.; De Cremer, G.; Neely, R. K.; Kubarev, A. V.; Van Loon, J.; Martens, J. A.; De Vos, D. E.; Roeffaers, M. B. J.; Hofkens, J. *Chem. Soc. Rev.* **2014**, *43*, 990-1006.

(6) Esfandiari, N. M.; Wang, Y.; Bass, J. Y.; Cornell, T. P.; Otte, D. A. L.; Cheng, M. H.; Hemminger, J. C.; McIntire, T. M.; Mandelshtam, V. A.; Blum, S. A. *J. Am. Chem. Soc.* **2010**, *132*, 15167-15169.

(7) Zhou, X.; Choudhary, E.; Andoy, N. M.; Zou, N.; Chen, P. *ACS Catal.* **2013**, *3*, 1448-1453.

(8) Ameloot, R.; Roeffaers, M.; Baruah, M.; De Cremer, G.; Sels, B.; De Vos, D.; Hofkens, J. *Photochem. Photobiol. Sci.* **2009**, *8*, 453-456.

(9) Blum, S. A. *Phys. Chem. Chem. Phys.* **2014**, *16*, 16333-16339.

(10) De Cremer, G.; Roeffaers, M. B. J.; Bartholomeeusen, E.; Lin, K.; Dedecker, P.; Pescarmona, P. P.; Jacobs, P. A.; De Vos, D. E.; Hofkens, J.; Sels, B. F. *Angew. Chem. Int. Ed.* **2010**, *49*, 908-911.

(11) Easter, Q. T.; Trauschke, V.; Blum, S. A. *ACS Catal.* **2015**, *5*, 2290-2295.

(12) Luo, W.; Sankar, M.; Beale, A. M.; He, Q.; Kiely, C. J.; Bruijnincx, P. C. A.; Weckhuysen, B. M. *Nat. Commun.* **2015**, *6*.

(13) Ristanović, Z.; Hofmann, J. P.; De Cremer, G.; Kubarev, A. V.; Rohnke, M.; Meirer, F.; Hofkens, J.; Roeffaers, M. B. J.; Weckhuysen, B. M. *J. Am. Chem. Soc.* **2015**, *137*, 6559-6568.

(14) Ristanović, Z.; Kerssens, M. M.; Kubarev, A. V.; Hendriks, F. C.; Dedecker, P.; Hofkens, J.; Roeffaers, M. B. J.; Weckhuysen, B. M. *Angew. Chem. Int. Ed.* **2015**, *54*, 1836-1840.

(15) Roeffaers, M. B. J.; De Cremer, G.; Libeert, J.; Ameloot, R.; Dedecker, P.; Bons, A.-J.; Bückins, M.; Martens, J. A.; Sels, B. F.; De Vos, D. E.; Hofkens, J. *Angew. Chem. Int. Ed.* **2009**, *48*, 9285-9289.

(16) Su, L.; Lu, G.; Kenens, B.; Rocha, S.; Fron, E.; Yuan, H.; Chen, C.; Van Dorpe, P.; Roeffaers, M. B. J.; Mizuno, H.; Hofkens, J.; Hutchison, J. A.; Uji-i, H. *Nat. Commun.* **2015**, *6*.

(17) Carrillo, A. I.; Schmidt, L. C.; Marin, M. L.; Scaiano, J. C. *Catal. Sci. Technol.* **2014**, *4*, 435-440.

(18) Xu, W.; Kong, J. S.; Yeh, Y.-T. E.; Chen, P. *Nature Mater.* **2008**, *7*, 992-996.

(19) Rybina, A.; Lang, C.; Wirtz, M.; Grußmayer, K.; Kurz, A.; Maier, F.; Schmitt, A.; Trapp, O.; Jung, G.; Herten, D. P. *Angewandte Chemie International Edition* **2013**, *52*, 6322-6325.

(20) Davies, I. W.; Matty, L.; Hughes, D. L.; Reider, P. J. *J. Am. Chem. Soc.* **2001**, *123*, 10139-10140.

(21) McTiernan, C. D.; Pitre, S. P.; Scaiano, J. C. *ACS Catal.* **2014**, *4*, 4034-4039.

(22) Hodgson, G. K.; Impellizzeri, S.; Scaiano, J. C. *Catal. Sci. Technol.* **2016**, *6*, 7113-7121.

(23) Chen, L.; Chen, G.; Leung, C.-F.; Yiu, S.-M.; Ko, C.-C.; Anxolabéhère-Mallart, E.; Robert, M.; Lau, T.-C. *ACS Catal.* **2015**, *5*, 356-364.

(24) Oliver-Messeguer, J.; Liu, L.; García-García, S.; Canós-Giménez, C.; Domínguez, I.; Gavara, R.; Doménech-Carbó, A.; Concepción, P.; Leyva-Pérez, A.; Corma, A. *J. Am. Chem. Soc.* **2015**, *137*, 3894-3900.

(25) Esfandiari, N. M.; Blum, S. A. *J. Am. Chem. Soc.* **2011**, *133*, 18145-18147.

(26) Hensle, E. M.; Blum, S. A. *J. Am. Chem. Soc.* **2013**, *135*, 12324-12328.

(27) Decan, M. R.; Impellizzeri, S.; Marin, M. L.; Scaiano, J. C. *Nat. Commun.* **2014**, *5*.

(28) Hodgson, G. K.; Impellizzeri, S.; Hallett-Tapley, G. L.; Scaiano, J. C. *RSC Adv.* **2015**, *5*, 3728-3732.

(29) Jiang, Z.; Zhou, W.; Tan, D.; Zhai, R.; Bao, X. *Surf. Sci.* **2004**, *565*, 269-278.

(30) Juel, M.; Samuelsen, B. T.; Kildemo, M.; Raaen, S. *Surf. Sci.* **2006**, *600*, 1155-1159.

(31) Kuchowicz, M.; Kołaczkiewicz, J. *Surf. Sci.* **2008**, *602*, 3721-3727.

(32) Nguyen, T.-D.; Dinh, C.-T.; Do, T.-O. *Langmuir* **2009**, *25*, 11142-11148.

(33) Nguyen, T.-D.; Dinh, C.-T.; Nguyen, D.-T.; Do, T.-O. *J. Phys. Chem. C* **2009**, *113*, 18584-18595.

(34) Nguyen, T.-D.; Mrabet, D.; Do, T.-O. *J. Phys. Chem. C* **2008**, *112*, 15226-15235.

(35) Xu, Q.; Hu, S.; Cheng, D.; Feng, X.; Han, Y.; Zhu, J. *J. Chem. Phys.* **2012**, *136*, 154705.

(36) Cheng, D.; Xu, Q.; Han, Y.; Ye, Y.; Pan, H.; Zhu, J. *J. Chem. Phys.* **2014**, *140*, 094706.

(37) Deniz, E.; Sortino, S.; Raymo, F. M. *J. Phys. Chem. Lett.* **2010**, *1*, 3506-3509.

(38) Impellizzeri, S.; Simoncelli, S.; Fasciani, C.; Luisa Marin, M.; Hallett-Tapley, G. L.; Hodgson, G. K.; Scaiano, J. C. *Catal. Sci. Technol.* **2015**, *5*, 169-175.

(39) Hudson, R.; Li, C.-J.; Moores, A. *Green Chem.* **2012**, *14*, 622-624.

4.3 Postprint Version of Supporting Information

*Synthesis of **2***

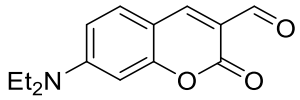

2

Compound **2** was prepared according to literature procedures.[S1] EI-MS: 245.1 $[M]^+$.^{1}H NMR (300 MHz, $CDCl_3$): δ 10.1 (1H, s), 8.2 (1H, s), 7.4 (1H, d, 7 Hz), 6.6 (1H, d, 8 Hz), 6.5 (1H, s), 3.4 (4H, q, 5 Hz), 1.2 (6H, t, 5 Hz). ^{13}C NMR ($CDCl_3$): δ 187.9, 35 161.8, 158.9, 145.3, 132.5, 114.5, 110.4, 108.4, 97.4, 45.4, 12.4.

*Synthesis of **1***

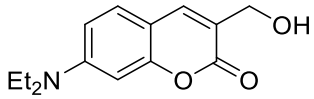

1

A solution of **2** (170 mg, 0.7 mmol) and $NaBH_4$ (25 mg, 0.7 mmol) in MeOH (25 mL) was stirred at 0°C for 20 min and later at room temperature for 3 h. The reaction was quenched with H_2O (25 mL) and the solution was extracted with $CHCl_3$ (3 $\times$ 15 mL). The organic phase was combined, dried over $MgSO_4$, filtered and the solvent was evaporated under reduced pressure. The mixture was purified by column chromatography [SiO_2/CH_2Cl_2-EtOAc 2:1 (v/v)] to yield the product (124 mg, 72%) as a yellow powder. EI-MS: 247.3 [M]+.^{1}H NMR (300 MHz, $CDCl_3$): δ 7.5 (1H, s), 7.2 (1H, d, 9 Hz), 6.6 (1H, d, 8 Hz), 6.4 (1H, s), 4.5 (2H, s) 3.4 (4H, q, 5 Hz), 1.2 (6H, t, 5 Hz). ^{13}C NMR ($CDCl_3$): δ 162.8, 156, 150.5, 140, 128.8, 120.2, 109, 108.2, 97.2, 61.5, 44.7, 12.4.

*Synthesis of the iodide salt of **3***

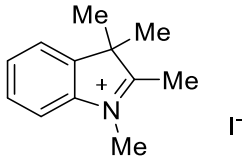

3

Compound **3** was prepared according to literature procedures.[S2] EI-MS: 174.1 $[M]^+$. ^{1}H NMR (300 MHz, $CDCl_3$): δ 7.5-7.63 (4H, m), 4.3 (3H, s), 3.1 (3H, s), 1.7 (6H, s). ^{13}C NMR ($CDCl_3$): δ 196.5, 148, 140.5, 127.9, 125.6, 119.8, 110.5, 42.8, 31.6, 27.2, 9.1.

*Synthesis of the hexafluorophosphate salt of **4***

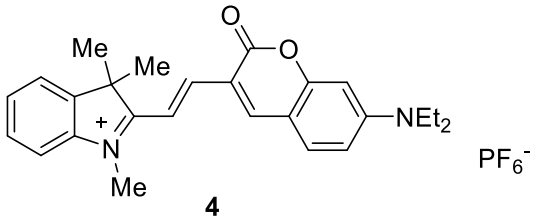

4

Compound **4** was prepared according to literature procedures.[S3] ESI-MS: 401.3 $[M]^+$. ^{1}H NMR (300 MHz, CD_3CN): δ 8.4 (1H, s), 8.1 (1H, d, 16 Hz), 7.9 (1H, d, 16 Hz), 7.7-7.5 (4H, m), 6.8 (1H, dd, 2 and 9 Hz), 6.5 (1H, d, 2 Hz), 3.9 (3H, s), 3.5 (4H, q, 7 Hz), 1.8 (6H, s), 1.2 96H, t, 7 Hz). ^{13}C NMR (CD_3CN): δ 180.9, 161.4, 158.7, 154.3, 150.7, 143, 141.5, 135, 128.9, 128.6, 122.4, 115.1, 114.5, 110.8, 108.7, 97.2, 52.5, 46, 35.8, 28.2, 12.8.

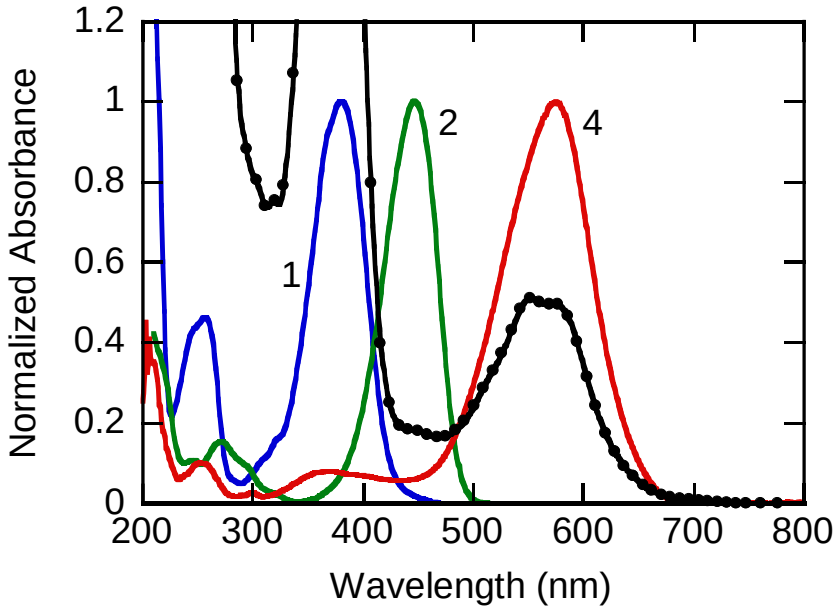

Figure S4.1 Normalized absorption spectra for compounds **1**, **2** and **4**. The black dotted trace depicts a typical absorption spectrum for reactions **a**-**d**.

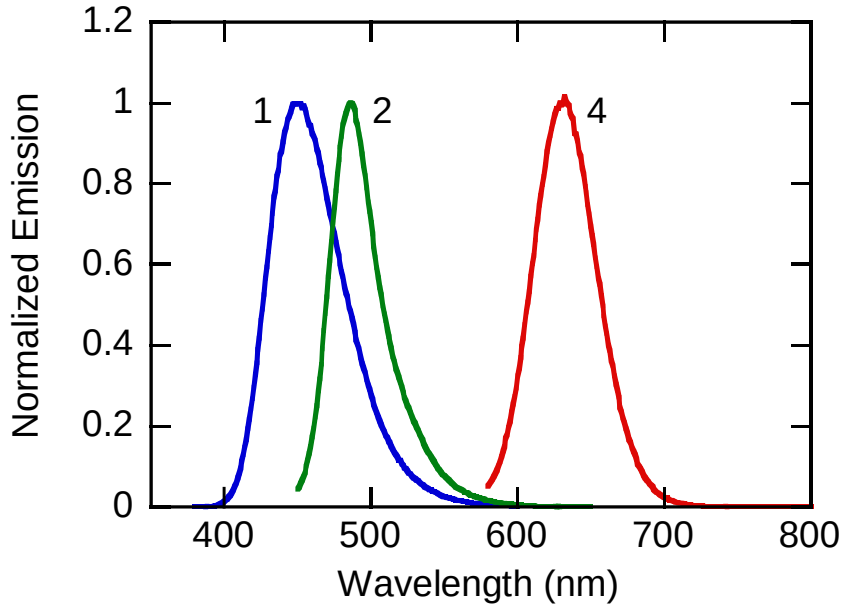

Figure S4.2 Normalized emission spectra for compounds **1** (λ_{Ex} = 370 nm), **2** (λ_{Ex} = 440 nm) and **4** (λ_{Ex} = 570 nm).

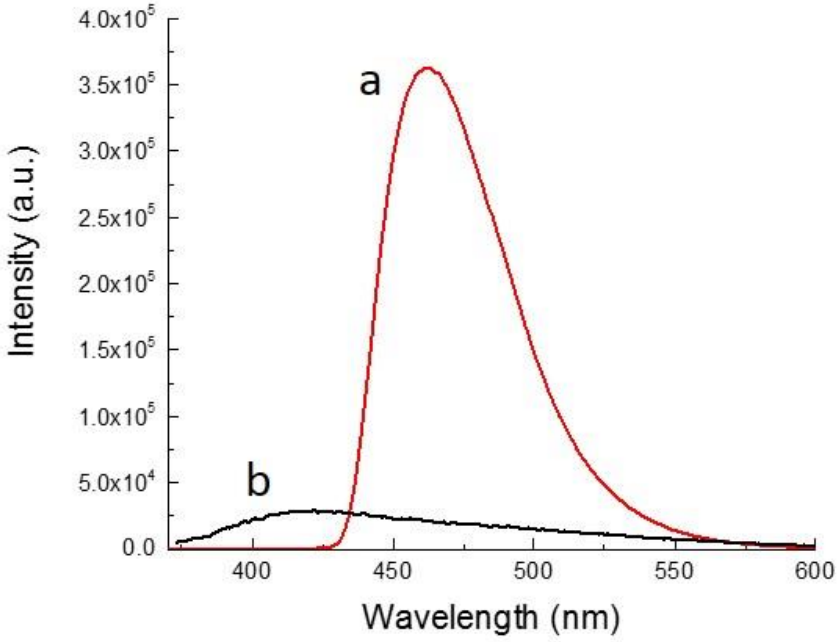

Figure S4.3 Emission spectrum of (**a**) supernatant obtained by centrifuging (3000 rpm, 30 min) a solution of Sm_2O_3NP and **1** in EtOH previously stirred at 65°C for 24 h and (**b**) unreacted polydisperse Sm_2O_3NP dissolved in DMSO. Note the emission of the activated alcohol species centred at 465 nm lies between the emission wavelengths of **1** (450 nm) and **2** (490 nm). λ_{Ex} = 350 nm.

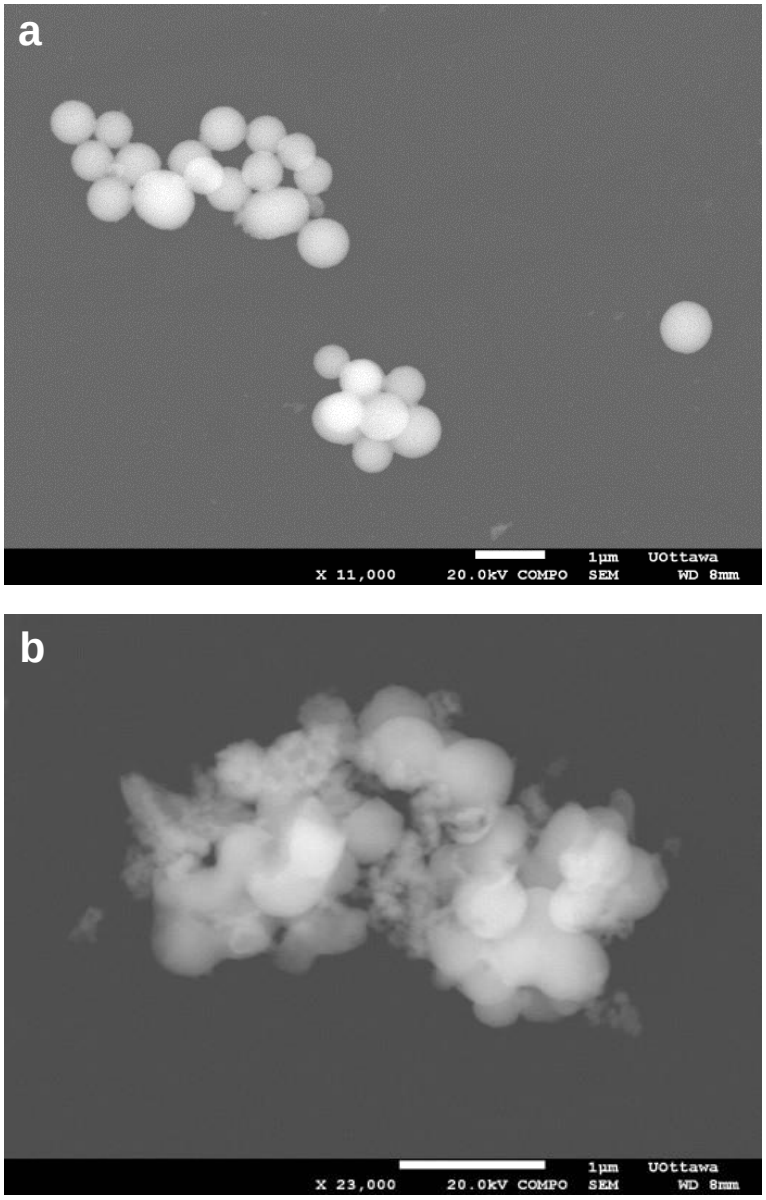

Figure S4.4 SEM image of Sm_2O_3NP before (a) and after (b) reaction **d**.

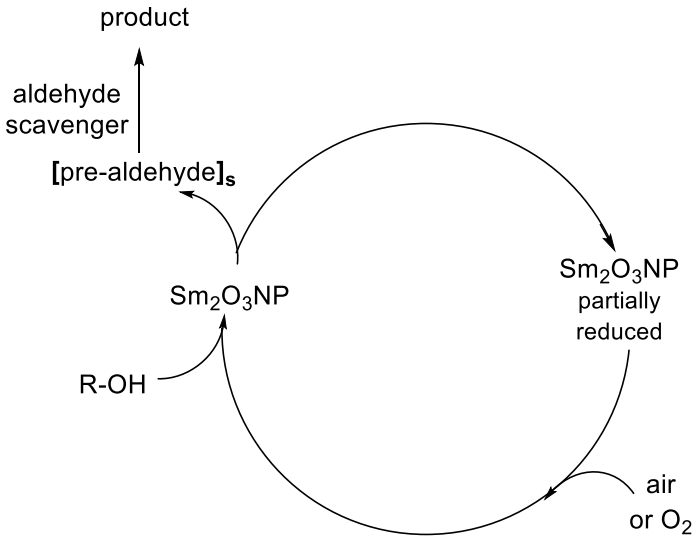

Figure S4.5 Proposed scheme for one-pot Sm_2O_3NP-catalyzed aldehyde chemistry and subsequent regeneration of the catalyst surface.

Single Molecule Fluorescence Microscopy (Video description):

Single molecule experiments were conducted by recording TIRFM image sequences while flowing an equimolar mixture (1–5 nM) of **1** and **3** in EtOH atop a glass microscope coverslip spin-coated with Sm_2O_3NP. These videos were recorded at a rate of 10 frames/s with an integration time of 100 ms, and ranged in length from 1000 to 2000 frames. The representative image sequence entitled Supplementary Video 1 is comprised of the first 250 frames of a 2000 frame video (to facilitate greater file compression) prior to background subtraction and shows bright fluorescence bursting events against a dark background in an 80×80 μm^2 area at 10 frames/s. This type of video should be viewed under dim light to well appreciate the bursting events and the repetitive locations at which they occur. These fluorescence bursting events represent the formation of single molecules of the fluorescent product **4** as a direct result of catalysis by Sm_2O_3NP. Repeated formation of single fluorescent molecules, and thus repeated bursting events, at individual locations indicate heterogeneous catalysis. The fluorescence intensity at various 3×3 pixel locations in such TIRFM image sequences can be plotted as a function of time in order to generate unique intensity-time trajectories for each location (e.g. Figure 4.2 in the main text).

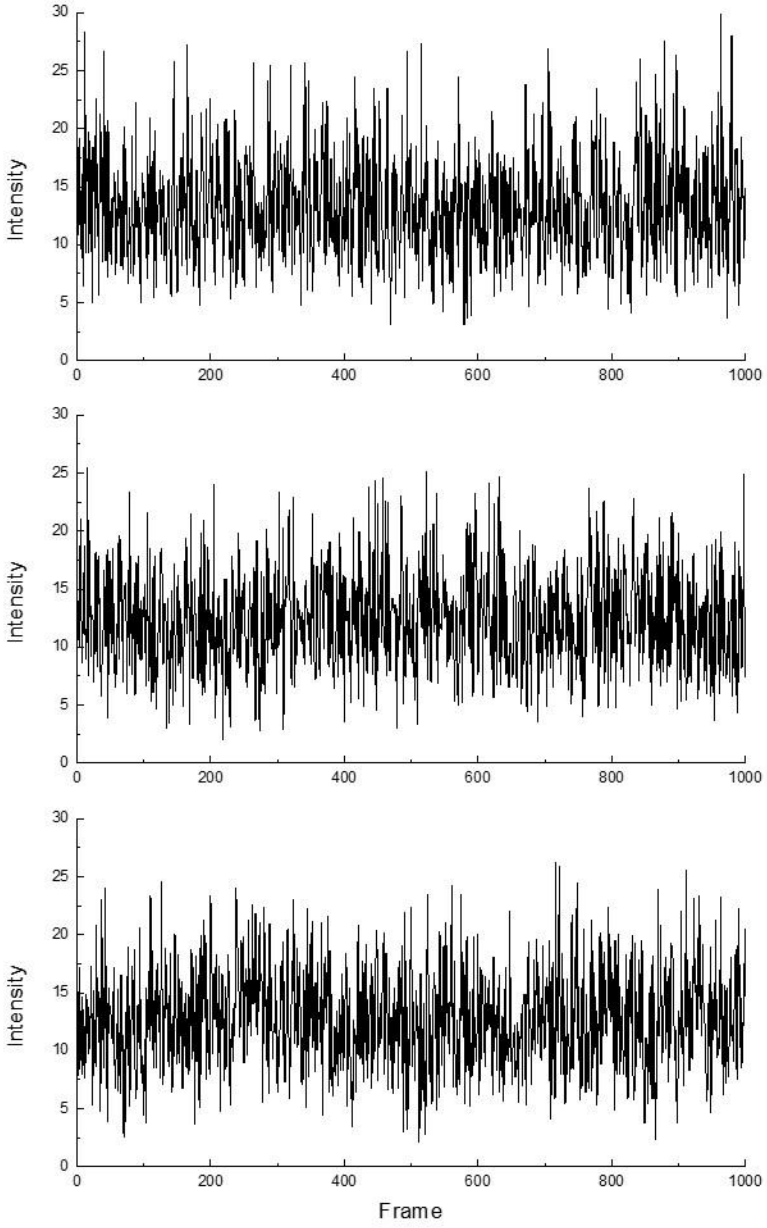

Figure S4.6 Representative intensity-time trajectories showing baseline background scattering, extracted from 3×3 pixel regions of interest in a 100 s TIRFM image sequence recorded at room temperature while flowing an equimolar solution of **1** and **3** atop a microscope coverslip spin-coated with Sm_2O_3NP. Exposure time was 100 ms per frame.

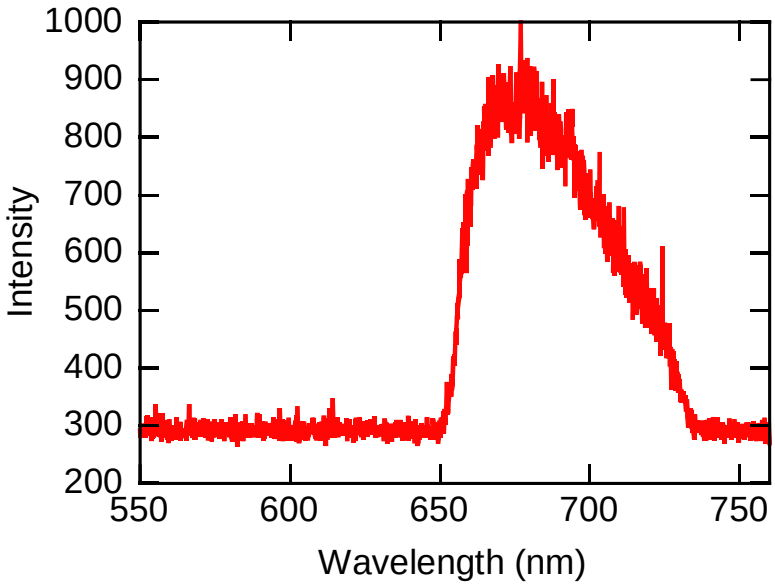

Figure S4.7 Spectral information of the detected bursting events measured by passing the epifluorescent signal through a spectrograph (λ_{Ex} = 637 nm) and using a 690/70 nm band pass emission filter installed into the Fluorescent Lifetime Imaging system.

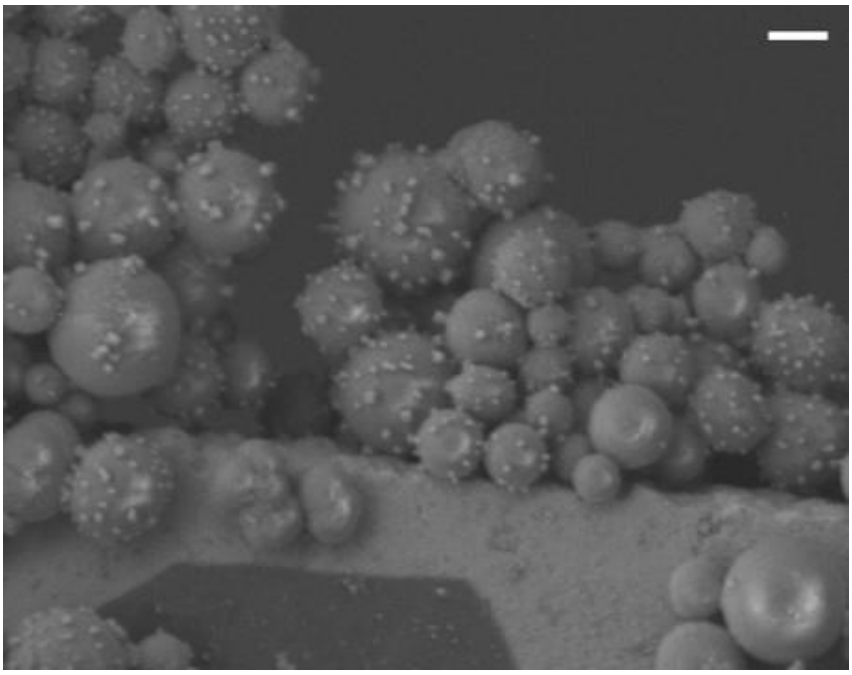

Figure S4.8 Representative SEM image demonstrating that small catalytic Sm_2O_3NP are already present in the original polydisperse nanomaterial. Scale bar is 1 µm.

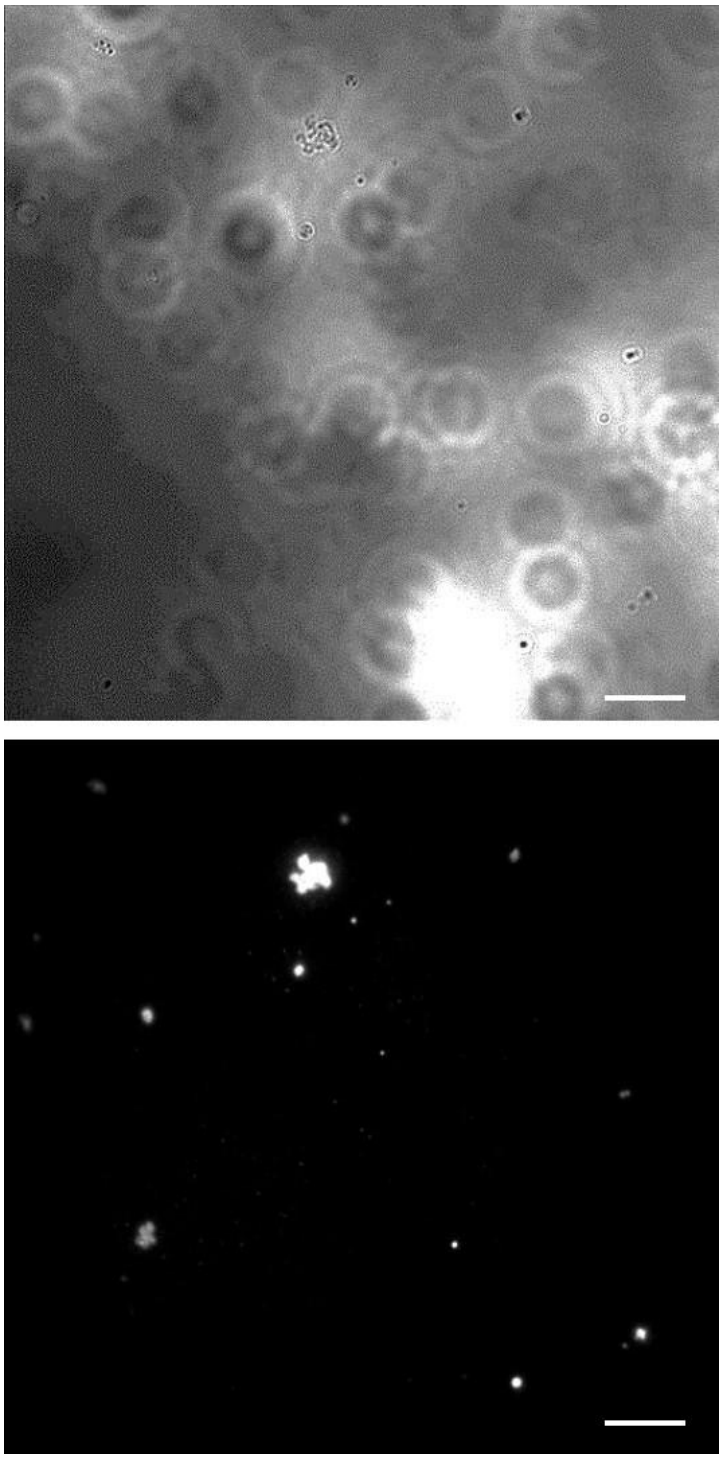

Figure S4.9 Widefield transmission (**a**) and TIRFM (**b**) images of Sm_2O_3NP spin-coated onto a microscope coverslip. Scale bars are 10 µm.

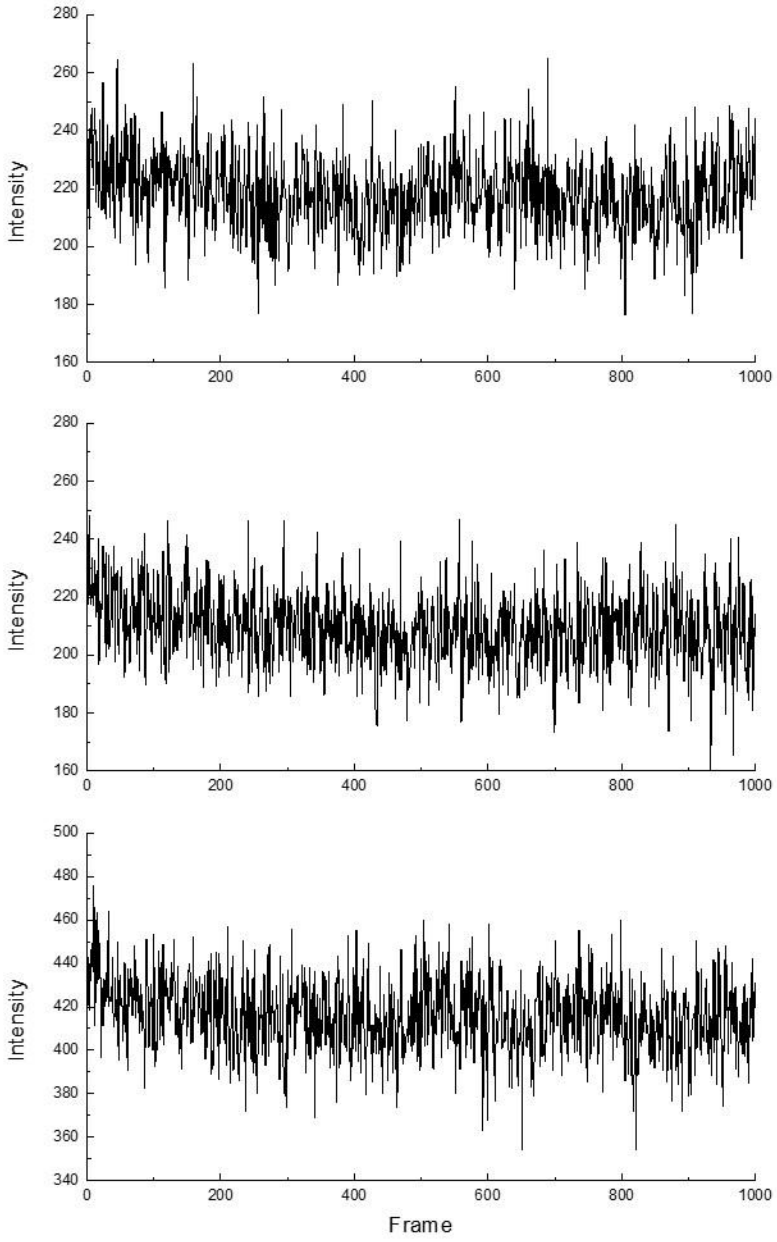

Figure S4.10 Representative intensity-time trajectories extracted from 3×3 pixel regions of interest located directly on or adjacent to large Sm_2O_3NP visible in a TIRFM image sequence recorded while flowing only EtOH atop a glass coverslip spin-coated with the catalyst. Exposure time was 100 ms per frame.

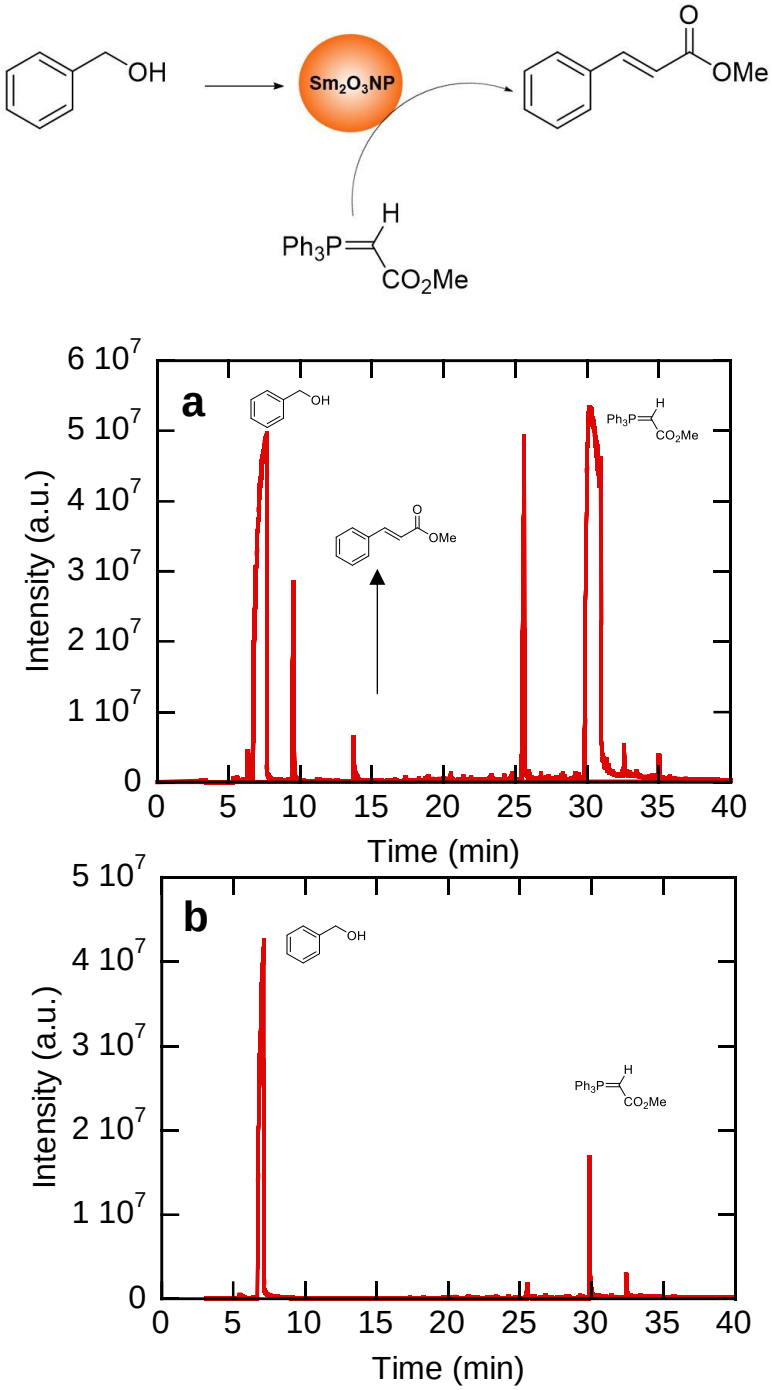

Figure S4.11 Top: proposed mechanism for the Sm_2O_3NP catalyzed alcohol oxidation and Wittig olefination as coupled processes. Bottom: gas chromatograms for the reaction between benzyl alcohol (7 min) and Sm_2O_3NP (**a**) in the presence and (**b**) in the absence of the Wittig reagent methyl(triphenylphosphoranylidene)acetate (32 min).

References

(S1) Wu, J.-S.; Liu, W.-M.; Zhuang, X.-Q.; Wang, F.; Wang, P.-F.; Tao, S.-L.; Zhang, X.-H.; Wu, S.-K.; Lee, S.-T. *Org. Lett*. **2007**, *9*, 33-36.

(S2) Tomasulo, M.; Sortino, S.; Raymo, F. M. *J. Org. Chem*. **2008**, *73*, 118-126.

(S3) Deniz, E.; Sortino, S.; Raymo, F. M. *J. Phys. Chem. Lett*. **2010**, *1*, 3506-3509.

This manuscript has been adapted from *Catal. Sci. Technol*. **2016**, *6*, 7113-7121, with permission, from the Royal Society of Chemistry. Small changes provide consistent formatting and clarity with respect to the overall thesis. Supplementary Video S1 may be very useful, and can be accessed online, free of charge, via the link above.

4.4 Accompaniment to Chapter 4

In addition to demonstrating that the catalytic activity of Sm_2O_3NP is not limited to Brønsted acid catalysis, this chapter highlighted another potential dividend of studying catalytic processes at the single molecule level. Mechanistic information, in this case the catalytic formation of a NP surface-bound activated moiety with aldehyde-like reactivity, can sometimes be uncovered when it would be difficult if not impossible to obtain via conventional bench scale methods. The sequential two-colour TIRFM experiment summarized in Figure 4.3 and used to conclusively demonstrate this interesting aspect of the catalytic mechanism, is a progressive step forward in the application of single molecule techniques in catalysis research.

Elucidation of the catalytic mechanism became a major focus of the investigation, perhaps overshadowing the general efficacy of Sm_2O_3NP for heterogeneous catalysis. It may be sensible to draw attention to the fact that Sm_2O_3NP were also qualitatively found to catalyze the oxidation of benzyl alcohol and subsequent Wittig olefination as coupled processes in one pot, and therefore that while the innovative fluorescence-shifting model system designed to facilitate monitoring the catalysis using TIRFM was useful for a mechanistic investigation, the oxidative catalytic activity of Sm_2O_3NP does extend to more synthetically relevant chemistry. In fact, the ability of Sm_2O_3NP to catalyze both reactions actually provides support for the very similar mechanism proposed in the literature to explain the same

codependent oxidation-Wittig olefination catalyzed by supported ruthenium NPs. An important distinction comes from the direct experimental evidence acquired here, using single molecule techniques, which complements rational deductions made upon the basis of bench scale results in the ruthenium-catalyzed system. The commonality in these two systems may even foreshadow similarities between the efficacies of samarium and ruthenium for other catalytic reactions. Added to the fact that the same supported ruthenium NPs were not effective at catalyzing the oxidation of the hydroxyl-functionalized coumarin substrate used here (unpublished results), further development of samarium-based nanomaterials may indeed point the way toward reducing reliance upon precious metal catalysts.

In demonstrating the catalytic versatility of unsupported Sm_2O_3NP in two similar examples of oxidative catalysis, this study also showcased the successful implementation of a supramolecular strategy devised to heterogenize the catalysis by manipulating the parameters of the system (in this case, the overall ionic strength). The need for such a solution was identified in Chapter 3, where it was found that the relatively high colloidal stability of the smallest Sm_2O_3NP, normally regarded as an advantageous feature in nanomaterials science, was actually undesirable from the viewpoint of performing pure heterogeneous catalysis.

Besides changing size, shape and composition of nanostructures, a viable alternative to manipulating the properties of the catalytic system is to modify the overall physicochemical properties of the nanocatalyst by integrating an additional component. This direction is explored in Chapter 5, where the knowledge of colloidal stability and higher catalytic activity of the smallest Sm_2O_3NP was incorporated into an effort to further develop the nanocatalyst for even greater utility in pure heterogeneous catalysis.

5. Heterogeneous Dual Photoredox-Lewis Acid Catalysis Using a Single Bifunctional Nanomaterial

5.1 Preamble to Chapter 5

Adsorbing colloidal NPs onto the surfaces of active or inactive matrices, or forming such supported NPs *in situ*, is becoming common practice in nanomaterials science. In catalysis, this protocol can allow for immobilization and heterogenization of an otherwise homogeneous or semi-heterogeneous catalyst. Further, the incorporation of optically and catalytically active supports can result in multifunctional nanocomposites featuring new and interesting combinations of their constituent properties, where possible synergistic interactions could lead to higher effectiveness in heterogeneous catalysis.

In the investigation to follow, the Sm_2O_3NP nanocatalyst was reimagined in the form of a samarium oxide/titanium dioxide nanocomposite material. In an effort to improve upon our existing nanocatalyst design, we explored different synthetic routes toward combining the most attractive catalytic features of Sm_2O_3NP (i.e. acidity, redox activity) with the optical and catalytic activities of various nano- and microstructured oxide supports. Titanium, and to a lesser extent cerium oxides, are known for their photocatalytic properties, and we reasoned that the successes we experienced with Sm_2O_3NP might be carried over to a samarium–titanium or samarium–cerium oxide nanocomposite material for purely heterogeneous photocatalysis. Serendipitously, this endeavor also drastically reduced the polydispersity of the samarium-based NPs relative to Sm_2O_3NP, greatly improving the efficiency of the preparation of the nanocatalyst. Remarkably, we also witnessed the emergence of considerable Lewis acidity alongside suppression of Brønsted acidity in the new nanomaterial relative to TiO_2 or Sm_2O_3NP alone. Other interesting effects of the choice of NP support are also included in the discussion below.

5.2 Postprint Version of Manuscript

First published in: *ACS Catal*. **2018**, *8*, 2914-2922.

Abstract

We report on heterogeneous dual photoredox-Lewis acid catalysis using a versatile and efficient nanocomposite: samarium oxide nanoparticle-decorated titanium dioxide. This emerging class of nanomaterials harnesses the Lewis acidity of the lanthanide, eliminates product contamination by the catalyst, and can be excited with visible light. Useful intermolecular and intramolecular net reductive and net neutral photoredox cyclization reactions are presented as examples of the general efficacy of this reusable heterogeneous nanocatalyst in synthetically relevant organic transformations.

Introduction

Heterogeneous and homogeneous catalysis are two sides of the same coin: they inherently offer different advantages to the modern chemist. Often the best option is not immediately evident, and ultimately the most suitable choice comes down to the specific requirements of the application. The steady rise in popularity of homogeneous catalysis is primarily attributable to the relative ease with which both regio- and stereoselectivity can be attained. Such control is indeed a strong asset in pharmaceutical research and natural product synthesis. However, the chemical industry has historically relied heavily upon heterogeneous catalysis for an abundance of important organic transformations owing to the high efficiency stemming from phase separation and catalyst reusability. While heterogeneous catalysts generally suffer from the propensity to yield wider product distributions, the continuing push toward more environmentally sustainable routes to synthetic building blocks and value-added chemicals has seen a resurgence in the field of heterogeneous catalysis. Ideally, it would be possible to combine the advantages of homogeneous and heterogeneous catalysis into a single reusable system.

In recent decades, photoredox catalysis has emerged as a powerful tool in synthetic organic chemistry, providing practical strategies for the preparation of a

myriad of fine chemicals under mild conditions.[1] Merging photoredox catalysis with transition metal catalysis in dual- or tricatalytic cycles has become a popular strategy for extending the utility of photoredox catalysts,[2] and pioneering work by Yoon and co-workers has opened a new frontier in the form of cooperative photoredox-Lewis acid homogeneous dual catalysis.[3] Despite these developments, few successful attempts have been made at heterogenizing dual photoredox-transition metal or photoredox-Lewis acid catalysis. In light of this, we identified an opportunity to combine our expertise in nanomaterials science, catalysis, and photochemistry to devise novel heterogeneous analogues of dual catalytic systems with the goal of mirroring established product yields and regioselectivities while improving overall efficiency by designing readily separable, reusable, and bifunctional heterogeneous nanostructured catalysts.

Lewis acids (LAs) often play critical, yet sometimes understated, roles in synthetic organic chemistry and photochemistry. They can serve to activate heteroatom-containing substrates by increasing their electrophilicity and shifting their reduction potentials to more positive values,[4] rendering them more susceptible both to nucleophilic attack and to photoreduction, respectively.[2b,3,5] Several reports have also documented the ability of LAs to impact reaction kinetics by stabilizing key photogenerated radical anion intermediates, leading to alternative reaction mechanisms not observed in nonphotochemical counterparts to these catalytic systems.[2b,3,6] Samarium and other lanthanides are well-known to form LA complexes, and some, such as SmI_2, can become powerful reducing agents under appropriate conditions.[7] Other Lewis acidic lanthanide complexes have also been shown to function as catalysts for Friedel–Crafts acylation, the Diels–Alder reaction, alcohol esterification, and the Mukaiyama aldol addition reaction.[8] Notably, lanthanide triflates, including $Sm(OTf)_3$, have demonstrated exceptional performance as LA catalysts, cocatalysts and as the basis for chiral additives in a variety of homogeneous catalytic and photocatalytic reactions ranging from nucleophilic additions[9] to photoreductive cyclizations[5b,6c] to stereoselective [3+2] and [2+2] photocycloadditions.[4b,6d,6e,6g,6h]

Photochemical cyclization reactions are ubiquitous in synthetic organic chemistry; they provide access to an array of valuable synthetic precursors and complex molecular scaffolds by enabling otherwise challenging bond formations.[10] Intermolecular and intramolecular variations of this class of reactions have given rise to a wealth of mechanistic knowledge and a multitude of practical synthetic routes to the preparation of polycyclic systems, four-membered ring motifs, and key intermediates in natural product synthesis.[10a,10b,11] In particular, the development of photoreductive cyclizations and especially [2+2] photocycloadditions are regarded by some as among the most significant contributions to the advancement of applied photochemistry in organic synthesis.[10a,11] Heterogenizing this class of catalytic reactions would therefore be a practical and worthwhile step forward for the academic and industrial chemistry communities (Scheme 5.1).

With all of these factors in mind, we set out to develop a multifunctional heterogeneous catalyst comprising a nanostructured semiconductor support decorated with Lewis acidic nanoparticles (NPs) that would allow for highly efficient preparation of a suite of useful photocyclization products by way of heterogeneous dual photoredox-LA catalysis. We reasoned that combining the known single electron transfer (SET) properties of semiconducting oxides such as ceria (CeO_2) and titania (TiO_2) with the acidic properties and redox activity of samarium oxide nanoparticles, on which we have previously reported,[12] might induce a synergistic effect that would instill Lewis acidity into the nanocomposite material or enhance that of the support, slow down counterproductive electron–hole recombination, and potentially extend the absorbance of the catalyst into the visible region. In this work, we describe the first example of purely heterogeneous dual photoredox-LA catalysis, using a single versatile nanocomposite composed of titanium dioxide decorated with samarium oxide NPs ($Sm_xO_y@TiO_2$). This new heterogeneous nanocatalyst is readily recoverable and fully reusable for intermolecular and intramolecular photoreductive cyclizations and [2+2] photocycloaddition chemistry, eliminates product contamination by the catalyst, paving the way for progress in the development of more efficient heterogeneous analogues to homogeneous systems employing cooperative Lewis acid and photoredox catalysis for organic synthesis.

Scheme 5.1 Homogeneous and heterogeneous dual catalytic strategies for photoreductive cyclizations and [2+2] photocycloadditions.

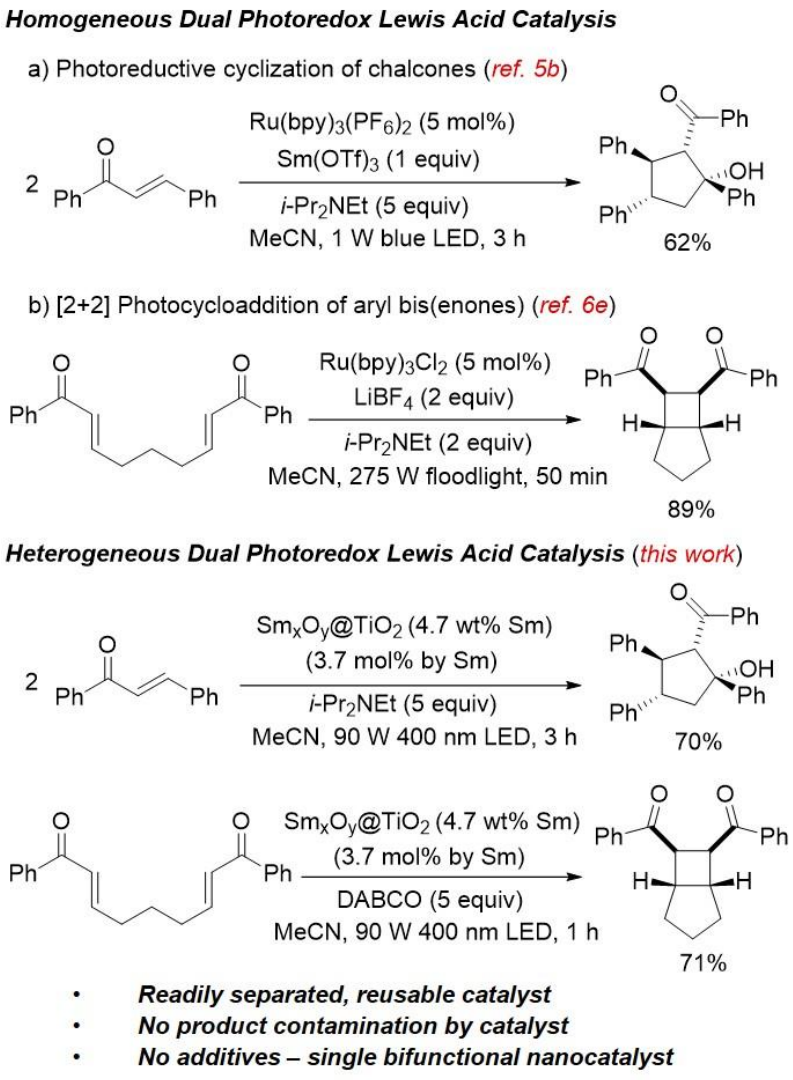

Results and Discussion

We elected to begin our investigation into heterogeneous dual photoredox-LA catalysis with the photoreductive cyclization of chalcones (Table 5.1). This family of molecules are biologically and pharmaceutically relevant and are also of interest in synthetic organic chemistry.[5b,13] For example, the cyclopentanol derivatives of chalcones can be accessed via a LA-mediated homogeneous photocatalytic cyclization that forms new C–C bonds in the process. The reaction can be initiated by SET from an excited photocatalyst to the starting material to form a radical anion

intermediate stabilized by an appropriate LA. Dimerization gives rise to a dienolate which then undergoes monoprotonation followed by a LA-mediated intramolecular aldol addition to form the final cyclized product in a net reductive photoredox mechanism.[1a,2b,5b] In the reported homogeneous system, the LA additive was further responsible for activating the substrate toward SET from the homogeneous photocatalyst $Ru(bpy)_3^{2+}$ (E_{red} −1.33 V vs SCE) by shifting its reduction potential[14] from −1.49 V vs SCE to a more positive value.

Table 5.1 Heterogeneous dual catalytic photoreductive cyclization of *trans*-chalcone.[a]

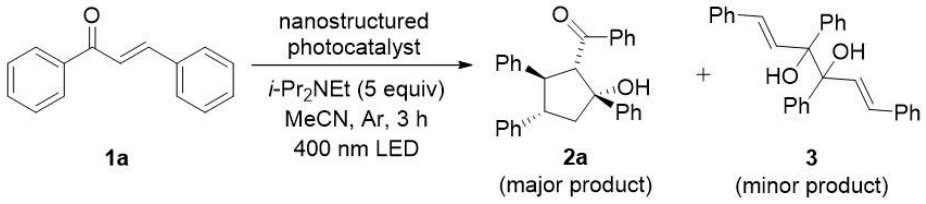

Entry	Catalyst	Yield[b] **2a** (%)	Yield[b] **3** (%)
1	**Sm_xO_y@TiO_2 (4.7 wt% Sm)**	**70**	**15**
2	Sm_xO_y@CeO_2 (< 5 µm) (0.29 wt% Sm)	40	10
3	Sm_xO_y@CeO_2 (< 5 µm) (0.42 wt% Sm)	15	4
4[c]	CeO_2 (< 5 µm)	31	8
5[c]	CeO_2 (< 25 nm)	37	9
6[c]	Sm_xO_y@CeO_2 (< 25 nm) (3.3 wt% Sm)	31	8
7	TiO_2	41	15
8[c,d]	TiO_2 + $Sm(OTf)_3$ additive	37	9

[a]Reaction conditions: chalcone (1 mmol), catalyst (60 mg), *i*-Pr_2NEt (5 mmol), 15 mL of dry MeCN, degassed with argon 20 min, irradiated with a 400 nm LED (90 W); irradiation time was optimized for 100% conversion in entry 1 and coincidentally matched the optimal irradiation time in ref 5b despite the different light sources used. Longer irradiation times did not result in significantly higher conversion to **2a** using either Sm_xO_y@TiO_2 or TiO_2 alone. [b]Determined by ^{1}H NMR spectroscopy using an internal standard. [c]The [2+2] cycloaddition product was detected in ≤5% yield. [d]Reaction conducted in the presence of 1.2 mM (0.0185 mmol, 11.0 mg) $Sm(OTf)_3$, corresponding to the molar amount of samarium present in entry 1. In all cases no linear dimer was detected.

We envisaged a scenario in which a nanostructured, samarium-decorated semiconductor oxide might be capable of catalyzing this reaction heterogeneously. We began by photochemically preparing two candidate nanocatalysts comprising samarium oxide NPs supported on titania (P25) and ceria, henceforth referred to as

$Sm_xO_y@TiO_2$ and $Sm_xO_y@CeO_2$, based on logical modifications to our previously reported work with larger, polydisperse, colloidal samarium oxide nanoparticles (Sm_2O_3NP).[12a] In the present work, NPs 1.2 ± 0.2 nm in diameter were observed on titania but none could be identified on ceria microparticles by TEM, likely due to a combination of small size, low Sm loading and the relatively large size (<5 μm) and thickness of the CeO_2 microparticles (Supporting Information (SI), Figures S5.1–S5.3). Characterization of these two novel nanomaterials by EDS (SI Figures S5.7–S5.8) detected samarium and XPS revealed the primary oxidation state to be Sm(III) but could not definitively rule out the presence of SmO or metallic samarium, hence the Sm_xO_y label selected for the materials (SI Figures S511–S5.12 and associated discussion). Intriguingly, ICP-MS determined that although both materials were prepared with an optimal loading of 5 mol% Sm, the final nanocomposites contained vastly different amounts of samarium (4.7 and 0.29 wt% for TiO_2 and CeO_2, respectively, SI Table S5.1).

Until now, literature reports describing samarium–semiconductor hybrid materials have been limited to the use of ionic samarium(III) as a dopant or co-dopant in TiO_2,[15] Gd_2O_3,[16] and $BiFeO_3$.[17] These studies have been mostly concerned with the degradation of organic dyes under aerobic conditions; none involve Sm-related Lewis acidity or employ inert atmosphere, and importantly, none of the materials contain samarium-based NPs. Indeed, $Sm_xO_y@TiO_2$ exhibited exceptional performance in the photoreductive cyclization of chalcone **1a** relative to $Sm_xO_y@CeO_2$ (Table 5.1, entries 1 and 2) and to the homogeneous catalytic system (62%, 3 h)[5b] under comparable optimized conditions (Scheme 5.1). Diffuse reflectance (DR) measurements showed that of the two nanomaterials, the absorbance of $Sm_xO_y@TiO_2$ extends further into the visible region and has a much better overlap with the emission of the 400 nm LED used for photoexcitation of the catalyst (SI Figure S5.15). Increasing the optimal loading of samarium on CeO_2 2-fold only resulted in a small increase in the actual Sm loading (0.42 wt%), and the yield of **2a** was actually negatively impacted, decreasing to roughly 50% of that obtained using unmodified commercial CeO_2 with a particle size <5 μm (Table 5.1, entries 3–4 and SI Figures S5.4, S5.9, S5.13). We attempted to increase the samarium loading further by switching to a commercial ceria

nanopowder with a particle size (<25 nm) more comparable to that of TiO_2. The presence of Sm_xO_y NPs 0.92 ± 0.2 nm in diameter was confirmed by a combination of TEM, EDS and XPS analyses (SI Figures S5.5–S5.6, S5.10, S5.14). The nanoscale CeO_2 did perform marginally better than the micron-range CeO_2 but although we were able to achieve a 3.3 wt% loading of samarium, the material could not match the superior catalytic activity of $Sm_xO_y@TiO_2$ (Table 5.1, entries 5 and 6).

These results are consistent with DR spectra, which illustrate that although the CeO_2-based materials do possess slightly smaller band gaps than TiO_2 (E_{bg} = 3.2 eV vs SCE),[18] $Sm_xO_y@TiO_2$ was the only samarium oxide-decorated nanocomposite to exhibit a change in the spectral line profile with respect to the unmodified support (SI Figures S5.16–S5.17). The addition of samarium (4.7 wt%, 2.5 mol%) resulted in the appearance of a clear band from 400 to 450 nm which resembles the known absorbance of colloidal Sm_2O_3NP (SI Figure S5.18).[12b] This effect has also been observed when titania is doped with 0.05–1.5 mol% ionic Sm(III) using microwave-assisted or autocombustion sol–gel procedures.[15a,15c] Whether as a result of metal ion doping or the formation of heterojunctions in semiconductor nanocomposites, red-shifted absorbance is a manifestation of a decrease to the band gap energy of the new overall material.[15c,17,19] The DR of 3.3 wt% $Sm_xO_y@CeO_2$ (<25 nm) is higher than that of $Sm_xO_y@TiO_2$ and extends comparably far into the visible region (SI Figure S5.17); however, lower catalytic activity (Table 5.1, entry 6) and a lack of the aforementioned spectral feature in the 400–450 nm region suggest that only in $Sm_xO_y@TiO_2$ was the band gap of the nanocomposite successfully modified with respect to the support (SI Figures S5.18-S5.19).

For lanthanide–titania hybrid materials, smaller band gaps arise from the presence of intraband gap electronic states corresponding to the $4f$ manifold, with the filled states near the valence edge of TiO_2 effectively forming the new highest occupied band of the nanocomposite material.[15a,15b,20] Similar effects on band gap energy have been reported for nanocomposites comprising TiO_2 decorated with various precious metal NPs (e.g. Pt, Pd, Ir, Au)[18b,21] as well as first-row transition metal elements like Cu,[22] and have been accredited to equilibration between the Fermi levels of the TiO_2 conduction band and the NPs on its surface.[21c] An important

distinction from the work reported herein is that samarium is more abundant than precious metals and plays an additional role as a LA (Figure 5.1). In some materials, as DR suggests to be the case for $Sm_xO_y@TiO_2$, visible light absorbance and charge transfer can be facilitated by the minor constituent of the nanocomposite (Sm_xO_y here) and charge separation managed by the native semiconductor component of the hybrid material.[19b] An additional benefit of nanocomposite catalysts is that hole-scavenging oxygen vacancies generated at heterojunctions (or at metal ion doping sites in other hybrid materials) can increase charge separation and slow down electron–hole recombination, making SET from the charge-separated photocatalyst to the substrate more efficient.[15a,19a,19b,23] When $Sm_xO_y@TiO_2$ was irradiated using solely visible (465 nm) or UV (365 nm) light, conversion of the starting material did eventually near completion, but yields of **2a** were lower in both cases (SI Table S5.2). From a practical perspective, it is clear that decorating TiO_2 with Sm_xO_y NPs allows the nanocomposite photocatalyst to perform efficient SET after excitation by visible light and that 400 nm represents an optimal excitation wavelength.

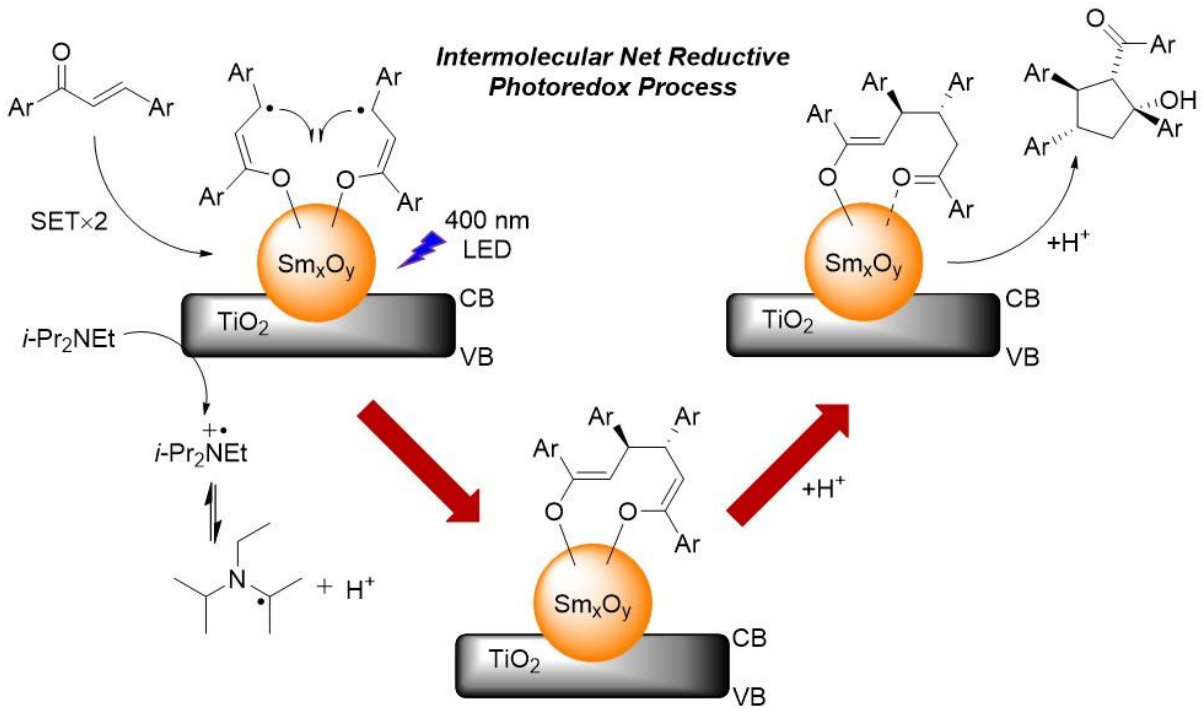

Figure 5.1 Proposed mechanism for the heterogeneous net reductive photoredox-Lewis acid catalytic reductive cyclization of *trans*-chalcones.

The net reductive heterogeneous photocatalytic mechanism proposed in Figure 5.1 closely resembles the previously described homogeneous catalytic mechanism,[2b,5b] but likely begins with coordination of two molecules of substrate to a single Sm_xO_y nanoparticle on the catalyst surface such that the two reactants come into close proximity. As in the homogeneous analogue, photoexcitation of the catalyst and two SET events are followed by radical–radical coupling to form a new carbon–carbon bond. Subsequent monoprotonation of the dienolate followed by intramolecular aldol addition furnishes the substituted cyclopentanol product. Interestingly, the LA samarium triflate has been proposed to take on multiple roles in the homogeneous catalytic version of this system. In addition to stabilizing the radical anion intermediate, it has been reported that a single Sm(III) atom facilitates the ring-closing final step by coordinating to both the enol and carbonyl functionalities of the dienolate, rendering the reaction highly selective toward the thermodynamically favoured stereoisomer **2a**. This is not necessarily the case in the heterogeneous mechanism, as the surface of each Sm_xO_y nanoparticle contains many closely spaced, nondiffusing Sm(III) atoms available for coordination. Contrary to homogeneous catalysis in solution, when a solid-phase catalyst such as nanostructured TiO_2 or $Sm_xO_y@TiO_2$ is used, the involvement of multiple LA sites would be less sterically hindered than coordination to a single atom. Nonetheless, the dienolate being anchored to a single NP rather than a single atom prior to cyclization appears to have had the same effect. The diastereoselectivity of the heterogeneously catalyzed reaction equaled that of the homogeneous system and was preserved regardless of whether $Sm_xO_y@TiO_2$ or the relatively weak LA TiO_2 was used (*vide infra*). It therefore seems reasonable that the enhanced activity exhibited by $Sm_xO_y@TiO_2$ may be the result of a combination of stronger Lewis acidity as well as a higher number or density of LA sites relative to the unmodified support.

We attribute the slightly higher catalytic activity of CeO_2 (<25 nm) relative to CeO_2 (<5 μm) to a difference in surface area to mass ratio, a well-known phenomenon in nanocatalysis. This may also contribute to the low samarium loadings achieved using ceria microparticles as supports, but based on the 3.3 wt% Sm achieved with the smaller ceria nanopowder versus 4.7 wt% with the comparably sized TiO_2, a more

general explanation could be that samarium simply has a greater affinity for titania over ceria. The latter is intrinsically a more reducible support than TiO_2 and therefore might reasonably be expected to act as a stronger Lewis acid, yet even as the surface area to mass ratio of ceria was increased toward that of TiO_2, its reactivity only approached but still did not match that of TiO_2 (Table 5.1, entries 4, 5 and 7). This could be due to faster electron–hole recombination. However, for Sm_xO_y@CeO_2, we speculate that the combination of Ce(IV), Sm(III), and Sm(II) might give rise to an internal pathway for nonradiative energy decay in which photoexcitation of Sm_xO_y could foreseeably initiate a charge transfer transition loop and impede SET to the substrate (Scheme 5.2).

Scheme 5.2 Possible charge transfer transition loop in samarium-decorated ceria, explaining the non-radiative dissipation of energy after light excitation.

$$Sm_xO_y + h\nu \longrightarrow Sm_xO_y^* \quad (1)$$

$$Sm(II)^* + Ce(IV) \longrightarrow Sm(III) + Ce(III) \quad (2)$$

$$Sm(III)^* + Ce(III) \longrightarrow Sm(II) + Ce(IV) \quad (3)$$

$$Sm(III) + Ce(III) \rightleftharpoons Sm(II) + Ce(IV) \quad (4)$$

According to the ground state reduction potentials of Sm(III) ($E_{red}^{III/II} \approx -1.6$ V) and Ce(IV) ($E_{red}^{IV/III} \approx -1.8$ V),[20a] Scheme 5.2 may be feasible. Additionally, polydisperse colloidal Sm_2O_3NP are thought to exist as a dynamic mixed oxides of primarily Sm_2O_3 with localized surface regions of the less stable SmO,[12a,12c] and when irradiated, at certain loadings their presence may impact the ability of ceria to cycle between CeO_2 and the less stable Ce_2O_3 state.

It is important to note that ICP-MS showed that Sm_xO_y@TiO_2 does not leach samarium and therefore that the nanomaterial functions as a purely heterogeneous catalyst (SI Table S5.1 and associated calculation). In all cases minor amounts of pinacol coupling of **1a** were observed and in some instances traces of the [2+2] photocycloaddition product were also detected. The reaction did not proceed significantly in the absence of the amine, the catalyst, or in the dark at 35°C (the temperature reached by the reaction mixture under irradiation; see SI Table S5.2 and

associated discussion). As is typical in heterogeneous photocatalysis using TiO_2-based materials, the role of the amine is primarily to turn over the photocatalyst by acting as a sacrificial electron donor to holes (h^+) trapped on the catalyst surface. However, the *α*-aminoalkyl radical formed after amine oxidation and rapid deprotonation (E_{red} −1.12 V vs SCE)[24] could also have contributed to reduction of **1a** (E_{red} −1.49 V) once the latter was activated by the LA samarium. In any event, $Sm_xO_y@TiO_2$ outperformed $Sm_xO_y@CeO_2$ and unmodified TiO_2 even when titania was used together with $Sm(OTf)_3$ in an equivalent molar quantity of samarium (Table 5.1, entries 1, 7 and 8). On the basis of these encouraging results, $Sm_xO_y@TiO_2$ was selected for further exploration of its potential as a heterogeneous photoredox-LA catalyst.

Table 5.2 Substrate scope for the heterogeneous photoreductive cyclization of chalcones **1a–f** catalyzed by $Sm_xO_y@TiO_2$.[a]

Entry	Substrate	Product	Time (h)	Yield[b] (%)	dr
	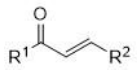	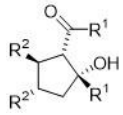			
1	**1a**, R^1 = Ph, R^2 = Ph	**2a**	3	70 (62)	>10:1
2	**1b**, R^1 = 4-MeO-Ph, R^2 = Ph	**2b**	5	67 (47)	>10:1
3	**1c**, R^1 = 4-Cl-Ph, R^2 = Ph	**2c**	3	90 (84)	>10:1
4	**1d**, R^1 = 4-Cl-Ph, R^2 = 4-F-P	**2d**	3	27 (78)	>10:1
5	**1e**, R^1 = Ph, R^2 = 4-F-Ph	**2e**	3	32 (59)	>10:1
6	**1f**, R^1 = Ph, R^2 = 4-MeO-Ph	**2f**	3	65 (54)	>10:1
7[c]	**1a**, R^1 = Ph, R^2 = Ph	**2a**	3	41 (62)	>10:1

[a]Reaction conditions: *trans*-chalcone (1 mmol), $Sm_xO_y@TiO_2$ (60 mg), *i*-Pr_2NEt (5 mmol), 15 mL of dry MeCN, degassed with argon 20 min, and irradiated with a 400 nm LED (90 W). [b]Determined by ^1H NMR spectroscopy using an internal standard. Yields in parentheses refer to the analogous homogeneous system from ref 5b. [c]Control reaction using unmodified TiO_2 as the catalyst.

We next investigated the scope of the reaction (Table 5.2). To our satisfaction, $Sm_xO_y@TiO_2$ was able to catalyze the photoreductive cyclization of a series of mono- and disubstituted chalcone derivatives bearing electron-donating and electron-withdrawing substituents in a similar fashion to $Ru(bpy)_3^{2+}$.[5b] Compared to the

homogeneously catalyzed system, our heterogeneous dual catalytic strategy produced significantly higher yields of the photoreductive coupling product for the parent chalcone as well as for substrates bearing either an electron-withdrawing group (EWG) at the 4′-position or an electron-donating group (EDG) at the 4′- or at the 4-position (**1a–c** and **1f**, Table 5.2, entries 1–3 and 6). In a similar trend to that observed in the homogeneously catalyzed reaction, $Sm_xO_y@TiO_2$ is less tolerant of EWGs at the 4-position, but unlike the system described by Xia and co-workers, here the yield remains low even when EWGs are simultaneously present at both the 4′- and the 4-positions (**1d–e**, Table 5.2, entries 4 and 5).

In addition to the convenience of easy separation of our heterogeneous catalyst from the reaction mixture by simple centrifugation, avoidance of product contamination by the catalyst and the absence of any additional additives to remove, another major advantage of heterogeneous catalysis is the potential for catalyst reusability. We were pleased to observe that $Sm_xO_y@TiO_2$ can be recovered and used to catalyze the photoreductive cyclization of **1a** for at least five cycles at the same laboratory bench scale (1 mmol starting material) without showing any evidence of diminished catalytic activity. In cycles two through five, the reaction still reached completion after 3 h of irradiation, suggesting that reusing the catalyst had no obvious impact upon the reaction kinetics (Figure 5.2). This high level of reusability goes a long way to demonstrating the advantages offered by heterogeneous catalysis. Aside from the obvious environmental benefit of reducing dependence on precious metals, from a purely economic perspective, the increased cost-effectiveness of replacing a system comprising commercially available $Ru(bpy)_3^{2+}$ and $Sm(OTf)_3$ (as in ref 5b) with $Sm_xO_y@TiO_2$ on an equivalent scale is over 90-fold for just the first use of the readily recoverable catalyst, including the cost of the samarium precursor lost during the preparation of the nanocatalyst (SI Table S5.3 and associated discussion).

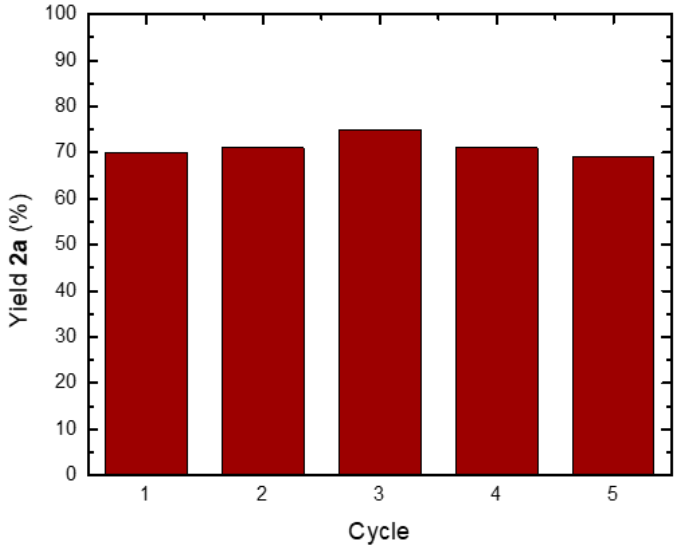

Figure 5.2 Reusability study of $Sm_xO_y@TiO_2$ in the heterogeneous photoreductive coupling of chalcone **1a** to form the cyclopentanol derivative **2a**. Reaction conditions were identical to those summarized in Table 5.1 and Table 5.2, including reaction time and scale, and the recovered catalyst was used without any additional pretreatment.

Turnover number (TON), the number of moles of substrate converted to product per mole of active sites prior to catalyst deactivation, and similarly turnover frequency (TOF), are important metrics routinely used to characterize and compare the efficacies of different catalysts. However, obtaining reliable values for TON and TOF can be difficult for many nanostructured heterogeneous catalysts, including $Sm_xO_y@TiO_2$, due to the presence of an unknown number of active sites. NPs might possess multiple active sites and their catalytic activities could differ greatly as a result of nonuniform size or spatial distributions on the support. In addition, many of the atoms making up each NP do not represent potential active sites because they are not located on the NP surface. In the case of $Sm_xO_y@TiO_2$, the problem is compounded further because the precise stoichiometry of the samarium oxide nanoparticle surface is uncertain. Therefore, commenting on turnover as a function of moles of samarium atoms or numbers of NPs does not allow for an easy and direct comparison to the known TONs or TOFs of other catalysts. For nanocomposites catalysts such as $Sm_xO_y@TiO_2$, where the support possesses some degree of

catalytic activity on its own, the presence of additional or cooperative active sites on the support must also be considered. Even the accurate molecular weight of the nanocomposite catalyst is an elusive quantity, and so incorporating moles of catalyst into TON and TOF calculations is not an option. Estimates of TON and TOF should therefore be made and interpreted with caution so as to avoid unreasonable comparisons with other heterogeneous or homogeneous catalysts. Upon the basis of these considerations, estimating TON and TOF of heterogeneous catalysts as functions of substrate and catalyst mass may become a useful convention.[25] By this method, TON was 187 with respect to mass of samarium and 9 with respect to total mass of the nanocomposite. However, both values should be regarded as low estimates because they are based upon just the first five cycles of use rather than until complete catalyst deactivation. Similarly, TOF was 12 and 0.6 h^{-1} as a function of mass of samarium or total catalyst mass, respectively (calculations available in the Supporting Information).

We expanded our investigation into the photocatalytic activity of $Sm_xO_y@TiO_2$ to include the intramolecular [2+2] photocycloaddition of bis(enones) **4a–c** and found that $Sm_xO_y@TiO_2$ is indeed a versatile heterogeneous catalyst. The [2+2] cycloaddition of unsaturated enones is often employed as a key step in natural product synthesis and is an important tool in the construction of synthetic building blocks.[10a,10b,11] Elegant strategies for the homogeneous photocatalytic version of this reaction using $Ru(bpy)_3^{2+}$ have been studied extensively by Yoon,[6c-e] and nonphotochemical routes have been investigated by Krische[10d,26] and Bauld.[27] We have also reported in the past that the reaction can be photocatalyzed heterogeneously by platinized titania ($Pt@TiO_2$).[18b]

Utilizing the Lewis acidity of $Sm_xO_y@TiO_2$ allowed us to make substantial improvements to the efficiency of the heterogeneously catalyzed reaction (Table 5.3). We obtained higher yields of the [2+2] cycloadducts **5a** and **5b** in a much shorter reaction time (71% **5a** and 72% **5b** in 1 h here vs 51% **5a** and 42% **5b** in 15 h using $Pt@TiO_2$ in ref 18b), under conditions that are now on par with the homogeneous catalytic system reported by Yoon (Scheme 5.1). Compared to $Pt@TiO_2$, we were also able to increase the selectivity for the desirable [2+2] cycloadduct to 78% for **5a** and

81% for **5b** and greatly improve the catalyst reusability up to at least three cycles without significant loss of activity (SI Figure S5.20). Using the previously described method, TON (based on three cycles) and TOF were 117 and 39 h^{-1} by mass of samarium and were 6 and 2 h^{-1} by total nanocomposite mass, respectively.

Table 5.3 Heterogeneous intramolecular [2+2] cycloaddition of bis(enones) **4a–c**.[a]

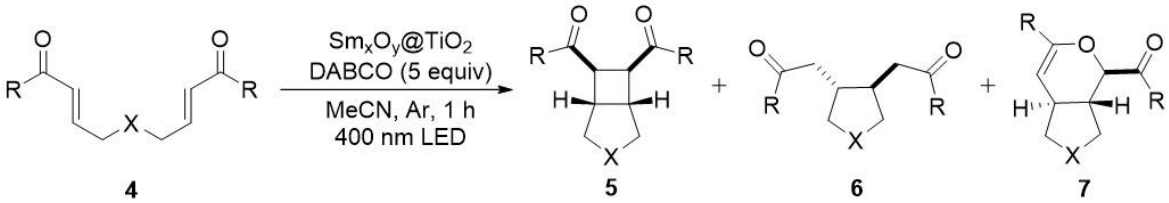

Entry	Substrate	Catalyst & Conversion[b] (%)	Product	Selectivity (%)	Yield[b] (%)	dr
1a	**4a**	$Sm_xO_y@TiO_2$ 91	**5a**	78	71	1.2:1
1b	X = CH_2		**6a**	10	9	>10:1
1c	R = Ph		**7a**	12	11	>10:1
2a	**4a**	TiO_2 83	**5a**	57	47	1.3:1
2b	X = CH_2		**6a**	22	18	>10:1
2c	R = Ph		**7a**	17	14	>10:1
3a	**4b**	$Sm_xO_y@TiO_2$ 89	**5b**	81	72	1.8:1
3b	X = CH_2		**6b**	4	4	>10:1
3c	R = 4-Cl-Ph		**7b**	15	13	>10:1
4a[c]	**4c**	$Sm_xO_y@TiO_2$ 73	**5c**	0	0[d]	–
4b[c]	X = CH_2CH_2		**6c**	18	13[e]	1.2:1
4c[c]	R = Ph		**7c**	74	54	1.4:1

[a]Reaction conditions: substrate (0.17 mmol), catalyst (20 mg), DABCO (5 equiv), 5 mL dry MeCN, degassed with argon 20 min, irradiated with a 400 nm LED (90 W). Longer irradiation times did not result in significantly higher conversion to the [2+2] cycloadduct using either $Sm_xO_y@TiO_2$ or TiO_2 alone. [b]Determined by ^{1}H NMR spectroscopy using an internal standard unless otherwise noted. [c]Irradiation time not optimized for conversion. [d]Isolated yields. [e]Yield determined by ^{1}H NMR spectroscopy performed on an impure fraction of the crude product mixture obtained after flash chromatography. DABCO = 1,4-diazabicyclo[2.2.2]octane.

Similar to the photoreductive cyclization of chalcones, $Sm_xO_y@TiO_2$ significantly outperformed unmodified TiO_2 in terms of yield but also in selectivity for **5a** (Table 5.3, entries 1a and 2a). Higher yield and selectivity for the [2+2] cycloadduct over the reductive coupling and [4+2] hetero-Diels–Alder products (**6a** and **7a**, respectively) relative to both TiO_2 and $Pt@TiO_2$ is most likely due to coordination to

samarium, mirroring results observed by Yoon upon addition of a LA.[6c,6e] Diastereoselectivity was again unaffected by modification of the TiO_2 support with samarium and remained high for **6a–b** and **7a–b**, matching results reported using $Pt@TiO_2$ or the homogeneous catalyst $Ru(bpy)_3^{2+}$ in the presence of a LA additive. However, here the diastereometric ratio was much lower for the [2+2] cycloadducts (Table 5.3). Conversion of a symmetric bis(enone) with identical aryl substituents possessing an EDG at the 4-position (R = 4-MeO-Ph) was less effective and not quantified.

Interestingly, Yoon reported that bis(enone) **4c**, bearing an additional methylene unit in the carbon tether, exclusively underwent the [4+2] hetero-Diels–Alder cycloaddition to form **7c**.[6g] While we also did not detect any trace of the [2+2] cycloadduct **5c** in our analogous heterogeneously catalyzed system, we did isolate the reductive coupling product **6c** with 18% selectivity (Table 5.3, entries 4a–c). Yoon suggested that **6c** could be the result of over-reduction and reductive cleavage of **7c** at longer irradiation times (>24 h). Although the quantities of reagents were only given in equivalents in that report, our system was irradiated for much less time (1 h), albeit with a different light source (90 W 400 nm LED at 2 mm vs 200 W tungsten filament bulb at 30 cm in ref 6g). In the homogeneously catalyzed system, the addition of 10 equiv of H_2O resulted in a dramatic increase in the yield and selectivity for **7c**, and the time required to reach complete conversion decreased from 9.5 to 1 h.[6g] We instead observed an opposing trend, with 10 equiv of H_2O resulting in a decrease in conversion from 73% to less than 60% in 1 h. These differences in reactivity do much to highlight the inherent divide between homogeneous and heterogeneous catalytic systems but could be viewed as an advantage or disadvantage depending upon the specific application.

A mechanism for the heterogeneous catalytic intramolecular [2+2] photocycloaddition of symmetric bis(enones) is proposed in Figure 5.3. Similar to the photoreductive cyclization of chalcones, the proposed heterogeneous catalytic mechanism for the major product closely follows that of the homogeneous catalytic system.[1a,2b] SET from the photoexcited nanocomposite catalyst to the LA-activated substrate forms the key radical anion intermediate stabilized by the LA Sm_xO_y NPs.

Subsequent intramolecular Michael addition leads to closing of the five-membered ring followed by cyclobutanation to afford the samarium-coordinated ketyl radical, which then gives up an electron to yield the cycloadduct **5** (one diastereomer shown for clarity). Unlike the photoreductive cyclization of chalcones then, the intramolecular [2+2] photocycloaddition of bis(enones) is a net neutral redox process and the possibility of a chain component in the overall mechanism should not be ignored. In principle, oxidation of the ketyl radical in the final step of the mechanism could proceed via SET to quench h^+ in the photocatalyst, or by reduction of another molecule of substrate to propagate a chain reaction. Since heterogeneous catalytic reaction mechanisms are often difficult to study and to know with certainty, Figure 5.3 focuses instead on what is likely to be the dominant pathway to the major [2+2] photocycloaddition product. Further work to elucidate the precise nature of the mechanism, extend the scope of the reaction, and improve diastereoselectivity is currently underway in our laboratory and may be the subject of a future report.

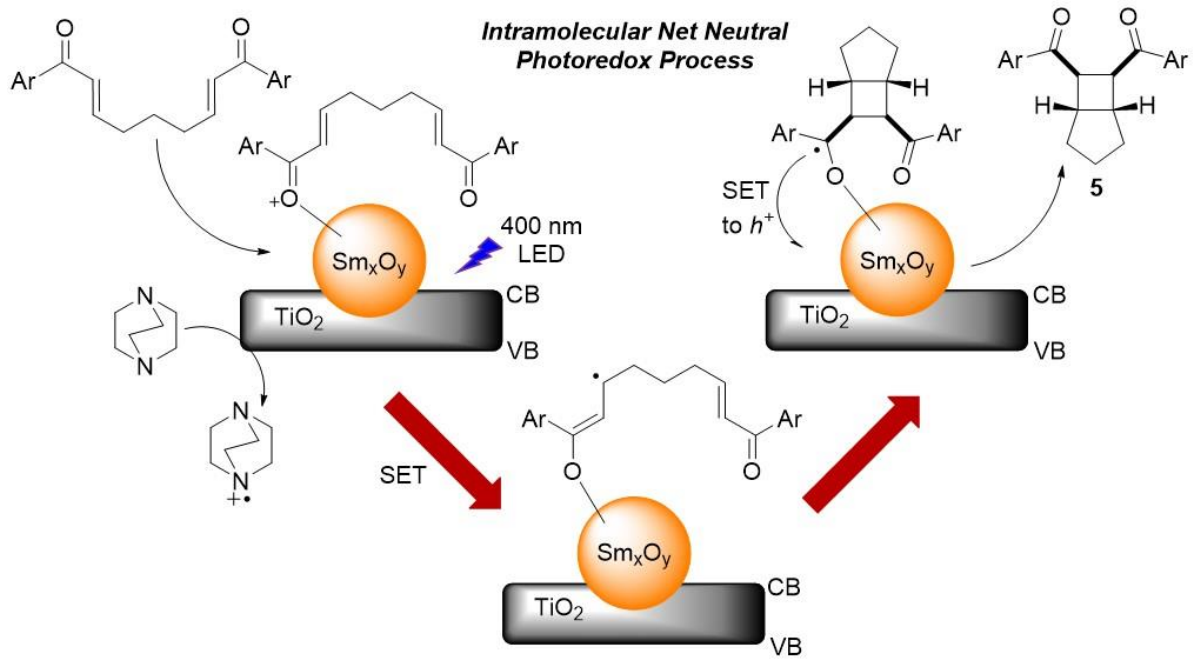

Figure 5.3 Proposed mechanism for the heterogeneous net neutral photoredox-LA dual catalytic intramolecular [2+2] photocycloaddition of symmetric aryl bis(enones).

Conclusion

In summary, we have described the efficacy and versatility of the first member of a new class of bifunctional nanomaterials, $Sm_xO_y@TiO_2$, in the first two examples of heterogeneous dual photoredox-Lewis acid catalysis. The nanocomposite material utilizes visible light to perform both net reductive and net neutral photoredox processes requiring LAs. It efficiently catalyzes the intermolecular photoreductive cyclization of a series of chalcones as well as the intramolecular [2+2] photocycloaddition of bis(enones), two classes of substrates and cyclization reactions with proven track records of high synthetic utility. Further, $Sm_xO_y@TiO_2$ is easily recovered, reusable for several cycles, functions as a purely heterogeneous catalyst without leaching, and may yet possess even more general applicability for heterogeneous dual photoredox-LA catalysis. This work demonstrates the potential for realizing systems that combine all the benefits of homogeneous and heterogeneous catalysis and should set in motion a wide range of new collaborative efforts across synthetic organic, industrial, and catalysis research.

References

(1) (a) Prier, C. K.; Rankic, D. A.; MacMillan, D. W. C. *Chem. Rev.* **2013**, *113*, 5322-5363; (b) Romero, N. A.; Nicewicz, D. A. *Chem. Rev.* **2016**, *116*, 10075-10166.

(2) (a) Kärkäs, M. D.; Bosque, I.; Matsuura, B. S.; Stephenson, C. R. J. *Org. Lett.* **2016**, *18*, 5166-5169; (b) Skubi, K. L.; Blum, T. R.; Yoon, T. P. *Chem. Rev.* **2016**, *116*, 10035-10074; (c) Twilton, J.; Le, C.; Zhang, P.; Shaw, M. H.; Evans, R. W.; MacMillan, D. W. C. *Nat. Rev. Chem.* **2017**, *1*, 0052; (d) Zhang, X.; MacMillan, D. W. C. *J. Am. Chem. Soc.* **2017**, *139*, 11353-11356; (e) Zuo, Z.; Ahneman, D.; Chu, L.; Terrett, J.; Doyle, A. G.; MacMillan, D. W. C. *Science* **2014**, *345*, 437-440.

(3) Yoon, T. P. *Acc. Chem. Res.* **2016**, *49*, 2307-2315.

(4) (a) Huo, H.; Shen, X.; Wang, C.; Zhang, L.; Rose, P.; Chen, L.-A.; Harms, K.; Marsch, M.; Hilt, G.; Meggers, E. *Nature* **2014**, *515*, 100-103; (b) Brimioulle, R.; Bach, T. *Science* **2013**, *342*, 840-843.

(5) (a) Vallavoju, N.; Selvakumar, S.; Jockusch, S.; Sibi, M. P.; Sivaguru, J. *Angew. Chem., Int. Ed.* **2014**, *53*, 5604-5608; (b) Zhao, G.; Yang, C.; Guo, L.; Sun, H.; Lin, R.; Xia, W. *J. Org. Chem.* **2012**, *77*, 6302-6306.

(6) (a) Blum, T. R.; Miller, Z. D.; Bates, D. M.; Guzei, I. A.; Yoon, T. P. *Science* **2016**, *354*, 1391-1395; (b) Ruiz Espelt, L.; McPherson, I. S.; Wiensch, E. M.; Yoon, T. P. *J. Am. Chem. Soc.* **2015**, *137*, 2452-2455; (c) Du, J.; Espelt, L. R.; Guzei, I. A.; Yoon, T. P. *Chem. Sci.* **2011**, *2*, 2115-2119; (d) Du, J.; Skubi, K. L.; Schultz, D. M.; Yoon, T. P. *Science* **2014**, *344*, 392-396; (e) Ischay, M. A.; Anzovino, M. E.; Du, J.; Yoon, T. P. *J. Am. Chem. Soc.* **2008**, *130*, 12886-12887; (f) Amador, A. G.; Sherbrook, E. M.; Yoon, T. P. *J. Am. Chem. Soc.* **2016**, *138*, 4722-4725; (g) Hurtley, A. E.; Cismesia, M. A.; Ischay, M. A.; Yoon, T. P. *Tetrahedron* **2011**, *67*, 4442-4448; (h) Lu, Z.; Shen, M.; Yoon, T. P. *J. Am. Chem. Soc.* **2011**, *133*, 1162-1164.

(7) (a) Beemelmanns, C.; Blot, V.; Gross, S.; Lentz, D.; Reissig, H.-U. *Eur. J. Org. Chem.* **2010**, *14*, 2716-2732; (b) Blot, V.; Reißig, H.-U. *Eur. J. Org. Chem.* **2006**, *22*, 4989-4992; (c) Cabrera, A.; Le Lagadec, R.; Sharma, P.; Luis Arias, J.; Alfredo Toscano, R.; Velasco, L.; Gavino, R.; Alvarez, C.; Salmon, M. *J. Chem. Soc., Perkin Trans. 1* **1998**, *0*, 3609-3618; (d) Chopade, P. R.; Davis, T. A.; Prasad, E.; Flowers, R. A. *Org. Lett.* **2004**, *6*, 2685-2688; (e) Gross, S.; Reissig, H.-U. *Org. Lett.* **2003**, *5*, 4305-4307; (f) Szostak, M.; Fazakerley, N. J.; Parmar, D.; Procter, D. J. *Chem. Rev.* **2014**, *114*, 5959-6039; (g) McDonald, C. E.; Ramsey, J. D.; Sampsell, D. G.; Butler, J. A.; Cecchini, M. R. *Org. Lett.* **2010**, *12*, 5178-5181.

(8) Mikami, K.; Mikami, Y.; Matsumoto, Y.; Nishikido, J.; Yamamoto, F.; Nakajima, H. *Tetrahedron Lett.* **2001**, *42*, 289-292.

(9) Kobayashi, S.; Nagayama, S. Aldehydes vs Aldimines. *J. Am. Chem. Soc.* **1997**, *119*, 10049-10053.

(10) (a) Bach, T. *Synthesis* **1998**, 683-703; (b) Winkler, J. D.; Bowen, C. M.; Liotta, F. *Chem. Rev.* **1995**, *95*, 2003-2020; (c) Lin, S.; Lies, S. D.; Gravatt, C. S.; Yoon, T. P. *Org. Lett.* **2017**, *19*, 368-371; (d) Baik, T.-G.; Luis, A. L.; Wang, L.-C.; Krische, M. J. *J. Am. Chem. Soc.* **2001**, *123*, 6716-6717.

(11) De Keukeleire, D.; He, S. L. *Chem. Rev.* **1993**, *93*, 359-380.

(12) (a) Hodgson, G. K.; Impellizzeri, S.; Hallett-Tapley, G. L.; Scaiano, J. C. *RSC Adv.* **2015**, *5*, 3728-3732; (b) Hodgson, G. K.; Impellizzeri, S.; Scaiano, J. C. *Chem. Sci.* **2016**, *7*, 1314-1321; (c) Hodgson, G. K.; Impellizzeri, S.; Scaiano, J. C. *Catal. Sci. Technol.* **2016**, *6*, 7113-7121.

(13) Gaonkar, S. L.; Vignesh, U. N. *Res. Chem. Intermed.* **2017**, *43*, 6043-6077.

(14) Alston, J. Y.; Fry, A. J. *Electrochim. Acta* **2004**, *49*, 455-459.

(15) (a) Khade, G. V.; Suwarnkar, M. B.; Gavade, N. L.; Garadkar, K. M. *J. Mater. Sci.: Mater. Electron.* **2016**, *27*, 6425-6432; (b) Štengl, V.; Bakardjieva, S.;

Murafa, N. *Mater. Chem. Phys.* **2009**, *114*, 217-226; (c) Xiao, Q.; Si, Z.; Zhang, J.; Xiao, C.; Tan, X. *J. Hazard. Mater.* **2008**, *150*, 62-67.

(16) Muneer, I.; Farrukh, M. A.; Javaid, S.; Shahid, M.; Khaleeq-ur-Rahman, M. *Superlattices Microstruct.* **2015**, *77*, 256-266.

(17) Irfan, S.; Shen, Y.; Rizwan, S.; Wang, H.-C.; Khan, S. B.; Nan, C.-W. *J. Am. Ceram. Soc.* **2017**, *100*, 31-40.

(18) (a) Cherevatskaya, M.; Neumann, M.; Füldner, S.; Harlander, C.; Kümmel, S.; Dankesreiter, S.; Pfitzner, A.; Zeitler, K.; König, B. *Angew. Chem., Int. Ed.* **2012**, *51*, 4062-4066; (b) McTiernan, C. D.; Pitre, S. P.; Ismaili, H.; Scaiano, J. C. *Adv. Synth. Catal.* **2014**, *356*, 2819-2824.

(19) (a) Borgarello, E.; Kiwi, J.; Graetzel, M.; Pelizzetti, E.; Visca, M. *J. Am. Chem. Soc.* **1982**, *104*, 2996-3002; (b) Dahl, M.; Liu, Y.; Yin, Y. *Chem. Rev.* **2014**, *114*, 9853-9889; (c) Wei, L.; Yang, Y.; Xia, X.; Fan, R.; Su, T.; Shi, Y.; Yu, J.; Li, L.; Jiang, Y. *RSC Adv.* **2015**, *5*, 70512-70521.

(20) (a) Morss, L. R. *Chem. Rev.* **1976**, *76*, 827-841; (b) Brik, M. G.; Sildos, I.; Kiisk, V. *Phys. B* **2010**, *405*, 2450-2456.

(21) (a) Elhage, A.; Lanterna, A. E.; Scaiano, J. C. *ACS Catal.* **2017**, *7*, 250-255; (b) Shiraishi, Y.; Takeda, Y.; Sugano, Y.; Ichikawa, S.; Tanaka, S.; Hirai, T. *Chem. Commun.* **2011**, *47*, 7863-7865; (c) Subramanian, V.; Wolf, E. E.; Kamat, P. V. *J. Am. Chem. Soc.* **2004**, *126*, 4943-4950.

(22) Wang, B.; Durantini, J.; Nie, J.; Lanterna, A. E.; Scaiano, J. C. Heterogeneous Photocatalytic Click Chemistry. *J. Am. Chem. Soc.* **2016**, *138*, 13127-13130.

(23) Eltermann, M.; Utt, K.; Lange, S.; Jaaniso, R. *Opt. Mater.* **2016**, *51*, 24-30.

(24) Wayner, D. D. M.; McPhee, D. J.; Griller, D. *J. Am. Chem. Soc.* **1988**, *110*, 132-137.

(25) Guo, X.-W.; Hao, C.-H.; Wang, C.-Y.; Sarina, S.; Guo, X.-N.; Guo, X.-Y. *Catal. Sci. Technol.* **2016**, *6*, 7738-7743.

(26) (a) Roh, Y.; Jang, H.-Y.; Lynch, V.; Bauld, N. L.; Krische, M. J. *Org. Lett.* **2002**, *4*, 611-613; (b) Wang, L.-C.; Jang, H.-Y.; Roh, Y.; Lynch, V.; Schultz, A. J.; Wang, X.; Krische, M. J. *J. Am. Chem. Soc.* **2002**, *124*, 9448-9453; (c) Yang, J.; Cauble, D. F.; Berro, A. J.; Bauld, N. L.; Krische, M. J. *J. Org. Chem.* **2004**, *69*, 7979-7984; (d) Yang, J.; Felton, G. A. N.; Bauld, N. L.; Krische, M. J. *J. Am. Chem. Soc.* **2004**, *126*, 1634-1635.

(27) (a) Felton, G. A. N.; Bauld, N. L. *Tetrahedron Lett.* **2004**, *45*, 8465-8469; (b) Felton, G. A. N.; Bauld, N. L. *Tetrahedron* **2004**, *60*, 10999-11010.

5.3 Postprint Version of Supporting Information

I. General Information

Acetonitrile (MeCN) was purified using a benchtop solvent purification system (LC Technology Solutions, Inc., SPBT-1) and stored over activated 3 Å molecular sieves. Distilled, 99.5% *N,N*-diisopropylethylamine (*i*-Pr_2NEt) was purchased from Sigma-Aldrich and stored under argon atmosphere. *trans*-chalcone 97% **1a** was purchased from Sigma-Aldrich and purified by flash chromatography (hexanes/EtOAc gradient) prior to use. All other reagents and solvents were purchased from commercial suppliers and used without further purification. All glassware and steel syringe needles were oven-dried for at least one hour prior to use. All ^{1}H and ^{13}C NMR spectra were recorded on either a Bruker Avance 400 (400 MHz), Bruker Avance 300 (300 MHz) or Bruker AvanceII 300 (300 MHz) spectrometer. ^{1}H and ^{13}C chemical shifts (δ) are reported in parts per million (ppm) relative to $CDCl_3$ solvent resonance signals at 7.26 ppm and 77.1 ppm, respectively. Diastereomer ratios were determined by NMR spectroscopy and verified by comparison to the literature wherever possible. Flash chromatography was performed using silica gel (230-400 mesh). Electron-Impact Mass Spectrometry (EI-MS) and positive-mode Electrospray Ionization Mass Spectrometry (ESI-MS) was conducted at the John L. Holmes mass spectrometry facility at the Department of Chemistry and Biomolecular Sciences at the University of Ottawa using a HRes, Concept S1, magnetic sector mass spectrometer and a Micromass Q-TOF I, respectively.

II. Synthesis of Substrates

General procedure for the synthesis of chalcone substrates:

Compounds **1a-b** were purchased from commercial suppliers. Compound **1c** was prepared according to a scaled down version of a previously published protocol.[1] A 50 mL round-bottom flask (rbf) was charged with 4'-chloroacetophenone (4 mmol, 0.52 mL, 1 eq.), benzaldehyde (4 mmol, 0.41 mL, 1 eq.) and 12 mL MeOH. Dropwise addition of 1 equivalent of NaOH dissolved in 4 mL MilliQ H_2O (18.2 MΩ cm^{-1} at 25°C) and continued stirring for a further 3 h at 35°C afforded the desired *α,β*-unsaturated

ketone as a white precipitate. The solid was filtered off and recrystallized from MeOH. Compounds **1d-f** were prepared by an analogous procedure using appropriate combinations of either acetophenone or 4'-chloroacetophenone with either 4-fluorobenzaldehyde or 4-methoxybenzaldehyde as required.

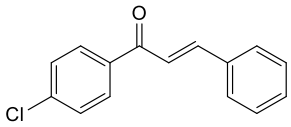

4-Chlorochalcone (**1c**, Table 5.2, entry 3): White crystalline solid. ^{1}H NMR (300 MHz, $CDCl_3$) δ 7.97 (dt, J = 8.72, 2.21 Hz, 2H), 7.82 (d, J = 15.67 Hz, 1H), 7.60-7.70 (m, 2H), 7.37-7.55 (m, 6H); ^{13}C NMR (400 MHz, $CDCl_3$) δ 189.3, 145.4, 139.3, 136.6, 134.8, 130.8, 130.0, 129.0, 128.6, 121.6; EI-MS $[C_{15}H_{11}OCl]^+$ calculated *m/z* 242.0493, found *m/z* 242.0469.

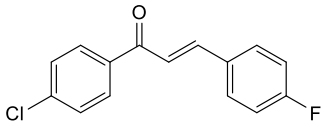

4-Chloro-4'-fluorochalcone (**1d**, Table 5.2, entry 4): White crystalline solid. ^{1}H NMR (300 MHz, $CDCl_3$) δ 7.96 (dt, J = 8.70, 2.21 Hz, 2H), 7.78 (d, J = 15.65 Hz, 1H), 7.70-7.59 (m, 2H), 7.48 (dt, J = 8.75, 2.19 Hz, 2H), 7.41 (d, J = 15.68 Hz, 1H), 7.12 (tt, J = 8.60, 2.32 Hz, 2H); ^{13}C NMR (400 MHz, $CDCl_3$) δ 189.1, 165.5, 163.0, 144.1, 139.4, 136.5, 131.0, 130.5, 129.9, 129.1, 121.3, 116.4, 116.2; EI-MS $[C_{15}H_{10}OClF]^+$ calculated *m/z* 260.0399, found *m/z* 260.0392.

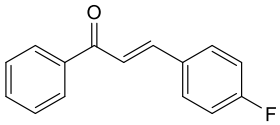

4'-Fluorochalcone (**1e**, Table 5.2, entry 5): White crystalline solid. ^{1}H NMR (300 MHz, $CDCl_3$) δ 7.98-8.06 (m, 2H), 7.78 (d, J = 15.74 Hz, 1H), 7.56-7.69 (m, 3H), 7.41-7.55 (m, 3H), 7.12 (tt, J = 8.60, 2.31 Hz, 2H); ^{13}C NMR (400 MHz, $CDCl_3$) δ 190.4, 165.4, 162.9, 143.6, 138.2, 132.9, 131.2, 130.4, 128.6, 121.9, 116.3, 116.1; EI-MS $[C_{15}H_{11}OF]^+$ calculated *m/z* 226.0788, found *m/z* 226.0780.

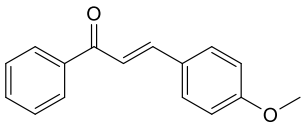

4'-Methoxychalcone (**1f**, Table 5.2, entry 6): Purification of the crude product by flash chromatography (hexanes/EtOAc) afforded a white solid. ^{1}H NMR (300 MHz, $CDCl_3$) δ 7.96-8.05 (m, 2H), 7.79 (d, J = 15.70 Hz, 1H), 7.46-7.66 (m, 5H), 7.42 (d, J = 15.63 Hz, 1H), 6.94 (dt, J = 8.86, 2.50 Hz, 2H), 3.86 (s, 3H); ^{13}C NMR (400 MHz, $CDCl_3$) δ 190.7,

161.8, 144.8, 138.6, 132.6, 130.3, 128.6, 127.7, 119.9, 114.5, 55.5; EI-MS $[C_{16}H_{14}O_2]^+$ calculated *m/z* 238.0988, found *m/z* 238.1010.

Synthesis of bis(enone) substrates:

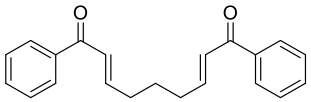

(2*E*,7*E*)-1,9-diphenylnona-2,7-diene-1,9-dione (**4a**, Table 5.3, entries 1-2): Prepared according to a modified literature protocol.[2] Glutaraldehyde (2.5 mmol, 0.5 mL 50 wt% aqueous solution) was added to the commercially available Wittig reagent (benzoylmethylene)triphenylphosphorane (6.25 mmol, 2.4 g) dissolved in 5 mL dry CH_2Cl_2 and the mixture was stirred for at least 48 h. The crude reaction was concentrated *in vacuo* to obtain 2-3 g of yellow residue. Purification by flash chromatography (6:1 hexanes:EtOAc v/v) afforded the title compound as a light yellow oil (304 mg, 1 mmol, 40% yield). ^{1}H NMR (400 MHz, $CDCl_3$) δ 7.89-7.96 (m, 4H), 7.56 (tt, J = 7.39, 1.59 Hz, 2H), 7.47 (tt, J = 7.50, 1.34 Hz, 4H), 7.06 (dt, J = 15.39, 6.87 Hz, 2H), 6.92 (dt, J = 15.45, 1.33 Hz, 2H), 2.40 (q, J = 7.24 Hz, 4H), 1.79 (quintet, J = 7.48 Hz, 2H); ^{13}C NMR (400 MHz, $CDCl_3$) δ 190.7, 148.6, 137.9, 132.8, 128.6, 126.6, 32.2, 26.8; EI-MS $[C_{21}H_{20}O_2]^+$ calculated *m/z* 304.1458, found *m/z* 304.1464.

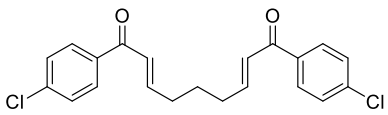

(2*E*,7*E*)-1,9-bis(4-chlorophenyl)nona-2,7-diene-1,9-dione (**4b**, Table 5.3, entry 3): Prepared according to an established literature protocol with some modifications.[3] A mixture of triphenylphosphine (27.8 mmol, 7.31 g) and 2-bromo-4'-chloroacetophenone (27.8 mmol, 5.55 g) in 250 mL THF was refluxed overnight and then cooled to room temperature. The phosphonium salt was filtered off, washed with ether and the white solid was dissolved in a 3:2 v/v mixture of distilled H_2O:CH_2Cl_2. The solution turned pink upon addition of 14 mL 2 M KOH (aq.) and after subsequent stirring overnight under ambient conditions the crude reaction was worked up via organic extraction with CH_2Cl_2 (3×100 mL) and the combined organic layers were washed with brine before being dried over $MgSO_4$. The solvent was evaporated under reduced pressure to yield the stabilized ylide as an orange oil (7.69 g, 18.5 mmol, 66% yield). Glutaraldehyde (4.63 mmol, 874 µL 50 wt% aq. solution) was added to all of

the stabilized Wittig reagent dissolved in 100 mL dry CH_2Cl_2 and the mixture was stirred overnight under ambient conditions. The crude reaction was then concentrated *in vacuo* and purification of the resulting residue by flash chromatography (15:1 hexanes:EtOAc v/v) afforded the title compound as a white solid (398 mg, 1 mmol, 23% yield). ^{1}H NMR (300 MHz, $CDCl_3$) δ 7.87 (d, J = 8.49 Hz, 4H), 7.44 (d, J = 8.58 Hz, 4H), 6.98-7.16 (m, 2H), 6.88 (d, J = 15.46 Hz, 2H), 2.40 (q, J = 7.11 Hz, 4H), 1.78 (quintet, J = 7.37 Hz, 2H); ^{13}C NMR (300 MHz, $CDCl_3$) δ 189.3, 149.1, 139.3, 136.2, 130.0, 129.0, 126.1, 32.3, 26.7; EI-MS $[C_{21}H_{18}O_2Cl_2]^+$ calculated *m/z* 372.0678, found *m/z* 372.0659.

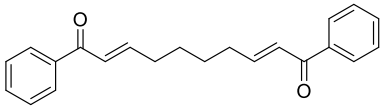

(1*E*,7*E*)-1,8-bis(benzoyl)-1,7-octadiene, 4c (Table 5.3, entry 5): First, hexane-1,6-dial was prepared by reaction of *trans*-cyclohexane-1,2-diol with sodium periodate according to literature protocols (285 mg, 2.5 mmol, quantitative yield).[4] Next, **4c** was prepared by a double Wittig reaction analogous to the protocol described for bis(enone) **4a**. Approximately 1.4 g (benzoylmethylene)triphenylphosphorane was dissolved in 50 mL dry CH_2Cl_2 and added to all 2.5 mmol of the hexane-1,6-dial. The mixture was stirred overnight at r.t. and then the solvent was evaporated under reduced pressure to obtain the crude product as a yellow oil. Flash chromatography (6:1 hexanes:EtOAc) provided the title compound (127 mg, 16% yield). ^{1}H NMR (300 MHz, $CDCl_3$) δ 7.88-7.98 (m, 4H), 7.56 (tt, J = 7.33, 1.74 Hz, 2H), 7.41-7.51 (m, 4H), 7.06 (dt, J = 15.41, 6.81 Hz, 2H), 6.90 (dt, J = 15.41, 1.22 Hz, 2H), 2.27-2.50 (m, 4H), 1.52-1.70 (m, 4H); ^{13}C NMR (400 MHz, $CDCl_3$) δ 190.9, 149.3, 138.0, 132.8, 128.6, 126.3, 32.7, 27.9; EI-MS $[C_{22}H_{22}O_2]^+$ calculated *m/z* 318.1614, found *m/z* 318.1641.

III. Synthesis of Catalysts

Nanocatalysts $Sm_xO_y@TiO_2$ and $Sm_xO_y@CeO_2$ were prepared based on a modified version of our previously reported synthesis of unsupported samarium oxide nanoparticles.[5] In brief, 250 mL MeCN obtained directly from the aforementioned solvent purification system (but not dried over activated molecular sieves) was immediately charged with 1 mM $Sm(NO_3)_3$•$6H_2O$ (Acros Organics) and 3 mM Irgacure-2959™ (Ciba Specialty Chemicals Inc.) photoinitiator along with an

appropriate mass of either TiO_2 (Aeroxide P25, Nippon Aerosil Co. Ltd.), CeO_2 (<5 μm, Sigma-Aldrich) or CeO_2 (<25 nm nanopowder, Sigma-Aldrich) such that the optimal Sm loading would be either 5 or 10 mol%. The Pyrex flask was sealed and the solution was purged with argon for 75 min while stirring and subsequently irradiated for 60 h using fifteen 8 W UVA bulbs (Hitachi, FL8-BL) installed in three time-controlled exposure panels (Luzchem, LZC-EXPO). The resulting solution was centrifuged for 30 min at 10,000 rpm, the supernatant was discarded and the remaining solid was dried under vacuum. The brownish crude nanocatalyst was then placed in a cellulose thimble and cleaned via soxhlet extraction with MeCN for a period of approximately 3 days. The beige/light brown solid was once again dried under vacuum and then fully characterized as described below. Non-photochemical methods of supporting samarium on TiO_2 were also attempted using $Sm(NO_3)_3•6H_2O$, $SmCl_3•6H_2O$ and SmI_2 (0.1 M in THF) but were largely unsuccessful.

IV. Catalyst Characterization

X-ray Photoelectron Spectroscopy (XPS) spectra were acquired on a Kratos Axis Ultra DLD spectrometer with a monochromatic Al Kα X-ray source operated at 140 W and 10^{-9} Torr. XPS spectra were analysed using standard CasaXPS software v2.3.15 and peak positions were corrected with reference to the core C 1s peak at 284.5 eV. Transmission Electron Microscopy (TEM) was performed on a JEOL JEM-2100F field emission TEM operating at 200 kV and Energy Dispersive X-ray Spectroscopy (EDS) was performed using an Oxford Instruments X-MAXN-80 EDS detector coupled to the same transmission electron microscope at the Centre for Catalysis Research and Innovation (CCRI) at the University of Ottawa. Samples were prepared by placing a drop of nanomaterial suspended in MeCN onto a carbon coated copper mesh grid (Electron Microscopy Sciences, CF-400-Cu) and evaporated under ambient conditions. Diffuse reflectance spectra were acquired on an Agilent Cary 7000 universal measurement UV-Visible-NIR spectrophotometer. UV-Visible absorbance spectra were acquired on a Varian Cary 50 Bio UV-Visible spectrophotometer. Inductively Coupled Plasma Mass Spectrometry (ICP-MS) was conducted on an

Agilent 8800 triple quadrupole ICP-MS at the Geochemistry Laboratories, Advanced Research Complex, University of Ottawa.

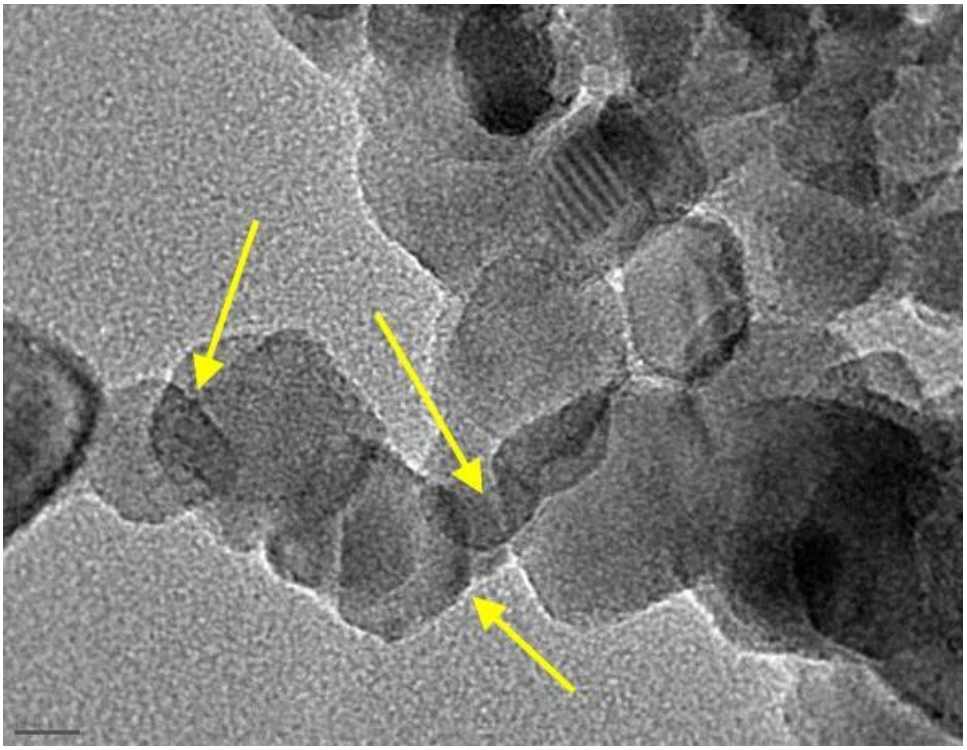

Figure S5.1 TEM image of 4.7 wt% Sm_xO_y@TiO_2. Scale bar is 10 nm. Arrows are intended to aid in identification of small Sm_xO_y particles present on the nanostructured TiO_2 support.

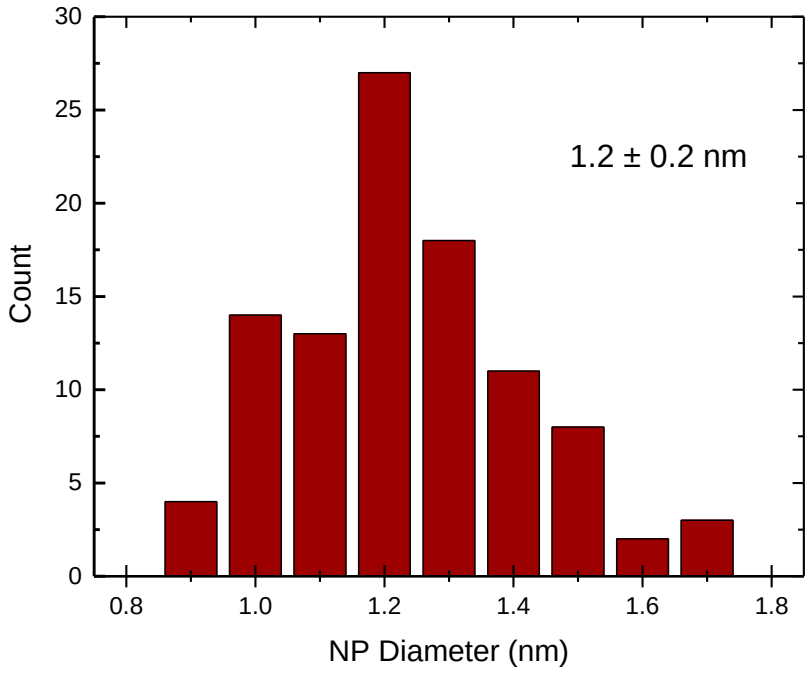

Figure S5.2 Size distribution of samarium oxide nanoparticles supported on TiO_2 obtained by manual counting and sizing of particles identifiable by TEM.

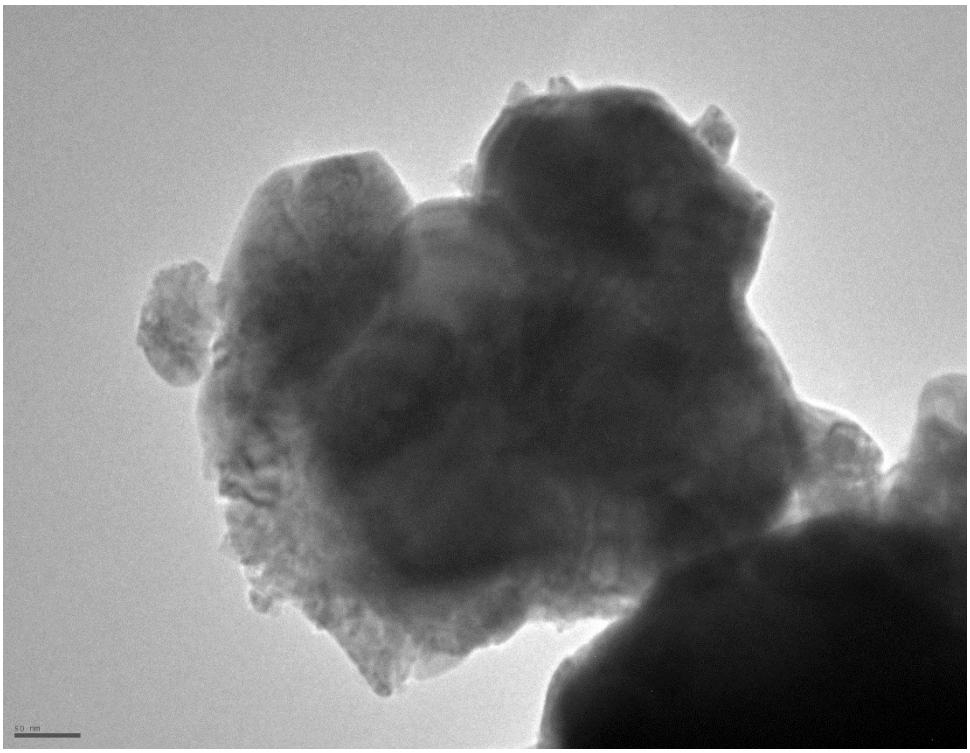

Figure S5.3 TEM image of 0.29 wt% Sm_xO_y@CeO_2 (<5 µm support). Scale bar is 50 nm.

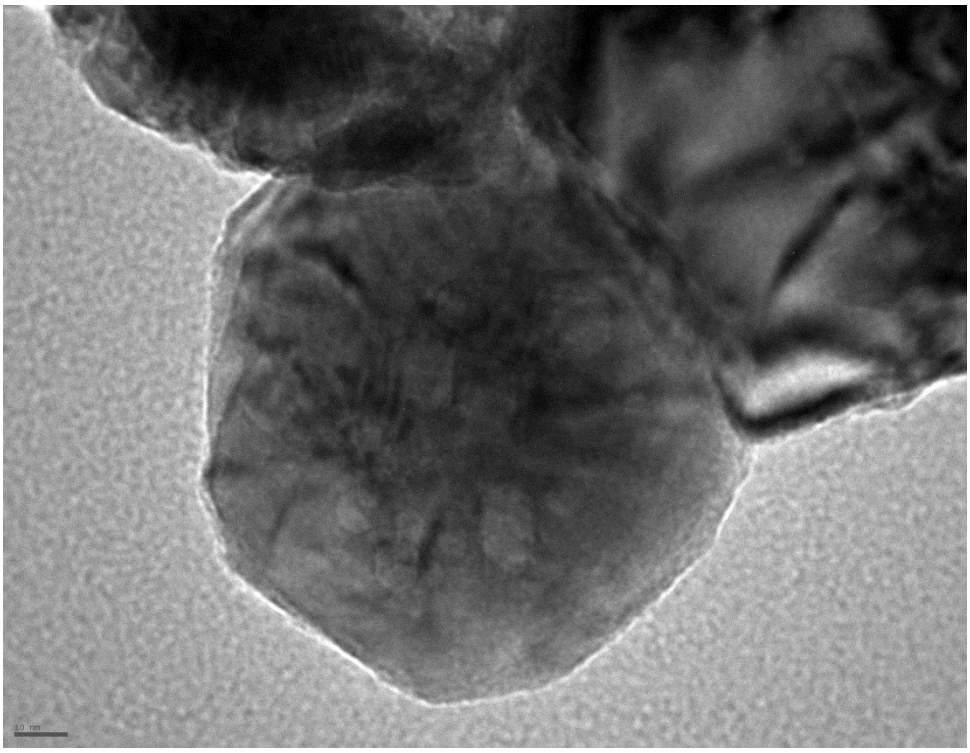

Figure S5.4 TEM image of 0.42 wt% Sm_xO_y@CeO_2 (<5 µm support). Scale bar is 10 nm.

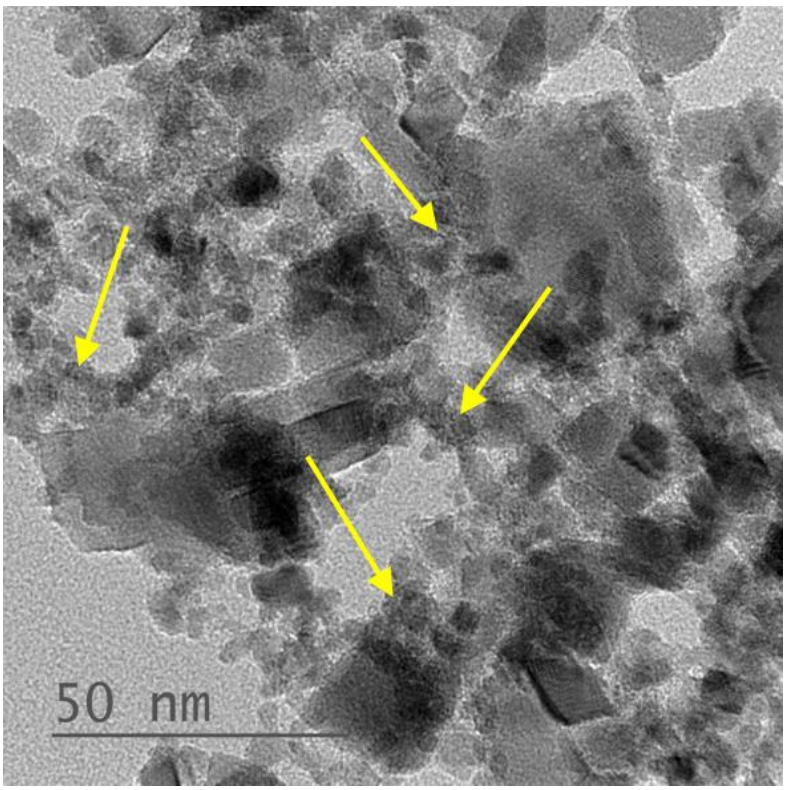

Figure S5.5 TEM image of 3.3 wt% Sm_xO_y@CeO_2 (<25 nm support). Scale bar is 50 nm. Arrows are intended to aid in identification of small Sm_xO_y particles present on the nanostructured CeO_2 support.

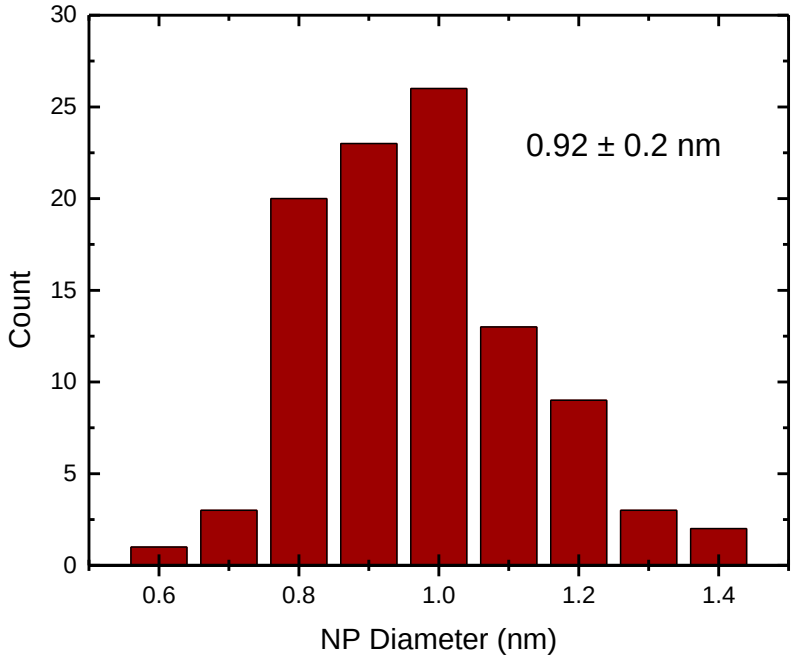

Figure S5.6 Size distribution of samarium oxide nanoparticles supported on nanosized (<25 nm) CeO_2 obtained by manual counting and sizing of particles identifiable by TEM.

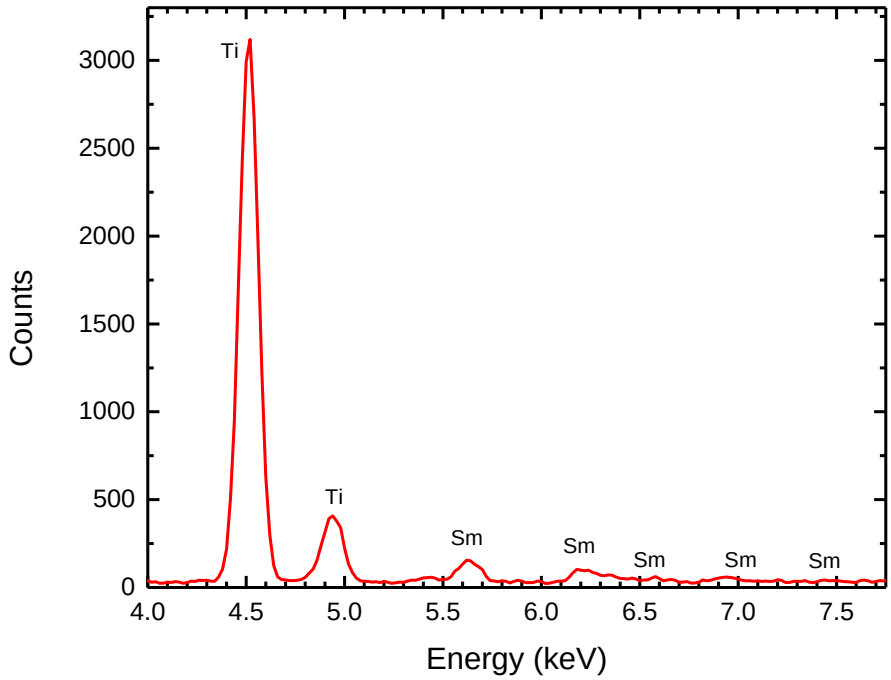

Figure S5.7 EDS spectrum of 4.7 wt% $Sm_xO_y@TiO_2$.

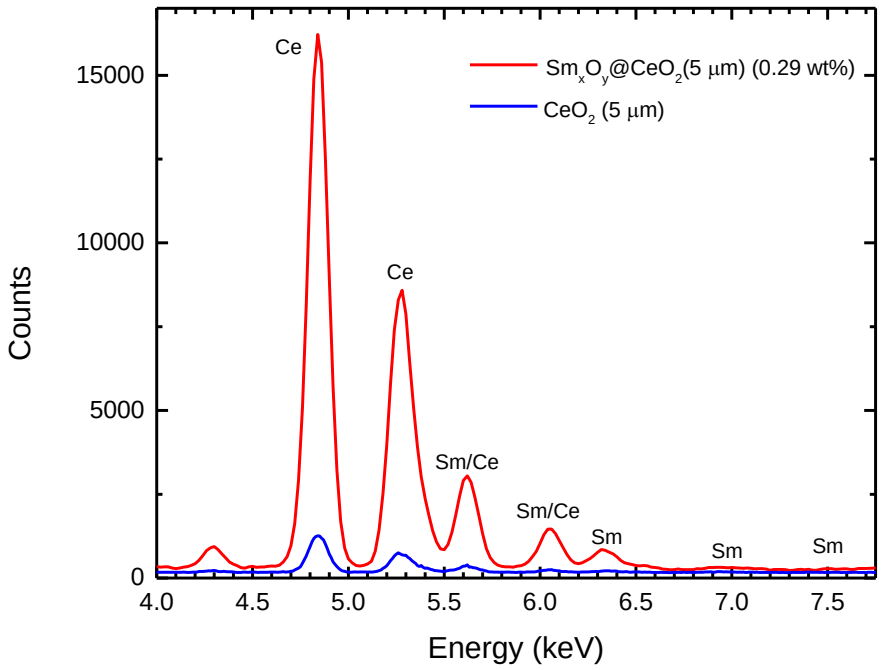

Figure S5.8 EDS spectra of 0.29 wt% Sm_xO_y@CeO_2 (<5 μm support) and CeO_2 (<5 μm).

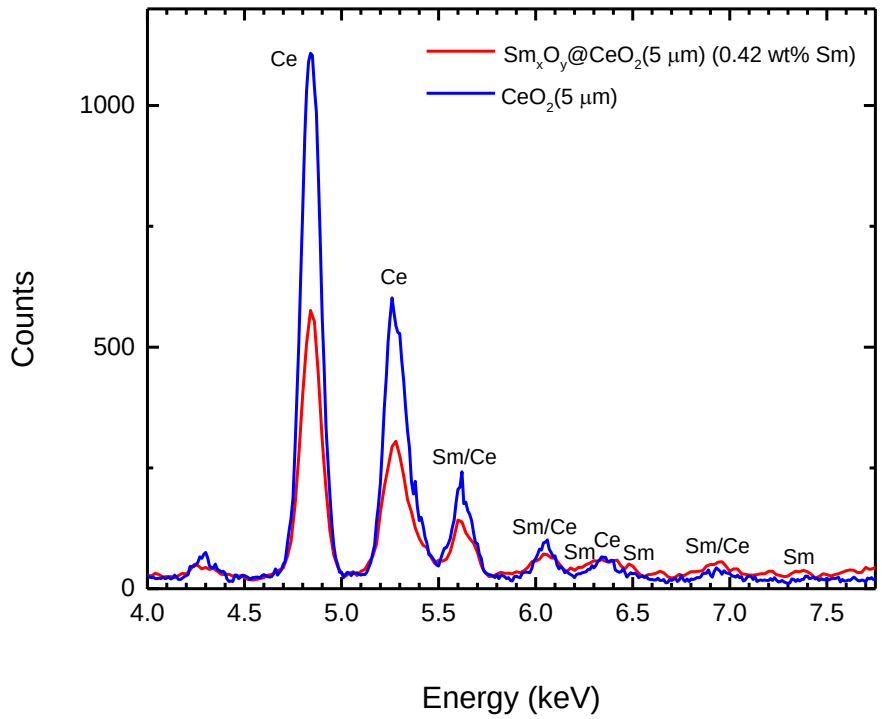

Figure S5.9 EDS spectra of 0.42 wt% Sm_xO_y@CeO_2 (<5 μm support) and CeO_2 (<5 μm).

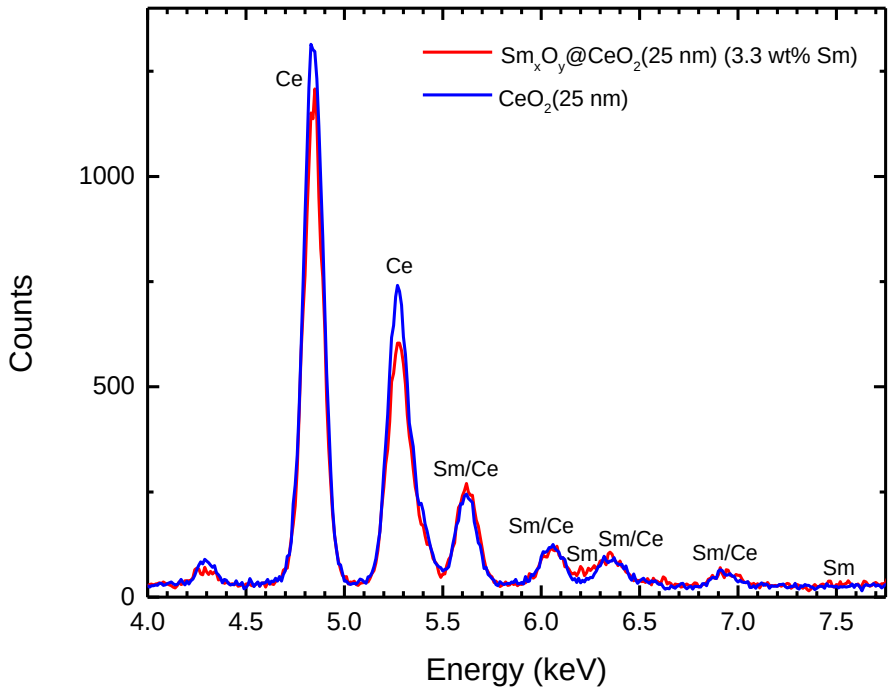

Figure S5.10 EDS spectra of 3.3 wt% $Sm_xO_y@CeO_2$ (<25 nm support) and CeO_2 (<25 nm) for comparison.

Although NPs of similar sizes were observable for $Sm_xO_y@TiO_2$ and $Sm_xO_y@CeO_2$ (<25 nm) by TEM (Figures S5.1 and S5.5), the relatively large size and thickness of the CeO_2 microparticles shown in Figures S5.3 and S5.4 combined with the extremely low <0.5 wt% loading of samarium did not allow any NPs to be identified. While EDS clearly detected samarium for $Sm_xO_y@TiO_2$ (Figure S5.7) the overlap between peaks for samarium and cerium made it more difficult to detect samarium supported on ceria. Nevertheless, careful comparison to the EDS spectrum of the unmodified CeO_2 microparticles and nanoparticles gives some indication of the presence of samarium supported on ceria (Figures S5.8-S5.10).

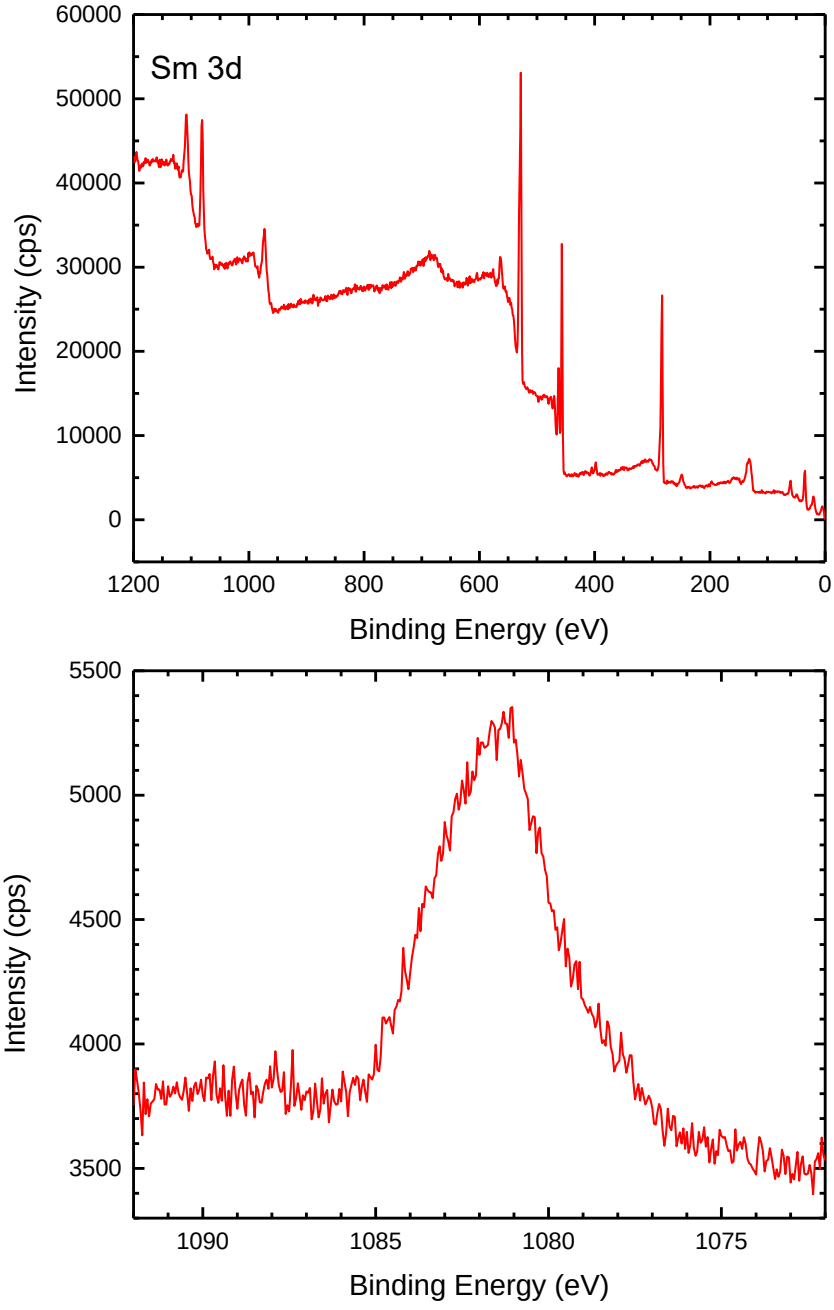

Figure S5.11 XPS spectra of 4.7 wt% Sm_xO_y@TiO_2 showing the characteristic doublet of Sm^{3+} between 1050-1150 eV.

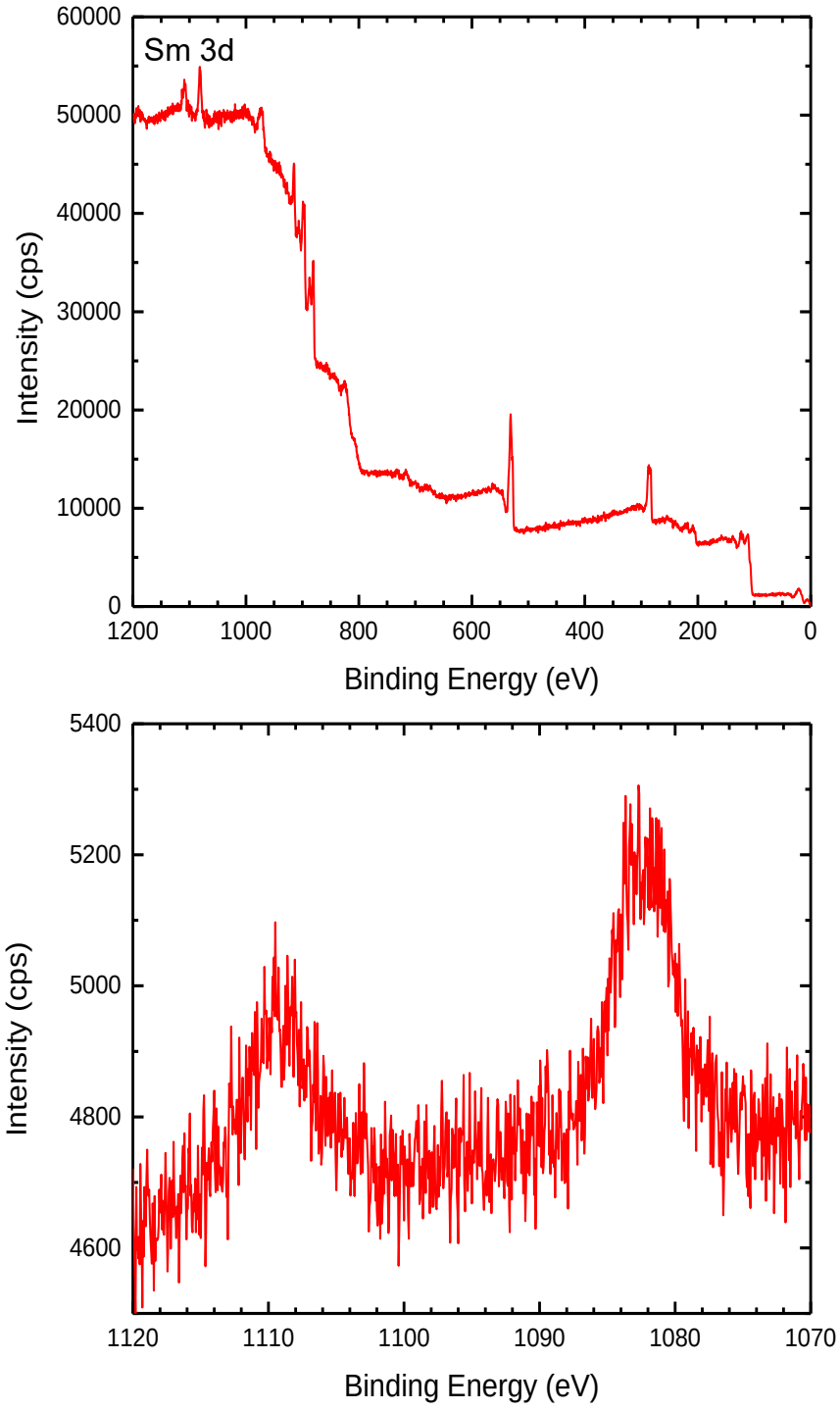

Figure S5.12 XPS spectra of 0.29 wt% $Sm_xO_y@CeO_2$ (<5 µm) showing the characteristic doublet of Sm^{3+} between 1050-1150 eV.

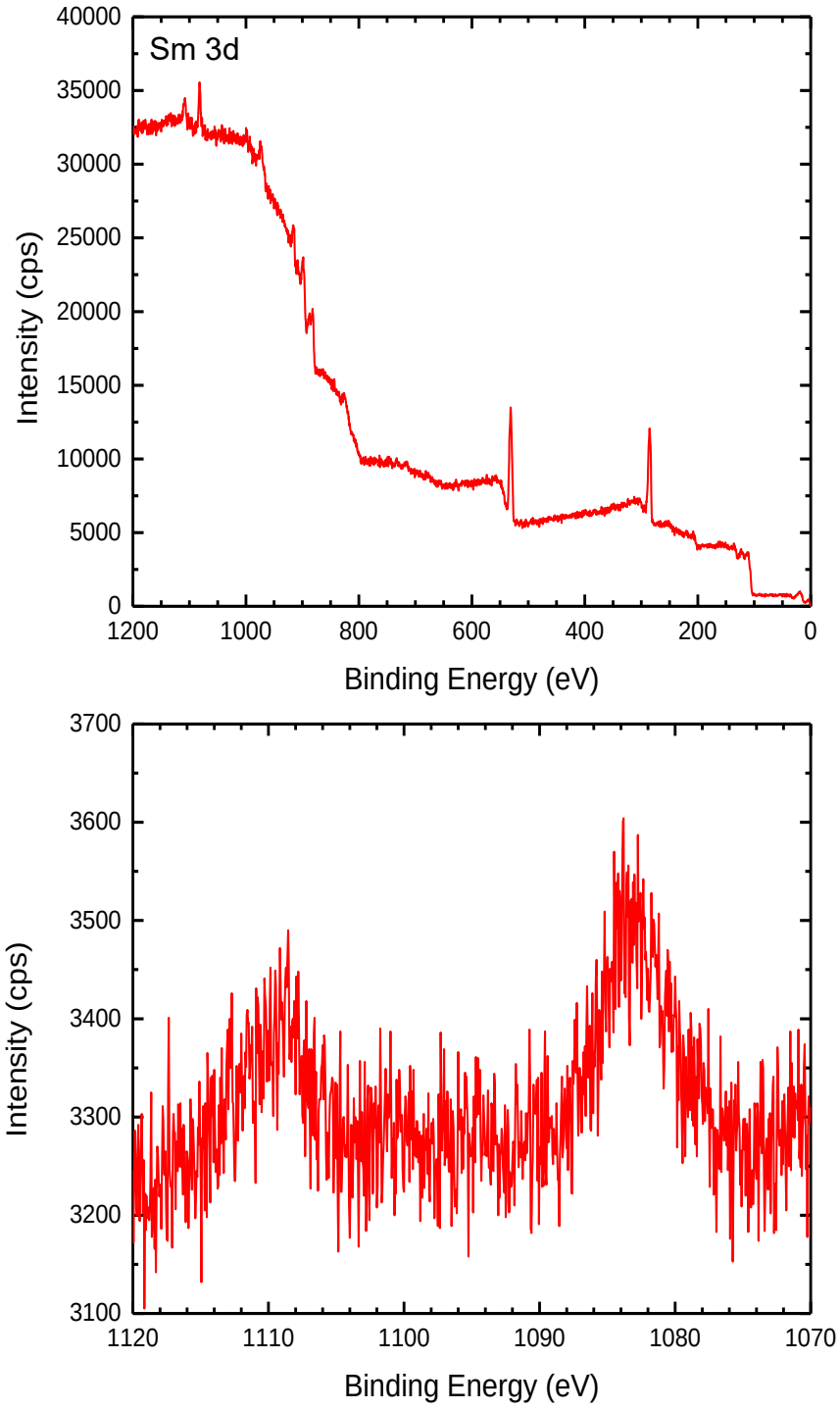

Figure S5.13 XPS spectra of 0.42 wt% Sm_xO_y@CeO_2 (<5 μm) showing the characteristic doublet of Sm^{3+} between 1050-1150 eV.

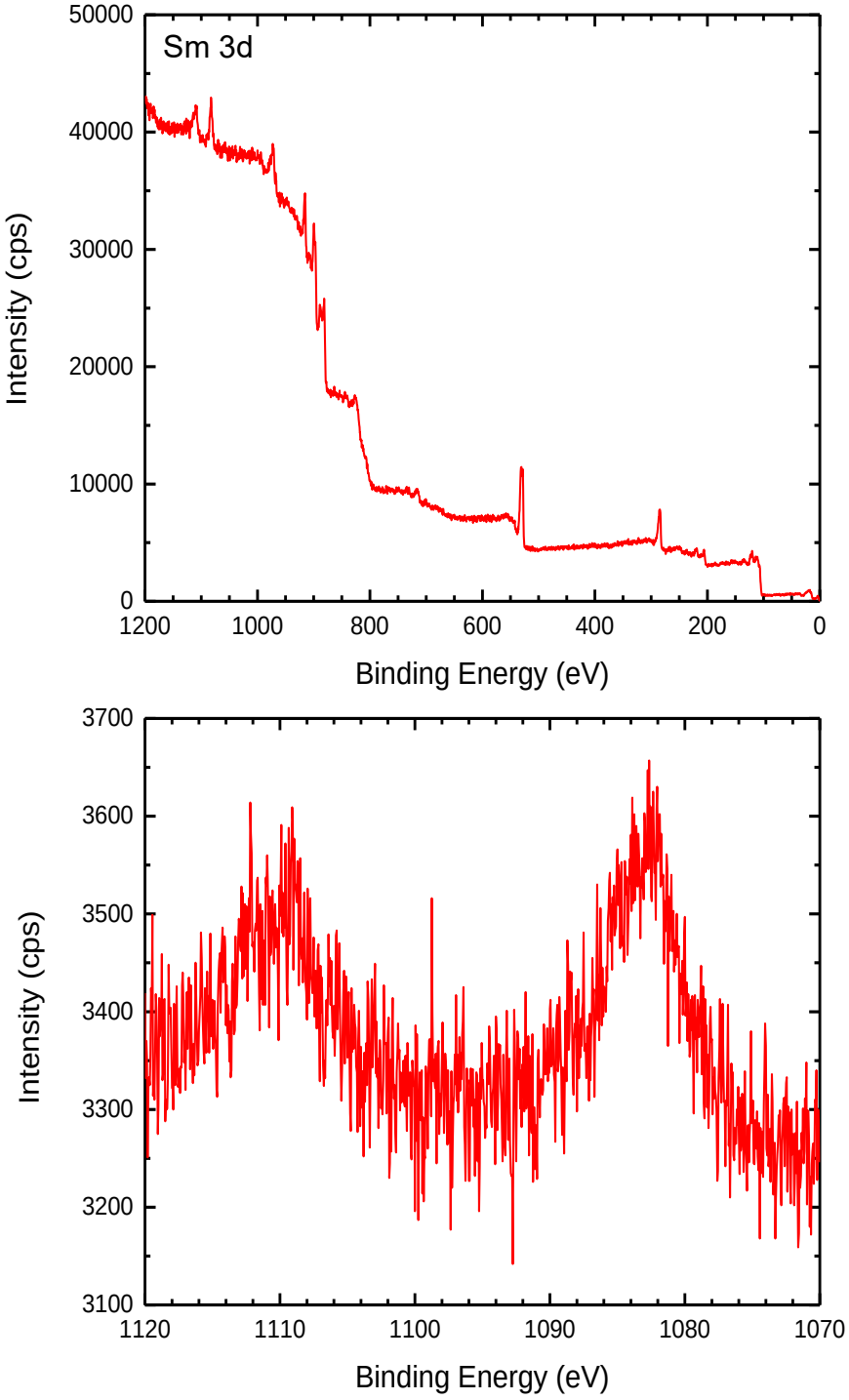

Figure S5.14 XPS spectra of 3.3 wt% Sm_xO_y@CeO_2 (<25 nm) showing the characteristic doublet of Sm^{3+} between 1050-1150 eV.

Similar to our previous report on the synthesis and characterization of larger, polydisperse, colloidal Sm_2O_3NP,[5] interpretation of XPS spectra to identify the presence or absence of different oxidation states of samarium should be done with caution. The doublet observed between 1080–1110 eV indicates the presence of Sm^{3+} and the lack of hyperfine splitting suggests the absence of Sm^{2+} and Sm^0. However, the latter two oxidation states can be difficult to detect for samarium, and if present may also have been generated *in situ* during the acquisition of the XPS spectrum. In addition, samarium oxide materials and specifically Sm_2O_3NP are known to be redox-active,[5-6] with localized surface regions reversibly fluctuating between SmO and Sm_2O_3. To be as accurate as possible, and to differentiate the new nanocomposite materials described in this report from larger colloidal Sm_2O_3NP based on their different physicochemical properties, we labeled our samarium-decorated semi-conductor nanocomposites Sm_xO_y@TiO_2 and Sm_xO_y@CeO_2.

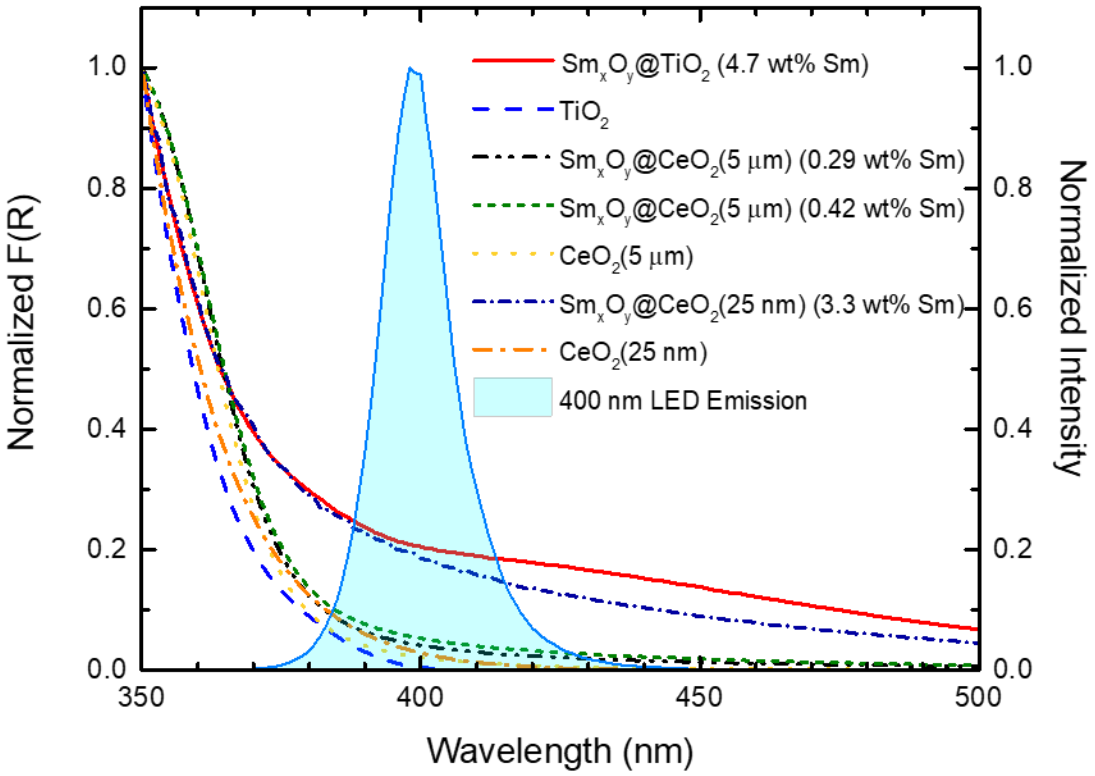

Figure S5.15 Diffuse reflectance spectra of the various nanomaterials compared to the emission profile of the 90 W 400 nm LED used for photocatalysis.

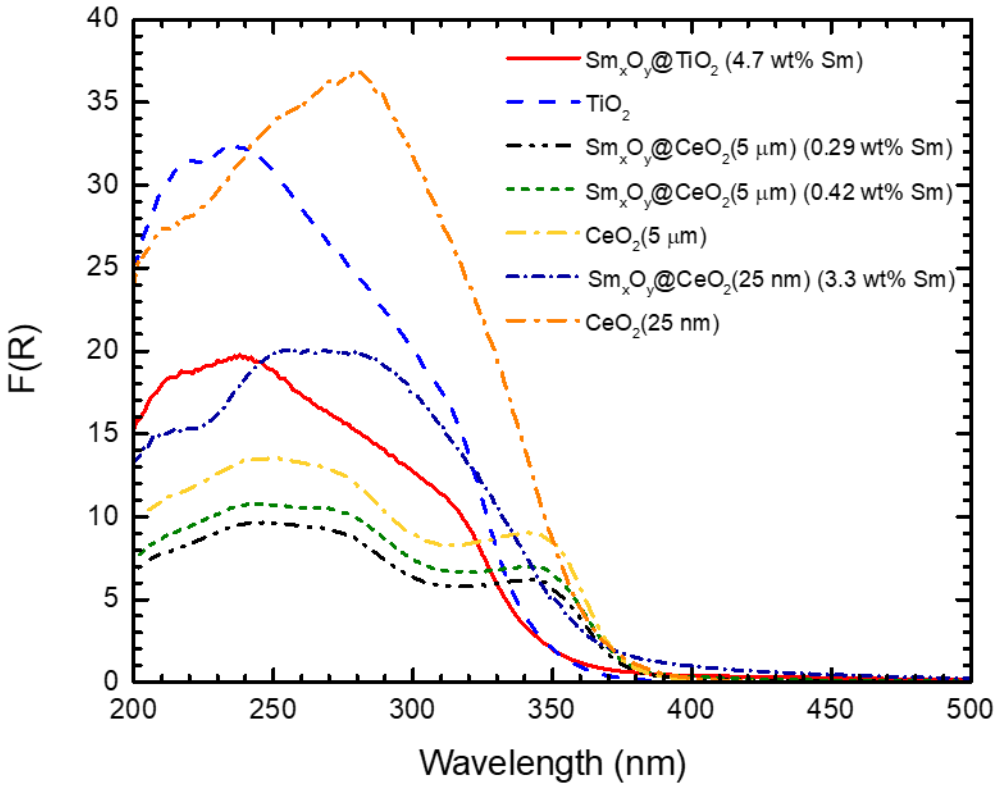

Figure S5.16 Full-scale diffuse reflectance spectra of the various nanomaterials prepared.

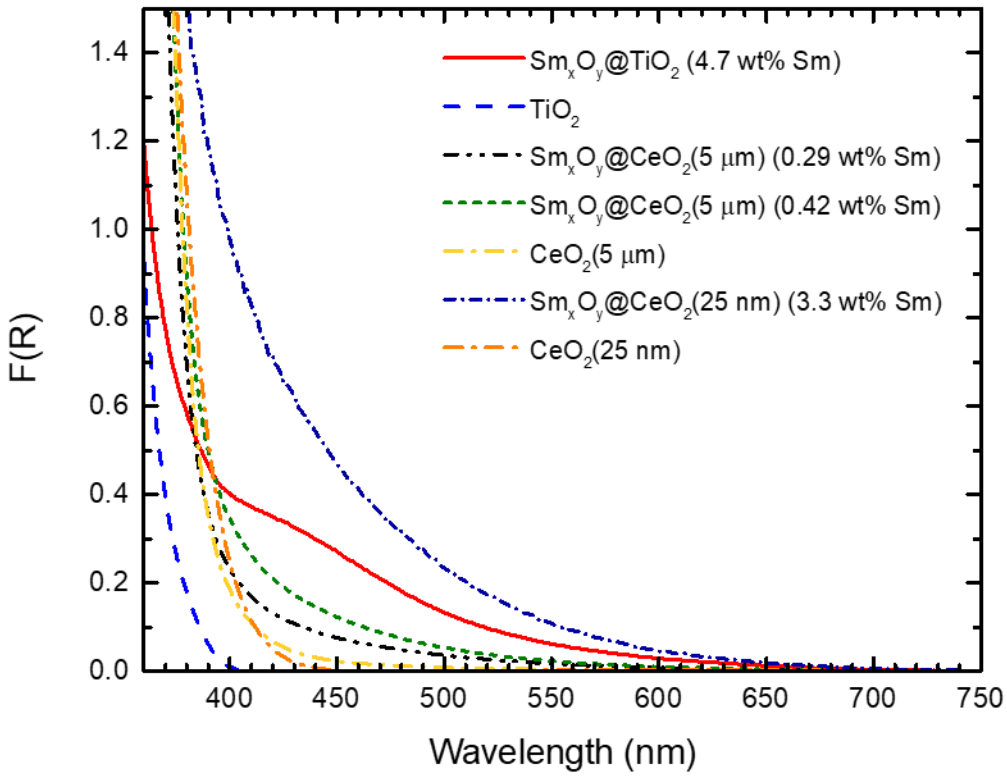

Figure S5.17 Zoomed in version of the diffuse reflectance of the various nanomaterials focusing primarily on the visible region of the electromagnetic spectrum.

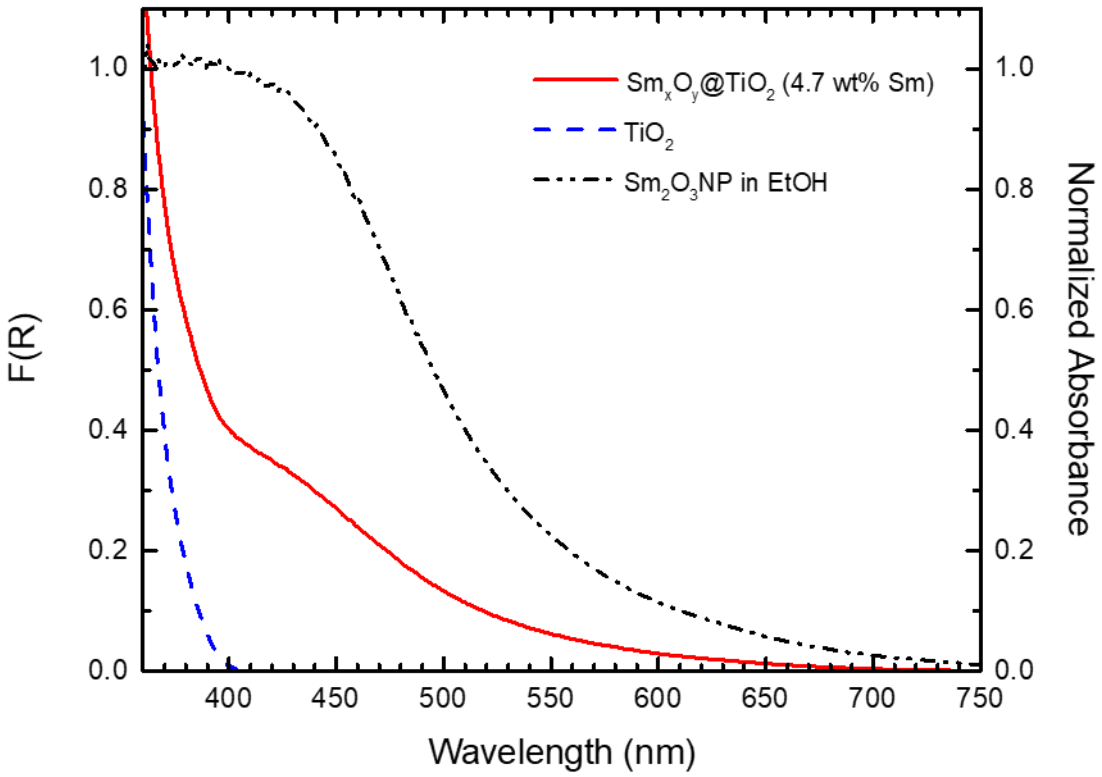

Figure S5.18 Visible region of the diffuse reflectance spectrum of $Sm_xO_y@TiO_2$ compared to that of unmodified TiO_2 and also to the normalized absorbance spectrum of a suspension of Sm_2O_3NP from our previous work, containing the smallest NPs of the polydisperse population (≈50–70 nm). Note the presence of the band at 400–450 nm in the DR spectrum of $Sm_xO_y@TiO_2$ and its resemblance to the absorbance profile of Sm_2O_3NP.

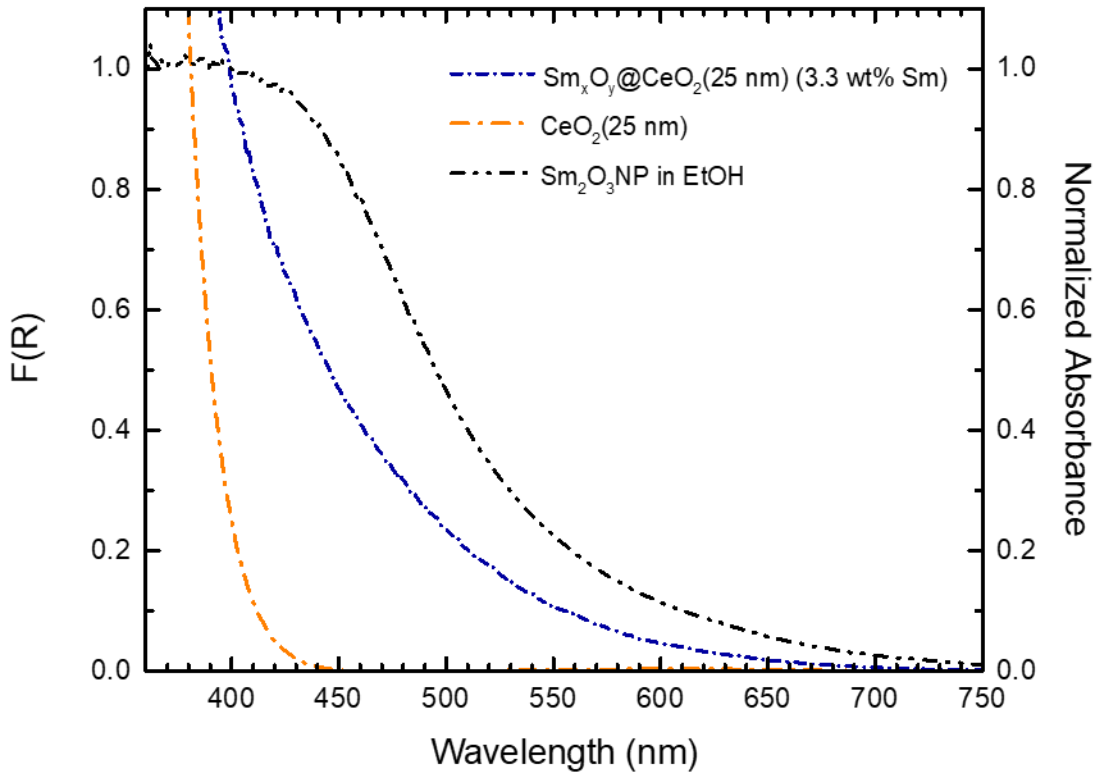

Figure S5.19 Visible region of the diffuse reflectance spectrum of 3.3 wt% Sm_xO_y@CeO_2 (<25 nm) compared to that of unmodified CeO_2 (<25 nm) and also to the normalized absorbance spectrum of a suspension of Sm_2O_3NP from our previous work, containing the smallest NPs of the polydisperse population (≈50–70 nm). Note the lack of a band between 400–450 nm observed for Sm_xO_y@TiO_2 in Figure S5.12.

Table S5.1 Summary of ICP-MS results showing Sm content (wt%) in various nanomaterials. Each value is the average result of three measurements.

Sample	$Sm_xO_y@TiO_2$	$Sm_xO_y@CeO_2$ (<5 µm)	$Sm_xO_y@CeO_2$ (<5 µm) double optimal loading	$Sm_xO_y@CeO_2$ (<25 nm)
Batch 1	4.63	0.287	0.422	3.31
Batch 2	4.88	-	-	-
Batch 3	4.63	-	-	-
Average	4.71	-	-	-

Determination of possible Sm leaching (performed using Batch 2 of $Sm_xO_y@TiO_2$):

Sm content before use (average of three measurements): 4.87606 wt%

Sm content after use (average of three measurements): 4.87474 wt%

Amount Sm leached: 0.0270302%

The level of Sm leached is less than three one-hundredths of one percent of the total samarium comprising the catalyst and was therefore considered negligible in the main text.

VI. Photocatalytic cyclizations

Photocatalytic reductive cyclization of chalcones **1a-f**:

To an oven dried 20 mL Pyrex test-tube was added 1 mmol of substrate, 60 mg catalyst and 15 mL dry MeCN. The reaction was purged with Ar for 20 min, during which time 5 equiv (880 µL) of pre-distilled *i*-Pr_2NEt stored under inert atmosphere was injected while stirring. The reaction was then irradiated for the noted timeframes using various LEDs. Upon completion the crude reaction mixture was centrifuged at 10,000 rpm for 25 min, the supernatant collected and the washing procedure was repeated three additional times with MeCN. The combined supernatants were passed through a 0.2 µm filter and the solvent was removed by rotary evaporation at 39°C under reduced pressure. The flask was then dried under high vacuum for at least 30 min before NMR spectroscopy was performed using phenanthrene as the internal standard.

Table S5.2 Control experiments for the photoreductive cyclization of chalcone **1a**.

Entry	Catalyst	Amine	Condition	Yield[a] **2a** (%)
1	Sm_xO_y@TiO_2 (4.7 wt% Sm)	*i*-Pr_2NEt (5 equiv)	dark 35°C	0
2	Sm_xO_y@TiO_2 (4.7 wt% Sm)	no amine	400 nm, 90 W, 3 h	2
3	no catalyst	*i*-Pr_2NEt (5 equiv)	400 nm, 90 W, 3 h	10
4	no catalyst	no amine	400 nm, 90 W, 3 h	3
5	no catalyst	no amine	dark 35°C	0
6	Sm_xO_y@TiO_2 (4.7 wt% Sm)	*i*-Pr_2NEt (5 equiv)	368 nm, 3 W, 8 h	41
7	Sm_xO_y@TiO_2 (4.7 wt% Sm)	*i*-Pr_2NEt (5 equiv)	408 nm, 5 W, 16 h	64
8	Sm_xO_y@TiO_2 (4.7 wt% Sm)	*i*-Pr_2NEt (5 equiv)	465 nm, 20 W, 16 h	40

[a]Determined by ^{1}H NMR spectroscopy using an internal standard.

Control reactions conducted in the dark were performed at 35°C in order to simulate the actual thermal conditions of reactions irradiated by LEDs and thereby avoid disregarding any thermal contribution to the apparent photocatalytic formation of the cyclization products. The temperature reached by reactions irradiated by LEDs was measured by immersing a thermocouple into solution under irradiation and monitoring the temperature over a period of over 20 min at which point the temperature had remained stable at 35 ± 0.5°C for roughly 10 minutes.

Cost effectiveness calculation:

Cost effectiveness of the heterogeneous $Sm_xO_y@TiO_2$ catalyzed system relative to homogeneous catalysis using $Ru(bpy)_3^{2+}$ and $Sm(OTf)_3$ as reported by Xia and coworkers (ref 5b in the main text) was estimated based on the following calculation, which compares the two reactions conducted on equivalent scales (1 mmol chalcone **1a**).

Table S5.3 Chemical costs related to homogeneous vs heterogeneous catalytic formation of **2a**.

Chemical	Cost/g ($CAD)	Supplier	Amount Used	Cost/Reaction ($CAD)	Total Chemical Cost/Reaction ($CAD)
$Sm(NO_3)_3$•$6H_2O$	3.49	Sigma-Aldrich	16.6 mg[a], 0.0372 mmol	0.058[a]	0.156[b]
TiO_2 (P25)	1.71	Sigma-Aldrich	57.2 mg, 0.716 mmol	0.098	
$Sm(OTf)_3$	12.65	Sigma-Aldrich	597 mg, 1 mmol	7.56	14.41
$Ru(bpy)_3(PF_6)_2$	159.50	Sigma-Aldrich	43 mg, 0.05 mmol	6.85	

[a]This amount includes the 5 mol% optimal Sm loading during catalyst preparation. [b]First catalyst use only.

$$\frac{homogeneous\ cost}{heterogeneous\ cost} = \frac{14.41\ \$CAD}{0.156\ \$CAD} = 92.4$$

According to this calculation, based on only the first use of the recyclable $Sm_xO_y@TiO_2$, the heterogeneous catalytic system is over 90-fold more cost-effective than the analogous homogeneously catalyzed system, even when accounting for the samarium precursor lost during synthesis of the catalyst. This estimate is based on current costs of the largest advertised (and least expensive) commercial quantities of starting materials available shipped to Canada from a single supplier (Sigma-Aldrich).

Photocatalytic Cycloadditions of bis(enones) **4a-c**:

Photocycloadditions of bis(enones) were conducted in a manner analogous to the photoreductive cyclization of chalcones. Oven-dried 20 mL Pyrex test tubes were charged with the substrate, catalyst, DABCO and 5 mL dry MeCN, sealed, purged with Ar for 20 min and irradiated for 1 h using a 400 nm LED. Workup was the same as for the photoreductive cyclization of chalcones. Diastereomer ratios were determined by ^{1}H NMR spectroscopy.

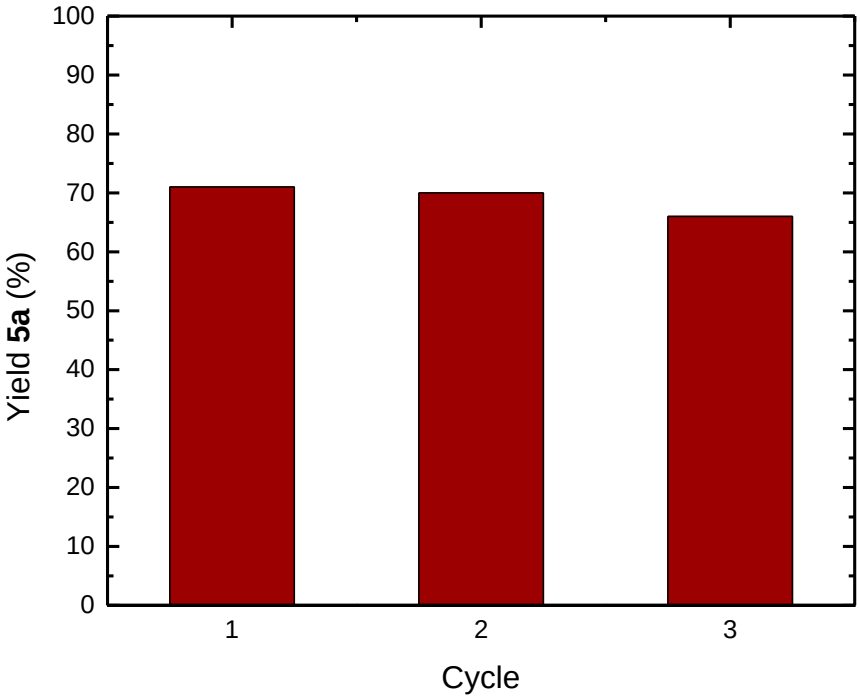

Figure S5.20 Reusability study of $Sm_xO_y@TiO_2$ in the heterogeneous [2+2] photocycloaddition of **4a** to form the cycloadduct **5a**.

For cycle 1, reaction conditions were identical to those summarized in Table 5.3. For cycle 2, the reaction was performed on an 85% scale relative to cycle 1 using 17 mg of recovered catalyst, 0.1445 mmol **4a**, 5 equivalents DABCO and 4.75 mL dry MeCN. For cycle 3, the reaction was performed on a 100% scale relative to cycle 1 with respect to substrate and amine (0.17 mmol **4a**, 5 equivalents DABCO and 5 mL dry MeCN) despite that only 17 mg of recovered catalyst was available. In addition, irradiation time was maintained at 1 h for all three cycles regardless of the noted changes to relative catalyst, substrate and amine concentrations. This series of experiments was conducted in an effort to determine the impact, if any, that small losses to recovered catalyst quantities might have on recyclability studies such as

those performed for the Sm_xO_y@TiO_2-catalyzed photoreductive coupling of **1a** in which reactant concentrations and irradiation time were kept constant and catalyst losses during the recovery process were considered negligible. This exercise also examined whether in cases where losses to recovered catalyst mass were clearly non-negligible, should total irradiation time be kept constant or scaled back in each trial to match decreases in catalyst and reactant amounts. Although in this case any effects appear to be minimal, they may be responsible for the slight decrease in yield of **5a** reported for cycle 3. In all cases, the recovered catalyst was simply obtained by centrifugation, dried under ambient conditions and weighed but was not further treated in any way before being reused for subsequent cycles.

VII. Turnover Number (TON) and Turnover Frequency (TOF) Calculations

Photocatalytic reductive cyclization of chalcone **1a**:

TON with respect to masses of substrate and samarium:

$$\text{TON} = \frac{(0.001\ \text{mol})(0.70\ \text{yield})\left(150.36\ \text{g mol}^{-1}\ \text{substrate MW}\right)(5\ \text{cycles})}{(0.060\ \text{g total catalyst})(0.047\ \text{Sm by weight})} = 186.6$$

TON with respect to masses of substrate and total nanocomposite:

$$\text{TON} = \frac{(0.001\ \text{mol})(0.70\ \text{yield})\left(150.36\ \text{g mol}^{-1}\ \text{substrate MW}\right)(5\ \text{cycles})}{(0.060\ \text{g total catalyst})} = 8.8$$

TOF with respect to masses of substrate and samarium:

$$\text{TON} = \frac{(0.001\ \text{mol})(0.70\ \text{yield})\left(150.36\ \text{g mol}^{-1}\ \text{substrate MW}\right)}{(0.060\ \text{g total catalyst})(0.047\ \text{Sm by weight})(3\ \text{h})} = 12.4\ \text{h}^{-1}$$

TOF with respect to masses of substrate and total nanocomposite:

$$\text{TON} = \frac{(0.001\ \text{mol})(0.70\ \text{yield})\left(150.36\ \text{g mol}^{-1}\ \text{substrate MW}\right)}{(0.060\ \text{g total catalyst})(3\ \text{h})} = 0.58\ \text{h}^{-1}$$

Photocatalytic Cycloadditions of bis(enone) **4a**:

TON with respect to masses of substrate and samarium:

$$\text{TON} = \frac{(0.00017\ \text{mol})(0.71\ \text{yield})\left(304.39\ \text{g mol}^{-1}\ \text{substrate MW}\right)(3\ \text{cycles})}{(0.020\ \text{g total catalyst})(0.047\ \text{Sm by weight})} = 117.3$$

TON with respect to masses of substrate and total nanocomposite:

$$\text{TON} = \frac{(0.00017\ \text{mol})(0.71\ \text{yield})\left(304.39\ \text{g mol}^{-1}\ \text{substrate MW}\right)(3\ \text{cycles})}{(0.020\ \text{g total catalyst})} = 5.5$$

TOF with respect to masses of substrate and samarium:

$$\text{TON} = \frac{(0.00017\ \text{mol})(0.71\ \text{yield})\left(304.39\ \text{g mol}^{-1}\ \text{substrate MW}\right)}{(0.020\ \text{g total catalyst})(0.047\ \text{Sm by weight})(1\ \text{h})} = 39.1\ \text{h}^{-1}$$

TOF with respect to masses of substrate and total nanocomposite:

$$\text{TON} = \frac{(0.00017\ \text{mol})(0.71\ \text{yield})\left(304.39\ \text{g mol}^{-1}\ \text{substrate MW}\right)}{(0.020\ \text{g total catalyst})(1\ \text{h})} = 1.8\ \text{h}^{-1}$$

VIII. NMR Spectra

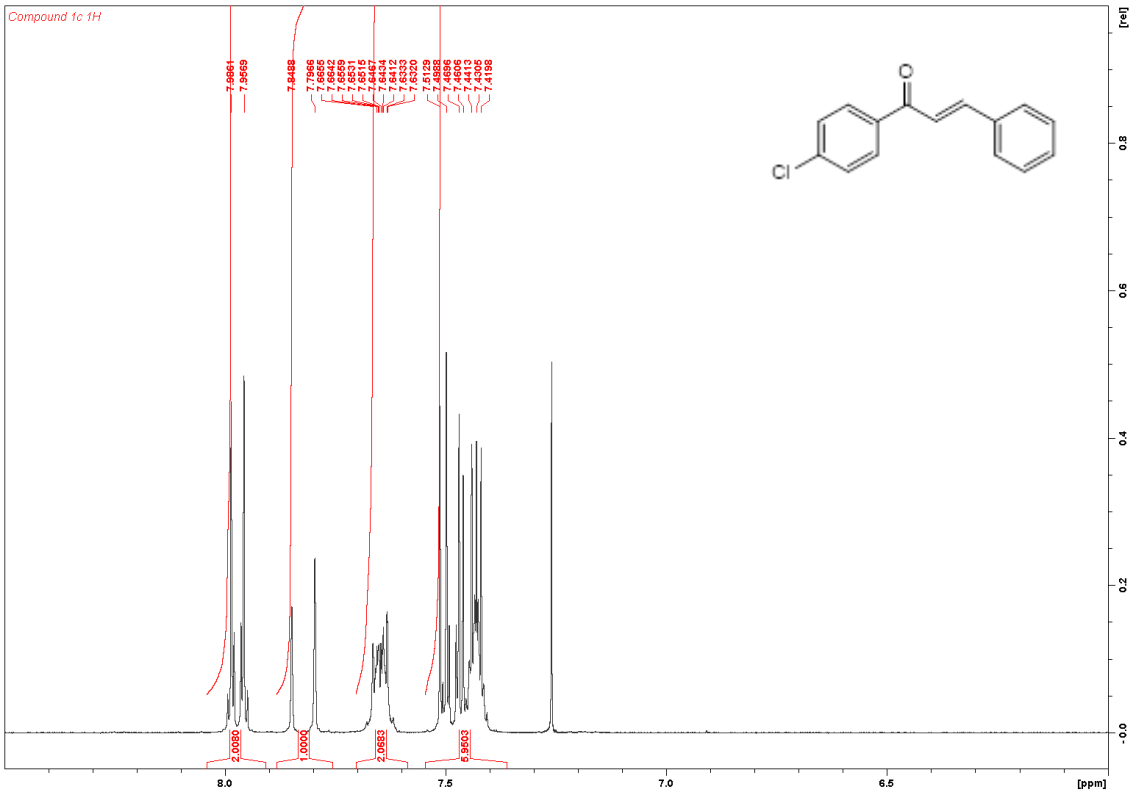

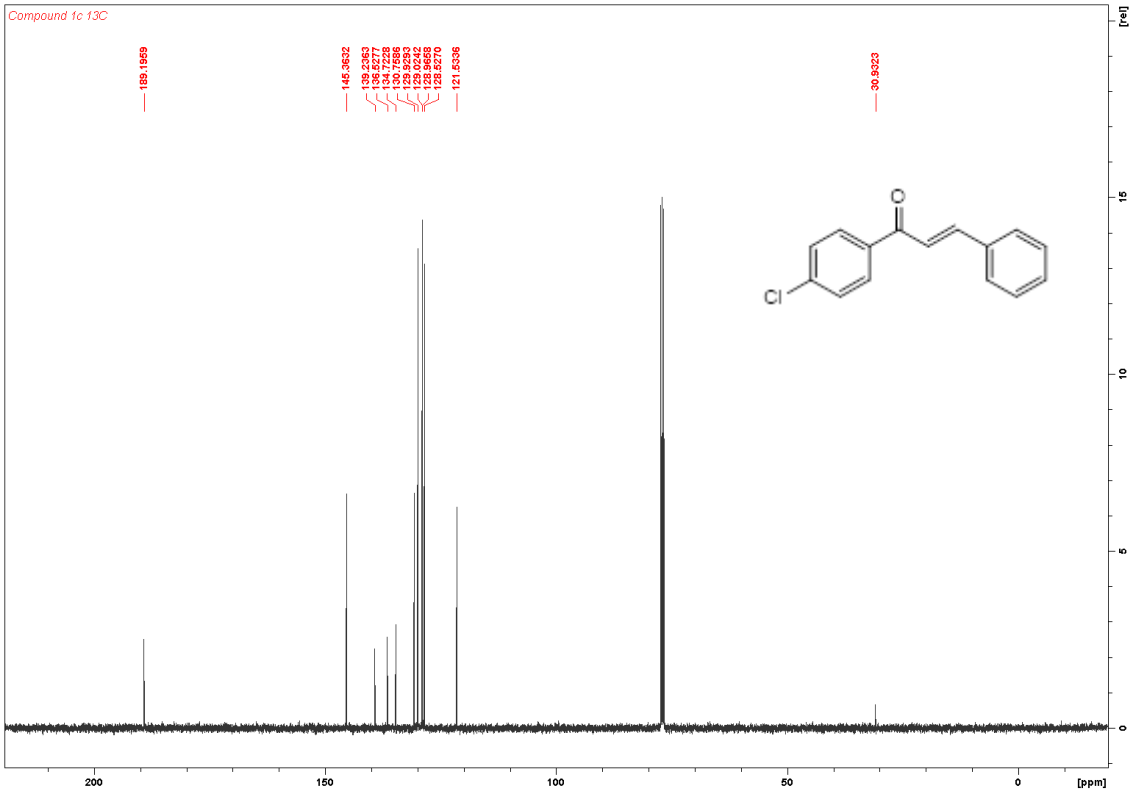

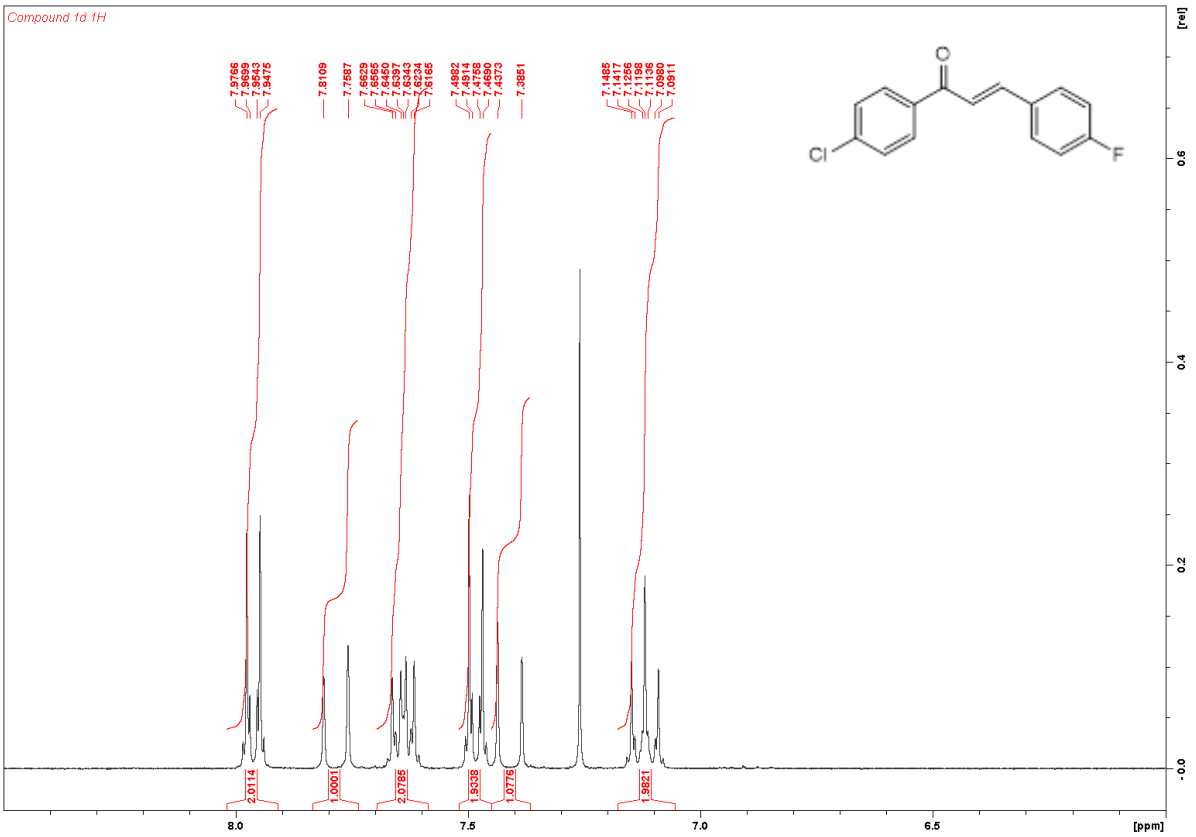
Compound 1d 1H
7.9766
7.9588
7.9543
7.9475
7.8109
7.7687
7.6629
7.6585
7.6540
7.6397
7.6343
7.6234
7.6165
7.4982
7.4914
7.4768
7.4690
7.4573
7.3851
7.1485
7.1417
7.1256
7.1198
7.1138
7.0980
7.0911
2.0114
1.0001
2.0785
1.9338
1.0776
1.9821
O
Cl
F
8.0
7.5
7.0
6.5
[ppm]
[rel]


Compound 1d 13C
189.0718
165.5136
163.0081
144.1089
139.3884
136.4987
131.0626
131.0251
130.6550
130.4700
129.9630
129.0586
121.2949
121.2721
116.2966
116.1722
50.9449
O
Cl
F
200
150
100
50
0
[ppm]
[rel]

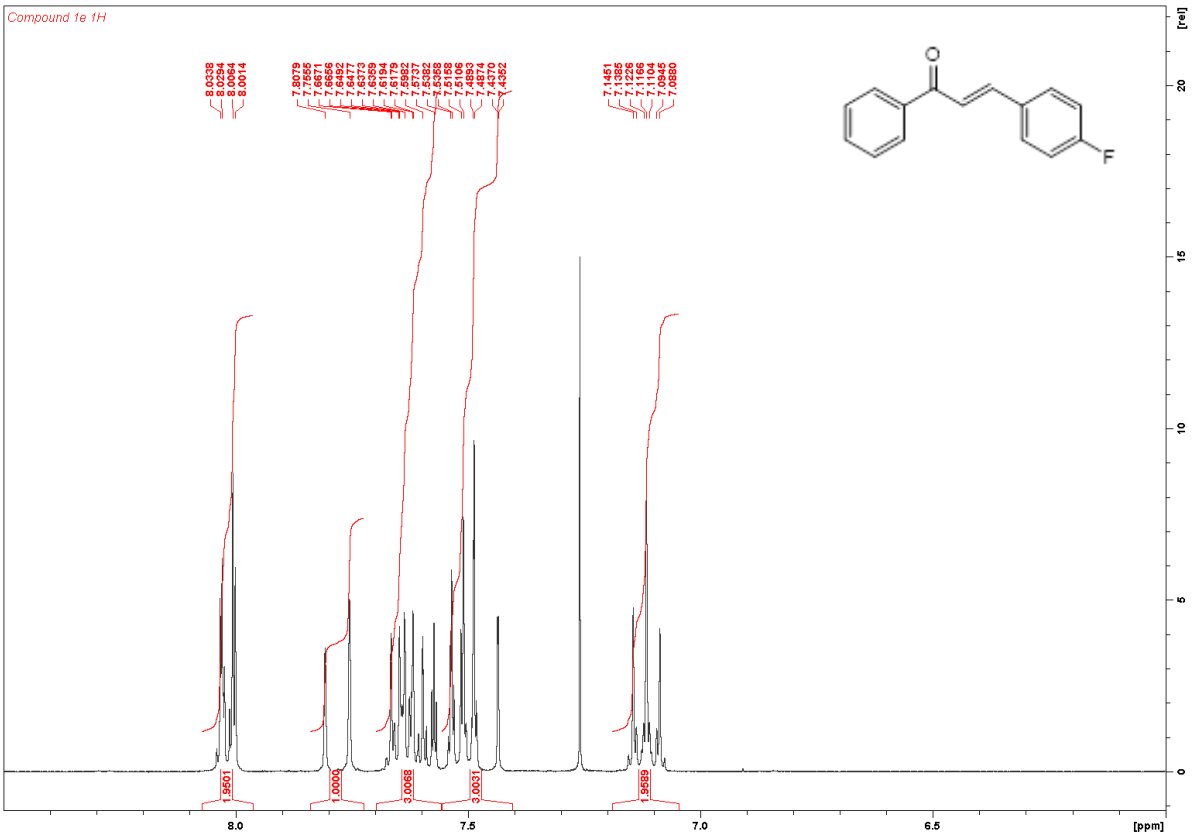
Compound 1e 1H
8.0338
8.0294
8.0064
8.0014
7.8079
7.7565
7.6871
7.6816
7.6492
7.6477
7.6373
7.6288
7.6194
7.6179
7.5882
7.5737
7.5387
7.5368
7.5166
7.5106
7.4893
7.4874
7.4370
7.4362
7.1451
7.1385
7.1226
7.1166
7.1044
7.0945
7.0880
1.9501
1.0000
3.0068
3.0031
1.9589
8.0
7.5
7.0
6.5
[ppm]
[rel]
F

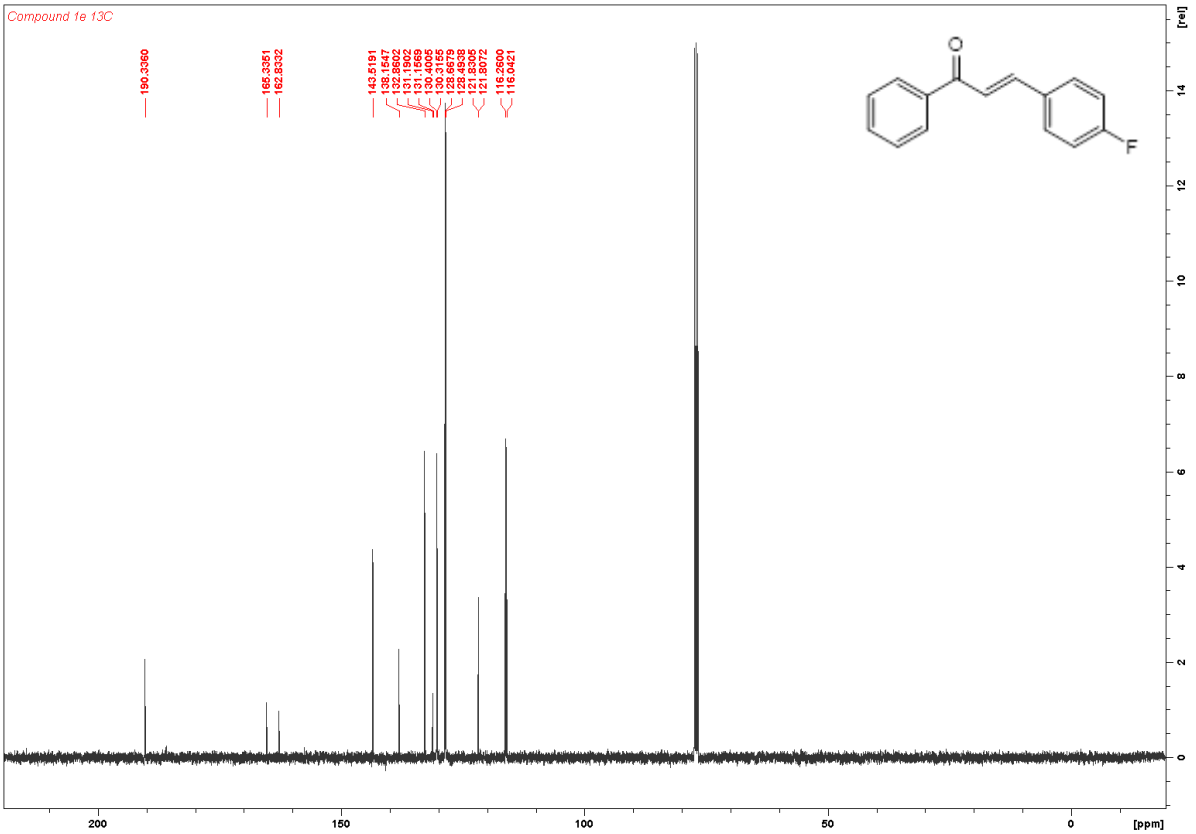
Compound 1e 13C
190.3360
165.3351
162.8332
143.5191
138.1547
132.8602
131.1902
131.1569
130.4065
130.3155
128.6679
128.4938
121.8075
121.8072
116.2620
116.0421
200
150
100
50
0
[ppm]
[rel]
F

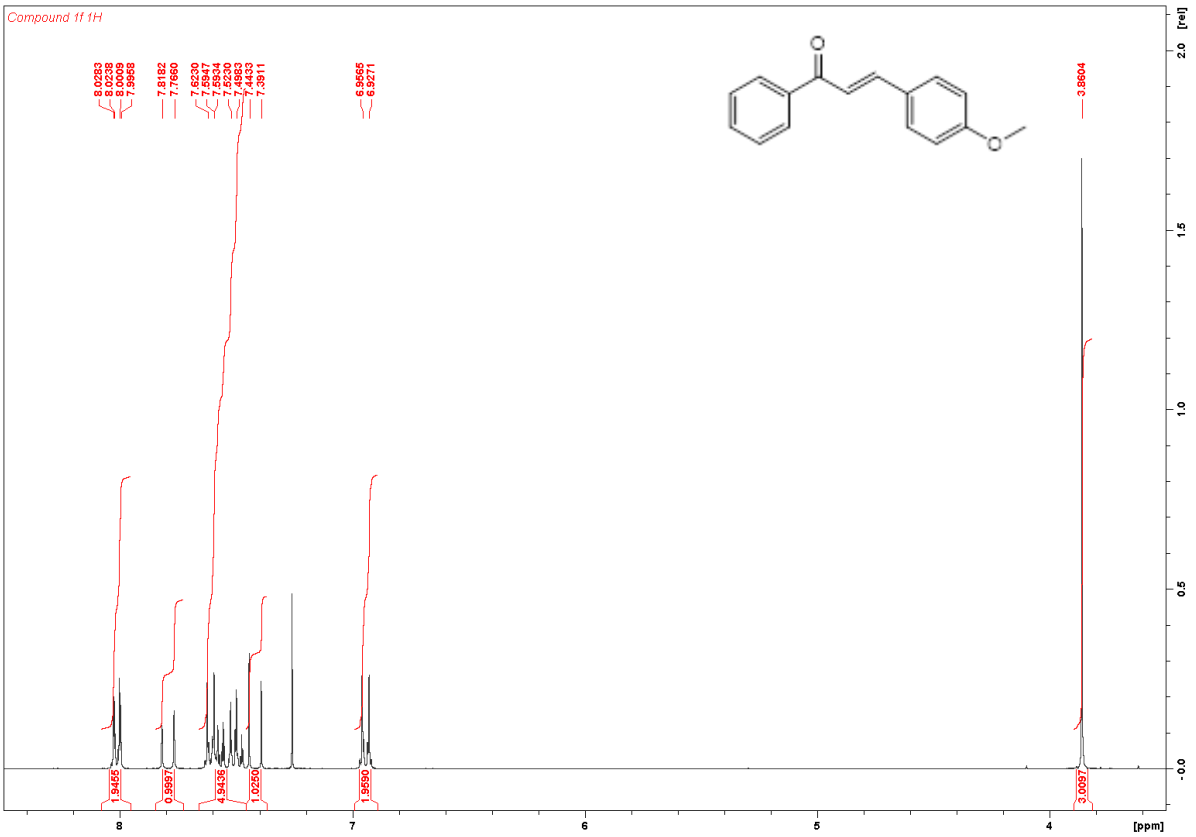
Compound 1f 1H
8.0283
8.0238
8.0093
7.9968
7.8182
7.7660
7.6239
7.6147
7.5944
7.5230
7.4983
7.4433
7.3911
6.9565
6.9271
3.8604
1.9455
0.9997
4.9436
1.0250
1.9990
3.0097
8
7
6
5
4
[ppm]
[rel]

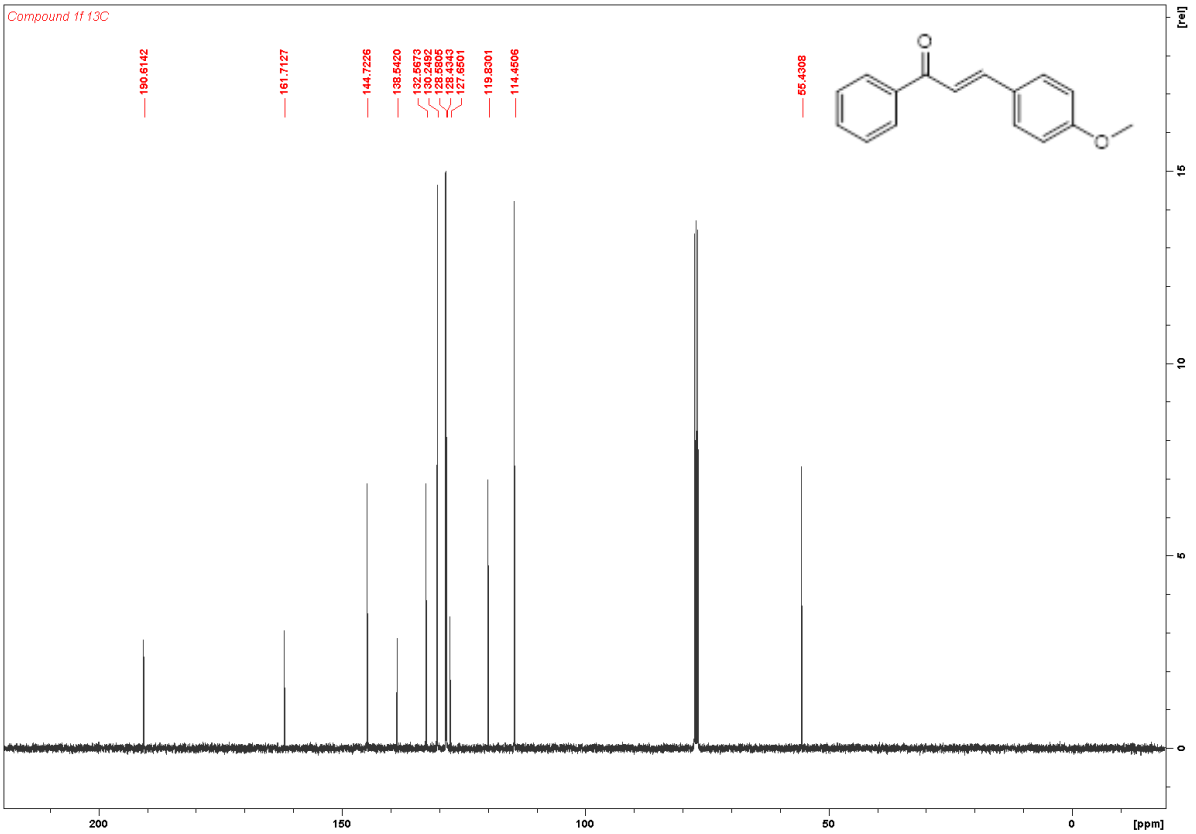
Compound 1f 13C
190.6142
161.7127
144.7226
138.5420
132.5673
130.2432
128.5805
128.4343
127.6501
119.8301
114.4506
55.4308
200
150
100
50
0
[ppm]
[rel]

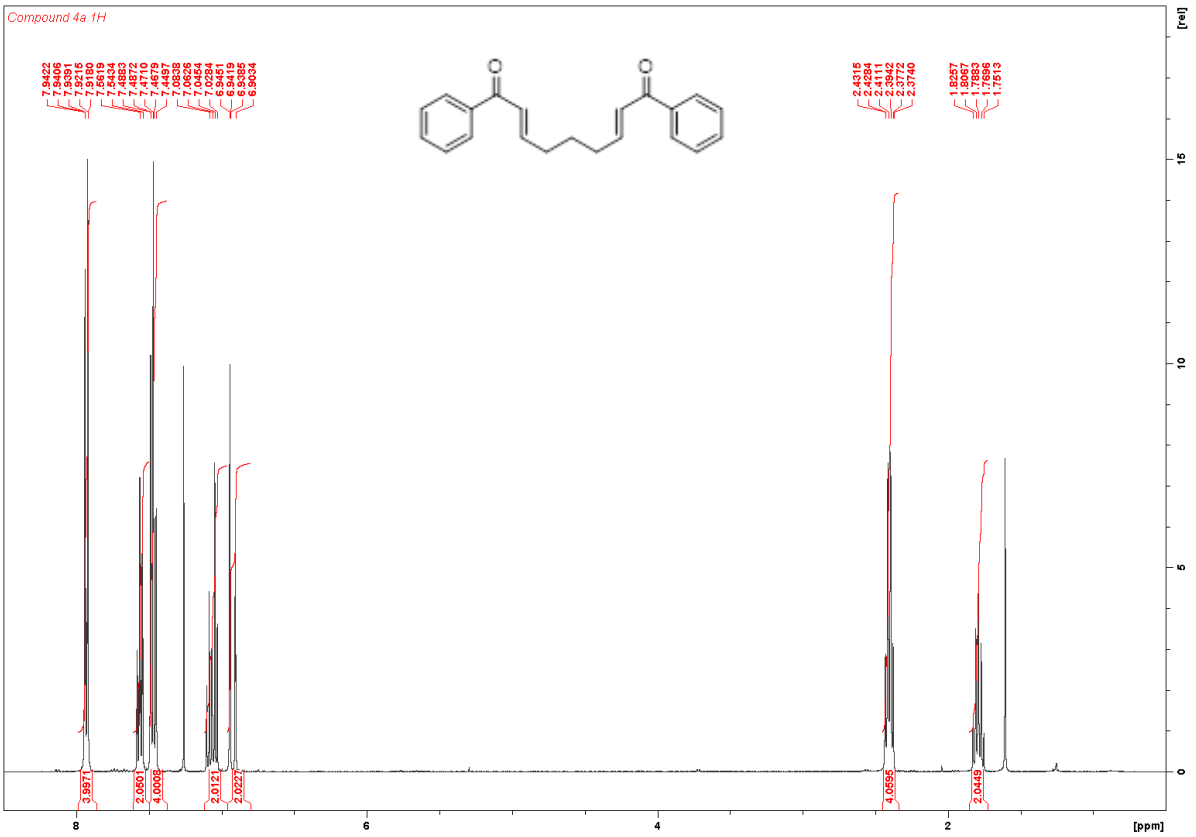
Compound 4a 1H
7.9422
7.9406
7.9391
7.9215
7.9180
7.5619
7.5434
7.4893
7.4872
7.4710
7.4679
7.4497
7.0628
7.0454
7.0284
6.9415
6.9385
6.9034
2.4315
2.4284
2.4111
2.3942
2.3772
2.3740
1.8257
1.8057
1.7883
1.7688
1.7513
3.9971
2.0501
4.0008
2.0121
2.0227
4.0556
2.0449
[rel]
[ppm]

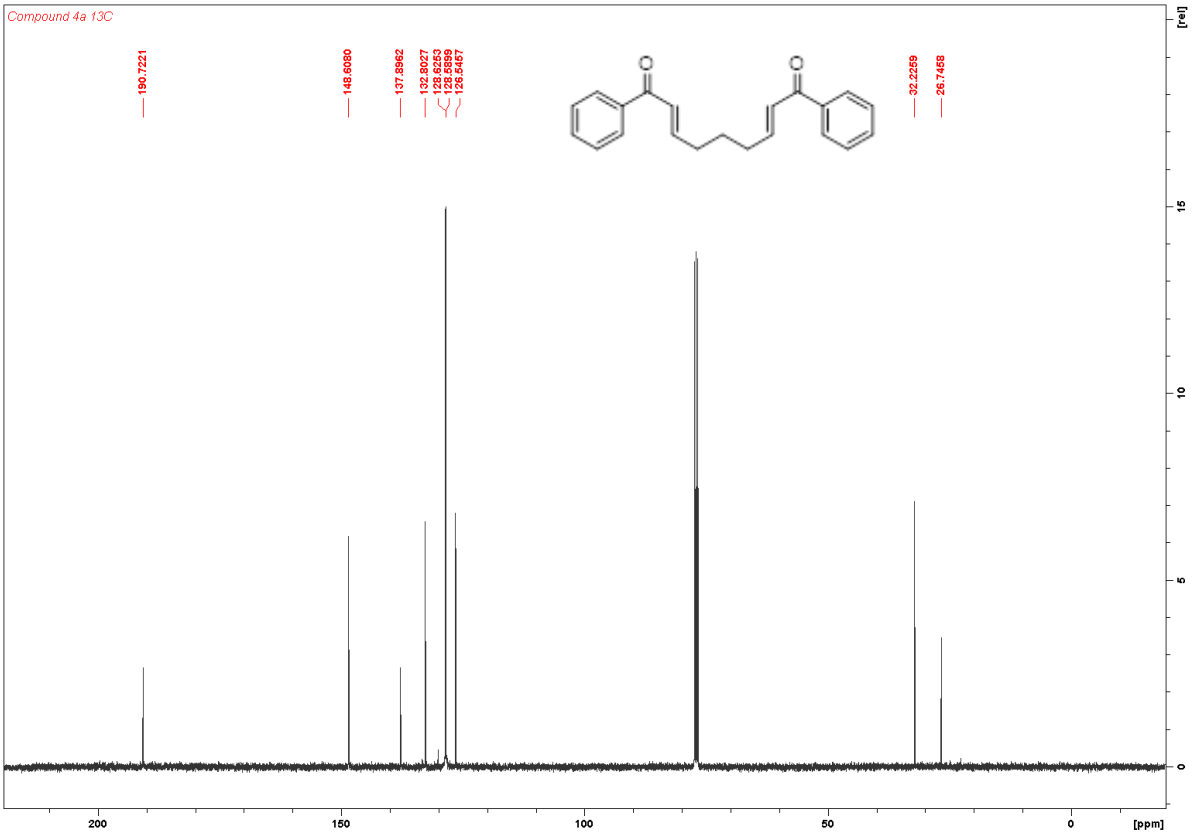
Compound 4a 13C
190.7221
148.6080
137.8962
132.8027
128.6253
128.5899
126.5467
32.2259
26.7458
[rel]
[ppm]

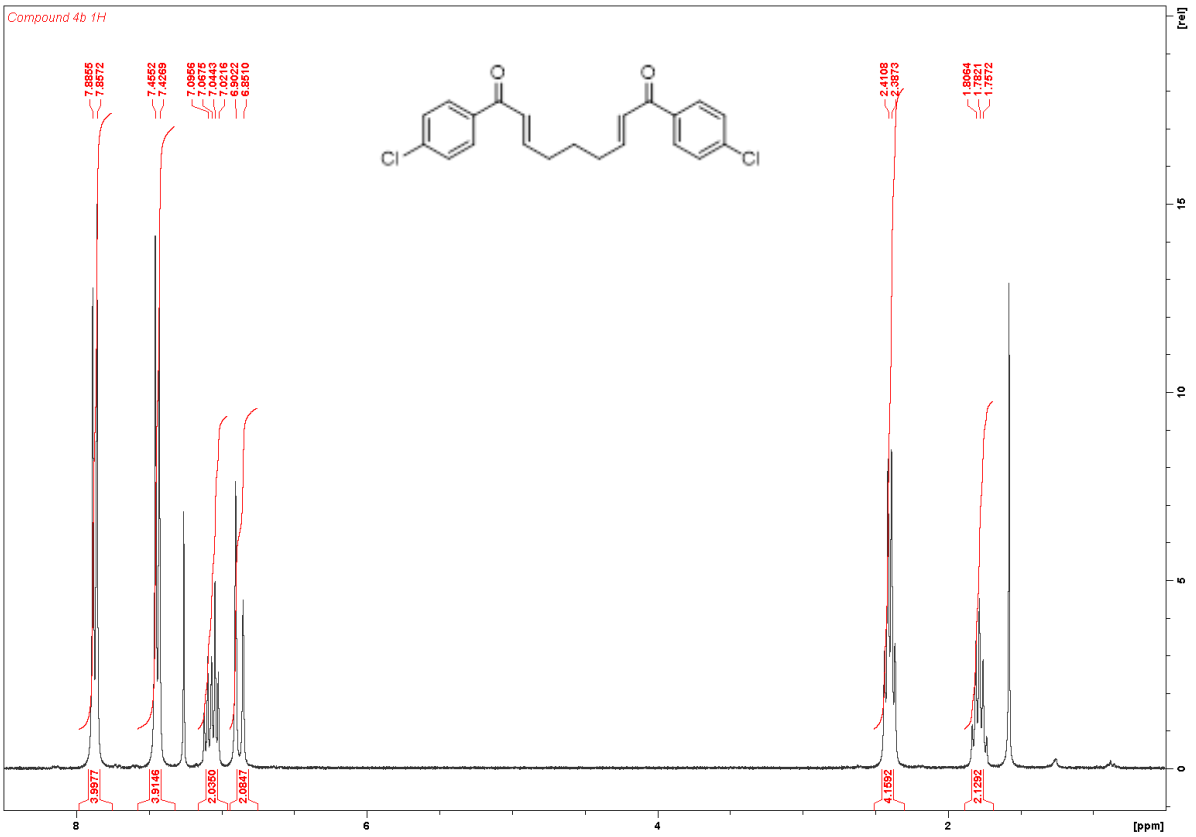
Compound 4b 1H
7.8855
7.8672
7.4552
7.4269
7.0986
7.0675
7.0443
7.0216
6.8922
6.8810
2.4108
2.3873
1.8064
1.7821
1.7572
Cl
Cl
3.9977
3.9146
2.0350
2.0847
4.1592
2.1292
8
6
4
2
[ppm]
[rel]
0
5
10
15

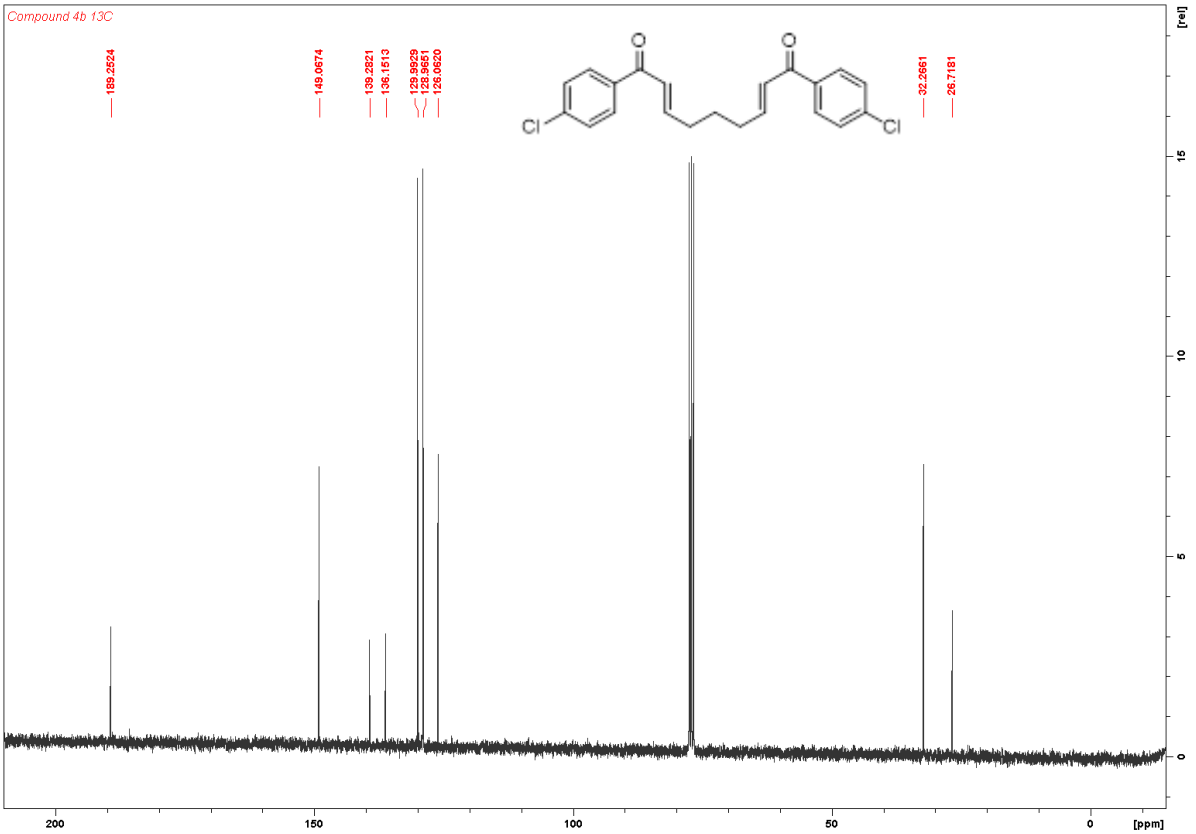
Compound 4b 13C
189.2524
149.0674
139.2821
136.1513
129.9929
128.9651
126.0620
32.2661
26.7181
Cl
Cl
200
150
100
50
0
[ppm]
[rel]
0
5
10
15

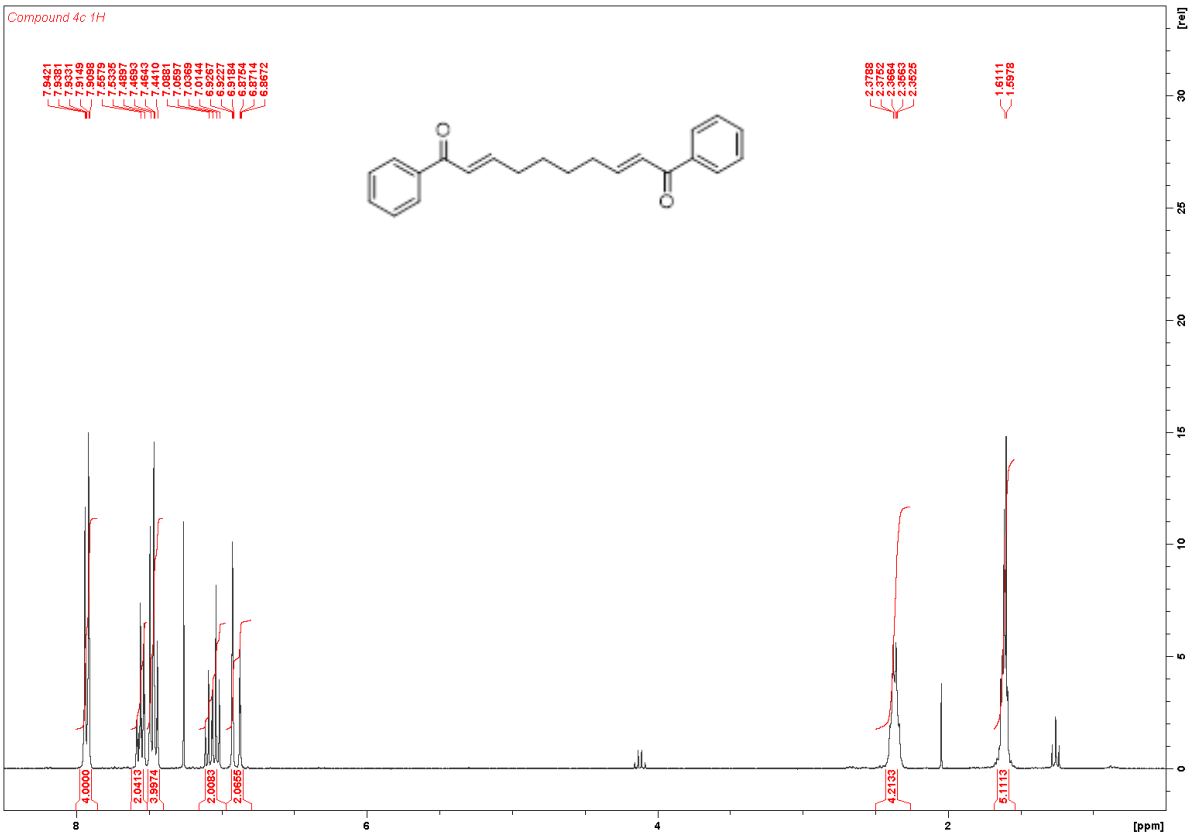
Compound 4c 1H
7.9421
7.9381
7.9331
7.9149
7.9098
7.5579
7.5335
7.4887
7.4693
7.4643
7.4410
7.0881
7.0697
7.0369
7.0144
6.9287
6.9127
6.8936
6.8754
6.8714
6.8672
2.3788
2.3752
2.3664
2.3563
2.3525
1.6111
1.5978
4.0000
2.0413
3.9974
2.0083
2.0655
4.2133
6.1113
8
6
4
2
[ppm]
[rel]

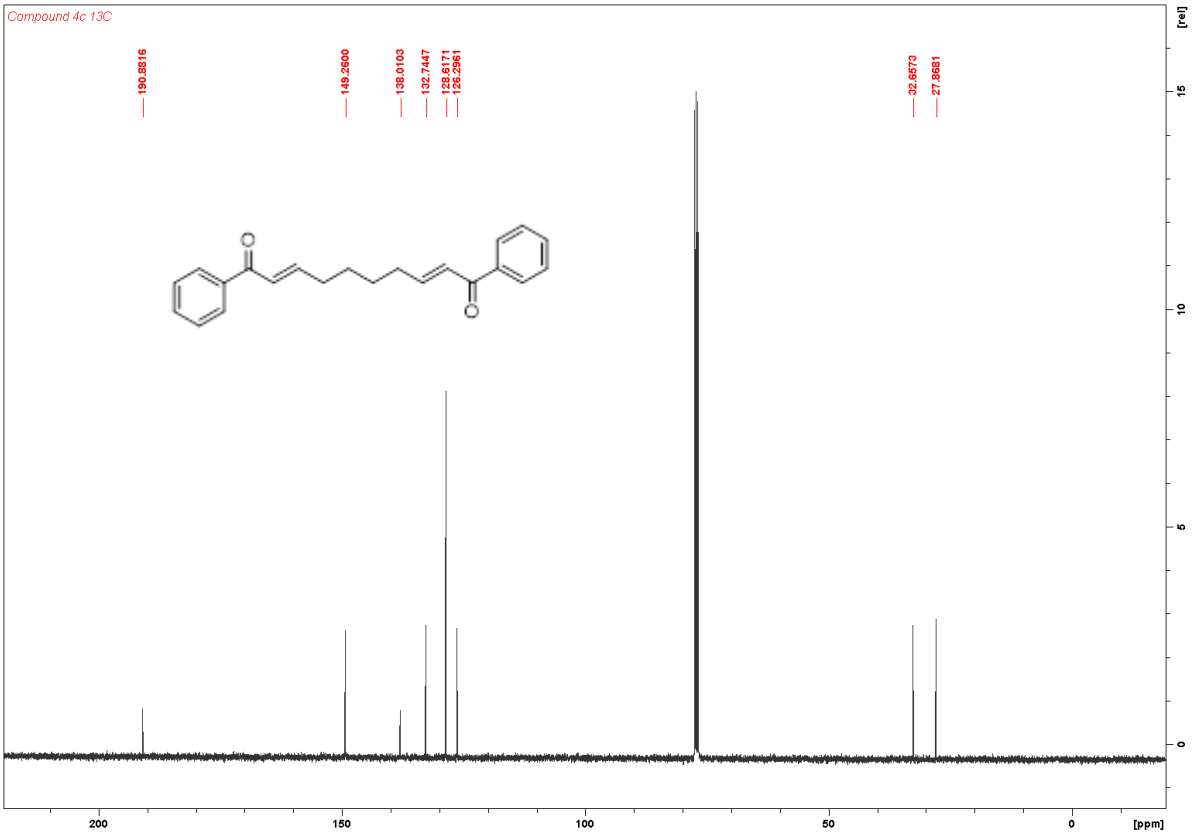
Compound 4c 13C
190.8816
149.2600
138.0103
132.7447
128.6171
126.2961
32.6573
27.8881
200
150
100
50
0
[ppm]
[rel]

IX. References

(1) Asahara, H.; Takeda, S.; Saigo, K.; Nishiwaki, N. *Tetrahedron Lett.* **2015**, *56*, 2504-2507.

(2) Li, K.; Alexakis, A. *Chem. Eur. J.* **2007**, *13*, 3765-3771.

(3) Yang, J.; Felton, G. A. N.; Bauld, N. L.; Krische, M. J. *J. Am. Chem. Soc.* **2004**, *126*, 1634-1635.

(4) López, S.; Fernández-Trillo, F.; Midón, P.; Castedo, L.; Saá, C. *J. Org. Chem.* **2005**, *70*, 6346-6352.

(5) Hodgson, G. K.; Impellizzeri, S.; Hallett-Tapley, G. L.; Scaiano, J. C. *RSC Adv.* **2015**, *5*, 3728-3732.

(6) Hodgson, G. K.; Impellizzeri, S.; Scaiano, J. C. *Catal. Sci. Technol.* **2016**, *6*, 7113-7121.

This manuscript has been adapted from *ACS Catal.* **2018**, *8*, 2914-2922, with permission, from the American Chemical Society. All changes were purely to facilitate consistent formatting and are non-scientific in nature.

5.4 Accompaniment to Chapter 5

This final chapter in the iterative design of a samarium-based nanomaterial for heterogeneous nanocatalysis indeed represents the culmination of the doctoral work presented in this dissertation. Building upon experimental results and insights from previous investigations, the evidence-based, step-wise evolution of the original Sm_2O_3NP catalyst to ultimately arrive at the rational design of an effective Sm_xO_y@TiO_2 nanocomposite symbolizes the achievement of the primary objectives of this doctoral research program. The final multifunctional material offers all of the benefits of pure heterogeneous catalysis, and has shown considerable potential as a more sustainable alternative to precious metal catalysts for synthetically relevant organic transformations.

The development of this exceptional nanomaterial may have taken a wildly different course without the insights gleaned from studies of catalysis by Sm_2O_3NP at the single molecule level. If a suitable system could be designed, it would be interesting to apply single molecule techniques to heterogeneous dual photoredox-Lewis acid catalysis by Sm_xO_y@TiO_2 in order to gain invaluable mechanistic insights.

Although it might be possible to construct a suitable system based on fluorescence modulation (OFF to ON activation or $\lambda_1 \rightarrow \lambda_2$ shifting), a TIRFM-based single molecule investigation of the mechanisms proposed in Chapter 5 would be severely hampered by the inability to differentiate between active sites corresponding to Sm_xO_y or TiO_2. Fortunately, this limitation did not prevent us from establishing that photocatalysis by Sm_xO_y@TiO_2 was a heterogeneous process. Nevertheless, a detailed mechanistic investigation incorporating both bench scale and other single molecule techniques might reveal whether each substrate molecule is initially coordinated to a Sm_xO_y NP, a LA site on the support, or whether multiple Sm_xO_y NPs are involved throughout the reaction (recall that TiO_2 did exhibit catalytic activity on its own). Indeed, the coexistence of both pathways as well as possible chain components might be related to product distribution or influence diastereoselectivity, with a more thorough understanding of the catalytic mechanisms leading to further insight on how best to optimize the nanomaterial further.

6. Conclusions and Outlook

6.1 Summary and Conclusions

Throughout this dissertation, the theme has consistently been one of using an iterative approach to the design and application of nanomaterials for heterogeneous catalysis. What began with the photochemical synthesis and characterization of a new nanomaterial led to the identification of Brønsted acidity (Chapter 2), which proved useful for the catalytic formation of a useful organic dye (Chapter 3). However, studying the system at the single molecule level revealed that the catalysis discussed in Chapter 3 would best be described as semi-heterogeneous. Although the nanocatalyst could be separated from the product with relative ease by simply increasing the ionic strength, room for improvement did still exist.

Further exploration into the utility of samarium oxide nanoparticles for applications in catalysis demonstrated that manipulating the parameters of the system by controlling ionic strength *in situ* was enough to make use of the additional advantages offered by pure heterogeneous catalysis (Chapter 4). This strategy allowed the full potential of the nanomaterial to be realized, and extended the application scope to include heterogeneous oxidative catalysis coupled to aldehyde chemistry. Not only did this allow efficient one-pot aldehyde chemistry to be conducted beginning with a less expensive and more synthetically accessible starting material, the behaviour of the nanocatalyst also precluded undesirable and often problematic over-oxidation to the corresponding carboxylic acid.

The successful implementation of single molecule fluorescence microscopy for evaluation of the catalytic performance of samarium oxide nanoparticles in both systems described in Chapters 3 and 4 resulted in truly unique mechanistic insights into the behaviour of a new nanocatalyst on an unprecedented level. In addition to

distinguishing between homogeneous, semi-heterogeneous and pure heterogeneous catalysis, it positively identified a subpopulation of smaller nanoparticles in a polydisperse sample as the true catalytically active species. In Chapter 4, studying catalysis using dual colour single molecule techniques went a step further by unequivocally demonstrating that the activated substrate with aldehyde-like reactivity was in fact bound to the surfaces of catalytic nanoparticles, an important aspect of the catalytic mechanism. This result also provided experimental support for a similar mechanism to explain coupled alcohol oxidation and Wittig olefination chemistry, and drew interesting parallels between the catalytic properties of samarium oxide and the less sustainable ruthenium nanostructured catalysts.

The innovative nature of the protocol developed for streamlined analysis of large quantities of data related to single molecule experiments vastly improved the efficiency of using TIRFM to study catalytic processes in real time, facilitating research on a much larger scale. The ability to investigate a higher number of systems, experimental conditions, and control reactions provided a statistically greater degree of reliability in results, as did the nature of the protocol itself. As explained in detail in Section 3.3, partial automation of the identification of fluorescence bursting events increased the accuracy and precision of TIRFM experiments, and removed a major element of unintentional bias from the analysis. The long-term impact of this advancement remains to be seen, but it seems reasonable that it might contribute largely to bringing this bottom up approach to catalysis research into the spotlight, and that facilitating faster, easier, more reliable data analysis could help single molecule techniques to reach a new higher level of accessibility to the modern chemist.

Upon the basis of the two investigations detailed in Chapters 3 and 4, improvements were made to the design of the original nanocatalyst in order to produce a second generation samarium oxide based nanomaterial that was still highly efficient, but even more effective, for pure heterogeneous catalysis (Chapter 5). This ultimate objective of the doctoral work presented in this thesis was achieved by integrating samarium oxide nanoparticles with nanostructured titanium dioxide to form a new nanocomposite material which combines desirable properties from each of its two constituents. As an unexpected side-benefit, the *in situ* photochemical formation of

the supported samarium oxide nanoparticle component of the nanocomposite resulted in a tremendous decrease in nanoparticle average size and polydispersity–another improvement over the original highly polydisperse samarium oxide nanomaterial in which the smallest nanoparticles were consistently found to be catalytically active. The real fruit of this marriage though, was the first reported example of a bifunctional nanomaterial for heterogeneous dual photoredox-Lewis acid catalysis. The exceptional efficiency and effectiveness of this nanomaterial, as described for two photocatalytic applications in Chapter 5, opens the door to a myriad of possibilities for heterogenizing synthetically relevant catalytic reactions while maintaining high product yields and selectivity. The rise in popularity of dual- and tricatalytic strategies, especially in homogeneous photoredox catalysis, combined with a clear need to develop more sustainable alternatives to common precious metal organocatalysts, highlights the impact of the work described in Chapter 5, and by extension, the innovative and iterative approach taken toward the design of novel nanomaterials for heterogeneous catalysis presented in this thesis as a whole.

6.2 Future Directions and Outlook

On the surface, this dissertation establishes that samarium-based nanomaterials can be both efficient and effective for synthetically relevant applications in heterogeneous catalysis. All things considered, the applied research presented in this doctoral thesis could make a significant contribution toward a decreased reliance upon precious metals in catalysis. No less importantly though, it reinforces the importance of fundamental research; it demonstrates that the development of new nanomaterials for sustainable heterogeneous catalysis can benefit from innovation of analytical techniques not traditionally used to study catalysis, such as single molecule fluorescence microscopy. Looking beyond these intangible barriers between research fields and acquiring interdisciplinary skills (e.g. computer programming for improved single molecule study of catalysis) is likely to become an increasingly valuable asset as research and technology continue to co-evolve at a rapid pace.

In terms of future experimental work stemming directly from this thesis, the most promising would surely originate from further exploration of the utility of the final

samarium oxide/titanium dioxide nanocomposite material for various applications in heterogeneous photocatalysis. Improving stereoselectivity would certainly be of value, as that is one metric by which heterogeneous catalysts notoriously underperform relative to their homogeneous counterparts. Expanding the current line of research to similar bifunctional catalytic nanomaterials based upon other members of the lanthanide series would be another avenue to consider. These elements are clustered together for a reason–electronic occupation of their 4f orbitals–but moreover, many of them exhibit similar chemistry, which is also distinct from the d-block transition metals. This concept has already been introduced within this thesis, through a preliminary investigation into the effects of employing other nanostructured and microstructured lanthanide-containing oxides as catalytically active supporting matrices for samarium oxide nanoparticles. Admittedly, the scope of this effort was limited to cerium, one of the few lanthanides to stand apart due to the greater resemblance of its electronic configuration to those of the d-block transition metals. Nevertheless, combining samarium with other lanthanides, possibly while experimenting with interchanging their respective roles (nanoparticle or support) within the nanocomposite material would certainly be a valid pursuit. Alternative supporting matrices, whether catalytically active or passive in nature, could also be of interest. Mesoporous silicon-based supports such as SBA-15 or MCM-41 would be intriguing, as would Brønsted or Lewis acidic niobium oxides.

Finally, future work on heterogeneous photocatalysis by nanocomposite materials composed of lanthanide-based nanoparticles on active supports might benefit from the application of other single molecule techniques which are able to overcome the limitations mentioned in Section 5.4. For example, AFM-Raman spectroscopy or fluorescence-coupled electron microscopy might aid in visually identifying active sites or the locations of nanoparticles atop a supporting matrix in real time, leading to valuable insights into heterogeneous nanocatalyst dynamics. In any event, many more opportunities for the efficient and effective application of new lanthanide-containing nanocomposites in heterogeneous catalysis are likely to exist, and may lie just beyond the nanomaterials horizon.

6.3 Claims to Original Research

- The first report of samarium oxide nanoparticles prepared by photochemical reduction.

- Development of Brønsted acidic samarium oxide nanoparticles for synthesis of coumarin 153.

- Development of a data analysis protocol for efficient, accurate, precise and partially automated localization of fluorescence activation or wavelength shifting in Total Internal Reflection Fluorescence Microscopy (TIRFM) experiments. Based on innovation of an established MatLab script for super-resolution microscopy, adapted and expanded for application to TIRFM.

- Development of redox active samarium oxide nanoparticles for oxidative catalysis and one-pot aldehyde chemistry.

- Development of samarium oxide/titanium dioxide and samarium oxide/cerium oxide nanocomposite materials for heterogeneous photocatalysis.

- The first examples of heterogeneous dual photoredox-Lewis acid nanocatalysis, conducted using $Sm_xO_y@TiO_2$ and $Sm_xO_y@CeO_2$.